COMPUTER SIMULATION STUDY OF APATITE MINERAL SURFACES AND INTERFACES WITH SILICATES

By
MKHONTO DONALD

Submitted in fulfillment of the requirement for the degree of
Doctor of Philosophy in the Department of Physics
School of Physical and Mineral Sciences,
in the Faculty of Science, Health and Agriculture
University of Limpopo (former University of the North),
Turfloop, South Africa.

Supervisor **Professor P.E. Ngoepe**
Co-Supervisor **Dr. N.H. de Leeuw**

February 2005

Abstract

We have derived a potential model for fluorapatite $Ca_{10}(PO_4)_6F_2$, fitted to structure, elastic constants and vibrational frequencies of the phosphate groups, which is compatible with existing calcite and fluorite potential models. We then modelled the structure and stabilities of the dry and hydrated $\{0\ 0\ 0\ 1\}$, $\{1\ 0\ \bar{1}\ 0\}$, $\{1\ 0\ \bar{1}\ 1\}$, $\{1\ 1\ \bar{2}\ 0\}$, $\{1\ 0\ \bar{1}\ 3\}$ and $\{1\ 1\ \bar{2}\ 1\}$ surfaces, which calculations confirmed the experimental dominance of the $\{0\ 0\ 0\ 1\}$ surface, which is prominently expressed in the calculated thermodynamic morphologies. The dehydrated morphology further shows the experimental $\{1\ 1\ \bar{2}\ 1\}$ twinning plane, while the $\{1\ 0\ \bar{1}\ 0\}$ cleavage plane is expressed in the hydrated morphology. Molecular adsorption of water has a stabilising effect on all six surfaces, where the surfaces generally show Langmuir behaviour and the calculated hydration energies indicate physisorption (73 - 88 kJ mol^{-1}). The chains of fluoride ions surrounded by hexagonal calcium channels can become distorted in two major ways during relaxation: either by a shortening/lengthening of the FF distances, when the channel is perpendicular to the surface, or by distortion of the CaF bonds when the channel is parallel to the surface. Both distortions occur when the channel runs at an angle to the surface. Other relaxations include compression of the calcium sub-lattice and rotation of surface phosphate groups.

We have modelled adsorption of a range of organic molecules onto different fluorapatite surfaces, due to the importance of organic/ inorganic interactions in biological situations. We have selected organic molecules that represent a model for the carboxylic acids, alkyl hydroxamates and those

that contain both the aldehyde and hydroxyl functional groups. Adhesion of these organic molecules on the surfaces has shown strong interaction between the surface's Ca ions and the molecule's oxygens, more especially the carbonyl oxygens than any other interactions. It was found that the number of interactions between the ions of adsorbate molecule and the mineral surfaces thus contribute significantly to the exothemicity of adsorption.

Further more, simulations of apatite thin films at a range of α-quartz surfaces have shown how the strength of adhesion between thin films of apatite material and ceramic silica surfaces is crucially dependent upon both the orientation of the film relative to the substrate and the nature of the silica surfaces, a finding that is important in a wide number of applications, from basic geological research on intergrowth of phosphate and silicate rock minerals to the search for more effective surgical implant materials. It was shown that although the unrelaxed quartz surface is more reactive toward the apatite film, the more regular thin film structures grown at the pre-relaxed quartz surfaces lead to more stable interfaces. Film growth at the unrelaxed quartz surface is energetically increasingly unfavorable, whereas growth at the pre-relaxed surface is calculated to continue beyond the first layer, where the adhesion energy is convergent with the layer growth of the thin film. Adhesion of apatite thin film on hydroxylated surfaces of α-quartz has shown to be energetically less favourable than at dry surfaces. This was because the thin film interact mainly with the hydroxyl ions on the surface of quartz. However, the adhesion energy is still convergent with layer growth of the thin film on the hydroxylated surfaces.

Declaration

I declare that the thesis hereby submitted to University of Limpopo for the degree of PhD has not been previously submitted by me for a degree at this or any university, and that the work herein is originally my own.

_____

Donald Mkhonto.

Acknowledgement

I'd like to take this opportunity and thank my supervisor: Professor Ngoepe P.E. for the initiation of the project, wonderful support, patience, encouragement, discussions to make sure that this project become a success. My co-supervisor: Doctor N.H. DeLeeuw for the support she gave me during the period of the study. The fruitful discussions we had at Reading University and Birkbeck College (while based University College London) UK and the inputs made to the success of the project as well as thorough reading of the thesis to completion. I also thank Dr. T.G Cooper, for the wonderful and fruitful discussions that we had on some part of the project.

The calculations on this thesis were done at the Materials Modeling Center (MMC) in the University of the North S.A, and Reading University in the UK as well as at the Birkbeck University of London (while based at the University College London (UCL)) UK.

I received great support from the team work involved in the laboratories I was working in. Firstly the MMC at the university of the North in South Africa. I thank the cooperation from all the members of the lab who made it a point there is a comfortable working environment for everyone and made it possible for discussions. The team working with Dr. N.H. de Leeuw both at Reading University and Birkbeck University of London for the warm welcome during all my visits and made sure the working conditions were perfect for the study.

I thank the sponsors of this project: National Research Foundation of South Africa (NRF), Council for Scientific and Industrial research (CSIR)

South Africa and University of the North, for financial support. The NRF-Royal Society (RS) initiative for financing the visits between S.A and UK. And also I like to thank Professor Ngoepe P.E. and professor Catlow C.R.A for coordinating NRF-RS initiative.

I like to thank all friends who gave me the wonderful support over the period of my study. The whole of my family for the patience they have shown, coupled with encouragement and support as well. Many thanks to my father and mother who always wish to see me at higher levels of education. I thank you for giving me such support.

And lastly my daughter *Amukelani* who unknowingly allowed me to be away from her for extended periods and also her mom *Zanele* for giving me the support and taking care of her during my absence.

Dedication

Dedicated to my daughter (*Amukelani*), the whole of the family: My mom (*Samaria*) and dad (*Gadeni*) and to the three brothers (*Depart*, *Hendry* and *Peace*) and the five sisters (*Phina*, *Sophy*, *Maggy*, *Comfort*, and *Nkateko*).

Contents

List of Figures

List of Tables

Chapter 1

1.1 INTRODUCTION

A mineral is a chemical compound that is normally crystalline and which has been formed as a result of geological or biological processes[1]. Apatite minerals are the most abundant phosphorus-bearing materials and are found in almost all igneous rocks and to a lesser extent in sedimentary and metamorphic rocks. The isomorphous series can be represented by fluorapatite $Ca_{10}(PO_4)_6F_2$, which is by far the most common, chlorapatite $Ca_{10}(PO_4)_6Cl_2$, hydroxyapatite $Ca_{10}(PO_4)_6(OH)_2$ and carbonate-apatite $Ca_{10}(PO_4,CO_3,OH)_6(F,OH)_2$.[2] Although complete solid solutions of the monovalent anions (OH^-,F^-,Cl^-) are obtained in synthetic apatites, it is not clear whether this is also the case in natural apatites.[3] In addition, a range of foreign cations is also found incorporated in the apatite lattice. The distribution of the different types of ions through the lattice influences physical properties such as melting, dissolution and diffusion behaviour and hence, insight in the microscopic structure of the apatite mixtures and the bulk distribution of the cations and anions, whether uniform or in domains,

will help understanding of these macroscropic properties.

In geological situations, apatites are often used as geo- and thermo-chronometers, either by measuring fission tracks of thorium and uranium,[4, 5, 6] argon dating[7] or the retention of ^{4}He, the decay product of uranium and thorium.[8, 9] In addition, the presence and isotopic composition of noble gases in apatites can give insight into mantle processes in the past. It is therefore necessary to understand diffusion behaviour of species such as helium, xenon and argon through the apatite if our interpretation of the data relating to these processes is to be reliable.[10, 11] Although the most common naturally occurring apatite is fluor-apatite, the presence of Cl^- ions substituting for the F^- ions is thought to affect He diffusion. Furthermore, because of their affinity for impurity ions, apatites may well become important as environmental sinks for the uptake of heavy metals and radio-active contaminants, such as lead and uranium.

More recently, there has been a growing interest in designing new materials to be used in repairing and reconstructing diseased and damaged parts of the human body including bones, which has led to increased research of calcium phosphate based minerals. Some calcium phosphate minerals have been chosen initially because of their chemical similarity to the main inorganic compounds constituting bone and their behaviour has been confirmed as bioactive.[12, 13]. A bioactive material is one that elicits a specific biological response at the interface of the material which results in the formation of a bond between the tissues and the material, shown first in 1969.[13] Bioactive materials include, bioactive glasses such as Bioglass;

bioactive glass-ceramics such as Ceravital, A/W glass ceramic, or machineable glass-ceramics; dense hydroxylapatite such as Durapatite or Calcitite, or bioactive composites such as polyethylene- Bioglass, polysulfone-Bioglass, and polyethylene-hydroxylapatite (Hapex) mixtures.[14, 15] They all form an interfacial bond with bone. However, the time dependence of bonding, the strength of bond, the mechanism of bonding and the thickness of the bonding zone differ for the various materials.

Hydroxy-apatite is the major constituent of mammalian bones and tooth enamel, and because of this importance as a natural bone material, apatite is a possible candidate in the manufacture of artificial bones. In addition, fluoridation of hydroxy-apatite can suppress dental decay, for example by the production of fluorapatite, which is less soluble than hydroxyapatite. Fluorapatite (FAP) $Ca_{10}(PO_4)_6F_2$, and hydroxyapatite (HAP) $Ca_{10}(PO_4)_6(OH)_2$ are thus two of the most commonly used minerals for clinical applications.

When healing diseased or broken bones, they can be anchored by an implant that should be easily accepted by the bones themselves. Apatite minerals show typical bioactive behaviour *in vivo* generating direct contact between the bone and the ceramic surfaces without intervention of fibrous tissue layers.[16] However they posses poor mechanical properties and this hence prevents them being used as load-bearing implants. Research has therefore been mostly concerned with development of calcium phosphate-based coatings on high strength substrates for prosthetic applications involving complex loading arrangements.[17]

Experimental investigations by de Lange et al. has shown that hydroxyapatite-

coated titanium implants form an intimate bone contact without any visible intermediate tissue layer.[18] Mean while other investigations has shown less degradation of fluorhydroxyapatite coatings of dental implants than hydroxylapatite and fluorapatite.[19]

The ceramic implants are used as a support for the crystallization and layer growth of apatite, aiding the acceptance of the implant material by the body. In the context of this latter application, synthetic apatite is found to nucleate and grow on the surfaces of ceramic silicate implants which then bonds to the living bone through these apatite layers.[20, 21] However, as the precise nature of the apatite thin film is not known there is a clear need to gain an understanding of the interactions between the apatite layers and the ceramic substrate at the atomic level.

The choice of different implants as candidates for substrates include bioglasses, such as silicates, and TiO_2. Research on the coating of the implants with phosphates involve different experiments,[22] but to date no computational studies have been carried out.

Apart from the fact that fluorapatite is the most common form of apatite in nature, it is also stable at high temperature and has shown favorable biological characteristics.[3, 23, 24] As apatites are thus important materials in both geological and biological situations, and because of their natural abundance as common accessory minerals in many types of rock, it is of basic interest to gain detailed understanding of crystal formation,[25] dissolution processes[26] and interfacial interactions between the crystalline and amorphous phases, where the surface structure and reactivity of the apatite

material is of direct relevance.

Our choice of ceramic substrate for the layer growth of apatite films in this study is α-quartz (SiO_4), which is one of the most abundant minerals at the earth's surface, and as such has been the subject of numerous studies. We use silica in this case as a model for bioglasses which we interface with the apatite, in the fluorapatite form. Studies on this mineral have included experimental investigations on growth and morphology of single crystals of natural α-quartz using X-ray techniques[27] as well as computer modeling of the surface structure and stability of α-quartz and the reaction of the surfaces with water.[28]

1.2 STRUCTURAL PROPERTIES

1.2.1 Apatite

Fluorapatite has a hexagonal crystal structure with space-group P63/m.[2, 3] The apatite structure is shown in figure 1 a and b, where the F^- ions in the structure are located one above the other in a column parallel to the c-axis. The fluoride ions in the hexagonal channels are surrounded by the calcium ions, whereby each F^- is coordinated to three calcium ions in the same a-b plane. We used the structure determined by Hendricks et al.[29] with a = b = 9.370 Å, c = 6.880 Å, where $\alpha = \beta = 90^0$, $\gamma = 120^0$.

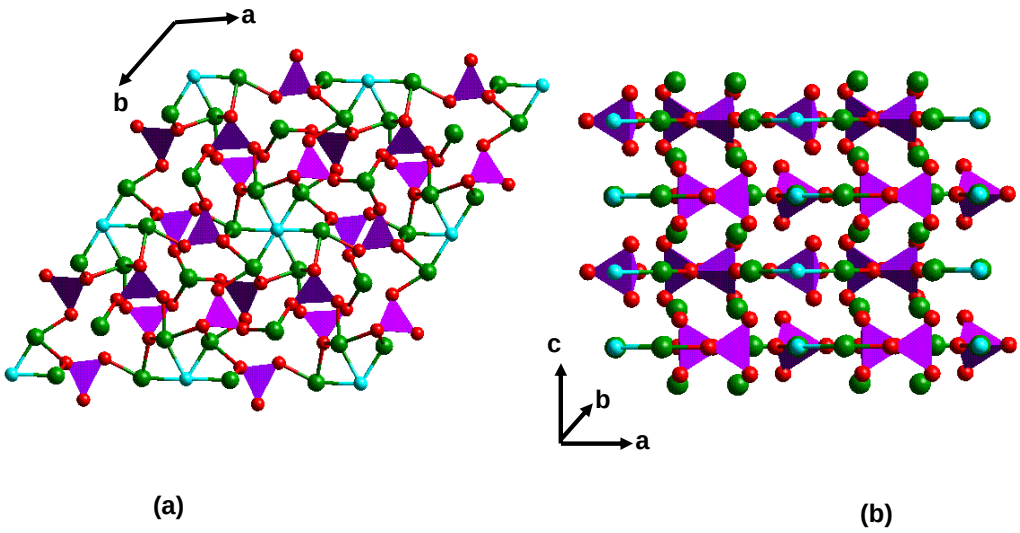

Figure 1.1: This figure shows the hexagonal structure of fluorapatite, (a) viewed down onto the {0 0 0 1} plane, and (b) a side view showing the F^- columns. (Ca = green, O = red, P = purple, F = light blue, PO_4 groups displayed as tetrahedra).

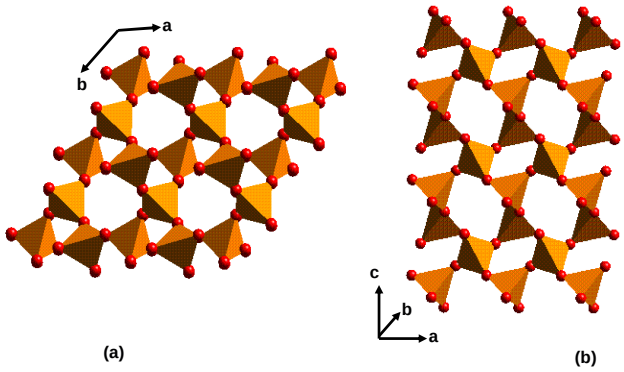

Figure 1.2: This figure shows the hexagonal structure of quartz (SiO_4), (a) viewed down onto the (0001) plane where the tetrahedral coordination of the Si to O is shown and (b) a side view. (Si = yellow and O = maroon.

1.2.2 Quartz

The mineral that we use as a model for the bioglass substrate for the interface studies with apatite is α-quartz. It has a hexagonal crystal structure like apatite with space group of $P3_121$, although of course with slightly different lattice vectors to which the apatite thin films have to accommodate themselves in the interface, which is fully explained in the section on the interfaces. α-Quartz has lattice parameters of a = b = 4.913 Å, and c = 5.404 Å as given by Deer[2] and standard lattice angles for a hexagonal structure ($\alpha = \beta = 90^0$, $\gamma = 120^0$). The α-quartz structure is shown in figure 1.2 a and b.

1.3 RATIONALE OF THE STUDY

The aim of the project is to use computational techniques to study important aspects of the surface chemistry of apatite materials, which are a group of calcium phosphate rich minerals. As calcium phosphate in general and apatites in particular are the main constituent of mammalian bones, studies of apatite minerals ($Ca_{10}(PO_4)_6$(F, OH, Cl)$_2$ where the end-members are called fluorapatite, hydroxyapatite and chlorapatite) at the atomic level is of topical interest in the field of bio-materials and bio-engineering, as especially the hydroxy and fluorapatite form are promising candidates for the manufacture of artificial bones. Studies of apatite minerals have shown that the mineral nucleates and attaches to ceramic implants,[20, 21] a factor that is important in enhancing the acceptance of the implant in the natural bone. Understanding the nature of the mineral surfaces forms the basis for the investigation of how the mineral can be interfaced with ceramic implants (bioglass) that are used to anchor damaged or broken bones. Using a ceramic implant that has been interfaced with a thin layer of apatite in vitro, would aid the acceptance of the implant in vivo.

Computer modelling techniques used in the study of materials at the atomic level have been used successfully to predict accurately bulk properties like equilibrium lattice constants, and to predict surface structures and reactivities, defects and the stability and epitaxial fitting of interfaces of various materials[28, 30, 31, 32]. The simulation of the bulk properties starts with the calculation of the structure itself (lattice constants) and the atomic coordinates, which is achieved by locating lattice parameters corresponding

to a minimum energy (energy minimization). The energy minimization technique is a fundamental method capable of describing ground state properties of a wide range of solids. In this study, atomistic simulation techniques based on the Born model of solids are used, mainly employing the METADISE code that embodies a range of potential functions to describe the interactions between atoms. The potential model is derived, according to the methods described in chapters 2 and 3 of this thesis.

1.4 OBJECTIVES OF THE STUDY

The specific objectives of this study are as follows:

1. Derivation of potential parameters that will best describe the bulk properties of the fluorapatite mineral, and inclusion of the water potential parameters for the description of hydration of the surfaces; Fitting of potential parameters to describe the interface of fluorapatite to a model of a ceramic silicate in the form of α-quartz; and obtaining parameters for the interaction of organic surfactants with fluorapatite surfaces.

2. Calculation of the bulk properties of the fluorapatite mineral using the newly derived potential model, i.e the lattice constants, atomic coordinates, elastic and dielectric constants and vibrational frequencies.

3. Simulation of the major fluorapatite surfaces and investigation of the effect of water on the surface structures and stabilities.

4. Calculation of the surface energies of the dry and hydrated fluorapatite surfaces as well as the hydration energies and subsequent calculation of the crystal morphologies and comparison with experiment.

5. Simulation of the adsorption of a range of organic molecules at the different surfaces of fluorapatite, investigating surface/ adsorbate structures and interactions, calculating the adsorption energies and establishing trends in adsorption behaviour as a consequence of difference in functional groups.

6. Investigation of the nature of interfaces of fluorapatite and α-quartz as a model for bioglass materials and ceramic implants, calculating the adhesion energies between the thin film of fluorapatite and the α-quartz surfaces, investigating the effect of thin film orientation on the stability of the interface,

and studying the effect of substrate hydration on the strength of interaction.

1.5 OUTLINE OF THE THESIS

This thesis provides a detailed report of our study of the fluorapatite mineral ($Ca_{10}(PO_4)_6F_2$). The bulk structural properties of the material have been calculated accurately, validating the newly derived potential parameters used in the simulations. Surface properties, surfactant adsorption, and interfaces with α-quartz have been studied using established and reliable atomistic simulation techniques.

The dissertation is divided into eight chapters: In the first chapter, we explain the importance of the fluorapatite mineral, review work published previously, and also discuss the crystal structures of the fluorapatite and α-quartz systems, before stating the objectives and rationale of the study.

In chapter two, we report on the theoretical methods that have been used in the current study i.e classical mechanics simulation methods and also a brief section on plane-wave pseudopotential methods, which are also widely used in computational materials research.

In chapter three, we give full details of the potential functions, method of potential derivation, and the potential parameters fitted and used in this study.

Chapter four contains a detailed report of the results obtained from our simulations of experimentally important surfaces of the fluorapatite mineral including hydration of the surfaces and the calculation of the crystal morphologies.

In chapter five we report on the results of simulations of the adsorption of different organic surfactants at the surfaces of the fluorapatite mineral. The effect of different functional groups of the adsorbates on the adsorption trends is discussed.

In chapter six we report in detail the interface of thin films of fluorapatite with dry and hydrated surfaces of α-quartz.

In chapter seven, we complete the thesis with an overall conclusion of the whole study and a recommendation for future work.

Chapter 2

TECHNIQUES

2.1 INTRODUCTION

Major progress has, in the past decades, been achieved in the calculation of structural, chemical, electrical, optical, magnetic and surface properties of materials. In calculations of materials properties using a computational approach, it is important to ensure that the system is in equilibrium. One way to achieve the equilibrium is to minimize the energy of the system and thus obtain the equilibrium parameters of the system that corresponds to the minimum energy. A large number of algorithms are available for energy minimization which are classified according to the order of the derivative of the total energy function that is employed in the calculation.

The development of theoretical approaches based on quantum mechanics played an important role in the prediction of many material properties, but before these methods were used widely, much progress had been made in the development of an atomistic simulation approach that has been widely used in the prediction of various properties of materials, including complex ionic

systems and biological systems. There are then two types of computational approaches used for the prediction of material properties, viz: the force field or empirical potential methods that avoid details of electronic structure and consider the interactions of atoms in a quasi-classical form, and quantum mechanical methods that take into account the motion and the interaction of electrons in a material. The $Ab-initio$ approach refers to the case where the methods are based on fundamental physical constants only, such as mass and charge of an electron, and no atom specific parameters are introduced and this is the term most commonly used for the quantum mechanical methods. In this work we have mainly based our investigations on the force field methods. Their application covers a wide range of materials, i.e. from systems in 0D (molecules) to systems in 3D (crystals). These methods have been used to study the surface structures and properties of the fluorapatite mineral, sorption at the surface and finally the interface of the fluorapatite thin film with α-quartz as the substrate. Thus in this chapter we outline the theory behind this latter modeling method and we also briefly discuss some of the modeling techniques available in this field of computational science.

2.2 CLASSICAL MECHANICS SIMULATIONS

Classical mechanics simulation techniques, often described as atomistic simulation methods are based on the Born model of solids[33], which assumes that the ions in the crystal interact via long-range electrostatic forces and short-range forces, including both the repulsions and the van der Waals attractions between neighbouring electron charge clouds, which are described

by simple analytical functions, which are treated in chapter 3.

2.3 Born Model of Solids

In the Born model of solids, it is assumed that the energy and its derivatives can be defined as the summation of all interactions between the atoms in the system which give rise to the total interaction and total net force acting on each atom due to the others. The basis of these methods is to calculate the total energy of the lattice, which is defined as the energy released when the ions making up the crystal lattice are brought together from infinite distance to the lattice sites. The energy of interaction of each one of the atoms is given by the equation:

$$U_i = \frac{1}{2}\sum_j \{\frac{q_i q_j}{4\pi\varepsilon_0 r_{ij}} + \phi_{ij} r_{ij}\} + \frac{1}{3}\sum_{jk} \phi_{ijk}(r_i, r_j, r_k) + \frac{1}{4}\sum_{jkl} \phi_{ijkl}(r_i, r_j, r_k, r_l) \tag{2.1}$$

Where the first term represent the long range coulombic energy and the short range two body interaction, and the second and third terms are the three and four body interactions. q_i and q_j are the charges on atoms i and j respectively, r_{ij} is the distance between them and ε_0 is the permittivity of free space. The lattice energy of the system is given by the summation of all these terms over all the ions in the unit cell under simulation, represented by the equation of the form:

$$U_{latt} = \sum_{Lij} \{\frac{q_i q_j}{4\pi\varepsilon_0 r_{ijL}} + \phi_{ijL} r_{ijL}\} + \sum_{Lijk} \phi_{Lijk}(r_i, r_j, r_k) + \sum_{Lijkl} \phi_{Lijkl}(r_i, r_j, r_k, r_l) \tag{2.2}$$

L is a set of lattice vectors representing the periodicity of the lattice in three dimensions. The terms on the right hand side of this equation are the same as in equation 2.1 above. The second term representing the three body interaction is often not included in simulation of systems that do not require angle-dependant potentials, just like the third term which represents the four body interaction. Each of the short range interaction terms is represented by a parameterized analytical expression described in chapter 3.

2.3.1 Coulombic Summation

$q_i q_j / 4\pi\varepsilon_0 r_{ij}$ represents the coulombic interaction, which is only slowly convergent as a function of the distance r between the ions. For this reason the summation is accurate for the simulation of isolated or non periodic systems, but it is not recommended for periodic systems. To make the interaction more quickly convergent, a different summation technique is used to sum the interactions.

2.3.2 Ewald Summation

The Ewald sum[34] is an excellent technique for calculating electrostatic interactions in periodic systems, which can be used to sum the long range interactions between particles and their infinite periodic images. The approach assumes that the lattice is periodic in three dimensions and in the description of the coulombic interaction, the charge density ρ for a point charge i is given by:

$$\rho_i = q_i \Delta(r_i - r_{latt}) \tag{2.3}$$

The delta function, which can take the value 0 or 1, is replaced by a gaussian function:

$$\rho_i = e^{(-\frac{(r_i - r_{latt})^2}{\eta^2})} \tag{2.4}$$

where η is the half width of the Gaussian. Now the original charge density can be written as:

$$\rho_i(r) = [\Delta(r_i - r_{latt}) - e^{(-\frac{(r_i - r_{latt})^2}{\eta^2})}] + e^{(-\frac{(r_i - r_{latt})^2}{\eta^2})} \tag{2.5}$$

This equation can be solved using Poisson's equation, which relates the density ρ to the second derivative of the potential ϕ[35]. In general, for a box which is positioned at a cubic lattice point $\mathbf{n} = n_x L, n_y L, n_z L$ where n_x,n_y,n_z are integers,[36] then we can describe r_{ijL} as $|r_{ij} + \mathbf{n}|$. The coulombic potential (ϕ^c) is now represented by two rapidly convergent series plus some constants or neutralising distributions:

$$\phi^{\mathbf{c}} = \phi^{\mathbf{r}} + \phi^{\mathbf{q}} + \phi^{\mathbf{0}} \tag{2.6}$$

Where $\phi^{\mathbf{r}}$ is the potential convergent in **r**-space and $\phi^{\mathbf{q}}$ is the potential convergent in reciprocal **q**-space. The potential for the first part ($\phi^{\mathbf{r}}$) becomes:

$$\phi^{\mathbf{r}} = \frac{1}{2} \sum_{i=1}^{N} \sum_{j=1}^{N} \sum_{|\mathbf{n}|=\mathbf{0}}^{\infty} {}' \frac{q_i q_j}{4\pi\varepsilon_0} \frac{erfc(\eta |r_{ij} + \mathbf{n}|)}{|r_{ij} + \mathbf{n}|} \tag{2.7}$$

which sums up all interactions of ions i and j over the whole lattice. $erfc(x)$ is the complementary error function of the form:

$$erfc(x) = 1 - (\frac{2}{\sqrt{\pi}}) \int_0^x e^{(-u^2)} du \tag{2.8}$$

The summation in equation 2.7 converges rapidly in real space and the convergence depends on the choice of η which can also be associated with the

choice of the cutoff such that only the interactions with other charges within the cutoff are included, i.e only terms in the series are those for which $|\mathbf{n}| = 0$. The contribution from the second charge distribution is:

$$\phi^{\mathbf{q}} = \frac{1}{2}\sum_{k\neq 0}\sum_{i=1}^{N}\sum_{j=1}^{N}\frac{1}{\pi L^3}\frac{q_i q_j}{4\pi\varepsilon_0}\frac{4\pi^2}{k^2}e^{(-\frac{k^2}{4\eta^2})}cos(\mathbf{k}.r_{ij}) \tag{2.9}$$

This summation is performed in reciprocal space. The vectors $\mathbf{k}$ are reciprocal vectors and are given by $\mathbf{k} = 2\pi\mathbf{n}/L^2$. This reciprocal sum also converges much more rapidly than the original point charge sum and together with $\phi^{\mathbf{r}}$ gives a more rapidly convergent solution of ϕ. The sum of Gaussian functions in real space includes the interaction of each Gaussian with itself and a third, self-term, must be subtracted:

$$\phi^{\mathbf{0}} = -\frac{\eta}{\sqrt{\pi}}\sum_{k=1}^{N}\frac{q_k^2}{4\pi\varepsilon_0} \tag{2.10}$$

Another correction term may be required depending upon the medium that surrounds the sphere of simulation boxes. For conductors, for example, where the surrounding space has infinite relative permittivity, no correction term is required. However if the surrounding medium is a vacuum (with a relative permittivity of 1) then the following energy must be added:

$$\phi^{\mathbf{0}}_{correction} = \frac{2\pi}{3L^3}\mid\sum_{i=1}^{N}\frac{q_i}{4\pi\varepsilon_0}r_i\mid^2 \tag{2.11}$$

So that the final expression is thus:

$$\phi^{\mathbf{c}} = \phi^{\mathbf{r}} + \phi^{\mathbf{q}} + \phi^{\mathbf{0}} + \phi^{\mathbf{0}}_{correction} \tag{2.12}$$

Further detail is given in Leach[36] and Kittel[35, 37].

2.3.3 Parry Method

In the Parry method[38], which is a special adaptation of the Ewald method for surfaces, the crystal is assumed to consist of a series of charged planes of infinite size. In the summation of the electrostatic interactions, the vectors are now divided into two: the in-plane vectors, ρ_{ij} and vectors perpendicular to the plane, u_{ij}. In the three dimensional case above (equation 2.9) it is assumed that the total charge of the simulation cell is zero and hence $k \neq 0$, however here that assumption is no longer valid and the $k = 0$ term which would make the equation tend towards infinity, has to be evaluated. Thus the summation of the coulombic energy is given as:

$$\phi = \frac{\pi}{A}\{-\mathbf{2u_{ij}erf}(\eta\mathbf{u_{ij}}) - \frac{\mathbf{2e}^{(-\eta^{\mathbf{2}}\mathbf{u_{ij}}^{\mathbf{2}})}}{\eta\sqrt{\pi}} + \sum_{\mathbf{k\neq 0}} \frac{\mathbf{e}^{(\mathbf{ik}\rho_{\mathbf{ij}})}}{\mathbf{k}}[\mathbf{e}^{(\mathbf{ku_{ij}})}\mathbf{erfc}(\frac{\mathbf{k}}{\mathbf{2}\eta} - \eta\mathbf{u_{ij}}) + \mathbf{e}^{(-\mathbf{ku_{ij}})}\mathbf{erfc}(\frac{\mathbf{k}}{\mathbf{2}\eta} - \eta\mathbf{u_{ij}})]\} \tag{2.13}$$

Where $\mathbf{k}$ is the two dimensional reciprocal lattice vector, A is the surface area, erf and $erfc$ are the standard and complementary error functions. More details on the derivation of equation 2.13 are given by Hayes *et al.*[39]

2.4 Static lattice Energy Minimisation

The minimum energy of a crystal is obtained by iteratively minimising the energy of the lattice with respect to the positions of the atoms making up the crystal. We have already defined in section 2.3 the energy of a lattice as: The energy released when the ions making up the crystal lattice are brought together from infinite distance to their current lattice sites. In static lattice energy minimisation the energy is calculated for the lattice for the

respective positions of the lattice atoms without taking into account any effects of temperature. Thus calculations are effectively done at 0K and ignoring the 0K vibrations. The first stage of the minimisation requires the structure to be equilibrated, meaning that the atoms will have to be brought to their mechanical equilibrium at either constant volume or at constant pressure.

2.4.1 Constant Volume Minimisation

For a constant volume minimisation, the cell dimensions are not allowed to vary while the ions/atoms are allowed to move within the simulation box. The energy is considered to be at its minimum when its derivative with respect to the ions's positions is zero, i.e when the strain on the ions is zero:

$$\frac{\partial \Psi}{\partial \mathbf{r_i}} = 0 \tag{2.14}$$

Where Ψ is the energy and $\mathbf{r_i} = (x_i, y_i, z_i)$ is the ion position for all i in the simulation box. One commonly used technique is the Newton-Raphson method[40], which applies a second derivative method to minimise the lattice energy. Below we show how Born and Huang[41] described the process for the crystal lattice energy Ψ which is expanded about point $\mathbf{r}$ to second order:

$$\Psi_{\mathbf{r}'} = \Psi_{\mathbf{r}'} + \mathbf{g}^T.\delta + \frac{1}{2}(\delta^T.\mathbf{W}.\delta) \tag{2.15}$$

Where Ψ is the energy, the superscript T correspond to the transpose of the vector, $\mathbf{g}$ is the first derivative with respect to all variables ($\mathbf{r}$) or it is the gradient,

$$\mathbf{g} = \nabla \Psi \tag{2.16}$$

δ is the displacement of a given ion,

$$\delta = \mathbf{r}' - \mathbf{r} \tag{2.17}$$

$\mathbf{W}$ is the second derivative matrix with respect to $\mathbf{r}$,

$$\mathbf{W} = \nabla^2 \Psi \tag{2.18}$$

Then assuming equilibrium conditions where the change in energy with respect to ion position is zero.

$$\frac{\partial \Psi}{\partial \delta} = 0 = \mathbf{g} + \mathbf{W}.\delta \tag{2.19}$$

which gives

$$\delta = -\mathbf{W}^{-1}.\mathbf{g} \tag{2.20}$$

For a harmonic system an optimum value of $\delta = \mathbf{r}' + \mathbf{r}$ would be obtained and hence the minimum would be evaluated in a single step. However, although the displacement normally gives rise to a lower energy configuration, the system is not generally harmonic and hence several iterations have to be performed before the equilibrium configuration is obtained. If the system is far from the minimum energy position(where the potential energy is not harmonic), the method is not very efficient as $\mathbf{W}$ (equation 2.18) and its inverse has to be calculated, which is computationally expensive.

The speed of calculation can be increased by approximating the inverted second derivative matrix instead of calculating it exactly for each iteration.[42, 43]

From equation 2.20 we can replace $\mathbf{W^{-1}}$ by the Hessian $\mathbf{H}$:

$$\delta = -\lambda \mathbf{H} \mathbf{g} \tag{2.21}$$

Where λ is a linear parameter initially set to 1, and δ is defined the same as in equation 2.17. Now at $k+1$ iteration, the ionic displacement is given by:

$$\delta_k = -\lambda_k \mathbf{H}_k \mathbf{g} \tag{2.22}$$

where

$$\delta_k = \mathbf{r}_{k+1} - \mathbf{r}_k \tag{2.23}$$

Thus the Hessian for the next iteration is approximated as:

$$\mathbf{H}_{k+1} = \mathbf{H}_k - \frac{(\delta_k . \delta_k^T)}{(\delta_k^T . \delta_k)} - \frac{\mathbf{H}_k . \delta_k . \delta_k^T . \mathbf{H}_k}{\gamma_k^T . \mathbf{H}_k . \gamma_k} \tag{2.24}$$

where

$$\gamma_k = \mathbf{g}_{k+1} - \mathbf{g}_k \tag{2.25}$$

and the superscript T correspond to the transpose of the vector, and the new position $k+2$ can be calculated. Hence only $\mathbf{g}$ (equation 2.16) has to be calculated for each iteration which is much faster computationally. However, since there are errors accumulated at each step, it is necessary to recalculate the $\mathbf{W^{-1}}$ every 10 to 30 iterations to readjust the Hessian $\mathbf{H}$.

Simpler gradient methods which give a quicker convergence are often used in the early stages to bring the energy close to its minimum. An alternative method is for example, the conjugate gradient method[44], which is based on a steepest descent. This method is much faster than the Newton-Raphson technique as the calculation of $\mathbf{W}$ is not necessary. However the conjugate gradients method does not exactly locate the minimum energy position, and it is only efficient for large systems where the Newton-Raphson technique is computationally expensive to use. Thus the conjugate gradients method

helps as an initial step to quickly guide the system towards a minimum where the potential energy surface becomes more harmonic, when the Newton-Raphson method is used to reach the final minimum. For calculations in this work we have used the conjugate gradients method followed by the Newton-Raphson method to find the minimum energy configurations.

2.4.2 Constant Pressure Minimisation

In constant pressure minimisation both unit cell dimensions and ion coordinates are allowed to vary. The minimisations are carried out simultaneously using the same approach as for constant volume minimisation, with the lattice vectors treated as additional variables. As in constant volume minimisations, the ions are at equilibrium in their minimised positions when the strain on them is zero (equation 2.14).

The strain on the unit cell is defined by:

$$\mathbf{r}' = (\mathbf{I} + \varepsilon).\mathbf{r} \tag{2.26}$$

Where $\mathbf{I}$ is the identity matrix, ε is the strain on the lattice vectors, $\mathbf{r}$ and $\mathbf{r}'$ are the transformed lattice vectors. Using the Voigt notation equation 2.26 can be written in a matrix form:

$$\begin{bmatrix} x' \\ y' \\ z' \end{bmatrix} = \begin{bmatrix} 1+\varepsilon_1 & \frac{1}{2}\varepsilon_6 & \frac{1}{2}\varepsilon_5 \\ \frac{1}{2}\varepsilon_6 & 1+\varepsilon_2 & \frac{1}{2}\varepsilon_4 \\ \frac{1}{2}\varepsilon_5 & \frac{1}{2}\varepsilon_4 & 1+\varepsilon_3 \end{bmatrix} \begin{bmatrix} x \\ y \\ z \end{bmatrix}$$

where x', y', z' and x, y, z are components of $\mathbf{r}'$ and $\mathbf{r}$ respectively.

The static pressure is given by the first derivative of the lattice energy with respect to the strain and can be determined using the chain rule:

$$P_{static} = \frac{\partial \Psi}{\partial \varepsilon_j} = \frac{\partial \Psi}{\partial \mathbf{r}} . \frac{\partial \mathbf{r}}{\partial \mathbf{r}^2} . \frac{\partial \mathbf{r}^2}{\partial \varepsilon_j} \tag{2.27}$$

The first term represents the first derivative, the second term equates to $\frac{1}{2\mathbf{r}}$ and the solution of the third term can be found by squaring the equation defining the bulk strains and differentiating:

$$\frac{\partial \mathbf{r'}^2}{\partial \varepsilon_j} = 2\mathbf{r}^{\alpha} . \mathbf{r}^{\beta} + 2\mathbf{r}^{\alpha} . \varepsilon . \mathbf{r}^{\beta} \tag{2.28}$$

In the equilibrium condition, there is no strain, i.e $\varepsilon = 0$, and equation 2.28 then becomes:

$$\frac{\partial \mathbf{r'}^2}{\partial \varepsilon_j} = 2\mathbf{r}^{\alpha} . \mathbf{r}^{\beta} \tag{2.29}$$

More information on these equations can be found from references[45] and [46].

The proportionality constant between the stress and strain can be calculated as well, which is the elastic compliance matrix, and the inverse of the second derivative of the energy with respect to strain. It is determined by expanding the lattice energy to second order:

$$\Psi(\mathbf{r'}) = \Psi(\mathbf{r}) + \mathbf{g} . \delta' + \frac{1}{2} \delta'^{T} . \mathbf{W} . \delta' \tag{2.30}$$

now δ' is the 3N+6 strain matrix containing the component of internal and bulk strain:

$$\delta' = \begin{bmatrix} \delta \\ \varepsilon' \end{bmatrix}$$

with ε' equal to six independent components of the symmetric strain matrix ε, and $\mathbf{r'}$ is the same as in equation 2.26 ($\mathbf{r'} = (\mathbf{I} + \varepsilon).\mathbf{r}$).

$\mathbf{W}$ (equation 2.18) now also includes mixed coordinates and strain derivatives and is of order 3N+6 by 3N+6.

$$\mathbf{W} = \begin{bmatrix} \frac{\partial^2\Psi}{\partial\mathbf{r}^2} & \frac{\partial^2\Psi}{\partial\mathbf{r}\partial\varepsilon} \\ \\ \frac{\partial^2\Psi}{\partial\varepsilon\partial\mathbf{r}} & \frac{\partial^2\Psi}{\partial\varepsilon^2} \end{bmatrix} = \begin{bmatrix} \mathbf{W_{rr}} & \mathbf{W}_{\varepsilon\mathbf{r}} \\ \\ \mathbf{W}_{\mathbf{r}\varepsilon} & \mathbf{W}_{\varepsilon\varepsilon} \end{bmatrix}$$

$\mathbf{W_{rr}}$ is the coordinate second derivative matrix of 3N by 3N, $\mathbf{W}_{\mathbf{r}\varepsilon}$ and $\mathbf{W}_{\varepsilon\mathbf{r}}$ are the mixed coordinates and strain second derivative matrices of 6 by 3N and 3n by 6 and $\mathbf{W}_{\varepsilon\varepsilon}$ is the strain second derivative matrix of 6 by 6.

Again if we apply the equilibrium condition where the strain is zero and splitting δ' into components of δ and ε, equation 2.30 can be written as:

$$\Psi(\mathbf{r}') = \Psi(\mathbf{r}) + \frac{1}{2}\delta.\mathbf{W_{rr}}.\delta + \delta.\mathbf{W}_{\mathbf{r}\varepsilon}.\varepsilon + \frac{1}{2}\varepsilon.\mathbf{W}_{\varepsilon\varepsilon}.\varepsilon \tag{2.31}$$

and differentiating with respect to δ and again applying the equilibrium condition, we have:

$$\frac{\partial\Psi}{\partial\delta} - 0 = \delta.\mathbf{W_{rr}} + \mathbf{W}_{\mathbf{r}\varepsilon} \tag{2.32}$$

thus

$$\delta = -\mathbf{W_{rr}}^{-1}.\mathbf{W}_{\mathbf{r}\varepsilon}.\varepsilon \tag{2.33}$$

Hence equation 2.31 can be written as:

$$\Psi(\mathbf{r}') = \Psi(\mathbf{r}) + \frac{1}{2}\varepsilon.[\mathbf{W}_{\varepsilon\varepsilon} - (\mathbf{W}_{\varepsilon\mathbf{r}}.\mathbf{W_{rr}}^{-1}.\mathbf{W}_{\mathbf{r}\varepsilon})].\varepsilon \tag{2.34}$$

The elastic constant c is defined as the second derivative of the lattice energy with respect to lattice strain, normalised to cell volume. Now if we differentiate equation 2.34 twice with respect to the strain ε, we get the elastic constant as

$$c = \frac{1}{V}[\mathbf{W}_{\varepsilon\varepsilon} - (\mathbf{W}_{\varepsilon\mathbf{r}}.\mathbf{W_{rr}}^{-1}.\mathbf{W}_{\mathbf{r}\varepsilon})] \tag{2.35}$$

and the strains are given by the stress divided by the elastic constant c. Assuming Hooke's law, the strain can be calculated as

$$\varepsilon = (P_{static} + P_{applied}).c^{-1} \tag{2.36}$$

and this can be used to evaluate the new coordinates after the strain. Because these expressions are approximations, this process continues iteratively until all the strains are removed.

2.5 METADISE Code

The METADISE (Minimum Energy Techniques Applied to Dislocation, Interface and Surface Energies)[47] computer simulation code which we have used for the calculation of the surface and adsorbate structures and energies, is designed to model dislocations, interfaces and surfaces. Following the approach of Tasker[48] the crystal is described as a series of charged planes parallel to the surface/interface and periodic in two dimensions, which are divided into two blocks each comprising two regions, region I and region II. Region I contains those atoms near the extended defect, in this case the surface or solid-solid interface and a few layers immediately below; these atoms are allowed to relax to their mechanical equilibrium. Region II contains those atoms further away, which represent the rest of the crystal and are kept fixed at their bulk equilibrium position. Figure 2.1 gives the schematic representation of the format. It is necessary to include region II to ensure that the total interaction energy of an ion at the bottom of region I is modelled correctly. The bulk of the crystal is simulated by the two blocks together while

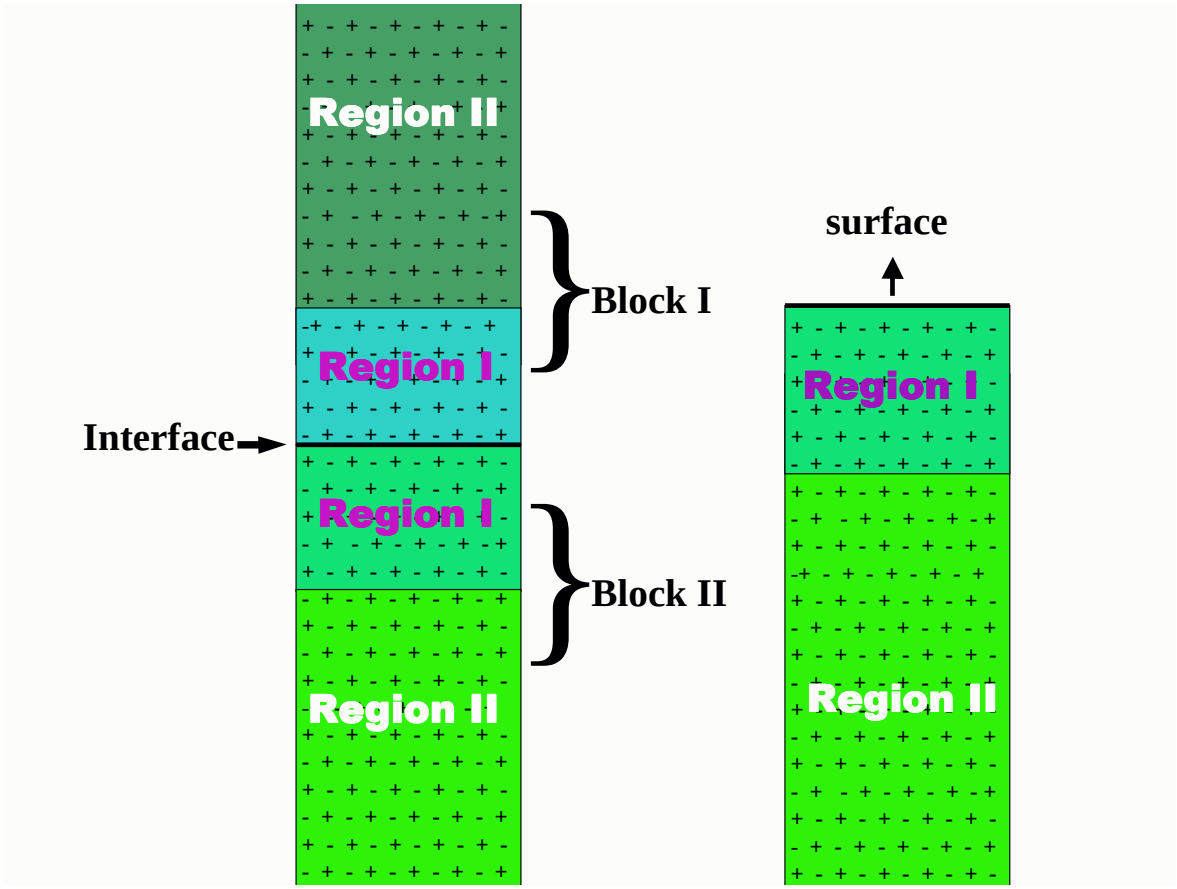

Figure 2.1: Schematic representation of the two region approach used in METADISE, showing the complete crystal with the two blocks together and half the crystal exposing the surface.

a surface is represented by a single block with the top of region I as the free surface. A solid/solid interface is created by fitting two surface blocks together in different orientations. Both regions I and II need to be sufficiently large for the energy to converge apart from a thin film, which only consists of a region I, where all ions are allowed to relax explicitly.

The energies of the blocks are essentially the sum of the energies of interaction between all atoms. The energy of the whole crystal is made up of two parts:

$$U_{latt} = U_I + U_{II} \tag{2.37}$$

Where U_I and U_{II} are the energies of region I and II respectively, with the energy of region I given as:

$$U_I = \sum_{i\in I, j\in I} \sum_{I} \Phi_{ij}(\mid r_{ij} - r_I \mid) + \frac{1}{2} \sum_{i\in I, j\in II} \sum_{I} \Phi_{ij}(\mid r_{ij} - r_I \mid) \tag{2.38}$$

Where Φ_{ij} is some suitable pair potential to be described in chapter 3. The first term describes the interactions between the ions in region I only and the second term is the boundary interaction energy describing the interaction between the ions at the bottom of region I and those at the top of region II. The entire interaction between the ions in region II can be ignored as the ions are kept fixed at their equilibrium positions and this is hence a constant term. The energy of region II thus consists only of the boundary interaction energy. The energy contribution of region II is then represented as:

$$U_{II} = \frac{1}{2} \sum_{i\in I, j\in II} \Phi_{ij}(\mid r_{ij} - r_I \mid) \tag{2.39}$$

The energy minimisation techniques employed in this work through this METADISE code, are exceedingly suitable techniques to investigate at the

atomic level surfaces and surfactant interactions as well as solid/solid interfaces between two complex materials, which necessitates large simulations cells containing thousands of ions. These techniques are now well-established in the field of solid state chemistry, especially in ionic solids where the Van Der Waals interactions play an important role, and they have been shown to be successful in the accurate structure and energy determination and prediction of a wide range of solids,[49] defects,[50] surfaces,[51] solid/solid,[52] and solid/liquid interfaces,[53] and sorption behaviour.[54] Similar minimisation techniques are employed in the General Utility Lattice Programme developed by Julian Gale.[55], which is used for some of the potential parameter derivation described in chapter 3.

2.5.1 Types of Surfaces

Surfaces are created when a crystal lattice is cleaved in different crystallographic directions according to the Miller indices. The creation of surfaces involves breaking the symmetry of the lattice or the crystal structure and leaves exposed atoms with dangling bonds. The arrangement of the exposed atoms at the surface depends mostly on the general arrangement of the atoms of the entire crystal, hence leaving the exposed atoms in different configurations and combinations. In the method we use (METADISE) as discussed above, the surfaces are considered as stacks of charged planes. Tasker[48] identified three different types of surfaces, namely: The type I surface, in which each plane has an overall zero charge. This surface consist of both anions and cations in stoichiometric ratio as shown in figure 2.2. The type II

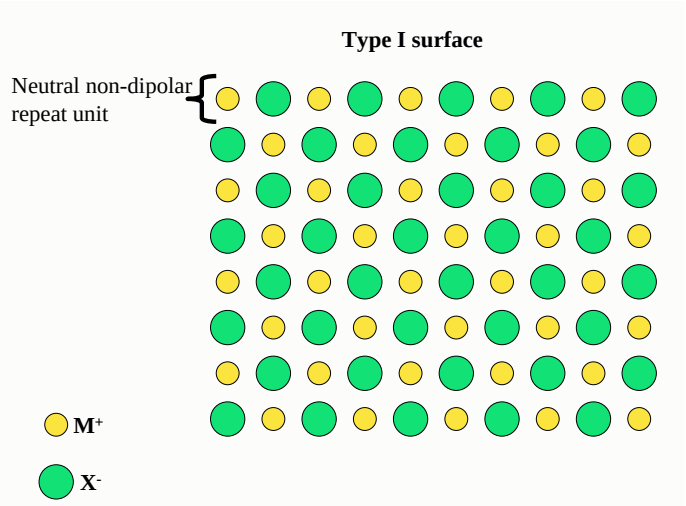

Figure 2.2: Stacking sequence showing type I surface consisting of neutrally charged layers of positive and negative ions.

surface, has charged planes, with the repeat unit consisting of more than one plane, arranged in such a way that there is no dipole moment perpendicular to the surface, shown in figure 2.3. Finally, the type III surface is made of a stack of alternately charged planes and has a dipole moment perpendicular to the surface, which is shown in figure 2.4. However Bertaut[56] demonstrated that when a dipole moment is present perpendicular to the surface, the surface energy diverges and increases with an increase in size of the unit cell. Hence the type III surface needs to be modified to remove the dipole before any energy minimisation can be carried out. Surface modifications include reconstruction, such as micro-faceting, the introduction of surface vacancies and the incorporation of impurities. Oliver[57] has shown that one way of correcting for the dipole in type III surfaces is by removing half of the

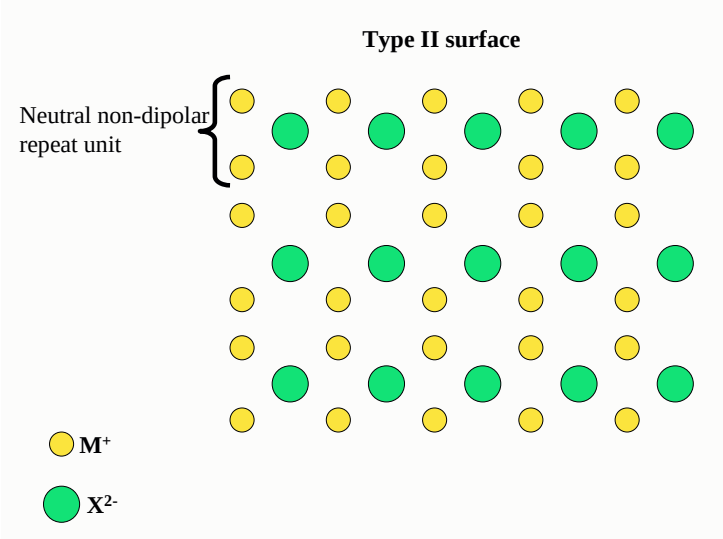

Figure 2.3: Stacking sequence showing the type II surface consisting of positively and negatively charge layers but with neutral charge and a non-dipolar repeat unit.

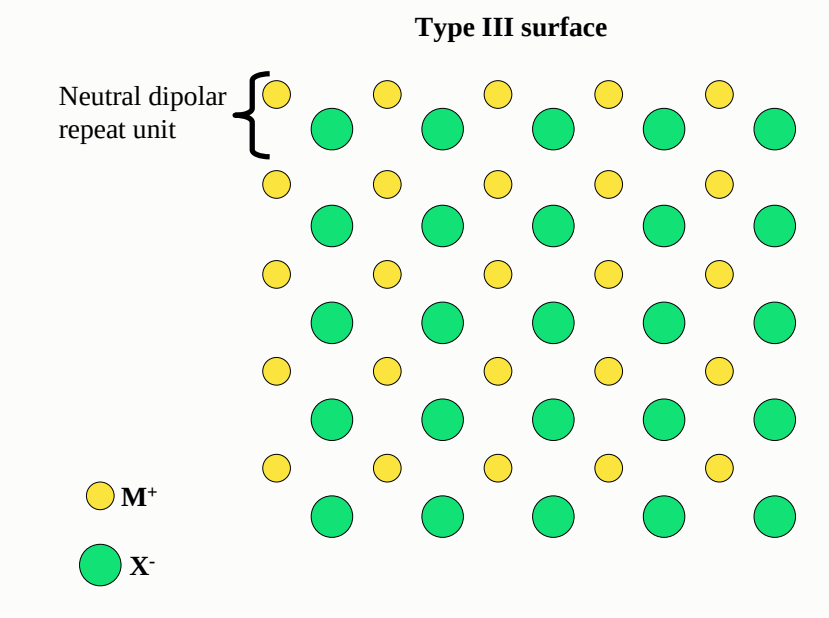

Figure 2.4: Stacking sequence showing the type III surface, consisting of alternating layers of positive and negative ions resulting in a dipolar repeat unit.

atoms from the top layer of the repeat unit of the surface and place them at the bottom of the simulation cell, resulting in a surface which is vacant in either surface cations or anions. These anion or cation vacancies can become reactive sites for sorption reactions, such as hydroxylation.

2.5.2 Calculation of Surface, Adsorption and Adhesion Energies

One of the key steps in studying material surfaces is to calculate their surface energies. The surface energy γ is a measure of the thermodynamic stability of the surface with a low, positive value indicating a stable surface. It is

given by:

$$\gamma = \frac{U_S - U_B}{A} \tag{2.40}$$

Where U_S is the energy of the surface block of the crystal, U_B is the energy of an equal number of atoms of the bulk crystal and A is the surface area. The surface energy is thus the energy required to cleave the crystal, exposing the surface. The energies of the blocks as discussed above are essentially the sum of the energies of interaction between all atoms.

For the hydrated surfaces the surface energies were calculated with respect to liquid water in order to assess the stability of the surface in an aqueous environment:

$$\gamma_H = \frac{U_H - (U_B + U_{H_2O(l)})}{A} \tag{2.41}$$

where U_H is the energy of the surface block, suitably hydrated, U_B is as described in equation 2.40, while $U_{H_2O(l)}$ is the energy of bulk water. The latter is the sum of the self-energy of water due to the intra-molecular forces, and the energy of condensation due to the intermolecular forces. Thus the new surface energy is simply equivalent to the sum of the energy required to cleave the crystal and then add water to the surface.

In addition to calculating the surface energy we calculate the adsorption energy U_{ads}, i.e. the energy to adsorb water onto the surface per water molecule, which is given by:

$$E_{ads} = \frac{U_H - (U_s + nU_{H_2O(g)})}{n} \tag{2.42}$$

Where n is the number of water molecules, U_s and U_H are as described in equation 2.40 and 2.41 respectively and $U_{H_2O(g)}$ is the energy of a gaseous

water molecule. We calculate this energy for a gaseous water to enable us to compare directly with experimental techniques such as temperature programmed desorption. The adsorption energies of different organic surfactants on the surfaces were calculated in the same manner as the adsorption energies of water molecules, by comparing the energy of the surface with the adsorbate and the sum of the energies of the pure surface and that of an isolated surfactant molecule:

$$U_{ads} = U_{(S+surfactant)} - (U_S + U_{surfactant}) \tag{2.43}$$

Where U_{ads} is the adsorption energy, U_S is the energy of the pure surface of the mineral, $U_{surfactant}$ is the energy of the surfactant molecule and $U_{S+surfactant}$ is the energy of the surface with an adsorbed surfactant molecule.

We calculate adhesion energies for an interface between two mineral surfaces in a similar way. The adhesion energy γ_{adh} is a measure of the stability of the interface with respect to the two surfaces of the materials, which is calculated as follows:

$$\gamma_{adh} = \frac{E_{int} - (E_{surf1} + E_{surf2})}{A} \tag{2.44}$$

where E_{int} is the energy of the interfacial system, E_{surf1} is the energy of the surface block of the first mineral, E_{surf2} is the energy the surface block of the second mineral and A is the area of the interfacial region.

2.6 Crystal Morphology

The equilibrium morphology of a crystal is determined by the surface free energy and the related growth rate of the various surfaces and provides a mea-

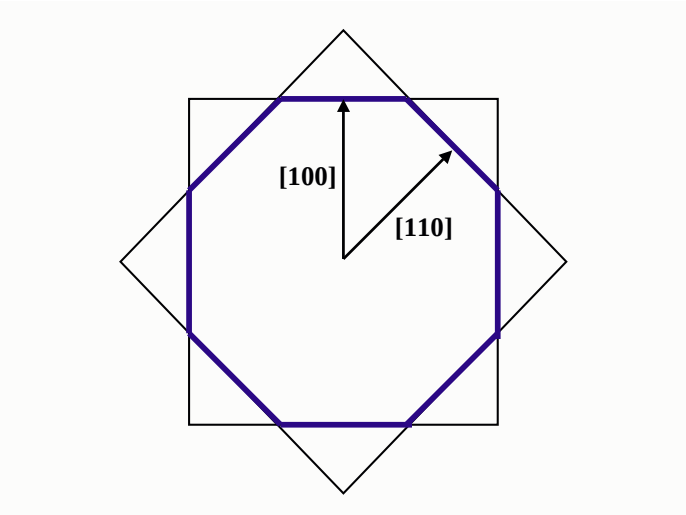

Figure 2.5: Schematic representation of equilibrium morphology due to two faces with equal specific free energy in two dimensions.

sure of the relative stabilities of the surfaces. Wulff's Theorem[58] showed that a polar plot of surface energy versus orientation of normal vectors would give the crystal morphology based on the approach of Gibbs,[59] who proposed that under thermodynamic control the equilibrium form of a crystal should possess minimal total surface free energy for a given volume. The equilibrium morphology thus is the shape of the crystal with minimum total surface free energy. If the crystal is limited in space by n flat surfaces, then:

$$\frac{\sigma_1}{h_1} = \frac{\sigma_2}{h_2} = \frac{\sigma_3}{h_3} ..... = \frac{\sigma_i}{h_i} = \frac{\sigma_n}{h_n} \tag{2.45}$$

Where σ_i is the specific free energy of the i^{th} face and h_i is the distance from the center of the crystal to the plane of the i^{th} face[60] normal to this face. A schematic example of crystal morphology is shown in figure 2.5. The bold line

indicates the equilibrium morphology for a case where the {100} and {110} surfaces have the same specific free energies and hence the same height, as the height of the face is directly proportional to its specific free energy. A surface with a high surface free energy is expected to have a large growth rate and this fast growing surface will not be expressed in the morphology of the resulting crystal. Only surfaces with low surface free energies and hence slow growing will be expressed. Molecular and lattice dynamics simulations have shown that the contribution of the excess entropy term to the surface free energy in ionic solids is small compared to the enthalpy term, as the differences between the entropies of the bulk and the surface are small.[61, 62] The surface energies then can be assumed to determine the equilibrium morphology of the crystal as follows:

$$E_S = \sum_i \gamma_i A_i = minimum\ for\ constant\ volume \tag{2.46}$$

Where E_S is the excess energy for the surface which has been defined by Stoneham[63] as:

E_S= [**cohesive energy of finite crystal**] − [**number of atoms**] **x** [**cohesion energy per atom in an infinite crystal**]

and γ_i and A_i are the surface and surface area of the i^{th} crystallographic face. At equilibrium, the surface with the highest surface energy,will be furthest away from the center of the crystal and hence have the smallest surface area. Similarly a surface with low surface energy, will grow more slowly resulting in a larger surface area and a distance closer to the center of the crystal.

2.7 Molecular dynamics

The static lattice calculations discussed in the previous sections disregard the effect of temperature, i.e. all calculations are at 0K ignoring the zero point energy. Molecular dynamics simulations, as the name suggests, include the dynamics of the particles due to the effect of temperature. The advantage of this method as compared to static lattice minimisation methods is that it is able to consider diffusion and anharmonic effects of the ions or molecules in a system over a period of time. Classical equations of motion are solved for a box containing N number of particles for example.[64] The classical equations are of the form:

$$\sum_{i=1}^{N} m_i v_i(0) = 0 \tag{2.47}$$

and

$$\sum_{i=1}^{N} m_i v_i^2(0) = 3NK_BT \tag{2.48}$$

where m_i and v_i are the mass and velocity of ion i respectively, N is a number of particles or atoms, K_B is the Boltzman constant and T is the simulation temperature. The N particles of the simulation box are initially given random velocities in such a way that the components of linear momentum of the whole system are zero and the kinetic energy of the combined particles corresponds to the desired simulation temperature.[65] The simulation is initiated in a number of equilibration time steps (Δt), and the number of these equilibration time steps depend on the nature of the system under study. Generally, depending also on the value of Δt, 5000 are sufficient for simple systems containing only the coulombic interactions and simple two body

potentials, but more than 10 000 are required for more complex systems.

During data collection, the equations of motion from classical mechanics are solved in a finite difference approximation at successive time steps (Δt), with the position and velocities of the particles calculated at each time step used for successive iterations.

$$F_i(t) = m_i a_i(t) \tag{2.49}$$

$$v_i(t + \Delta t) = v_i(t) + a_i(t)\Delta t \tag{2.50}$$

$$r_i(t + \Delta t) = r_i(t) + v_i(t)\Delta t \tag{2.51}$$

F_i is the force on the i^{th} particle, v_i is its velocity, m_i is the mass of the particle, t is the time and Δt is the time step. The calculation of the force acting on each particle is the most time consuming part in this form of calculation and it is the one that must be carried out with greatest possible efficiency.

There are different methods that can be used in the calculation of these classical equations. Because lattice vibrations are of the order of 10^{-13} to 10^{-12} seconds, the time step Δt is set to a lower value to make sure that the simulation samples all the lattice vibrations within each time step. Normally it is set at about 10^{-15} to 10^{-14} seconds.

Finite Difference Method: Having the velocity $v(t)$ at time t, the next step is to find the velocity v at time $(t + \Delta t)$. The estimated properties at time $t + \Delta t$ by Taylor expansion are:

$$r^p(t + \Delta t) = r(t) + \Delta t v(t) + \frac{1}{2}\Delta t^2 a(t) + \Delta t^3 b(t) + ... \tag{2.52}$$

$$v^p(t+\Delta t) = v(t) + \Delta t a(t) + \frac{1}{2}\Delta t^2 b(t) + ... \tag{2.53}$$

$$a^p(t+\Delta t) = a(t) + \Delta t b(t) + ... \tag{2.54}$$

$$b^p(t+\Delta t) = b(t) + ... \tag{2.55}$$

Where the superscript p marks predicted values of the properties, r and v are position and velocity respectively, a is the acceleration and b is the third derivative of r with respect to t. More details on the expansion are given in references[66, 67, 68].

Verlet Algorithm: This algorithm is one of the most widely used methods of integrating the equations of motion[69], which involves the direct solution of the forces acting on the particle $F_i(t) = m_i a_i(t)$. The method is based on position $r(t)$ and $r(t+\Delta t)$ and on the acceleration at positions $t+\Delta t$ and $t-\Delta t$:

$$r(t+\Delta t) = r(t) + \Delta t v(t) + \frac{1}{2}\Delta t^2 a(t) + ... \tag{2.56}$$

$$r(t-\Delta t) = r(t) - \Delta t v(t) + \frac{1}{2}\Delta t^2 a(t) + ... \tag{2.57}$$

Then addition of the two equations above gives the Verlet algorithm:

$$r(t+\Delta t) = 2r(t) - r(t-\Delta t) + \Delta t^2 a(t) \tag{2.58}$$

However there is some loss of numerical precision that needs modification. The modification used is called half-step or "leap-frog" scheme[70, 71] which uses the algorithm:

$$r(t+\Delta t) = r(t) + \Delta v(t + \frac{1}{2}\Delta t) \tag{2.59}$$

$$v(t+\frac{1}{2}\Delta t) = v(t-\frac{1}{2}\Delta t) + \Delta t a(t) \tag{2.60}$$

$r(t)$ is the current position, $a(t)$ the acceleration and $v(t - \frac{1}{2}\Delta t)$ is the mid-step velocity . The velocity equation is implemented first and the velocities leap over the coordinates to give the next mid-step velocity $v(t + \frac{1}{2}\Delta)$, when the current velocity is calculated.

$$v(t) = \frac{1}{2}(v(t + \frac{1}{2}\Delta t) + v(t - \frac{1}{2}\Delta t)) \tag{2.61}$$

This is similar to the Verlet equation but here the velocities are included which make it more accurate than the original Verlet algorithm.

A Verlet algorithm that stores positions, velocities and acceleration all at the same time t, minimizing random errors has been proposed by Swope *et al.*[72]

$$r(t + \Delta t) = r(t) + \Delta t v(t) + \frac{1}{2}\Delta t^2 a(t) \tag{2.62}$$

$$v(t + \Delta t) = v(t) + \frac{1}{2}\Delta t[a(t) + a(t + \Delta t)] \tag{2.63}$$

Where only the storage of $r(t)$, $v(t)$ and $a(t)$ is required. This method gives velocities at $t + \Delta t$ making calculation of the kinetic energy of the system easier.

Beeman Algorithm: This sophisticated algorithm uses:

$$r(t + \Delta t) = r(t) + \Delta t v(t) + \frac{1}{6}[4a(t) - a(t - \Delta t)]\Delta t^2 \tag{2.64}$$

$$v(t + \Delta t) = v(t) + [\frac{1}{6}[2a(t + \Delta t) + 5a(t) - a(t - \Delta t)]]\Delta t \tag{2.65}$$

It is more accurate than the Verlet algorithm in calculating the velocities, but its complexity makes it computationally expensive. Details of this algorithm is documented in reference[73].

Boundary Conditions and Ensembles

The aim of computer simulation is to produce a model that has the same structural arrangements, the same energies and physical properties as the actual material under investigation.[74] Ideally the model should be as large as possible, but the size is limited by the computational expense and hence only a few tens of atoms in accurate electronic structure calculation methods based on quantum mechanics can be carried out, although thousands of atoms can be modeled in the atomistic simulation approach, including static lattice and molecular dynamics simulations.

The simulation box containing the particles under study is therefore duplicated periodically through space to give an infinite "lattice". As the particle moves in the simulation box during the simulation under the influence of interatomic forces exerted by its neighbours, its image in the replica boxes moves in exactly the same way, even to the extent that should a particle leave a simulation box, its image enters the box through the opposite side. There are no walls at the boundary of the central simulation box but the number of particles in the box is usually conserved.

There are also different, thermodynamic conditions under which a simulation can be run. The number N of particles in the simulation box is usually kept constant, as mentioned above, the volume V of the system can also be kept constant and if the total energy $E = (potential + kinetic)$ of the system is also kept constant, then the system corresponds to the microcanonical ensemble in statistical thermodynamics (NVE). Alternatively the temperature T of the system may be kept constant and the system then corresponds to the

canonical ensemble (NVT). One ensemble that closely imitates the physical reality is the isothermal-isobaric ensemble(NpT), when the pressure of the system is constrained to be constant, correspondingly varying the volume of the simulation box.

Molecular dynamics calculations can be executed using any of a number of different computational simulation codes, one of which is DL_POLY.[75]

2.8 QUANTUM MECHANICS SIMULATIONS

Various codes that have been implemented for the calculation of properties of materials employ quantum mechanical techniques. Quantum mechanics provides a rigorous framework for the description of inter-atomic interactions and, in principle, allows the determination of the energy hyper surface of any atomic system to any desired degree of accuracy. In this section we briefly discuss the theory behind quantum mechanical calculations based on the Density Functional Theory. These methods are embodied in for example the CASTEP code[76, 77] that performs an electronic + geometry optimisation of the system, providing structural properties such as lattice parameters and atomic positions and electronic, magnetic and optical properties of the system. The CASTEP code employs plane-wave pseudopotential methods which will be described later, whereas other codes such as CRYSTAL [78] use local orbitals to perform the $ab-initio$ or first principle calculations of the ground state energy, electronic wave function and properties of isolated or periodic systems.

Prediction of the electronic and geometric structure of a solid requires

calculation of the quantum mechanical total energy of the system and minimization of that energy with respect to the electronic and nuclear coordinates.The calculation of the total energy, electronic structure, and ground state properties of a system requires solution of the time independent, non relativistic Schrödinger equation

$$H\psi = E\psi \tag{2.66}$$

Where H is the hamiltonian and ψ is the wave function. However, to calculate the total energy, a number of simplifications and approximations are made in practice. Since there is a large difference in mass between the electrons and the nuclei and the forces on the particles are the same, electrons respond instantaneously to the motion of the nuclei. By using the Born Oppenheimer approximation, which assumes that the electrons are always in equilibrium with respect to the nuclear motion, the Hamiltonian can be simplified to treat only interactions involving the electrons. However further simplifications need to be introduced to allow the energy calculation to be performed accurately. These include the density functional theory (DFT), and pseudopotential approximation.

2.8.1 Density Functional Theory

An important advance in the calculation of the energy of electrons and atoms and the forces on each atom was made by Kohn and Sham[79], who showed how a mean field theory could be applied to this problem. In their method, the electron density plays a crucial role so that, although the term has more

general applicability, the Kohn-Sham method is commonly referred to as density functional theory (DFT). This has since advanced to become a very important method for determining the energy of many-electron, and therefore many-atom systems. In addition Kohn-Sham density functional theory is equally applicable to molecules (bounded electrons of atoms) and crystalline materials (where a specific unit cell is repeated throughout space)[80]. Density functional theory is a unified approach in the sense that it provides accurate structural, energetic and electronic properties not only for solids and surfaces, but also for molecules. It starts with a consideration of the entire electron system. The total energy of the system is expressed as a functional of the total electron density ($\rho(\mathbf{r})$), which in turn depends on the positions of the atoms (R(x)).

$$E = E\left[\rho(\mathbf{r}), R(x)\right] \tag{2.67}$$

The total energy is then decomposed into three contributions, a kinetic energy T, a coulomb energy U, due to a classical electrostatic interactions among all charged particles in the system which can be written as

$$U[\rho] = U_{en}[\rho] + U_{ee}[\rho] + U_{ion-ion} \tag{2.68}$$

where U_{en} is for electron-nuclei interaction or external potential and U_{ee} is for electron-electron interaction and a term called the exchange correlation energy (E_{xc}), that captures all many body interactions.

$$E\left[\rho\right] = T_0 + U\left[\rho\right] + E_{xc}\left[\rho\right] \tag{2.69}$$

This composition is formally exact, but the actual expressions for the many-body and correlation interactions are unknown. As an approximation the exchange-correlation energy is taken from known results of an interacting electron system of constant density (homogeneous electron gas) and it is assumed that exchange and correlation effects are not strongly dependent on inhomogeneities of the electron density away from a reference point $\mathbf{r}$.

Thus the local electron density can be used to evaluate the exchange and correlation effects of a volume element around $\mathbf{r}$. The necessity in this case is to determine the set of wave functions ψ_i, that minimize the Kohn-Sham energy functional. These are given in the solution of the following effective one particle Schrödinger equations, which are also referred to as Kohn-Sham equations.

$$\varepsilon_i \Psi_i(\mathbf{r}) = \left[-\frac{\hbar^2}{2m}\nabla^2 + V_{ion}(\mathbf{r}) + V_H(\mathbf{r}) + V_{xc}(\mathbf{r}) \right] \Psi_i(\mathbf{r}) \tag{2.70}$$

ψ_i is the wave function of the electronic state i and ε_i is the Kohn-Sham eigenvalue. The terms of the equation above are derived from the total energy given in equation 2.70. Corresponding to the three terms in the total energy expression, namely: the kinetic energy, the coulomb energy and the exchange-correlation energy, the effective one-particle hamiltonian of the Kohn-Sham equations contains a kinetic operator, a coulomb potential operator and an exchange-correlation operator. The latter is related to the exchange correlation energy by

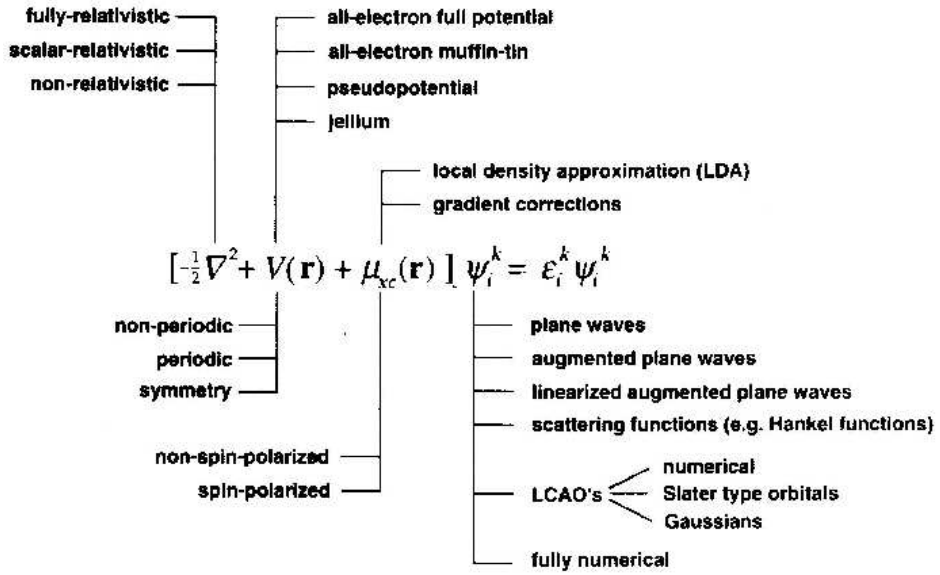

Figure 2.6: Different options that are used to solve the Kohn-Sham equation

$$V_{xc}(\mathbf{r}) = \frac{\partial \mathbf{E_{xc}}\left[\rho(\mathbf{r})\right]}{\partial \rho(\mathbf{r})} \tag{2.71}$$

V_H is the Hartree potential of the electrons given by

$$V_H(\mathbf{r}) = e^2 \int \frac{\rho(\mathbf{r}')}{|\mathbf{r} - \mathbf{r}'|} d^3\mathbf{r}' \tag{2.72}$$

The one particle wave functions, which are the solutions of equation 2.72, are related to the total electron density by

$$\rho\left(\mathbf{r}\right) = \sum n_i |\psi_i(\mathbf{r})|^2 \tag{2.73}$$

The total electron density of equation 2.74 together with the one-particle wave functions allows the calculation of the total energy. Since the total

density varies with the position of the atoms, density functional theory allows the calculation of the total energy as a function of the position of the atoms.

According to the Hohenberg-Kohn theorem the exchange-correlation energy can be described as a function of electron density. This exchange and correlation energy can be described by the use of the local density approximation (LDA). In this approximation, it is assumed that the exchange correlation energy per electron at a point $\mathbf{r}$ in the electron gas, $\varepsilon_{xc}(\mathbf{r})$, is equal to the exchange and correlation energy per electron in a homogeneous electron gas that has the same density as the electron gas at point $\mathbf{r}$.

$$E_{xc}\left[\rho(\mathbf{r})\right] = \int \varepsilon_{xc}(\mathbf{r})\rho(\mathbf{r})d^3\mathbf{r} \tag{2.74}$$

and

$$\frac{\delta E_{xc}\left[\rho(\mathbf{r})\right]}{\delta\rho(\mathbf{r})} = \frac{\partial\left[\rho(\mathbf{r})\varepsilon_{\mathbf{xc}}(\mathbf{r})\right]}{\partial\rho(\mathbf{r})} \tag{2.75}$$

with

$$\varepsilon_{xc}(\mathbf{r}) = \varepsilon_{xc}^{hom}\left[\rho(\mathbf{r})\right] \tag{2.76}$$

In LDA it is assumed that the electrons are "near sighted", i.e. that the detailed inhomogeneous structure of the electron density near a reference point is not important.

In performing the calculations, LDA is known to underestimate the bond lengths in molecules and cell parameters in crystals. In order to overcome this deficiency, Perdew and Wang[81] developed a gradient-corrected LDA version called the generalised gradient approximation (GGA). However, although an improvement, this approximation is known to overestimate the cell parameters.

2.8.2 Plane Wave Basis

In obtaining the solution of the Kohn-Sham equations, some difficulties have to be overcome. A wave function must be calculated for each electron and because each electronic wave function extends over the entire system, the basis set that is required to expand each wave function is too large. However, this problem can be dealt with by performing calculations on periodic systems applying the Bloch's theorem to the electronic wave functions. Bloch's theorem states that in a periodic solid each electronic wave function can be written as the product of the periodic part of the cell and the wavelike part.

$$\psi_i(\mathbf{r}) = exp\,[i\mathbf{k}.\mathbf{r}]\,f_i(\mathbf{r}) \tag{2.77}$$

From this equation we can write the planewaves whose wave vectors are reciprocal lattice vectors of the crystal as

$$f_i(\mathbf{r}) = \sum_G c_{i,G} exp\,[i\mathbf{G}.\mathbf{r}] \tag{2.78}$$

Where G is the reciprocal lattice vector and defined by $\mathbf{G}.l = 2\pi m$ for all l where l is the lattice vector of the crystal and m is an integer. Hence

$$\psi_i(\mathbf{r}) = \sum_G c_{i,k+G} exp\,[i(\mathbf{K}+\mathbf{G}).\mathbf{r}] \tag{2.79}$$

.

The infinite number of electrons in the solid are accounted for by an infinite number of **K** points and only a finite number of electronic states are occupied at each **K** point. Bloch's theorem changes the problem of calculating an infinite number of electronic wave functions to one of calculating a finite number of electronic wave functions at an infinite number of **K** points.

Bloch's theorem states that the electronic wave functions at each **K** point can be expanded in terms of a discrete plane wave basis set. In this case the coefficients $c_{i,k+G}$ for the plane waves with small kinetic energy $(\frac{\hbar^2}{2m})|\mathbf{k}+\mathbf{G}|^{\mathbf{2}}$ are more important than those with large kinetic energy.

The plane-wave basis set can be truncated to include only plane waves that have kinetic energies less than some particular cutoff energy. The truncation of the plane-wave set at a finite cutoff energy will lead to an error in the computed total energy. However it is possible to reduce the magnitude of the error by increasing the value of the cutoff energy.

Now substitution of equation 2.79 into 2.70 and integration over **r** gives a secular equation:

$$\sum_{G'}\left[\frac{\hbar^2}{2m}|\mathbf{k}+\mathbf{G}|^2\delta_{GG'}+V_{ion}(\mathbf{G}-\mathbf{G'})+V_H(\mathbf{G}-\mathbf{G'})+V_{xc}(\mathbf{G}-\mathbf{G'})\right]c_{i,k+G'}=\varepsilon_i c_{i,k+G} \tag{2.80}$$

Solution of equation 2.80 can be found by diagonalization of a Hamiltonian matrix whose matrix elements $\mathbf{H_{k+G,k+G'}}$ are given by the terms in the square brackets. The size of the matrix is determined by the choice of cutoff energy $(\hbar^2/2m)|\mathbf{k}+\mathbf{G_c}|^{\mathbf{2}}$, and will generally be too large for systems that contain both valence and core electrons. However the use of the pseudopotential approximation helps to overcome this problem.

2.8.3 Pseudopotential Approximation

Though Bloch's theorem gives some solution to specific problems on the expansion of the plane waves, very large numbers of plane waves are needed

to expand the tightly bound core orbitals and to follow rapid oscillation of the wave functions of the valence electrons in the core region. Thus the use of plane-waves for an all electron calculation would be computationally expensive. In many respects, core electrons are fairly inert and not involved in chemical bonding. Hence they are not important in the determination of the structural stability and low energy response properties of molecules and crystals. The behavior of the valence electrons is the one that normally determines the physical and chemical properties of systems. To reduce the cost of calculations where all electrons are considered explicitly, the pseudopotential approximation is employed, which allows the electronic wave function to be expanded using a much smaller number of plane-wave basis states. The core electrons are assumed to be frozen, and they together with the strong ionic potential are replaced by a weaker pseudopotential that acts on a set of pseudo wave functions rather than the true wave functions.

The most general form of pseudopotential is

$$V_{NL} = \sum_{lm} |lm > V_l < lm| \tag{2.81}$$

Where lm are the spherical harmonics and V_l is the pseudopotential of the angular momentum l.

Chapter 3

POTENTIAL MODEL

In interatomic potential-based simulation, the reliability of calculated structures, energies and surface energies depends on the quality and the accuracy of the potential model, which describes the interatomic interactions within the systems. There are different ways one can obtain the potential parameters for a particular system. They can be obtained by direct calculation using quantum mechanical methods, where there are no experimental data to compare with, or by empirical fitting, in which case the parameters are derived by simultaneously fitting to the available experimental data, e.g lattice constants, vibrational frequencies, bond dissociation energies and the mineral structure itself. From a review by Harding[82], it is clear that the uncertainties in the numerical results of calculations are quite often due to deficiencies in the potential model rather than the actual calculation.

In this chapter we supply the various potential parameters used in this work and we describe how they were derived and how their accuracy was tested.

3.1 ELECTRONIC POLARISABILITY OF IONS

In ionic solids, the mutual electronic polarisation cannot be ignored or neglected[82], although for many calculations involving potentials, the rigid ion model gives acceptable results. The rigid ion model where each ion is modelled as a point charge, is acceptable in reproducing the structural parameters for a rigid system, but the lattice vibrations will be poorly modelled as they are strongly coupled to polarisability. This model would therefore give poor results for defect energies, but this problem can be overcome by fitting short range parameters to model static dielectric constants and overestimating the polarisation due to lattice relaxation to compensate for the shortfall due to neglecting the polarisability. However, this correction will not work on all calculations involving potentials, for example in molecular dynamics simulations where time is included and there are various models available for including polarisability in the simulations.

3.1.1 Point Polarisation Model

The point polarisation model provides a simple way of including the electronic polarisability, by allowing a fixed point dipole to develop on each ion. The dipole is of magnitude μ and is related to the polarisability α and the effective field E acting on the ion.

$$\mu = \alpha E \tag{3.1}$$

Thus the energy of the interacting dipole can be calculated in a computationally inexpensive manner. However, although this model has been used

to calculate defect energies[83], these defect energies were significantly lower than the experimental values due to the fact that this method does not take into account the coupling between the short range repulsion and the polarisability. In addition, the defect energies from this model are also underestimated because the omission of the coupling results in an overestimation of the polarisation. Some critical distance r_{crit}, as shown by Faux[84], exists between the approaching ion and this distance caused the energy to diverge.

$$r_{crit}(ij) = (4\alpha_i\alpha_j)^{\frac{1}{6}} \tag{3.2}$$

3.1.2 Shell Model

A different model for the inclusion of electronic polarisation of the atoms is the shell model by Dick and Overhouser[85]. This model describes the ion in a simple mechanical way, as a core and a massless shell. The core represents the nucleus of the atom, which contains all the ion's mass and a charge Q and the shell approximately represents the valence electrons and has a charge q. The total charge of the the ion is the sum of Q and q. Figure 3.1 below gives the schematic representation of the shell model.

The core and the shell are connected by a harmonic spring with constant k giving rise to an interaction energy:

$$U(r_i) = \frac{1}{2}k_i r_i^2 \tag{3.3}$$

Where k is the force constant for the harmonic spring connecting the two and r is the distance between them. The position of the core gives the exact position of the ion in the crystal while the position of the shell has no physical

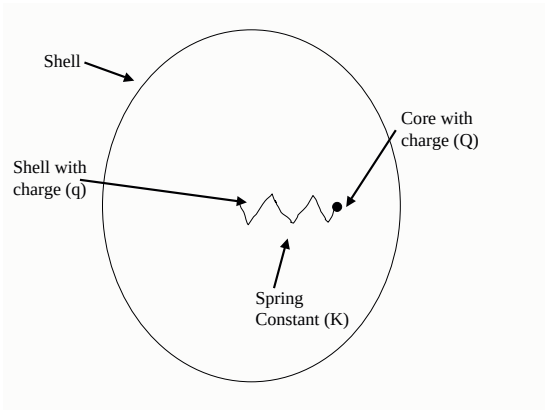

Figure 3.1: Schematic representation of the shell model.

meaning although initially it is given the same coordinates as those for the core. The spring constant and the charges of the core and shell determine the polarisability of the ion:

$$\alpha_i = \frac{q^2}{4\pi\varepsilon_0 k_i} \tag{3.4}$$

Where q is the charge on the shell and k is the force constant for the harmonic spring connecting the core and spring and ε_0 is the permittivity of free space. q and k are found by empirical fitting to the dielectric properties, elastic constants or phonon dispersion curves of the material. The polarisation of an ion is described in terms of displacement of its shell with respect to the core. Introducing the shell model doubles the number of species compared to a rigid model. As large number of species means that the number of degrees of freedom is increased, introduction of the shell model hence increases the simulation time.

The use of the shell model in a molecular dynamics simulation code, such

as DL_POLY, is a bit different but the principle remains the same. The shell now has some mass, which is insignificantly small compared to the core and deducted from the core mass. It is kept so small to ensure that no exchange of energy occurs between itself and the core during simulation.

3.2 SHORT RANGE TWO BODY POTENTIAL FUNCTIONS

The interactions between neighboring electron charge clouds are represented by short range potential functions. They can be grouped into two-body, and many body (three and four body) potential functions. The many body potential functions are used when covalent and partially covalent bonds are present in the system to be simulated. The interaction often contains attractive (van der Waals) and repulsive parts. The bonded and non-bonded interactions are represented by different analytical forms, the most important of which we discuss in this section.

3.2.1 Bond Harmonic potential Functions

The harmonic function is used to model the interaction between two bonded ions and is given by the analytical equation:

$$U(r_{ij}) = \frac{1}{2}k_{ij}(r_{ij} - r_0)^2 \tag{3.5}$$

Where k_{ij} is the bond force constant, r_{ij} is the interionic separation between the ions i and j, and r_0 is the separation at equilibrium. The potential is harmonic as the energy depends on the square of the displacement of the

bond length (r_{ij}) from the equilibrium value and it is only appropriate for small deviations from the equilibrium bond distance. For bond distances further away from equilibrium, a different potential function is needed and is discussed in the following section part.

3.2.2 Morse Potential Function

Interactions at bond distances which display or possess anharmonicity are described well by the Morse potential function, which is used, for example for the OH bond in hydroxy group[86]. We also use it for the P-O interactions in the PO_4 group within the apatite system. The Morse potential function has the form:

$$U(r_{ij}) = D(1 - e^{[-\alpha(r_{ij} - r_0)]})^2 - D \tag{3.6}$$

Where D is the bond dissociation energy, r_0 is the equilibrium separation and α is a variable that can be determined by spectroscopic data and is a slope of the potential energy well. For this Morse potential used in materials applications, the potential energy is zero at infinite separation of the two ions, and the potential energy is at its minimum at the equilibrium bond distance. The form is represented graphically in figure 3.2.

The Morse potential can also include a subtraction of the coulomb interaction which is used routinely in biological applications, where the coulomb interaction between nearest neighbours in molecules are not taken into account.

$$U(r_{ij}) = D(1 - e^{[-\alpha(r_{ij} - r_0)]})^2 - D - \frac{Cq_iq_j}{r} \tag{3.7}$$

Where C is the fraction of the coulombic subtraction, where the value of 1.0

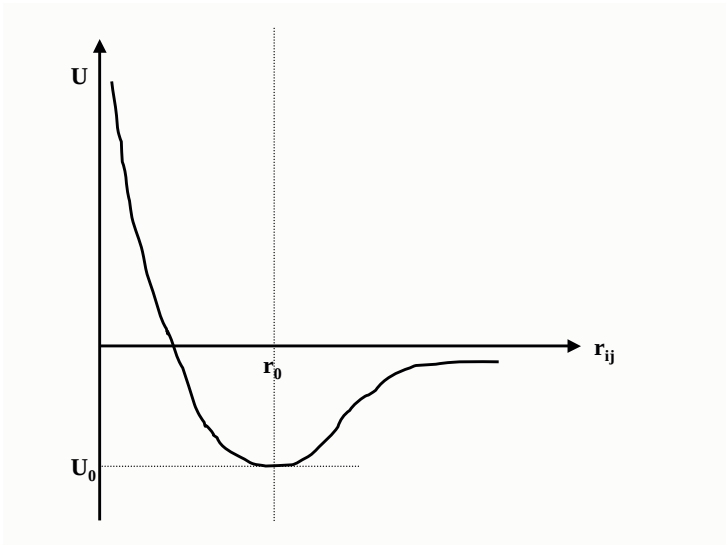

Figure 3.2: Graphical representation of the Morse potential function.

means that no coulombic interaction exists between the atoms. For a value of C=0 the equation reduces to the original Morse potential with full coulombic interaction. q_i and q_j are the charges of the ions i and j respectively. Morse potentials are generally used to describe the bonded interaction between two nearest neighbours, where interactions between the next nearest neighbours and those further away are represented by different potential functions for non-bonded interactions.

3.2.3 Lennard Jones Potential function

One of the potential functions describing the interaction between non-bonded ions is the Lennard Jones potential, which is used especially for large systems. The potential is made up of an attractive term, usually r^{-6}, and a repulsive

term, usually r^{-12}:

$$U(r_{ij}) = \frac{A}{r_{ij}^{12}} - \frac{B}{r_{ij}^{6}} \tag{3.8}$$

A and B are variable parameters derived empirically.

3.2.4 Buckingham Potential Function

The Buckingham potential is widely used for two body non-bonded interactions in ionic solids. In this potential the repulsive term of the Lennard Jones potential is replaced by an exponential term:

$$U(r_{ij}) = A_{ij} e^{(\frac{-r_{ij}}{\rho_{ij}})} - \frac{C_{ij}}{r_{ij}^{6}} \tag{3.9}$$

Where A_{ij} and ρ_{ij} are the size and the hardness of the ion respectively, and C_{ij} is the term included to model dispersion. The short range repulsion is represented by the first term and the long range attraction which dominates at larger separations is represented by the second term as is the case in the Lennard Jones potential. The inclusion of the exponential function makes the computation using the Buckingham potential more expensive, but this exponential function is a more accurate estimate of the repulsive term. The second term is sometimes omitted and the value of the parameter A is then adjusted to take into consideration the long range attractions. The resulting potential is called a Born-Mayer potential.

3.3 MANY BODY THREE-FOUR POTENTIAL FUNCTIONS

So far the potential parameters discussed above have addressed the interactions involving two neighbouring ions. No directionality in the bonding has been taken into consideration. However there are interactions that do contain directionality, which is taken into account by three body and four body interactions. The potential parameters discussed below address two types of interactions between next nearest neighbour atoms and beyond.

3.3.1 Three Body Potential Function

The three body potential is used to describe the interaction between three (covalently) bonded species, shown in figure 3.3, where atoms j and k are joined in the middle by a third atom i. The energy is proportional to the deviation of the angle from equilibrium where θ_{ijk} is the angle between atoms j and k. The three body potential is also called the bond bending term. It introduces an energy penalty for deviation of the bond angle from the equilibrium value, inferring the directionality of the bonding. The three body potential function is of the form:

$$U = \frac{1}{2}k_{ijk}(\theta_{ijk} - \theta_0)^2 \tag{3.10}$$

where k_{ijk} is the bond-bending force constant between the bonds ij and ik and θ_0 is the equilibrium angle.

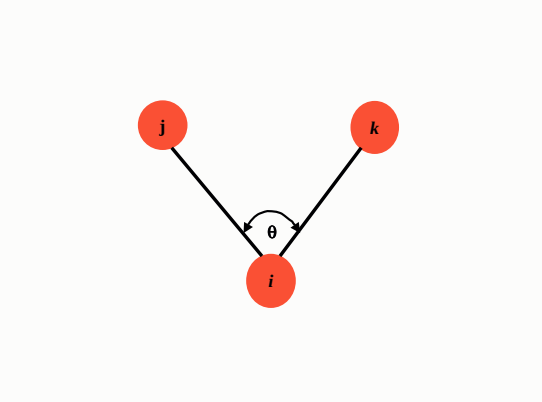

Figure 3.3: Schematic representation of the three body interaction.

3.3.2 Four Body Potential function

The four body potential, also called the torsional function, is used to model systems which have a planar nature due to π bonding. In a plane of four atoms i, j, k, l as in figure 3.4, the torsional or dihedral angle is the angle between the plane containing i, j and k and the plane j, k and l. It has the form:

$$U = k_{ijkl}[1 - scos(n\theta_{ijkl})] \tag{3.11}$$

Where k_{ijkl} is the torsional force constant, $s = \pm 1$ depending on which conformation has the lowest energy. The planes are defined between the ions, i, j and k and between j, k and l where the potential energy is n times the angle between these planes, depending on the number of identical rotations about the $j - k$ axis.

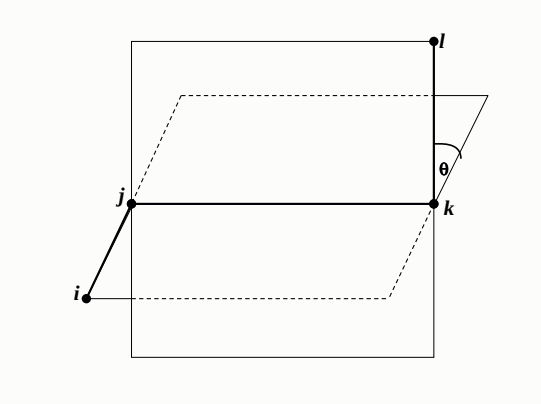

Figure 3.4: Schematic representation of the four body bonding, showing the angle between the plane containing atoms i, j and k and the plain containing j, k and l.

3.4 POTENTIAL DERIVATION

Potential parameters can be obtained in two different methods. One is to use an empirical derivation fitting and the second one is to use the direct calculation method. Empirical fitting uses classical calculation methods that involve the potential functions discussed above to derive/ adjust the potentials by comparison to a range of experimental data, while the direct calculation method uses electronic structure calculation methods to map the potential energy landscape which is then used to derive the interatomic potential parameters.

3.4.1 Empirical Fitting

During the empirical fitting, the structural and lattice properties are almost always used to determine the potential parameters.[87] Preferably data such

as elastic and dielectric constants should be available in addition to structural data.[88] Phonon dispersion curves and vibrational frequencies can be used as well to supplement the data for fitting. The main aim is to vary the potential parameters while calculating these experimental properties, where adjustments are made until they are reproduced as closely as possible.The aim of the fit is to minimise the "sum of squares", which is a measure of the quality of the fit. This sum of squares is calculated as follows:

$$F = \sum_{all-observables} w(f_{calc} - f_{obs})^2 \tag{3.12}$$

Where f_{calc} and f_{obs} are the calculated and observed quantities used for the fitting, and w is a weighting factor. The weighting factor depends on a number of considerations including the relative magnitude of the quantities and the reliability of the data. In general the lattice parameters are given a higher weighting factor as these are measured more accurately than the other properties. As there are an infinite number of possible fits depending on the weighting factor, there is no such thing as a unique fit, but a good fit should be obtained if sufficient experimental data are available. The reliability of the derived potentials can also be enhanced by fitting not only to a single structure, but by concurrently fitting to multiple structures.

3.4.2 Direct Calculation Method

The direct calculation method of deriving potential parameters is based on quantum mechanical calculations, either by electron gas methods[89] or *ab initio* calculations using Hartree-Fock[90] or local density approximation methods[91] and also with embedded atom methods (EAM)[92, 93, 94, 95].

The interaction energy between a pair cluster or periodic array of atoms can be calculated for a range of distances and the resulting potential energy curve is fitted to a suitable functional form. Thus this method can calculate potentials for any interaction, but it may be dependant on the availability of suitable basis sets.

3.5 TRANSFERABILITY OF POTENTIALS

Potential parameters are mainly derived and fitted to the bulk structure of the material even though a surface environment is different from the bulk. In semi-conductors, where the surface involves breaking bonds, and metals where the surface means a sudden change in the electron density, there is often a problem with transferability from bulk potential parameters to surfaces. However, in ionic materials after relaxation, the Madelung potentials are 90% or more of the bulk values and hence the change of ionic radii is negligible. Previous calculations [96] of energies and surface relaxations of Cr_2O_3, using different potentials that reproduced bulk properties, did not show any significant differences. Hence, in ionic materials, potentials that reproduce bulk properties accurately are expected to be sufficiently accurate for surface calculations as well.

In addition, the transfer of potentials derived for one compound to another is also possible. For example potentials derived for binary oxides[97, 98] have been successfully transferred to ternary systems[97, 99, 100, 101, 98], whereas potentials for alkali chlorate and bromate salts have been transferred to the divalent strontium chlorite salt, which resulted in the reasonable repro-

duction of experimental data[102]. An interatomic potential for the titanium oxides was shown to be transferable across different stoichiometries, polymorphs and Ti oxidation states,[103] and the derivation of a new force field for gallium and gallophosphate microporous solids from existing potentials for zeolites and their aluminophosphate analogues by Girard[104] gave results within reasonable accuracy.

3.6 POTENTIALS USED IN THIS WORK

As the reliability of calculated properties depends on the accuracy of the potential model, we have derived potentials which are suitable for the description of our system of interest, namely the fluorapatite mineral including water; the fluorapatite/α-quartz system and also several organic adsorbates, viz: methanoic acid, hydroxyethanal, hydroxamic acid, and methylamine. The energy minimisation codes employed for the derivation of the potential model and the calculation of the bulk crystal properties were PARAPOCS[105] and GULP,[106] while the surfaces and interfaces were modelled using the code METADISE,[47]

3.6.1 Deriving The Potential for The Fluorapatite and Water

Although other potential models for fluorapatite are available, by Lee et al.[107] and Meis et al.,[108] apatite co-exists with both calcite ($CaCO_3$) and fluorite (CaF_2) in mineral deposits and hence we sought to derive a potential model for fluorapatite which was compatible with existing models for calcite

and fluorite, so that in future we may model interfaces and substitutional defects between these three minerals. The Ca-O and Ca-F parameters in the fluorapatite potential were therefore taken from the calcium carbonate and calcium fluoride potentials developed by Pavese et al.[109] and Catlow et al.[110] respectively, where the oxygen and fluorine core-shell charges and interactions were also kept at the values derived by Pavese et al. and Catlow et al. for calcite and fluorite.[109, 110] All other potential parameters, i.e.: the interactions between oxygen and fluoride ions and between oxygen and phosphorus within the phosphate groups, were fitted empirically to a variety of experimental parameters, such as crystal structure and elastic constants, bond dissociation energies and vibrational data of the phosphate group. All short-range interactions involving anions are between the shells apart from the Morse potential in the phosphate group, which acts between the phosphorus and oxygen cores.

The O-F short-range interactions were fitted to the fluorapatite structure and elastic constants and optimised using the GULP program.[106] They are described by an effective Buckingham potential that has been described in equation 3.9. However, in an effective pair potential as used here, the A_{ij} and r_{ij} terms have become more or less fused, which means they are interdependent and hence their physical meaning is less certain.

The bonding between the phosphorus and oxygen ions within the phosphate group, which is partially covalent as shown by electronic structure calculations of fluorapatite,[111] is described by a Morse potential, described in equation 3.6. The value of D was taken as the experimental bond dis-

sociation energy of a single P-O bond, which is 335 kJmol^{-1}.[112] The four P-O bond-lengths in the experimental fluorapatite structure are not equal (1.5-1.8 Å) but as the Morse potential is capable of modelling anharmonicity, interionic distances away from the equilibrium bond distance can also be simulated. r_0 was therefore set at 1.6 and α was then fitted to the four phosphate stretching modes, which were obtained for apatite by Taylor et al. using Raman and inelastic neutron scattering techniques.[113] We fitted the α parameter to the mean value of the four Raman active vibrational frequencies as potential models often underestimate the coupling between modes and fitting to the four individual modes would therefore be meaningless.

Finally, a bond-bending term (equation 3.10) was introduced to allow directionality of bonding between the phosphorus and oxygen ions in the phosphate group. The equilibrium angle ($\theta_{ijk} - \theta_0$), was set at the ideal tetrahedral angle of 109.47^0, which setting reflects the fact that the phosphorus is covalently bonded in a distorted tetrahedral geometry to three oxygen atoms at a distance of approximately 1.5-1.6 Å and a fourth at approximately 1.8 Å. The elastic constants were found to be fairly sensitive to the force constant and hence allowed us a mechanism for the derivation of k_{ijk}, which was fitted to reproduce the experimental elastic constants.

Although the potential model for fluorapatite used in this work was fitted to bulk properties as discussed above, it is generally possible for ionic materials to transfer potential parameters to surface calculations. For example, the $CaCO_3$ potential parameters, which were used in the derivation of the fluorapatite potential model in this work, were derived by Pavese et al.

for bulk calcite,[109] but they have subsequently been shown to accurately reproduce experimental surface features and processes,[114, 115, 116, 117]. Since the surfaces considered in this work leave the phosphate group intact like the carbonate group in the calcium carbonate potential, the bulk derived potential model will be adequate.

The potential model above was then used to energy minimise the bulk structure, before creating and optimising the surfaces of fluorapatite using the METADISE code. As one of our objectives is to study the surfaces in realistic situations, we have also derived potential parameters for the interaction of water with the apatite surfaces.

Water Potential

The charges of the water molecules are $(H^{0.4+})_2O^{0.8-}$. These charges remain the same when molecular water interact with the fluorapatite mineral, however they are modified when dissociated interaction with α-quartz occurs where the water is represented by two ions in the form of H and OH, as we shall see when discussing the interfaces with hydroxylated α-quartz surfaces. The potential parameters used for the intra- and intermolecular water interactions are those described in a study of MD simulations on MgO surfaces[118], where the intramolecular interactions between oxygen and hydrogen atoms are described by a Morse potential and intermolecularly by a Buckingham potential. The steric effect that the electron lone pairs on the oxygen atom have on the geometry of the water molecule was included by partially removing the electrostatic interactions between the two hydrogen

atoms and between hydrogen and oxygen atoms in the water molecule (by half), making the hydrogen atoms less repulsive, much as electrostatic interactions within organic molecules are routinely removed in potential models for biological applications.[118] For the interactions between water molecules and fluorapatite surfaces (the Ca-water and O-water interactions) we used the potential parameters previously fitted to calcite,[114] which were successfully used in simulations of water adsorption at calcium carbonate surfaces and the calculation of crystal morphologies and dissolution from calcite steps.[115, 119, 120] In addition, these potential parameters reproduce the experimental heat of formation of calcium carbonate from its aqueous ions to an acceptable degree of accuracy (within 20 kJmol^{-1}), even though the parameters were not fitted to this process. Table 3.1 has the potential parameters derived for fluorapatite and the water interactions.

Calculated Properties

Upon energy minimisation of the bulk crystal, using the potential model derived above and listed in Table 3.1, the lattice parameters of fluorapatite were calculated at a = b = 9.375 Å, c = 6.871 Å, $\alpha = \beta = 90^0, \gamma = 120^0$. Table 3.2 lists the calculated and experimental crystallographic coordinates of the constituent atoms, from which we see that the calculated structure is in good agreement with the experimental crystal structure, especially noting that there are no symmetry constraints in the calculations, that is once the simulation cell has been created from the space-group, all species in the simulation cell are free to move relative to each other and the cell itself is allowed

Table 3.1: Fluorapatite and water potential parameters (The short range cutoff was set to 20 Å)

	charge(e)			
Ion	core		shell	core-shell interaction /eV $Å^{-2}$
Ca	+2.000			
P	+1.180			
H	+0.400			
F	+1.380		-2.380	101.2000
Phosphate oxygen (O)	+0.587		-1.632	507.4000
water oxygen (Ow)	+1.250		-2.050	209.4496
Buckingham Potential				
Ion pair	A/eV	ρ/Å	C/eV $Å^6$	
Ca - O	1550.0	0.29700	0.0	
Ca - O_w	1186.6	0.29700	0.0	
Ca - F	1272.8	0.29970	0.0	
O - O	16372.0	0.21300	3.47	
O - O_w	12533.6	0.21300	12.09	
O - F	583833.7	0.21163	7.68	
F - F	99731834.0	0.12013	17.02423	
F - O_w	79785221	0.12013	26.78752	
H - O	396.3	0.23000	0.0	
H - O_w	396.3	0.25000	10.0	
H - F	715.34	0.25	10.0	
Morse Potential				
Ion pair	D/eV	$\alpha/Å^{-1}$	r_0/Å	
P_{core} - O_{core}	3.47	2.030	1.600	
H - O_w	6.203713	2.22003	0.92376	
Lennard-Jones Potential				
Ion pair	A/eV$Å^{12}$	B/eV $Å^6$		
O_w - O_w	39344.98	42.15		
Three-body Potential				
Ion pair	k/eV rad^{-2}	θ_0		
O_{core} - P - O_{core}	1.322626	109.470000		
H - O_w - H	4.199780	108.693195		
Intramolecular Coulombic interaction (%)				
H - Ow	50			
H - H	50			

to both expand or contract and to deform. A comparison of calculated and experimental physical properties of the material is made in Table 3.3, from which it is clear that the elastic constants are reproduced accurately, which is as expected as they were used for fitting the potential model. The P-O Morse potential was fitted to the mean value of the vibrational stretching frequencies of the phosphate group and the agreement between calculated and experimental values of the individual stretch frequencies are therefore not as good as the other properties to which the potential model was fitted.

Experimentally, there is no agreement on values for the dielectric constant of apatite. Our calculated values of 7.1 and 4.5 do not agree very well with the experimental measurements of 10.4 and 8.3 by Shannon and Rossman.[121] However, these experimental values, which were obtained from a very substituted material containing many impurity ions, differ considerably from the generally accepted value of 7.4 for the dielectric constant of apatite,[122] which is also in line with those of similar materials such as 6.2 for forsterite (Mg_2SiO_4), 6.1-6.9 for calcium carbonate ($CaCO_3$) and 7.4 for fluorite (CaF_2). In addition, more recently the dielectric constant of apatite thin films was measured at 5.7.[123] We would therefore consider that the agreement between the calculated and experimental static dielectric constants is adequate, especially given the fact that the potential parameters were not fitted against these properties.

Table 3.2: Calculated and experimental crystallographic data for $Ca_{10}(PO_4)_6F_2$.

Space group						
	$P6_3/m$			$P6_3/m$		
	Calculated[a]			Experimental[29]		
a,b,c	9.3750	9.3750	6.8712	9.3700	9.3700	6.8800
α, β, γ	90	90	120	90	90	120
	X	**Y**	**Z**	**X**	**Y**	**Z**
Ca	0.3333	0.6667	-0.0004	0.3333	0.6667	0.0000
Ca	0.2504	-0.0050	0.2500	0.2500	0.0000	0.2500
P	0.4071	0.3744	0.2500	0.4170	0.3610	0.2500
O	0.3311	0.4874	0.2500	0.3333	0.5000	0.2500
O	0.5967	0.4693	0.2500	0.6000	0.4670	0.2500
O	0.3556	0.2652	0.0656	0.3333	0.2500	0.0630
F	0.0000	0.0000	0.2500	0.0000	0.0000	0.2500

[a]No symmetry constraints in the calculation.

Table 3.3: Calculated and experimental physical properties of $Ca_{10}(PO_4)_6F_2$.

Property	Calculated	Experimental
Elastic constants/10^{10} Pa		
C_{11}	150.6	152.0[a]
C_{33}	176.6	185.7[a]
C_{44}	53.2	42.8[a]
C_{12}	62.8	50.0[a]
C_{13}	73.6	63.1[a]
Bulk modulus/GPa		
	98.8	93.4[b]
Static relative permittivity		
11	7.1	10.4[c]
33	4.5	8.3[c]
Phosphate mode/cm^{-1}		
ν_1	802	963[d]
ν_2	428	435[d]
ν_3	1072	1046[d]
ν_4	724	590[d]

[a][124], [b][125], [c][121], [d][113].

3.6.2 Deriving The Potential for the Fluorapatite/ Quartz Interface

When calculating the interfaces of materials, one has to make sure that the potential model used will describe both materials surfaces well. In this study we model interfaces with α-quartz as a substrate and fluorapatite as a thin film that will be deposited on the silica surface. We employed an established potential model for the silicate substrate[126] and the newly developed potential for apatite, which has been shown to be accurate in describing both bulk properties in section 3.6.1 and surface properties of the material in chapter 4. Because to our knowledge there are no experimental results of similar work on these material and hence no data to use when fitting the potential, the potential parameters describing the interactions between the apatite film and silicate surface were derived following the approach of Schroder et al.[127] which has been shown to be a reliable method for potential derivation and adjustment where no experimental data are available.[114, 54] Potentials that were used for this part of the work are shown in table 3.4.

The interface between the quartz and fluorapatite can be modelled not only with the dry quartz surface but also when the quartz is hydrated, depending on whether one would like to investigate the interface in ultra high vacuum or under ambient conditions. Although cleavage of the surfaces is normally done in air or in wet conditions, the water can then be removed

Table 3.4: Potential parameters used for fluorapatite/ α-quartz interface. (The short range cutoff was set to 20 Å)

	charge (e)			
Ion	core		shell	core-shell interaction /eV Å^{-2}
Ca	+2.000			
P	+1.180			
Si	+4.000			
F	+1.380		-2.380	101.2000
Phosphate oxygen (O_p)	+0.587		-1.632	507.4000
Silicate oxygen (O_s)	+0.84819		-2.84819	74.92038
Buckingham Potential				
Ion pair	A/eV	r/Å	C/eV Å^6	
Ca - O_p	1550.0	0.29700	0.0	
Ca - O_s	2966.5	0.29700	0.0	
Ca - F	1272.8	0.29970	0.0	
Si - F	2545.6	0.29970	0.0	
Si - O_s	1283.91	0.32052	10.66158	
Si - O_p	670.9	0.32052	3.76	
O_p - O_p	16372.0	0.21300	3.47	
O_p - O_s	16372.0	0.21300	3.47	
O_p - F	583833.7	0.21163	7.68	
O_s - O_s	22764.3	0.14900	27.88	
O_s - F	1117385.1	0.21163	14.6	
F - F	99731834.0	0.12013	17.02423	
Morse Potential				
Ion pair	D/eV	α/Å^{-1}	r_0 Å	
P_{core} - $O_{p_{core}}$	3.47	1.900	1.600	
Three-body Potential				
Ion pair	k/eV rad^{-2}	θ_0		
$O_{p_{core}}$ - P - $O_{p_{core}}$	1.322626	109.47		
$O_{s_{shell}}$ - Si - $O_{s_{shell}}$	2.09724	109.47		

from the surface later. However there will be some dissociated water in the form of adsorbed H and OH species that are not necessarily easy to remove from the surface[128, 129]. The most realistic model of the interface is therefore the one that takes into account the presence of the H and OH at the quartz surfaces.

Care is taken when fitting the parameters for the H and OH species because although the H and OH resembles water, the representation is not exactly the same as the charges of the H and the O are different from those in the water molecule. The charge on the hydrogen remains +0.4, but in order to obtain a charge of -1 for the hydroxy group, the overall charge for the hydroxy-oxygen becomes -1.4 rather than the -0.8 in the water (H_2O) molecule.

The charges for the ions in α-quartz are $Si^{4+}O_4^{2-}$, and when interacting with molecular water rather than dissociated water, the water would be interfaced directly with the α-quartz surface without affecting the charges of the quartz atoms. Now we have the dissociated H and (O_H) species which are ions with charges: $H^{0.4+}$ and $(O_H)^{1.4-}$ where the (OH) group are two bonded ions, and these protons and hydroxy groups form chemical bonds to the quartz surfaces. Hence we need to adjust the charge on some of the oxygens of the quartz to $O^{1.4-}$ when they bond to protons as follows: A dissociated water molecule was adsorbed on every surface cation-oxygen pair and in effect every surface oxygen was replaced by two hydroxyl groups, i.e., in Kröger-Vink notation,

$$H_2O + O_o^x \rightarrow (OH)_o^{\bullet} + (OH)_i^{'} \tag{3.13}$$

resulting in SiOH groups at the surface as detected by Koretsky et al.[129] using diffuse reflectance infrared spectroscopy. The $O^{1.4-}$ oxygens should be the ones exposed to the surface of the α-quartz as they are the ones that will react with the proton to form an OH group. After the hydroxylation of the α-quartz surfaces, the $\{0\ 0\ 0\ 1\}$ surface contain geminal hydroxyl groups, which do not interact with each other, but they are interacting vicinally to the neighbouring group with an O - H bond length of 2.09 $\mathring{A}$. While the $\{1\ 0\ \bar{1}\ 0\}$ surface also has vicinal hydroxyl groups interacting closely with each other at a distance of 1.92 $\mathring{A}$ between the oxygens and hydrogens. The potentials fitted to suit this kind of simulation are shown in table 3.5, with the interactions between the other species similar to the ones in table 3.4.

3.6.3 Potential Parameters Used for Fluoarapatite With Organic Surfactants

The organic surfactant molecules used in this work are described using the potential parameters of the consistent valence force field (cvff).[130] The molecules are neutrally charged overall, and partial charges are used for the individual atoms in each molecule. The non bonded interactions between the atoms of the molecules are described using Lennard Jones potential functions and Morse potentials are used for the bonded interactions. For the nearest neighbour and the next nearest neighbour interactions of the atoms of the molecule, a complete coulombic subtraction is used. Similar potential parameters to the ones we used have been successfully used to model the sorption

Table 3.5: Potential parameters used for fluorapatite/ α-quartz interface with inclusion of the hydroxyl group on α-quartz surfaces. (The short range cutoff was set to 20 Å)

charge (e)				
Ion	core		shell	core-shell interaction /eV Å^{-2}
Ca	+2.000			
P	+1.180			
Si	+4.000			
H	+0.4			
water hydrogen (H_w)	+0.4			
F	+1.380		-2.380	101.2000
Phosphate oxygen (O_p)	+0.587		-1.632	507.4000
Silicate oxygen (O_s)	+0.84819		-2.84819	74.92038
hydroxide oxygen (O_H)	+0.900		-2.300	74.92038
water oxygen (O_w)	+1.250		-2.050	209.449602
Buckingham Potential				
Ion pair	A/eV	r/Å	C/eV Å^6	
Ca - O_p	1550.0	0.29700	0.0	
Ca - O_s	2966.5	0.29700	0.0	
Ca - F	1272.8	0.29970	0.0	
Ca - O_H	1250.0	0.34370	0.0	
Ca - O_w	1186.6	0.297	0.0	
Si - F	2545.6	0.29970	0.0	
Si - O_s	1283.91	0.32052	10.66158	
Si - O_p	670.9	0.32052	3.76	
Si - O_H	983.556	0.32052	10.66158	
Si - O_w	562.032	0.32052	10.66158	
O_p - O_p	16372.0	0.21300	3.47	
O_p - O_s	16372.0	0.21300	3.47	
O_p - F	583833.7	0.21163	7.68	
O_p - O_H	22764.0	0.149	4.92	
O_p - O_w	12533.6	0.213	12.09	
O_s - O_s	22764.3	0.14900	27.88	
O_s - F	1117385.1	0.21163	14.6	
O_s - O_H	22764.0	0.149	13.94	
O_s - O_w	22764.0	0.149	28.92	
O_w - O_H	22764.0	0.149	17.14	
O_H - O_H	22764.0	0.149	6.97	

F - F	99731834.0	0.12013	17.02423
F - O_H	35000.0	0.175	15.4
F - O_w	79785220.99	0.12013	26.78752
H - O_s	396.27	0.25	0.0
H_w - O_s	396.27	0.25	0.0
H - O_p	312.0	0.25	0.0
H_w - O_p	396.27	0.2300	0.0
H - O_H	312.0	0.25	0.0
H_w - O_H	311.97	0.25	0.0
H - O_w	396.27	0.25	0.0
H_w - O_w	396.27	0.25	10.0
H - F	415.0	0.2463	0.0
H_w - F	715.339	0.25	0.0
Lennard-Jones Potential			
Ion pair	A/eVÅ^{12}	B/eV Å^6	
O_w - O_w	39344.98	42.15	
Morse Potential			
Ion pair	D/eV	α/Å^{-1}	r_0 Å
P_{core} - $O_{p_{core}}$	3.47	1.900	1.600
Morq potential			
Ion pair	D/eV	α A^{-1}	r_0/A
H - O_H	7.0525	3.1749	0.9485
H_w - O_w	6.203713	2.220030	0.92367
H_w - H_w	0.000000	2.840499	1.50000
Three-body Potential			
Ion pair	k/eV rad^{-2}	θ_0	
$O_{p_{core}}$ - P - $O_{p_{core}}$	1.322626	109.47	
$O_{s_{shell}}$ - Si - $O_{s_{shell}}$	2.09724	109.47	
$H_{w_{core}}$ - $O_{w_{shel}}$ - $H_{w_{core}}$	4.199780	108.693195	

of organic molecules with surfaces of calcium fluoride.[131]

The potential parameters used in this work for all the organic surfactants are described and listed in the tables below.

Methanoic Acid Potential

Table 3.6 lists the potential parameters for methanoic acid (HCOOH). The atoms of the molecule are labelled as: OD for the carbonyl oxygen; OH for the hydroxyl oxygen atom; HO for the hydroxyl hydrogen atom; CD for the carbonyl carbon atom; and HC for the hydrogen atom attached to the carbonyl group.

Methanoic Potential with Fluorapatite Mineral Surface.

The potential parameters for the interaction of the methanoic acid with the fluorapatite mineral surface were transferred from those derived for the interaction of methanoic acid and calcium carbonate and calcium fluoride.[54] Buckingham potentials were used for interactions between surface Ca atoms and the oxygen atoms of the methanoic acid, and Lennard-Jones potentials for interactions between surface oxygen atoms and the carbon and hydrogen atoms of methanoic acid.

In table 3.7 we list the potential parameters that were used to model the methanoic acid molecules on fluorapatite surfaces. Because the partial charges of the calcium and oxygen atoms in fluorapatite are the same as for calcium carbonate, the same potentials were used for the interactions of methanoic acid with fluorapatite as those that were derived for methanoic acid with calcium carbonate, which had been shown to give reli-

Table 3.6: Methanoic acid potential parameters.

Ion	**Charges (e)**		
OD core	-0.380		
OH core	-0.380		
CD core	0.310		
HC core	0.100		
HO core	0.350		
Lennard-Jones potential parameters			
Ion pair	A/eVÅ^{12}	B/eVÅ^{6}	
OD-OD	11822.6	21.61	
OD-CD	38994.3	35.23	
OD-HC	1908.1	5.55	
OD-HO	1908.1	5.55	
OD-OH	11822.6	21.61	
OH-CD	38994.3	35.23	
OH-HC	1908.1	5.55	
OH-HO	1908.1	5.55	
OH-OH	11822.6	21.61	
Morse potential parameters			
Ion pair	D/eV	α/Å^{-1}	r_0/Å
CD-HC	4.66	1.77	1.10
OH-HO	4.08	2.28	0.96
CD-OH	4.29	2.00	1.37
CD-OD	6.22	2.06	1.23
Three-body Potential parameters			
Ion pair	k_{ijk}/eV rad^{-2}	θ_0	
HO-OH-CD	4.29	112.0	
HC-CD-OH	4.72	110.0	
OD-CD-HC	4.72	120.0	
OD-CD-OH	12.45	123.0	

Table 3.7: Potential parameters used for the methanoic acid with fluorapatite mineral surface.

Buckingham potential parameters			
Ion pair	A/eV	ρ/Å	C/eVÅ^6
Ca-OH	563.64	0.297	0
Ca-OD	563.64	0.297	0
OH-O (shell)	37898119	0.12013	11.3
OD-O (shell)	37898119	0.12013	11.3
OH-F (shell)	37898119	0.12013	25.1
OD-F (shell)	37898119	0.12013	25.1
Lennard-Jones potential parameters			
Ion pair	A/eVÅ^{12}	B/eVÅ^6	
HC-O (shell)	2915.25	4.222	
CD-O (shell)	3315.91	19.846	
HO-O (shell)	2915.25	4.222	
HC-F (shell)	2915.25	9.378	
CD-F (shell)	3315.91	44.012	
HO-F (shell)	2915.25	9.378	

able results.[54]

Hydroxamic Acid Potential

The potential parameters for the hydroxamic acid molecule (HC(=O)NHOH) are listed in table 3.8. The atoms are labeled as OD for the carbonyl oxygen atom; OH for the hydroxyl oxygen atom; HO for the hydroxyl hydrogen atom; CD for the carbonyl carbon atom; N the nitrogen atom; HC the hydrogen atom attached to the carbonyl group atom; and NH for the hydrogen atom

attached to the nitrogen atom.

Hydroxamic Acid with Fluorapatite Mineral Surface

Table 3.9 lists the potential parameters used for the hydroxamic acid molecules with the fluorapatite surface. The interactions between the hydroxamic acid molecules and the fluorapatite surface atoms are based on the potential derived for methanoic acid with calcium carbonate and calcium fluoride[54], which are then adapted to the partial charges of the hydroxamic acid atoms, following the method by Schröder at al.[127]

Methylamine Potential

The potential parameters in table 3.10 are those for the methylamine (H_2CNH_3) molecule. The atoms are labeled as CN for the carbon atom; N for the nitrogen atom; H for the methyl hydrogen atoms; and NH for the amine hydrogen atoms.

Methylamine with Fluorapatite Mineral Surface Potential

The potential parameters for the methylamine with the fluorapatite surface are given in table 3.11. These potentials between methylamine and the fluorapatite mineral surface are also adapted from the methanoic acid parameters according to the partial charges on the atoms of the methylamine molecule obtained from the consistent valence force field.

Table 3.8: Potential parameters for the hydroxamic acid.

Ion	**Charges (e)**	
OD core	-0.380	
OH core	-0.208	
CD core	0.167	
HC core	0.213	
HO core	0.350	
N core	-0.422	
HN core	0.280	
Lennard-Jones potential parameters		
Ion pair	A/eVÅ^{12})	B/eVÅ^{6}
OD-OD	11822.6	21.61
OD-CD	38994.3	35.23
OD-HC	1908.1	5.55
OD-HO	1908.1	5.55
OD-OH	11822.6	21.61
OD-N	34072.2	33.9
OD-HN	1908.1	5.55
OH-CD	38994.3	35.23
OH-HC	1908.1	5.55
OH-HO	1908.1	5.55
OH-OH	11822.6	21.61
OH-N	34072.2	33.94
OH-HN	1908.1	5.55
N-N	98200.9	53.31
N-CD	112380.0	55.33
N-HC	5499.1	8.71
N-HN	5499.1	8.71
N-HO	5499.1	8.71
CD-CD	128606.4	57.43
CD-HC	6293.1	9.04
CD-HO	6293.1	9.04
CD-HN	6293.1	9.04

Morse potential parameters			
Ion pair	D/eV	α/Å^{-1}	r$_0$/Å
CD-HC	4.66	1.77	1.10
OH-HO	4.08	2.28	0.96
CD-OD	6.22	2.06	1.23
HN-N	3.99	2.28	1.03
N-CD	4.16	2.00	1.32
N-OH	3.23	2.00	1.30
Three-body potential parameters			
Ion pair	k$_{ijk}$/eV rad^{-2}	θ_0	
HC-CD-N	3.86	120.0	
HC-CD-OD	4.72	120.0	
OD-CD-N	5.84	120.0	
CD-N-HN	3.22	115.0	
CD-N-OH	4.29	120.0	
HN-N-OH	3.00	122.0	
N-OH-HO	5.02	109.0	
Four-body potential parameters			
Ion pair	k$_{ijkl}$/eV		
HC-CD-N-HN	1.2		
HC-CD-N-OH	3.2		
OD-CD-N-OH	3.2		
CD-N-OH-HO	0.5		
HN-N-OH-HO	0.5		
CD-N-HN-OH	0.1		

Table 3.9: Potential parameters for interactions of hydroxamic acid with fluorapatite mineral surface.

Buckingham potential parameters			
Ion pair	A/eV	ρ/Å	C/eVÅ^6
Ca-OH	308.52	0.297	0
Ca-OD	563.64	0.297	0
Ca-N	625.94	0.297	0
OH-O (shell)	37898119	0.12013	11.3
OD-O (shell)	37898119	0.12013	11.3
N-O (shell)	37898119	0.12013	11.3
OH-F (shell)	37898119	0.12013	25.1
OD-F (shell)	37898119	0.12013	25.1
N-F (shell)	37898119	0.12013	25.1
Lennard-Jones potential parameters			
Ion pair	A/eVÅ^{12}	B/eVÅ^6	
HC-O (shell)	2915.25	4.222	
HN-O (shell)	2915.25	4.222	
CD-O (shell)	3315.91	19.846	
HO-O (shell)	2915.25	4.222	
HC-F (shell)	2915.25	9.378	
CD-F (shell)	3315.91	44.012	
HO-F (shell)	2915.25	9.378	
HN-F (shell)	2915.25	9.378	

Table 3.10: Methylamine potential parameters.

Ion	**Charges (e)**		
N core	-0.50		
CN core	-0.08		
H core	0.10		
HN core	0.14		
Lennard Jones potential parameters			
Ion pair	A/eVÅ^{12}	B/eVÅ^{6}	
N-N	98200.9	53.31	
N-H	5499.1	8.71	
N-NH	5499.1	8.71	
CN-CN	128606.4	57.43	
Morq potential parameters			
Ion pair	D/eV	αÅ^{-1}	r_0/Å
N-HN	3.77	2.28	1.03
N-CN	2.92	2.29	1.47
H-CN	1.77	4.66	1.11
Three-body potential parameters			
Ion pair	k_{ijk}/eV rad^{-2}	θ_0	
H-CN-H	3.39	106.4	
H-CN-N	3.57	110.0	
CN-N-HN	3.09	105.5	
HN-N-HN	4.92	109.5	
Four-body potential parameters			
Ion pair	k_{ijkl}/eV		
H-CN-N-HN	0.80		

Table 3.11: Potential parameters for the interaction of methylamine with the fluorapatite mineral surface.

Buckingham potential parameters			
Ion pair	A/eV	ρ/Å	C/eVÅ^6
Ca-CN	308.52	0.297	0
Ca-N	625.94	0.297	0
N-F (shell)	44902983	0.12013	30.13
N-O (shell)	44902983	0.12013	13.60
CN-O (shell)	7184477	0.12013	8.91
CN-F (shell)	7184477	0.12013	19.74
Lennard-Jones potential parameters			
Ion pair	A/eVÅ^{12}	B/eVÅ^6	
H-O (shell)	2915.25	4.222	
HN-O (shell)	2915.25	4.222	
H-F (shell)	2915.25	9.378	
HN-F (shell)	2915.25	9.378	

Hydroxyethanal Potential

Table 3.12 lists the potential parameters for the hydroxyethanal ($HC(=O)CH_2OH$) molecules. The atoms are labeled as: OD for the carbonyl oxygen; OH for the hydroxyl oxygen atom; HO for the hydroxyl hydrogen atom; CD for the carbonyl carbon atom; HC for the hydrogen atoms attached to the hydroxyl carbon atom; COH for the hydroxyl carbon atom; and HCO for the hydrogen atom attached to the carbonyl group.

Potential for Hydroxyethanal and Fluorapatite Mineral Surface

The final potential parameters in table 3.13 are for the interactions of the hydroxyethanal molecule with fluorapatite surface. These were also adapted according to the partial charges on the atoms of the hydroxyethanal molecule obtained from the consistent valence force field.

Having derived and collected the necessary potential parameters for our investigations, in the next three chapters we describe how they are used to model the water-fluorapatite interface (chapter 4), the sorption of organic molecules at fluorapatite surfaces (chapter 5) and the adhesion of apatite thin films at dry and hydrated surfaces of α-quartz (chapter 6).

Table 3.12: Hydroxyethanal potential parameters.

Ion	**Charges (e)**	
OD core	-0.380	
OH core	-0.380	
CD core	0.167	
HC core	0.100	
HO core	0.350	
COH core	-0.170	
HCO core	0.213	
Lennard Jones potential parameters		
Ion pair	A/eVÅ^{12}	B/eVÅ^{6}
OD-OD	11822.6	21.61
OD-CD	38994.3	35.23
OD-HC	1908.1	5.55
OD-HCO	1908.1	5.55
OD-OH	11822.6	21.61
OD-HO	1908.1	5.55
OH-CD	38994.3	35.23
OH-HC	1908.1	5.55
OH-HCO	1908.1	5.55
OH-HO	1908.1	5.55
OH-OH	11822.6	21.61
CD-CD	128606.4	57.43
CD-HC	6293.1	9.043
CD-HO	6293.1	9.043
CD-HCO	6293.1	9.043
CD-COH	128606.4	57.43
COH-HC	6293.1	9.043
COH-HO	6293.1	9.043
COH-HCO	6293.1	9.043

Morse potential parameters			
Ion pair	D/eV	α/Å^{-1}	r$_0$/Å
CD-HCO	4.66	1.77	1.10
OH-HO	4.46	2.28	0.96
COH-OH	4.12	2.00	1.42
COH-HC	4.66	1.77	1.11
CD-OD	6.22	2.06	1.23
CD-COH	3.26	1.93	1.52
Three-body potential parameters			
Ion pair	k$_{ijk}$/eV rad^{-2}	θ_0	
OD-CD-HCO	4.72	120.0	
OD-CD-COH	5.84	120.0	
HCO-CD-COH	3.86	120.0	
HC-COH-HC	3.39	106.4	
HC-COH-OH	4.89	109.5	
CD-COH-HC	3.86	109.5	
COH-OH-HO	5.02	106.0	
CD-COH-OH	6.00	109.5	
Four-body potential parameters			
Ion pair	k$_{ijkl}$/eV		
HO-OH-COH-CD	0.39		
HO-OH-COH-HC	0.39		

Table 3.13: Potential parameters for the interaction of hydroxyethanal with the fluorapatite mineral surface.

Buckingham potential parameters			
Ion pair	A/eV	ρ/Å	C/eVÅ^6
Ca-OH	563.64	0.297	0
Ca-OD	563.64	0.297	0
Ca-COH	252.15	0.297	0
OH-O (shell)	37898119	0.12013	11.3
OD-O (shell)	37898119	0.12013	11.3
COH-O (shell)	16954421	0.12013	8.91
OH-F (shell)	37898119	0.12013	25.1
OD-F (shell)	37898119	0.12013	25.1
COH-F (shell)	16954421	0.12013	19.7
Lennard-Jones potential parameters			
Ion pair	A/eVÅ^{12}	B/eVÅ^6	
HC-O (shell)	2915.25	4.222	
HCO-O (shell)	2915.25	4.222	
CD-O (shell)	3315.91	19.846	
HO-O (shell)	2915.25	4.222	
HC-F (shell)	2915.25	9.378	
CD-F (shell)	3315.91	44.012	
HCO-F (shell)	2915.25	9.378	
HO-F (shell)	2915.25	9.378	

Chapter 4

STRUCTURES AND STABILITIES OF DRY AND HYDRATED SURFACES.

In this chapter we investigate the structure and stability of a range of fluorapatite surfaces. In addition, we describe how water interacts with the surfaces and affects the relative stabilities.

Having derived a satisfactory potential and obtained an optimised bulk structure, we next created a range of surfaces with low Miller indices as these surfaces have the smallest inter-planar spacings and as a result are often the most stable.[132] In addition to the intrinsic importance of the surface study, it is also important to identify the most stable apatite surfaces as we will need these for our investigation of solid/solid interfaces between fluorapatite and α-quartz which is discussed in chapter 6. The surfaces studied here are the $\{0\ 0\ 0\ 1\}$, $\{1\ 0\ \overline{1}\ 0\}$, $\{1\ 0\ \overline{1}\ 1\}$, $\{1\ 1\ \overline{2}\ 0\}$, $\{1\ 0\ \overline{1}\ 3\}$ and $\{1\ 1\ \overline{2}\ 1\}$ planes. The $\{0\ 0\ 0\ 1\}$ and to a lesser extent $\{1\ 0\ \overline{1}\ 0\}$ surfaces are experimental cleavage planes, while the $\{1\ 1\ \overline{2}\ 1\}$ and $\{1\ 0\ \overline{1}\ 3\}$ planes occur as twinning planes in

the natural crystals. Previous electronic structure calculations of fluorapatite have shown that the phosphate groups themselves have considerable covalent character but as a group act as a polyanion[111, 133] and we therefore kept the phosphate groups intact when creating the surfaces.

Based on the approach by Tasker as described in chapter 2, our simulation cell is a series of charged planes periodic in two dimensions comprising of two regions: I and II, where both regions must be sufficiently large for the energy to converge. The energies of the blocks are the sum of energies of interaction between all atoms in the crystal. We carried out a series of test calculations to find the right size of simulation cell of both regions I and II. We started with a size of region I = 1 and region I+II = 10, i.e region I is equivalent to one unit cell deep and region II just below it equal to nine unit cells, and similar tests were done for region I = 2, 3, 4, 5, 6 and 7 with the corresponding region II = 18, 27, 36, 45, 54 and 63. In each case we optimised both the bulk (block I+II) and the surface structure (block I only) and obtained the total energy. We then calculated the surface energies, which as mentioned in chapter 2 gives a measure of the thermodynamic stability of the surface, with a low positive value indicating a stable surface. For all seven sizes of regions, we calculated the surface energies for both relaxed and unrelaxed surfaces. An unrelaxed surface is a plane, where the surface is created from the relaxed bulk structure, but without further optimisation of the surface simulation cell. When this surface simulation cell is further energy minimised, we obtain the relaxed surface. It is important that we do surface energy calculations for the relaxed surfaces, as in real situations

Table 4.1: Calculated surface energies on different region sizes for {0 0 0 1} and {1 1 $\overline{2}$ 1} surfaces.

Surface	Region size	$\gamma_{unrelaxed}$	$\gamma_{relaxed}$
{0 0 0 1}			
	1	1.1926	0.7779
	2	1.1927	0.7747
	3	1.1927	0.7746
	4	1.1927	0.7746
	5	1.1927	0.7746
	6	1.1927	0.7746
{1 1 $\overline{2}$ 1}			
	1	2.6028	1.2239
	2	2.6190	1.1333
	3	2.6199	1.1159
	4	2.6199	1.1150
	5	2.6199	1.1150
	6	2.6199	1.1150

surfaces relax immediately upon cleavage. The test calculations were done on two surfaces: the {0 0 0 1} and {1 1 $\overline{2}$ 1} planes (table 4.1), to ensure that the convergence was not an artefact of the shape of the surface simulation cells. Based on the convergence of the surface energies with size of regions I and II as evident from table 4.3, we choose to do all our surface calculations with regions I = 4 and II = 36.

Table 4.2: Surface energies of bulk-terminated and geometry optimised dehydrated/dry fluorapatite surfaces

Surface	$\gamma_{unrelaxed}/\mathrm{Jm}^{-2}$	$\gamma_{relaxed}/\mathrm{Jm}^{-2}$
$\{0\ 0\ 0\ 1\}$	1.19	0.77
$\{1\ 0\ \overline{1}\ 0\}$	2.84	1.32
$\{1\ 0\ \overline{1}\ 1\}$	1.81	1.00
$\{1\ 1\ \overline{2}\ 0\}$	2.28	1.12
$\{1\ 0\ \overline{1}\ 3\}$	2.98	1.94
$\{1\ 1\ \overline{2}\ 1\}$	2.62	1.11

4.0.4 Dry Surfaces

We first calculated the surface energies of both the bulk-terminated and geometry optimised dry surfaces (Table 4.3), from which we see that the $\{0\ 0\ 0\ 1\}$ surface is by far the most stable surface with the lowest surface energy, both before and after relaxation. This surface has only one possible surface termination unlike the other planes and its stability is rather remarkable as this surface is a reconstructed dipolar type III surface and hence contains surface calcium vacancies, which were introduced to remove the dipole (as is discussed in chapter 2). The low surface energy of the $\{0\ 0\ 0\ 1\}$ surface, however, agrees very well with the fact that the $\{0\ 0\ 0\ 1\}$ surface is the major cleavage plane of apatite.[2]

{0 0 0 1} Surface

A side-view of the unrelaxed, bulk-terminated surface is shown in figure 4.1(a), where we see the calcium vacancy at the surface and the column of fluoride ions perpendicular to the surface. The distance between the surface calcium and the three oxygen ions below is 2.41 Å, while the bond-length between the surface oxygen atom and its phosphorus atom is 1.54 Å. The fluoride ions are in the plane of the phosphorus and calcium ions and the distance between them down the column is 3.43 Å, which is indicated in figure 4.1(a), with a Ca-F bond-length of 2.37 Å. Upon geometry optimisation of the surface (shown in figure 4.1b), we observe considerable relaxation of the first and to a lesser extent second and third surface layers, especially of the calcium and fluoride sub-lattices. The phosphate groups remain intact, with just a little rotation of the oxygen in the topmost surface layer towards the surface calcium ion, although the O-P bond-length remains virtually the same at 1.55 Å. The Ca-O bond-lengths to the three oxygen ions below also remain the same at 2.40 Å, but the calcium ion has also relaxed into the surface to form three additional bonds to the rotated surface oxygen ions at a short bond-length of 2.36 Å. The column of fluoride ions has become distorted with the topmost ion relaxing out of the surface, while the second ion moves more into the bulk. The resulting F-F distance at 3.86 Å is considerably longer than in the bulk material (3.43 Å). In addition, the second to third F-F distance has shortened to 3.20 Å, while the third to fourth F-F distance has again lengthened with respect to the bulk distance to 3.50 Å.

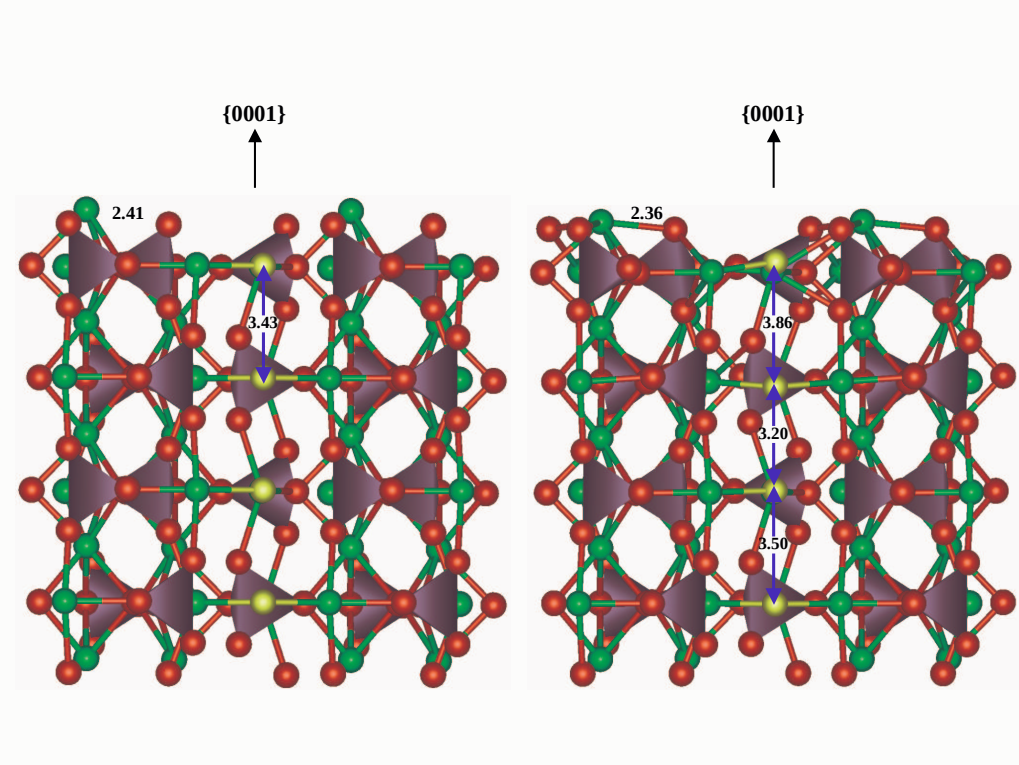

Figure 4.1: Sideview of (a) the bulk-terminated and (b) the geometry optimised {0 0 0 1} surface, showing alternating lengthening and shortening of the F-F distances into the bulk material with all bond distances shown in Å. (Ca = green, O = red, P = purple, F = light blue, PO_4 groups displayed as tetrahedra.

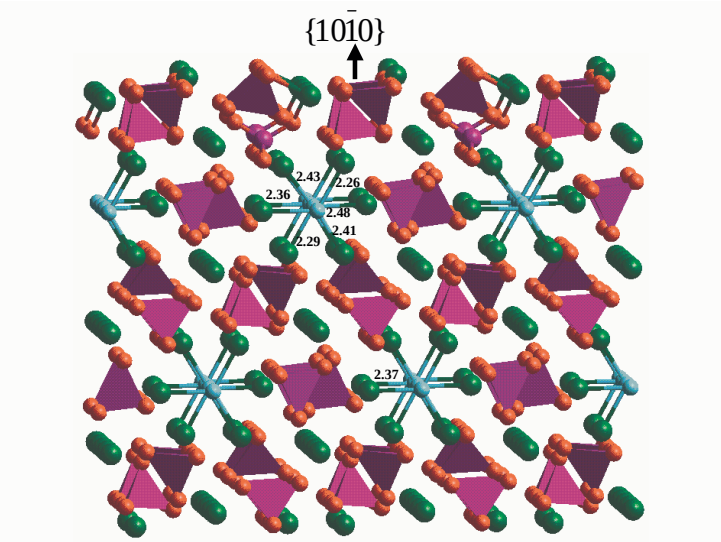

Figure 4.2: Sideview of the geometry optimised $\{1\ 0\ \bar{1}\ 0\}$ most stable surface, showing distortion of the Ca-F bonds in the hexagonal channels with all bond distances shown in Å. (Ca = green, O = red, P = purple, F = light blue, PO_4 groups displayed as tetrahedra.

Hence, this rumpling of the fluoride sublattice is a much more extensive effect (approximately 12 Å into the bulk) than the surface relaxation of the calcium, which only significantly affects the topmost calcium ions. Despite the distortion of the fluoride chain, the Ca-F bond-lengths at 2.36-2.38 Å remain virtually at their bulk value.

{1 0 $\bar{1}$ 0} Surface

The $\{1\ 0\ \bar{1}\ 0\}$ surface can be terminated in four different ways and we energy minimised all four terminations shown in figure 4.2-5. Figure 4.2 shows the most stable surface termination where a layer of Ca atoms is exposed in the

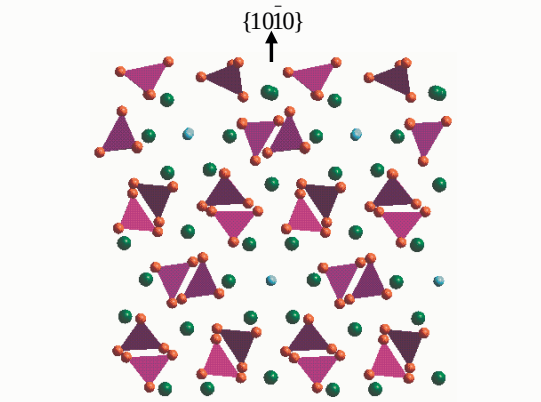

Figure 4.3: Sideview of the geometry optimised $\{1\ 0\ \bar{1}\ 0\}$ second stable surface. (Ca = green, O = red, P = purple, F = light blue, PO_4 groups displayed as tetrahedra.

top most layer of the surface. Just below the surface calcium atoms is another layer of Ca atoms, followed by two layers of PO_4 groups. The F^- atoms are deeper into the bulk material. Figure 4.3 shows a surface termination in which a layer of PO_4 groups is the most exposed in the surface. This layer is then followed by another layer of PO_4 groups and then followed below with a layer of Ca atoms and another layer of Ca atoms deeper into the bulk surface structure. This surface termination is the second most stable after the termination shown in figure 4.2 above. The third stable termination is shown in figure 4.4. In this figure we see that we again have a layer of Ca atoms on top of the surface, this time followed by a layer of PO_4 groups. Below is another layer of Ca atoms which is then followed by a layer with a mixture of F^- and Ca atoms. The least stable termination is shown in figure 4.5. Here we see that the top of the surface constitutes two consecutive layers of PO_4

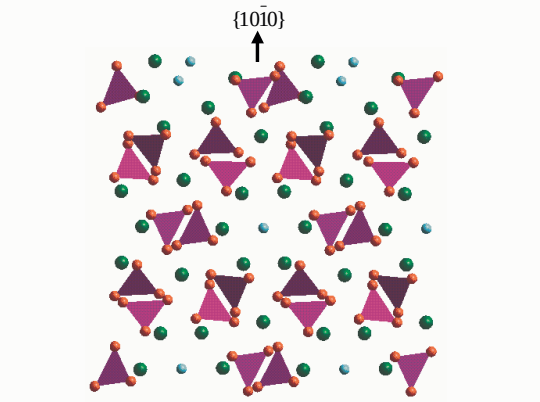

Figure 4.4: Sideview of the geometry optimised $\{1\ 0\ \bar{1}\ 0\}$ third stable surface. (Ca = green, O = red, P = purple, F = light blue, PO_4 groups displayed as tetrahedra.

groups, followed by three layers of Ca atoms. In the most stable termination (figure 4.2), the F^- columns lie in the plane of the surface, rather than perpendicular to the surface as in the case of the $\{0\ 0\ 0\ 1\}$ surface above, where the fluoride channels are kept intact. Even so, we can see from Table 4.4 that this surface is much less stable than the $\{0\ 0\ 0\ 1\}$ surface, although the surface energy decreases considerably upon geometry optimisation of the bulk-terminated surface to the fully relaxed plane.

This stabilisation is again due to relaxation of the surface calcium ions into the surface, hence forming new bonds with surface oxygen ions which have become accessible due to rotation of the surface phosphate groups (figure 4.2). The fluoride channel is again distorted, but unlike the $\{0\ 0\ 0\ 1\}$ surface above, this time the F-F distances remain at their bulk value of 3.43 Å. The distortion now occurs between the fluoride ions and surrounding cal-

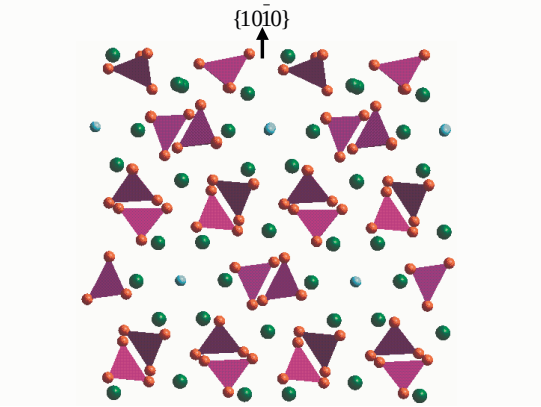

Figure 4.5: Sideview of the geometry optimised $\{1\ 0\ \bar{1}\ 0\}$ least stable surface. (Ca = green, O = red, P = purple, F = light blue, PO_4 groups displayed as tetrahedra.

cium ions, whereby alternate fluoride ions relax into the bulk, with shortening of the Ca-F bonds below the fluoride and lengthening of the one above, and up towards the surface, with shortening of the Ca-F bond below the fluoride ion. The chain of fluoride ions is also slightly rumpled parallel to the surface, alternating towards the sides of the channel, with shortening or lengthening of the relevant Ca-F bond-lengths in the plane of the surface. The different Ca-F bond-lengths are shown in figure 4.2.

$\{1\ 0\ \bar{1}\ 1\}$ Surface

The $\{1\ 0\ \bar{1}\ 1\}$ surface has the lowest surface energy of the dry surfaces after the $\{0\ 0\ 0\ 1\}$ surface and it has two possible ways of termination. The most stable termination is shown in figure 4.6. We see on this termination a top layer of Ca atoms where the next layer comprises a mixture of Ca and PO_4

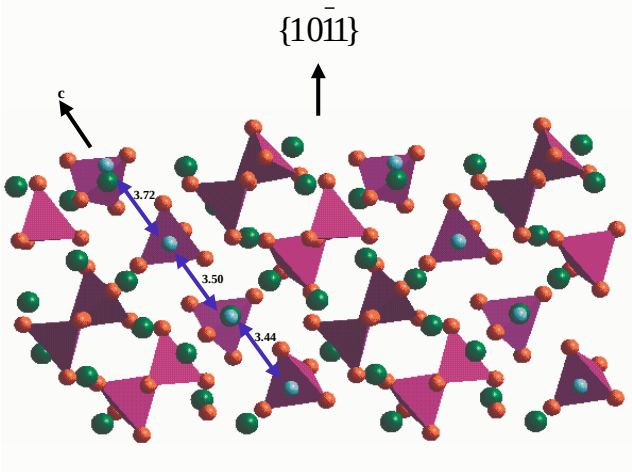

Figure 4.6: Sideview of the geometry optimised {1 0 $\bar{1}$ 1} most stable surface, showing lengthening of the F-F distances in the surface region with all bond distances shown in Å. (Ca = green, O = red, P = purple, F = light blue, PO4 groups displayed as tetrahedra.

groups. The third layer close to the surface has both Ca and F^- atoms. The second termination is shown in figure 4.7, where the top layer again comprises of Ca atoms. The second layer has the PO_4 groups, and the third and fourth layers are Ca and PO_4 groups respectively. The F^- atoms are in the fifth layer into the bulk. It has the fluoride columns running diagonally through the crystal with respect to the surface. Again, there is distortion of the fluoride sublattice in the channel, with the distance from the surface F^- ions to the next ions in the channel expanding from the bulk value of 3.43 Å to 3.72 Å. However, this time the next F-F distance is not contracted as in the {0 0 0 1} surface, but is also expanded to 3.50 Å. Thus, the distortion is an expansion of the fluoride chain in the surface region, rather than alternate

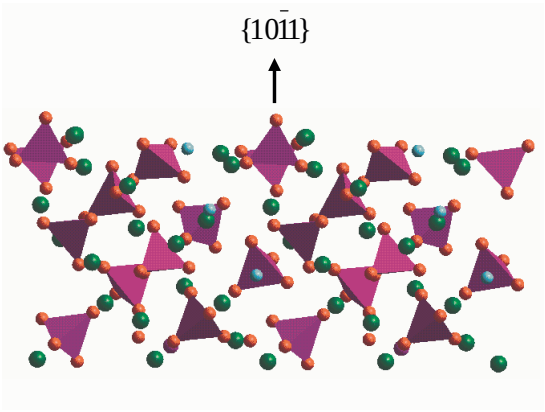

Figure 4.7: Sideview of the geometry optimised {1 0 $\bar{1}$ 1} least stable surface. (Ca = green, O = red, P = purple, F = light blue, PO4 groups displayed as tetrahedra.

lengthening and shortening of the interionic distances as was the case in the {0 0 0 1} surface. The Ca-F distances in the surface region are also distorted. One of the Ca-F bonds to the surface fluoride ions, which are coordinated to only two calcium ions, has expanded somewhat to 2.39 Å, but the other Ca-F bond has contracted substantially to 2.23 Å. The fluoride ion diagonally below the surface fluoride, also has two contracted bond-lengths to the calcium atoms below and in the plane (2.33 and 2.36 Å) but the calcium ion above it has relaxed away towards the surface, with a resulting Ca-F bond-length of 2.53 Å. Thus, in the surfaces where the fluoride channels are either perpendicular or parallel to the surface, we see either distortion of the F-F bond distances or of the Ca-F bond-lengths. However, in the {1 0 $\bar{1}$ 0} surface, which has the fluoride channels lying at an angle with respect to the surface, we find that on geometry optimisation both F-F and Ca-F distortion occurs

in the surface region.

{1 1 $\overline{2}$ 0} Surface

The {1 1 $\overline{2}$ 0} surface can be terminated in three different ways. The most stable optimised termination is shown in figure 4.8, in which we see the top layer of the surface comprising Ca atoms. The second and third layers are PO_4 groups, followed by another two layers of Ca atoms. The F^- atoms are farther away from the surface into the bulk. Figure 4.9 shows the second stable termination where the top layer has Ca atoms and the second and third layers are PO_4 groups respectively. The third layer consists of Ca atoms and again we see the F^- atoms are farther into the surface in the sixth layer, where they are mixed with the Ca atoms. The least stable termination is shown in figure 4.10, where the top layer comprises PO_4 groups, the second layer has a mixture of Ca and F^- atoms and the third layer has a mixture of Ca and PO_4 groups. After geometry optimisation we see a distortion of the layer of the F^- atoms. In the bulk it forms a horizontal packing, while in the optimised surface structure the top layer has now formed a zigzag partan. The F-F distance has increased as well from the bulk value of 3.43 Å to 3.92 Å, as shown in figure 4.8. The Ca-F distances in the surface are also distorted from the bulk value of 3.37 Å. One Ca-F distance has significantly contracted to 2.14 Å and another one to 2.36 Å, because the Ca atoms on top of the surface relax into the bulk structure during optimisation, as was the case with the dominant {0 0 0 1} surface.

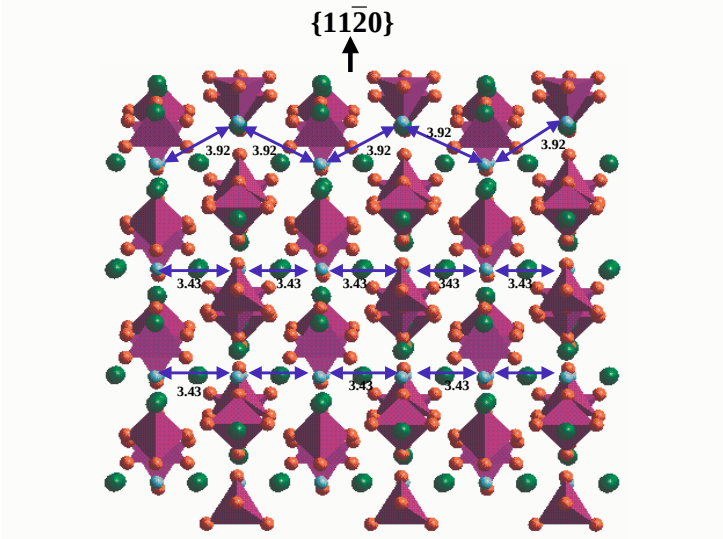

Figure 4.8: Sideview of the geometry optimised most stable {1 1 $\bar{2}$ 0} termination, with all bond distances shown in Å. (Ca = green, O = red, P = purple, F = light blue, PO4 groups displayed as tetrahedra.

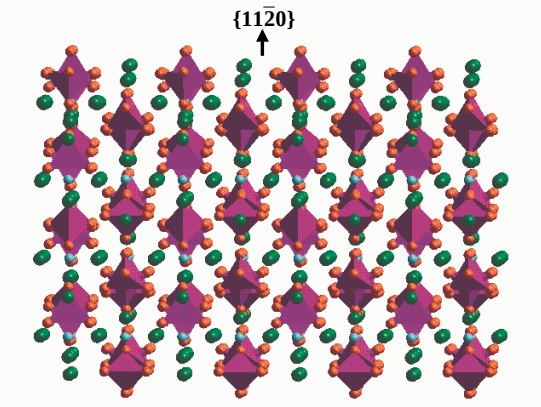

Figure 4.9: Sideview of the geometry optimised second stable {1 1 $\bar{2}$ 0} termination. (Ca = green, O = red, P = purple, F = light blue, PO4 groups displayed as tetrahedra.

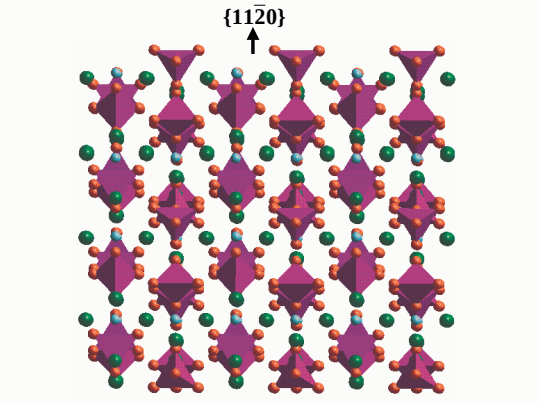

Figure 4.10: Sideview of the geometry optimised least stable {1 1 $\bar{2}$ 0} termination. (Ca = green, O = red, P = purple, F = light blue, PO4 groups displayed as tetrahedra.

{1 1 $\bar{2}$ 1} Surface

The {1 1 $\bar{2}$ 1} surface is the third most stable surface after relaxation (table 4.4) and has two possible terminations. The most stable termination shown in figure 4.11 has a layer containing a mixture of both Ca and PO_4 groups at the top of the surface. The second and third layers contain PO_4 groups and the fourth layer has a mixture of F^- and Ca atoms. The second and less stable termination is shown in figure 4.12, in which we see the top layer of the surface comprising Ca atoms where the second layer is a mixture of both Ca and F^- atoms. The third and fourth layers both comprise PO_4 groups. Upon relaxation, the F^- diagonal channel near the top of the surface is distorted. The F^- ions move up to the surface layer while the Ca atoms move into the bulk. This distortion result in the increase of the F-F distances from the bulk values of 3.43 Å to 4.06 Å, 4.11 Å and 3.15 Å as shown in figure 4.11.

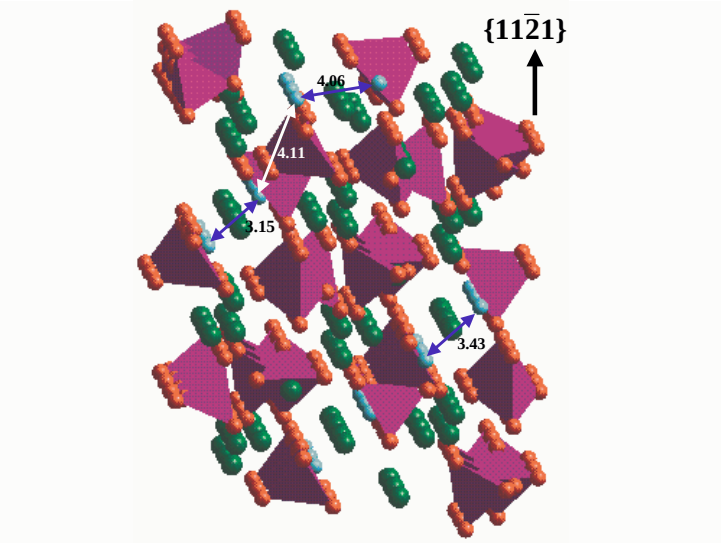

Figure 4.11: Sideview of the geometry optimised most stable {1 1 $\bar{2}$ 1} termination, with all bond distances shown in Å. (Ca = green, O = red, P = purple, F = light blue, PO4 groups displayed as tetrahedra.

The Ca-F distances have also contracted to 2.21 Å and 2.45 Å in the surface.

{1 0 $\bar{1}$ 3} Surface

The last surface we have studied is the {1 0 $\bar{1}$ 3} surface. This surface has two possible terminations and it is the least stable surface as seen from table 4.4. The most stable termination of the two is shown in figure 4.13, where we find that the top layer of the surface contains Ca atoms. The second layer has a mixture of both Ca and PO_4 groups and the third layer contains both Ca and F^- atoms. The fourth layer again consist of PO_4 groups. The second and least stable termination is shown in figure 4.14, in which we see the top layer of the surface comprising Ca atoms. The second layer has PO_4 groups

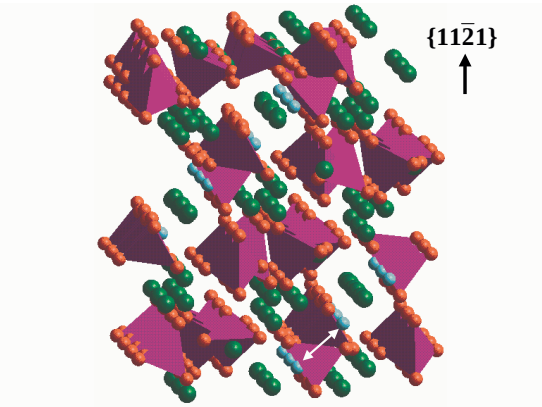

Figure 4.12: Sideview of the geometry optimised least stable $\{1\ 1\ \bar{2}\ 1\}$ termination. (Ca = green, O = red, P = purple, F = light blue, PO4 groups displayed as tetrahedra.

and Ca atoms together, while the third layer has a mixture of PO_4 groups, F^- and Ca atoms. The fourth layer contains a combination of PO_4 groups and Ca atoms. Similar to the other surfaces discussed above, relaxation causes the Ca atoms at the top of the surface to relax into the bulk structure whereas the F^- atoms close to the surface move towards the surface, which results in the extension and contraction of the F-F distances. Some F-F distances have contracted to 2.94 Å or extended to 3.68 Å. The other values are shown in figure 4.13. The Ca-F distances have also distorted as a result of the relaxation. We see some short Ca-F distances of 2.188 Å compared to the bulk value of 3.37 Å, whereas other Ca-F distances are 2.32 Å and 2.35 Å, all due to the relaxation of the Ca atoms into the bulk structure during energy minimisation of the surface.

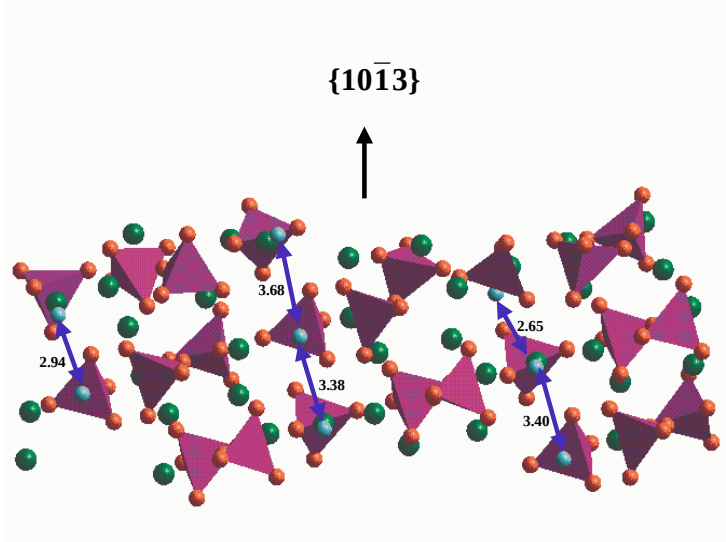

Figure 4.13: Sideview of the geometry optimised most stable {1 0 $\bar{1}$ 3} termination, with all bond distances shown in Å. (Ca = green, O = red, P = purple, F = light blue, PO4 groups displayed as tetrahedra.

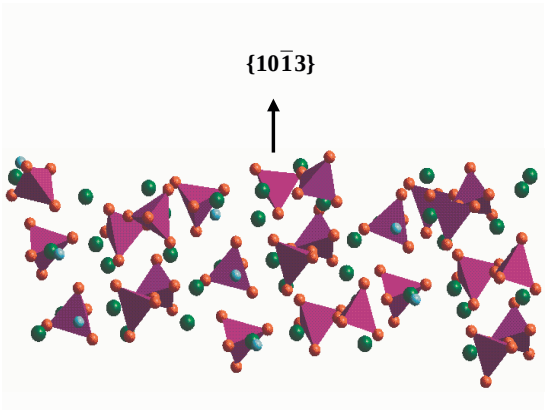

Figure 4.14: Sideview of the geometry optimised least stable {1 0 $\bar{1}$ 3} termination. (Ca = green, O = red, P = purple, F = light blue, PO4 groups displayed as tetrahedra.

4.1 Hydrated Surfaces

We next hydrated the surfaces in a series of partial coverages up to full monolayer coverage, which is here defined as the maximum number of water molecules that could be accommodated on the surface before formation of a second water layer occurred. It was shown in a molecular dynamics study of water adsorption at MgO surfaces, that there is a clear difference between the monolayer of water adsorbed at the mineral surface and the bulk water, the liquid structure of which was disturbed by the adsorbed water molecules, leading to a gap of low water density in between the two types of water.[118] Only the adsorbed water monolayer was shown to affect the structure and energy of the underlying surface and in this study we therefore only consider an adsorbed monolayer.

For the hydrated surfaces the surface energies were calculated with respect to liquid water in order to assess the stability of the surface in an aqueous environment. The surface energies for the hydrated surfaces were calculated from the equation 2.41: $\gamma_H = \frac{U_H - (U_B + U_{H_2O(l)})}{A}$, where U_H is the energy of the surface block, suitably hydrated, while $U_{H_2O(l)}$ is the energy of bulk water. The latter is the sum of the self-energy of water due to the intramolecular forces, and the energy of condensation due to the intermolecular forces. For associative adsorption the self-energy and energy of condensation were calculated from molecular dynamics simulations and found to be -878.0 kJmol^{-1} and -43.0 kJmol^{-1} respectively.[118] This latter value agrees well with the experimental value of -43.4 kJmol^{-1}.[134] Thus the new surface energy is simply equivalent to the sum of the energy required to cleave the

Table 4.3: Surface and hydration energies of hydrated fluorapatite surfaces.

Surface	$\gamma_{hyd}/\mathrm{Jm}^{-2}$	$\mathrm{E}_{hyd}/\mathrm{kJmol}^{-1}$	Coverage ($\mathrm{H_2O/nm^2}$)
$\{0\ 0\ 0\ 1\}$	0.45	-73	6.6
$\{1\ 0\ \bar{1}\ 0\}$	0.75	-87	7.8
$\{1\ 0\ \bar{1}\ 1\}$	0.61	-83	6.0
$\{1\ 1\ \bar{2}\ 0\}$	0.72	-88	5.4
$\{1\ 0\ \bar{1}\ 3\}$	1.67	-78	4.6
$\{1\ 1\ \bar{2}\ 1\}$	0.88	-81	3.7

crystal and then add water to the surface.

In addition to calculating the surface energy we calculate the adsorption energy U_{ads}, that is the energy to adsorb water on the surface per water molecule, which is given by equation 2.42: $E_{ads} = \frac{U_H - (U_s + nU_{H_2O(g)})}{n}$, where n is the number of water molecules and $\mathrm{U}_{H_2O(g)}$ is the energy of a gaseous water molecule. We need of course to be confident that in each case the most stable configuration of the surface with adsorbed water is found, locating as far as possible the global rather than a local minimum. Thus many possible configurations were investigated, varying both adsorption sites, coverage and initial position of the water molecules. All energies quoted are those of the most stable relaxed surface configurations found. The surface and hydration energies of the hydrated surfaces are collected in Table 4.3, from which we see that hydration has a stabilising effect on all the surfaces considered. However, the $\{0\ 0\ 0\ 1\}$ surface is still the dominant plane, followed by the $\{1\ 0\ \bar{1}\ 1\}$ surface.

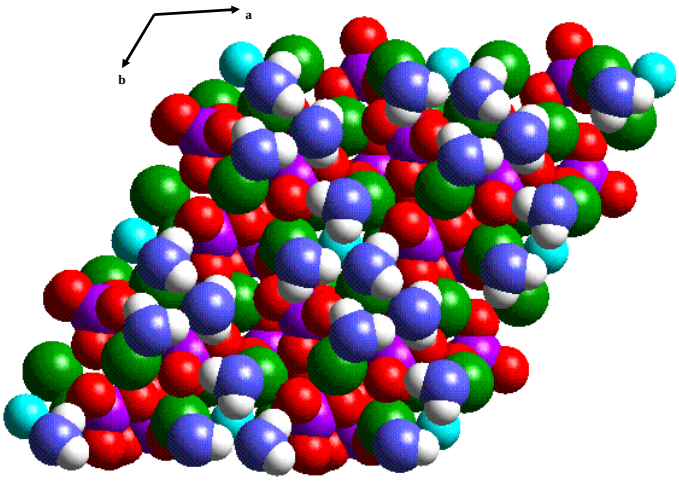

Figure 4.15: Plan view of the hydrated {0 0 0 1} surface, showing an irregular adsorption pattern with clustering of the water molecules round the surface calcium ions (Ca = green, O = red, O_{water} = blue, P = purple, F = light blue, H = white).

Hydrated {0 0 0 1} Surface

Figure 4.15. shows a bird's eye view of the {0 0 0 1} surface with a full monolayer of adsorbed water. The water molecules do not adsorb in a regular pattern, which is sometimes the case for mineral surfaces, for example at the dominant calcite {1 0 $\bar{1}$ 4} and fluorite {1 1 1} surfaces.[54] However, the apatite {0 0 0 1} plane with its surface calcium vacancies is itself a much less regular surface than these calcite and fluorite planes, and instead of a regular pattern of adsorption, the water molecules cluster around the remaining surface calcium ion and to a lesser extent the exposed calcium ions in the second layer. The major interaction of the water molecules is by their oxygen ions

with these surface calcium ions at bond distances of between 2.39 to 2.62 Å, while secondary interactions include hydrogen-bonding to surface oxygen (1.86-2.25 Å) and fluoride ions (2.34-2.94 Å). Additional stabilisation of the water layer is provided by a network of intermolecular hydrogen-bonding between the water molecules themselves (2.09-2.74 Å). The presence of water has lessened the relaxation of the surface ions somewhat through the provision of extra bonding by the surface ions to water molecules. For example, the surface calcium ions have not receded into the bulk material as much and the fluoride channel is distorted to a lesser extent (between 3.24 to 3.81 Å instead of 3.20 to 3.86 Å, a fluctuation of 16% instead of 19%).

Hydrated {1 0 $\bar{1}$ 0} Surface

Figure 4.16. shows a side view of the {1 0 $\bar{1}$ 0} surface with adsorbed monolayer of water molecules. Again the water molecules cluster around the surface calcium ions but do not form a regular adsorption pattern. Like the dry {1 0 $\bar{1}$ 0} surface, the F-F distance in the channel remains at its bulk value of 3.43 Å, but the Ca-F bonds are still distorted from their bulk value of 2.37 Å to the values shown in figure 4.16. Thus, similar to the {0 0 0 1} surface above, hydration of the {1 0 $\bar{1}$ 0} does not lead to distorted fluoride channels, although the distortion of the channels in the surface region is less than for the unhydrated {1 0 $\bar{1}$ 0} plane, both for the expansion and contraction of Ca-F bonds.

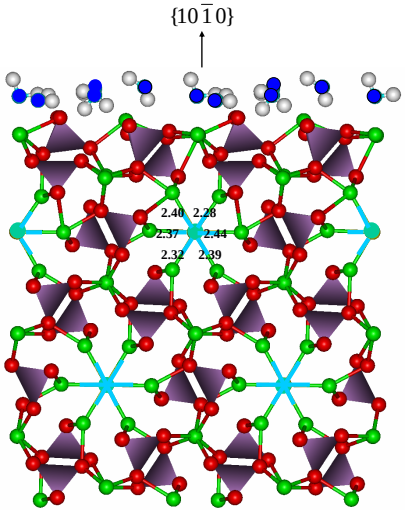

Figure 4.16: Side view of the hydrated $\{1\ 0\ \bar{1}\ 0\}$ surface, showing a decreased distortion of the hexagonal channels, with all bond distances shown in Å. (Ca = green, O = red, O_{water} = blue, P = purple, F = light blue, H = white, PO4 groups displayed as tetrahedra).

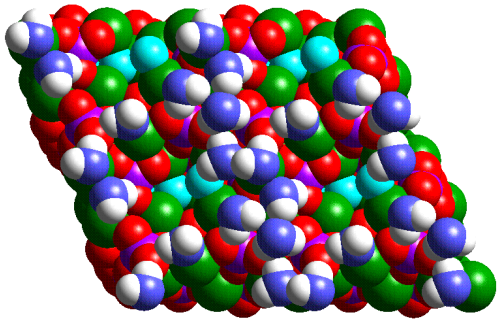

Figure 4.17: Plan view of the hydrated {1 0 $\bar{1}$ 1} surface, showing an irregular adsorption pattern with clustering of the water molecules round the surface calcium ions (Ca = green, O = red, O_{water} = blue, P = purple, F = light blue, H = white).

Hydrated {1 0 $\bar{1}$ 1}, {1 1 $\bar{2}$ 0}, {1 0 $\bar{1}$ 3} and {1 1 $\bar{2}$ 1} Surfaces

A similar situation is seen upon hydration of the {1 0 $\bar{1}$ 1} surface. The F-F distances are no longer contracted or expanded from their bulk value, but the Ca-F bonds are still distorted to a certain extent, similar to the hydrated {1 0 $\bar{1}$ 0} surface. Adsorption of water at the {1 1 $\bar{2}$ 0}, {1 0 $\bar{1}$ 3} and {1 1 $\bar{2}$ 1} surfaces shows similar behaviour to the three surfaces described above, with the water molecules mainly coordinating by their oxygen atoms to the surface calcium atoms but also forming hydrogen-bonded interactions to surface oxygen and fluoride ions and where possible to other water molecules. In all cases, the effect of the adsorbed water is to lessen surface relaxation and bond distortion. Plan views of monolayer coverages of water on these four different surfaces are shown in figures 4.17-20.

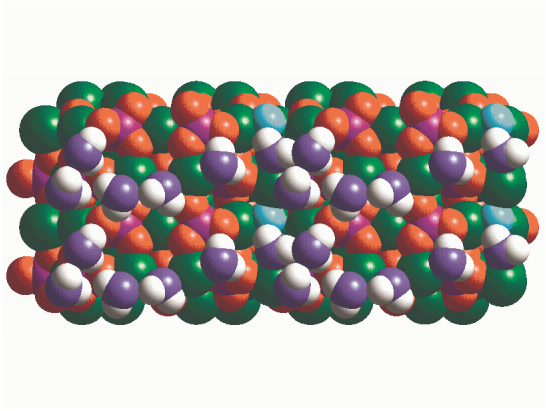

Figure 4.18: Plan view of the hydrated $\{1\ 1\ \overline{2}\ 0\}$ surface, showing an irregular adsorption pattern with clustering of the water molecules round the surface calcium ions (Ca = green, O = red, O_{water} = blue, P = purple, F = light blue, H = white.)

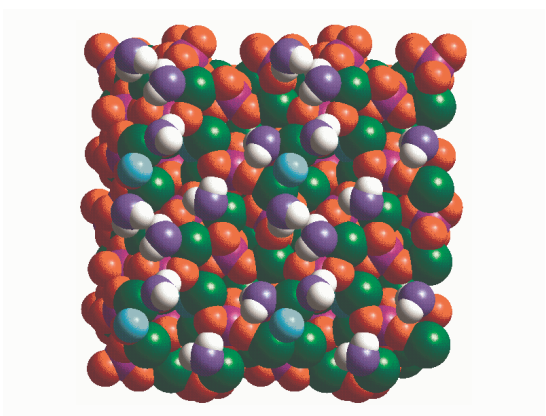

Figure 4.19: Plan view of the hydrated $\{1\ 1\ \overline{2}\ 1\}$ surface, showing an irregular adsorption pattern with clustering of the water molecules round the surface calcium ions (Ca = green, O = red, O_{water} = blue, P = purple, F = light blue, H = white).

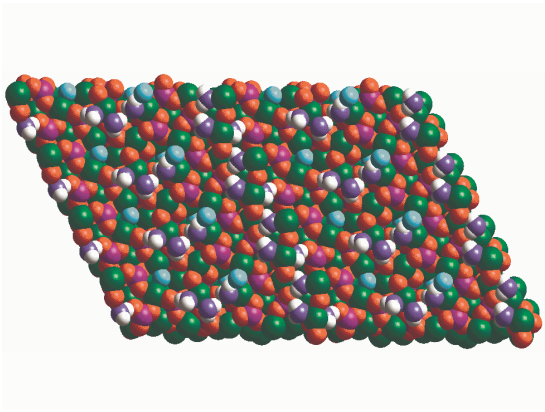

Figure 4.20: Plan view of the hydrated $\{1\ 0\ \bar{1}\ 3\}$ surface, showing an irregular adsorption pattern with clustering of the water molecules round the surface calcium ions (Ca = green, O = red, O_{water} = blue, P = purple, F = light blue, H = white).

Hydration Energies

The average hydration energies for the adsorption of full monolayers of water on the surfaces are listed in Table 4.5. They do not vary much from surface to surface, due to the very similar adsorption behaviour at the different surfaces, and the range from -73 kJmol^{-1} at the $\{0\ 0\ 0\ 1\}$ surface to -88 kJmol^{-1} at the $\{1\ 0\ \bar{1}\ 1\}$ surface indicates physisorption of the (molecular) water at all surfaces. In addition, rather than the average hydration energies for the adsorption of a full layer of water, in figure 4.21 we show a graph of the sequential hydration energies for the different surfaces, where the energy plotted *versus* number of water molecules is the energy released

at each addition of a successive water molecule at the surface in question. When adsorbing water at the surfaces, a whole range of starting configurations and adsorption sites for the water molecules were calculated and the values shown are those releasing the most energy at each step, thus ensuring that the most reactive site available was chosen for each successive addition. It is clear from the graph in figure 4.21 that most surfaces exhibit more or less Langmuir behaviour, especially after the initial adsorption of the first water molecule, with the notable exception of the $\{1\ 0\ \overline{1}\ 3\}$ surface, which shows more variation in its hydration energies with the addition of successive water molecules. This surface is a less tightly packed surface than the others with a large surface area of 2.4 nm^2 per unit cell as compared to 0.8 nm^2 for the $\{0\ 0\ 0\ 1\}$ surface, leading to many more different adsorption sites than on the closely packed surfaces. The $\{1\ 1\ \overline{2}\ 1\}$ also has a fairly large surface area per unit cell (1.1 nm^2) and this surface also shows a less regular adsorption behaviour than the other planes. Figures 4.22-24 shows a sequence of attached water molecules onto $\{1\ 0\ \overline{1}\ 3\}$ surface from one molecule to five, after which a second water layer starts to form. After monolayer coverage (figure 4.20), we still notice some empty spaces on the surface due to its large surface area and even though further adsorption does not occur these surfaces sites, either because the particular areas are not particularly hydrophilic or the water prefers to form clusters, as is for example seen on the CaF_2 $\{1\ 1\ 1\}$ surfaces where water desorbs from the surface to form droplets [135]. However, the open nature of the surface and water monolayer offers a large variety of adsorption sites and configurations, causing the non-langmuir be-

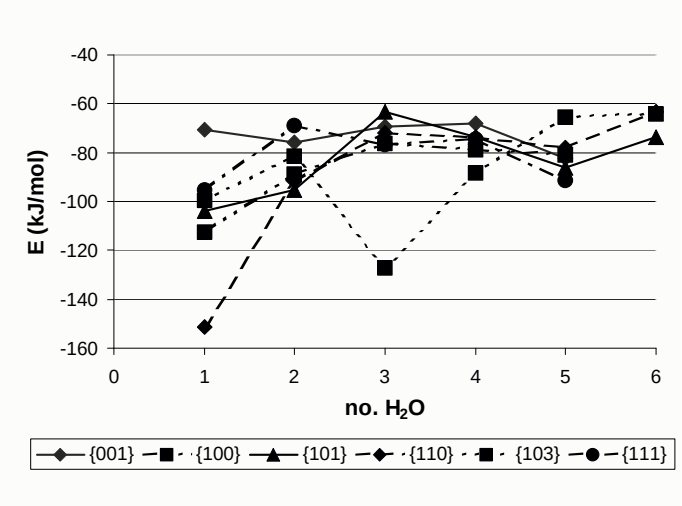

Figure 4.21: Sequential energies of adsorption of successive water molecules at the apatite surfaces.

haviour.

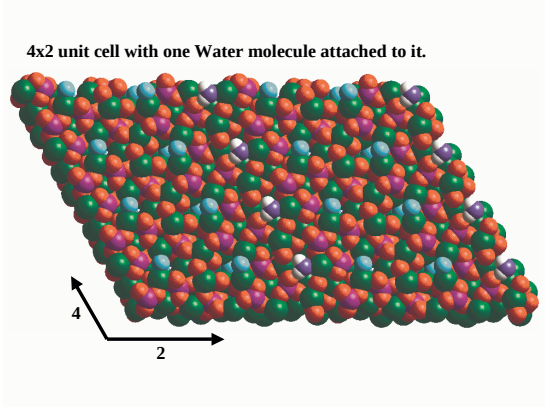

Figure 4.22: Plan view of the hydrated $\{1\ 0\ \bar{1}\ 3\}$ surface, showing only one molecule of water adsorbed onto the surface Ca = green, O = red, O_{water} = blue, P = purple, F = light blue, H = white.

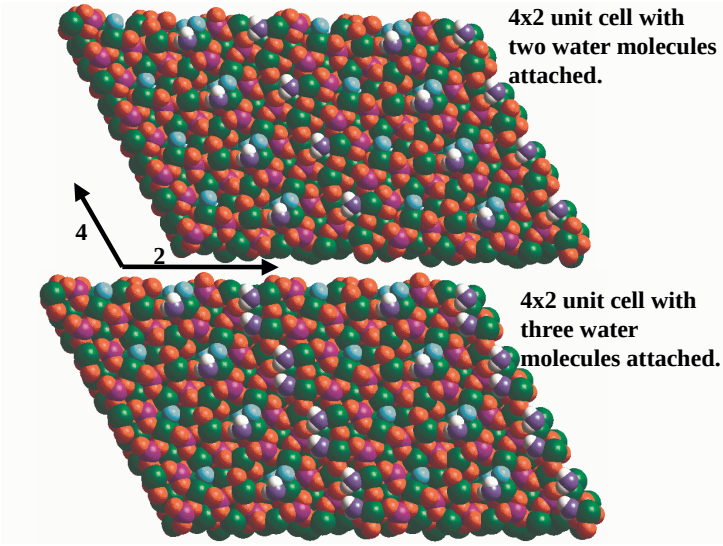

Figure 4.23: Plan view of the hydrated $\{1\ 0\ \bar{1}\ 3\}$ surface, showing two and three water molecules adsorbed onto the surface. Ca = green, O = red, O_{water} = blue, P = purple, F = light blue, H = white.

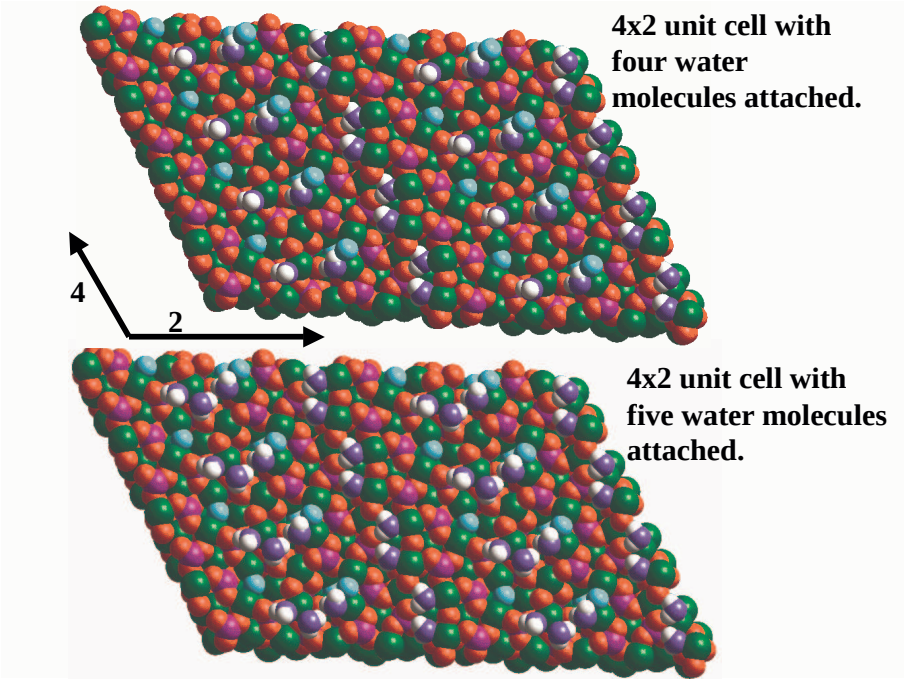

Figure 4.24: Plan view of the hydrated $\{1\ 0\ \bar{1}\ 3\}$ surface, showing four and five water molecules adsorbed onto the surface. Ca = green, O = red, O_{water} = blue, P = purple, F = light blue, H = white.

4.2 MORPHOLOGIES

The equilibrium morphology of a crystal is determined by the surface energy and the related growth rate of the various surfaces and provides a measure of the relative stabilities of the surfaces. The theory of morphologies was treated in more detail in chapter 2. As described, a surface with a high surface free energy is expected to have a large growth rate and this fast growing surface will not be expressed in the morphology of the resulting crystal. Only surfaces with low surface free energies and hence slow growing will be expressed. Molecular and lattice dynamics simulations have shown that the contribution of the excess entropy term to the surface free energy in ionic solids is small compared to the enthalpy term, as the differences between the entropies of the bulk and the surface are small.[61, 62] In addition, although Mulheran showed that the change in surface free energy with temperature may be significant,[136] Allan and coworkers calculated that this change is similar for different surfaces.[62, 137] Hence, for ionic solid surfaces the surface energies are good approximations for the surface free energies, especially taking into account that in morphology calculations only the relative values of the surface free energies of the different faces are important. Thus, the surface energies can be assumed to determine the equilibrium morphology of the crystal and indeed the prediction of morphologies of even complex oxides on the basis of static surface energies has been shown in the past to successfully reproduce experimental morphologies.[138, 139] Although in metals and more covalent solids the contribution of entropy to the surface free energy may be more important,[140] recent electronic structure calcu-

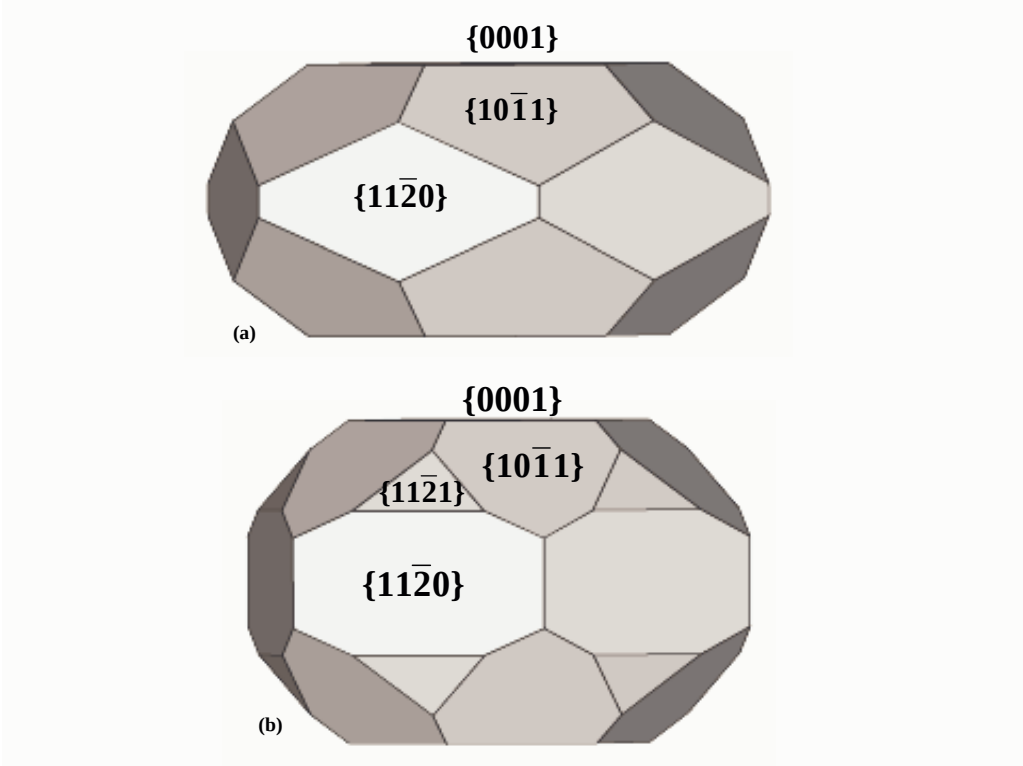

Figure 4.25: Calculated thermodynamical morphologies of (a) the unrelaxed and (b) the fully relaxed apatite crystals.

lations have shown that fluorapatite is a highly ionic solid, where the PO_4 groups act as polyanions,[111, 133] in a similar way to other solids containing molecular anions, such as carbonates and sulfates. For both these systems, accurate morphologies have been predicted on the basis of the static surface energies, which were found to agree with experimentally observed morphologies.[119, 141, 142]

Figure 4.25 shows the calculated morphologies of the fluorapatite crystal,

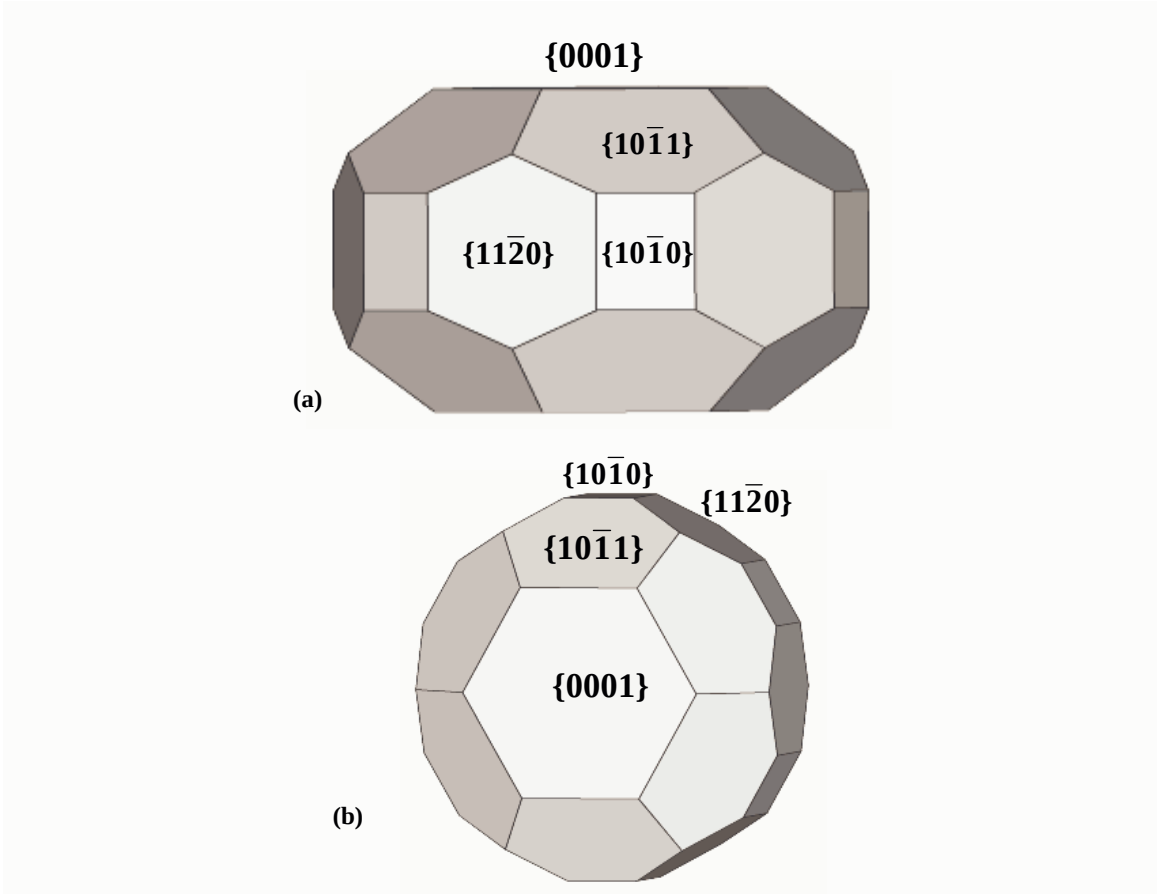

Figure 4.26: . (a) Side and (b) plan view of the calculated thermodynamical morphologies of the hydrated apatite crystal.

indicating the surfaces expressed in the morphologies. Figures 4.25(a) and (b) show the morphologies calculated respectively from the unrelaxed and relaxed surface energies in Table 4.3, where the dominant {0 0 0 1} surface is expressed in both cases. When surface relaxation is taken into account, the {1 1 $\overline{2}$ 1} surface has become relatively more stable with respect to the {1 0 $\overline{1}$ 1} and {1 1 $\overline{2}$ 0} surfaces and hence it appears in the relaxed crystal morphology (figure 4.25(b)), in agreement with experimental crystal growth where the surface is found to be a twinning plane for the intergrowth of apatite crystals.[2] When the surfaces are hydrated, the morphology (figure 4.26) changes again due to the dissimilar stabilisation of the different surfaces by the adsorption of water. The {1 1 $\overline{2}$ 1} surface has disappeared again, but now the {1 0 $\overline{1}$ 0} surface has become relatively more stable and is hence expressed in the hydrated morphology. The presence of both {0 0 0 1} and {1 0 $\overline{1}$ 0} surfaces in the hydrated morphology again agrees with experiment, where both these surfaces are found as cleavage planes[2] and as crystal growth features.[143] Figure 4.26(b) is a different view of the same hydrated morphology as in figure 4.26(a), looking down upon the {0 0 0 1} surface. From the combination of both perspectives, we can see that the hydrated crystals have a rounded hexagonal shape and are fairly flat platelets, in agreement with experimental apatite crystals in bone, which are found to be nano-sized platelets.[107, 144]

4.3 Discussion

In this chapter we have employed surface simulation techniques to model different surfaces of the fluorapatite system. We have successfully reproduced the experimentally predicted stable surfaces and also investigated the effect of water on the surface structures and morphology of this complex material.

The {0 0 0 1} surface is by far the most stable surface, both under dehydrated and hydrated conditions, and is expressed in all three morphologies: bulk-terminated, dry and hydrated crystals. The {0 0 0 1} surface's dominance is in agreement with its rôle as the major experimental cleavage plane. When surface relaxation of the crystal is taken into account, the morphology of the dry crystal also expresses the major experimental $\{1\ 1\ \overline{2}\ 1\}$ twinning plane, while the hydrated crystal morphology shows the other $\{1\ 0\ \overline{1}\ 0\}$ cleavage plane in addition to the {0 0 0 1} surface.

The type of distortion of the fluoride chains in the calcium channels depends upon the orientation of the channels with respect to the surface. When the channels are perpendicular to the surface, only F-F distortion occurs within the channels, whereas when the channels lie in the plane of the surface, the F-F distances are unchanged but the Ca-F bonds are distorted, as was also seen in Lee et al.'s study of slabs of apatite material,[107] and the F-F chains form a zig-zag pattern through the channel. A mixture of both distortions occurs when the channels lie at an angle to the surface.

Hydration of the surfaces shows Langmuir behaviour, apart from the rather unstable and open-structured $\{1\ 0\ \overline{1}\ 3\}$ surface, where the energies of sequential hydration show more variation. The calculated hydration energies

clearly indicate physisorption of the water molecules. The adsorption of water and hence increased coordination of the surface ions has a stabilising effect on all surfaces, particularly the four closest-packed planes, the $\{0\ 0\ 0\ 1\}$, $\{1\ 0\ \overline{1}\ 0\}$, $\{1\ 0\ \overline{1}\ 1\}$ and $\{1\ 1\ \overline{2}\ 0\}$ surfaces, whose surface energies all decrease by 35% to 43% upon hydration. The overall effect of the water monolayer is to lessen the relaxation of the surface regions compared to the dehydrated surface, leading to more bulk-like terminations. The surface energies of the two twinning planes, the $\{1\ 0\ \overline{1}\ 3\}$ and $\{1\ 1\ \overline{2}\ 1\}$ surfaces, which have much less close-packed structures are less severely affected by water adsorption, only decreasing by 14-21% from their value in the dry crystal. Although these surfaces are less closely packed than the other four, their interlayer spacings are smaller. Hence, although the atoms in the surface region are not as well coordinated laterally to other surface ions, they are more closely coordinated to ions below the surface. The major stabilisation of these two surfaces is therefore due to extensive relaxations and rotations of the dry surfaces, decreasing their surface energies by 35-57% with respect to the bulk-terminated surfaces.

Figure 4.27, for example, shows how upon geometry optimisation of the surface, significant rotation of the phosphate groups occurs, even four layers into the surface (15 Å), while the surface fluoride ions move out of the surface, forming extra bonds to surface calcium ions which move into the bulk material. As a result these surface species do not gain as much from the extra coordination through water adsorption as the more closely packed surfaces which coordinate to a lesser extent to deeper layers.

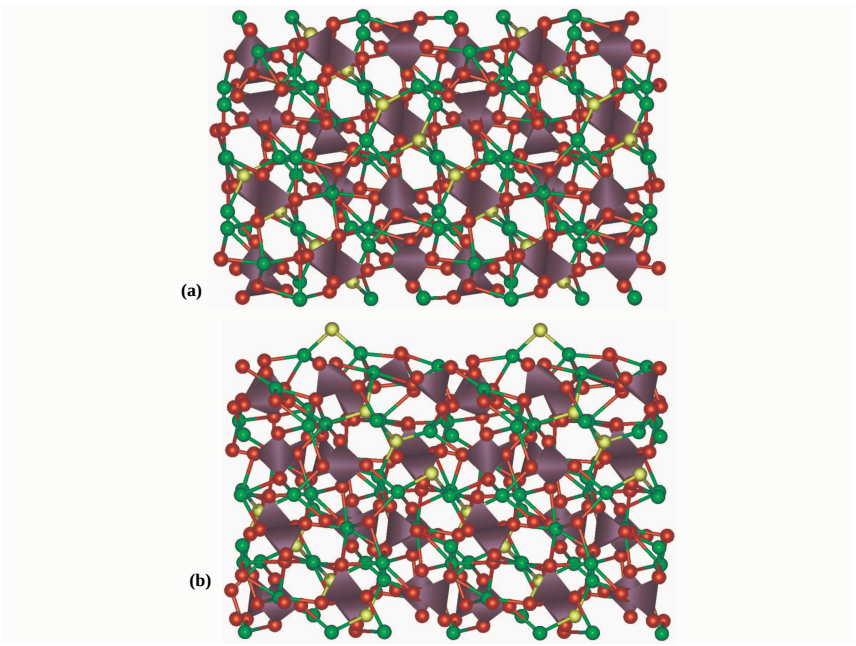

Figure 4.27: Side view of (a) the bulk-terminated and (b) the fully geometry optimised structure of the $\{1\ 1\ \overline{2}\ 1\}$ surface, showing extensive surface relaxations and phosphate rotations throughout a surface region of approximately 15 Å (Ca = green, O = red, P = purple, F = yellow, PO_4 groups displayed as tetrahedra).

Having studied in detail the surface structures of the major apatite surfaces and the effect of water on their stability and the crystal morphology, we will proceed to investigate their reactivities towards organic adsorbates and the interface with silicate materials in the next chapters.

Chapter 5

SURFACE ADSORPTION OF ORGANIC SURFACTANTS ON FLUORAPATITE

In this chapter we report our modelling of the adsorption of a range of organic molecules onto different fluorapatite surfaces, due to the importance of organic/ inorganic interactions in biological situations. We have modelled four representatives of different types of organic molecules, namely; methanoic acid (CHOOH), hydroxamic acid (HC(=O)NHOH), methylamine (H_2CNH_3) and hydroxyethanal (HC(=O)CH_2OH). We have modelled these particular molecules to investigate which functional groups form strong interactions with the surfaces of fluorapatite. Methanoic acid is a model for the carboxylic acids. Hydroxamic acid contain the head group of alkyl hydroxamates and hydroxyethanal contains both the aldehyde and hydroxyl functional groups.

5.1 Surfactant Molecules

In this study we have used neutral adsorbates molecules and we have only studied undissociated molecules. Preliminary investigations have shown that the use of fully associated molecules in the simulations gives good agreement between calculated adsorption trends and experimentally found behaviour[54] and, in any case the presence of proton in the adsorbate molecule does not prevent the relevant oxygen atom from interacting with the mineral surface species as will be described below.

5.1.1 Methanoic acid

Figure 5.1 shows the structure of methanoic acid, which is a simple plana carboxylic acid. The figure also shows the partial charges given to each atom of the molecule as used in the potential parameters discussed in chapter 3.[130] Both oxygens are given the same partial charge of -0.38. The carbonyl oxygen (which is doubly bonded to the carbon) is the most accessible and the molecule will probably get attached to the surfaces through this ion. However the hydroxyl oxygen (the oxygen being part of the hydroxyl group of the acid) can sometimes interact with the surface ions as well or at some instance both oxygens interact actively with the surfaces. Weaker interactions with surface atoms can occur through hydrogen-bonding via the carbonyl hydrogen (hydrogen bonded to carbon) and hydrogen of the hydroxyl group (hydrogen that is part of hydroxyl group of the acid).

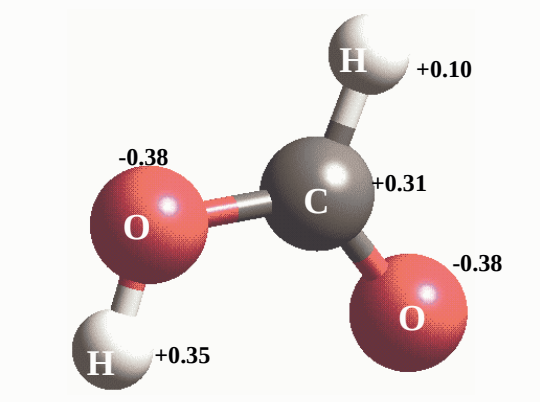

Figure 5.1: Methanoic acid molecule, showing the partial charges on different atoms. C = dark grey, O = pink, H = white.

5.1.2 Hydroxamic Acid

Hydroxamic acid (so called throughout this study) is the smallest of the Alkyl hydroxamates which contain the hydroxyl amide and carbonyl functional groups, with the general form RC(=O)NHOH, where here R=H. We have considered two different isomeric configurations of the hydroxamic acid. One with both oxygens on the same side of the molecule and we label this as the "cis" form (figure 5.2), and the "trans" form, where the oxygen atoms are on opposite sides of the molecule as shown in figure 5.3, although they are not formally "cis" or "trans" isomers. Trans-hydroxamic acid is the most stable of the two forms. There is however free rotation of the molecule about C-N allowing the interchange between the two forms, but we have considered the initial configurations as described in the "cis" and "trans" forms. The reason for considering both initial configurations is that we initially position

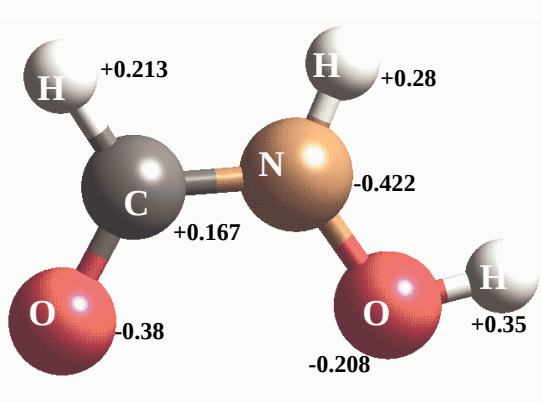

Figure 5.2: "Cis" hydroxamic acid molecule, showing the partial charges on different atoms. C = dark grey, O = pink, H = white and N = light brown.

the molecules a short distance above the surface. As a result the molecules already feel the electrostatic attractions and repulsions of the surface and as a consequence the molecules may stay in their initial form. So in order to find the most stable surfactant/surface configuration it is necessary to consider the adsorption in both initial forms. We also rotate the whole molecule in different configurations with respect to the surface to find the most stable adsorption energy.

In the cvff forcefield, the nitrogen atom of the hydroxamic acid molecules is assigned the most negative partial charge (-0.422e). This nitrogen is bonded to a hydrogen atom, an oxygen and a carbon, which makes it generally not accessible to coordinate to the surfaces. Hence the hydroxamic acid molecules tend to coordinate via one, or both, of their oxygen atoms to calcium atoms on the mineral surface. The atoms on hydroxamic acid are referred to in the same way as we described for the methanoic acid above.

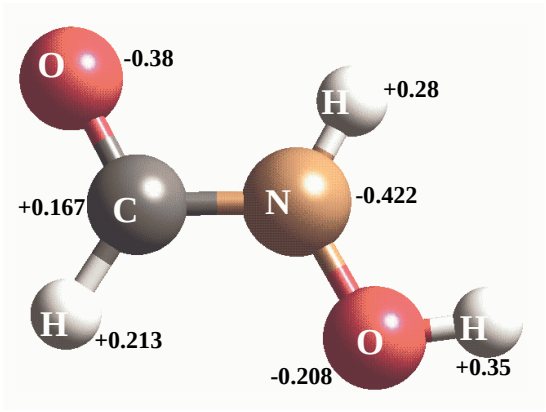

Figure 5.3: "Trans" hydroxamic acid molecule, showing the partial charges on different atoms. C = dark grey, O = pink, H = white and N = light brown.

The oxygen that is part of the carbonyl group is referred to as the carbonyl oxygen atom, and the one that is part of the hydroxyl group is referred to as the hydroxyl oxygen atom. There are three distinct types of hydrogen atoms in the hydroxamic acid molecules; the one that is part of the hydroxyl group, which we refer to as the hydroxyl hydrogen atom; the one that is part of the carbonyl group, which we refer to as the carbonyl hydrogen atom; and the one that is part of the amide group, which we will refer to as the amide hydrogen atom.

5.1.3 Methylamine

Figure 5.4 shows the methylamine molecule structure. The methylamine molecule is used in this study to investigate the adsorption of molecules with only the amine functional group, without the hydroxamic acid. Methylamine

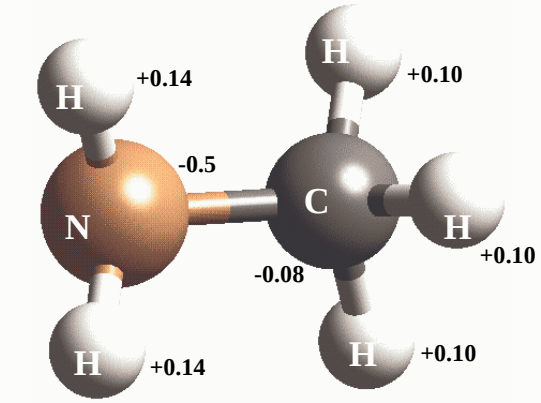

Figure 5.4: Methylamine acid molecule, showing the partial charges on different atoms. C = dark grey, H = white and N = light brown.

is the smallest molecule of the amine group of molecules, and contains both an amine and a methyl group. The nitrogen atom is the only atom with a significant negative charge of -0.50e, and since the interactions between adsorbate and surface are mostly electrostatic in nature, the methylamine molecules coordinate via this atom to the positive surface calcium atoms. The two different types of hydrogen atoms present in methylamine comprise the three that are part of the methyl group (bonded to carbon), which we refer to as the methyl hydrogen atoms; and the two that are part of the amine group (bonded to nitrogen), which we will refer to as the amine hydrogen atoms.

5.1.4 Hydroxyethanal

The last molecule we consider is hydroxyethanal, similar in structure to hydroxamic acid but with two carbon atoms in the backbone instead of a car-

bon and a nitrogen. This molecule will be used in our study to investigate the difference between a C-OH and a N-OH group and also compare with methanoic acid, where the C=O and C-OH groups are both part of the same carbon, whereas hydroxyethanal contains both the hydroxyl and aldehyde functional groups. Separately we will again consider two different extreme configurations, which we will label as the "cis" and "trans" forms according to whether the oxygen atoms are on the same or opposite sides of the hydroxyethanal molecule as shown in figures 5.5 and 5.6. In the cvff forcefield both the oxygen atoms are assigned the same partial charge (-0.38e), and the hydroxyethanal molecule can coordinate to the surfaces by either or both of the oxygen atoms. Like hydroxamic acid, the molecules are generally expected to coordinate via their carbonyl oxygen atoms as this is the more accessible of the two oxygen atoms. Similar to the previous molecules, when referring to the hydroxyethanal molecule the oxygen that is part of the hydroxyl group will be referred to as the hydroxyl oxygen atom and the oxygen that is part of the carbonyl (aldehyde) group will be referred to as the carbonyl oxygen atom. The three hydrogen atoms present in the molecule will be referred to as; the hydroxyl hydrogen atom which is the hydrogen that is part of the hydroxyl group; the carbonyl hydrogen atom, i.e the hydrogen that is part of the carbonyl group; and the two hydrogen atoms that are attached to the hydroxyl carbon atom, which we will refer to as the hydroxyl carbons hydrogen atoms.

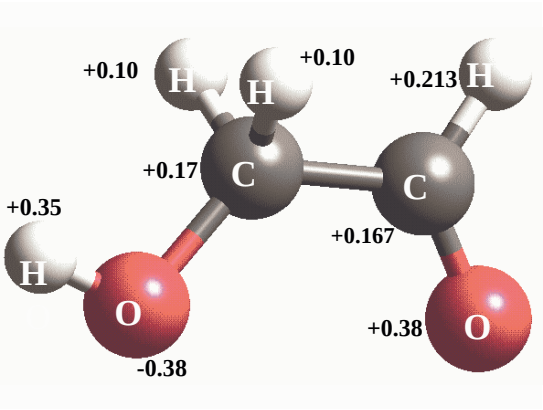

Figure 5.5: "Cis" hydroxyethanal molecule, showing the partial charges on different atoms. C = dark grey, H = white and O = pink.

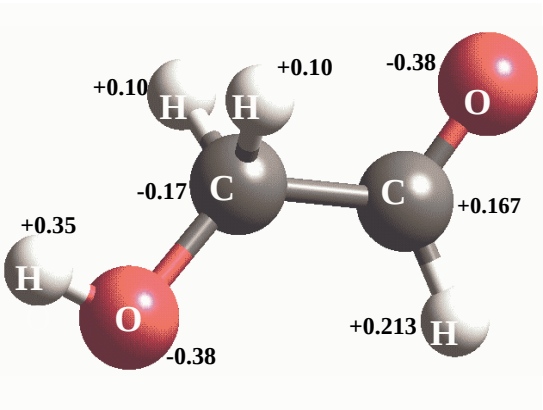

Figure 5.6: "Trans" hydroxyethanal molecule, showing the partial charges on different atoms. C = dark grey, H = white and O = pink.

5.2 Surfaces and adsorption energies

We have modelled the adsorption of the surfactants to all the six surfaces that we have investigated in chapter 4 on the stability of their dehydrated and hydrated state, viz; {0 0 0 1}, {1 0 $\overline{1}$ 0}, {1 0 $\overline{1}$ 1}, {1 1 $\overline{2}$ 0}, {1 1 $\overline{2}$ 1}, and {1 0 $\overline{1}$ 3}. We have added one surfactant per surface simulation cell and investigated its adsorption sites and configuration at the surface and calculated the various adsorption energies. The METADISE simulation program was used in this study where the surfactants were adsorbed to the different surfaces and allowed to relax to their mechanical equilibrium and have calculated the adsorption energies according to equation 2.53. As mentioned above we have considered different starting configurations of the molecules on the surfaces to ensure that the lowest energy mineral/surfactant configuration was found rather than a local minimum. The adsorption energies were calculated with respect to the gaseous surfactant molecules. The energy of the isolated methanoic acid molecule is -19.85 eV and the two hydroxamic acid molecules have energies of the isolated molecules of -25.82 eV for the "cis" form and -26.00 eV for the "trans" form which gives an energy difference between the two of 0.18 eV (17.37 kJmol^{-1}). Methylamine has a self-energy of -15.31 eV. The two different forms of hydroxyethanal have the same self energy of -31.10 eV for the "cis" form and -31.11 eV for the "trans" form which gives and energy difference between the two of 0.01 eV (0.96 kJmol^{-1}). In table 5.1 we show the different adsorption energies of the different surfactants at all different surfaces.

Table 5.1: Adsorption energies of all different surfaces with different surfactant molecules.

surface	Methanoic acid	hydroxamic cis	Hydroxamic trans	methylamine
{0 0 0 1}	-105.2	-112.2	-112.4	-30.3
{1 0 $\bar{1}$ 0}	-170.1	-203.0	-116.4	-83.0
{1 0 $\bar{1}$ 1}	-136.0	-185.8	-132.9	-52.0
{1 1 $\bar{2}$ 0}	-171.5	-185.4	-172.0	-95.3
{1 1 $\bar{2}$ 1}	-138.0	-169.7	-115.5	-51.3
{1 0 $\bar{1}$ 3}	-105.3	-98.4	-99.4	-25.0

surface	Hydroxyethanal cis	hydroxyethanal trans
{0 0 0 1}	-142.1	-122.8
{1 0 $\bar{1}$ 0}	-196.3	-214.6
{1 0 $\bar{1}$ 1}	-193.0	-135.9
{1 1 $\bar{2}$ 0}	-212.6	-159.6
{1 1 $\bar{2}$ 1}	-185.8	-187.3
{1 0 $\bar{1}$ 3}	-134.8	-137.4

5.2.1 Methanoic acid

{0 0 0 1} surface

The adsorption of methanoic acid on the {0 0 0 1} is least energetically favorable of all the surfaces with an adsorption energy of -105.2 kJmol^{-1}, almost the same adsorption energy as on the {1 0 $\bar{1}$ 3} surface (a difference of about 0.1 kJmol^{-1}). The acid is attached to the surface through its carbonyl oxygen to a surface Ca at a distance of 2.21 Å. The molecule has rotated and now the two hydrogens are on the same side and, it is adsorbed flat on the surface and in this way it also interacts weakly to surface oxygens through its hydrogen atoms at distances of 2.54, and 2.60 Å. The overall surface structure of the fluorapatite is not changed from the pure relaxed {0 0 0 1} surface. Figure 5.7 shows the plan view of the surface with the adsorbed methanoic acid molecule.

{1 0 $\bar{1}$ 0} surface

Figure 5.8 shows the adsorption of the methanoic acid on the {1 0 $\bar{1}$ 0} surface which releases ta similar adsorption energy (-170.1 kJmol^{-1}) as the {1 1 $\bar{2}$ 0} surface at -171.5 kJmol^{-1}. Again the methanoic acid molecule adsorb flat on the surface of the fluorapatite and interacts mainly with the surface Ca ions through attachment of the carbonyl oxygen atom at a short distance of 2.15 Å. We also see some rotation of the carbonyl hydrogens and the hydroxyl hydrogens in attempt to form further interactions with the surface oxygen atoms of the fluorapatite at distances; 2.55, 2.59 and 2.69 Å. The apatite surface structure again has not changed from pure relaxed {1 0 $\bar{1}$ 0} surface.

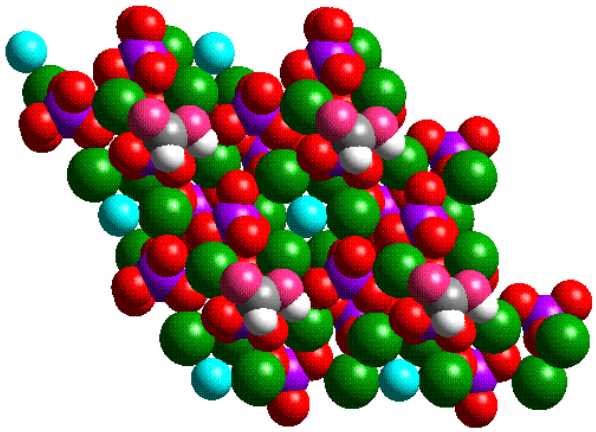

Figure 5.7: Methanoic acid attached to the {0 0 0 1} surface. Key: Ca = green, P = purple, F = light blue, $O_{apatite}$ = red, C = dark grey, H = white and $O_{methanoicacid}$ = pink.

{1 0 $\bar{1}$ 1} surface

The adsorption of the methanoic acid onto this {1 0 $\bar{1}$ 1} surface releases an energy of -136.0 kJmol^{-1}. Again we see no change on the surface structure of the apatite mineral after the adsorption of the acid molecule. However there is a close interaction of the carbonyl oxygen with the surface Ca at a short distance of 2.20 Å, and structure of the acid molecule twisted slightly to allow the weak interaction between the hydroxyl hydrogen atom to the surface fluorine ions at a distance of 2.37 Å. With the fluoarapatite surface structure remaining the same as the pure relaxed surface, there is no close interaction between the carbonyl hydrogens to the surface oxygens. The plan view of the surface with the adsorbed molecule is shown in figure 5.9.

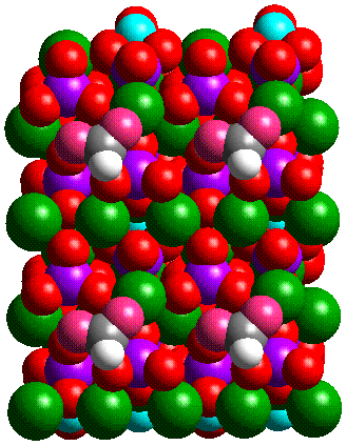

Figure 5.8: Methanoic acid attached to the $\{1\ 0\ \overline{1}\ 0\}$ surface. Key: Ca = green, P = purple, F = light blue, $O_{apatite}$ = red, C = dark grey, H = white and $O_{methanoicacid}$ = pink.

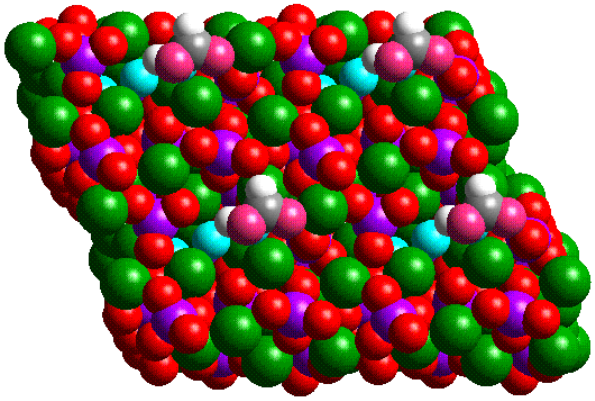

Figure 5.9: Methanoic acid attached to the $\{1\ 0\ \overline{1}\ 1\}$ surface. Key: Ca = green, P = purple, F = light blue, $O_{apatite}$ = red, C = dark grey, H = white and $O_{methanoicacid}$ = pink.

{1 1 $\overline{2}$ 0} surface

The adsorption of methanoic acid onto the {1 1 $\overline{2}$ 0} is the most energetically favourable of all the surfaces with an adsorption energy of -171.5 kJmol^{-1}. The structure of this apatite surface has relaxed more than the other surfaces, with some PO_4 groups rotating to allow the oxygens to move into the bulk. The acid is attached to the surface Ca atoms through its carbonyl oxygen. There are two calcium atoms not far from each other on the surface and the methanoic acid prefers to adsorb at an intermediate position between the two calcium atoms at distances of 2.47 Å from each, with the interaction between the hydroxyl hydrogen and the surface oxygen at 2.39 Å. The long-range surface structure, however, remains unaltered with the zigzag pattern of the layer of fluorine ions close to the surface still showing. A plan view of the surface with the methanoic acid surfactant is shown in figure 5.10.

{1 1 $\overline{2}$ 1} surface

The adsorption of methanoic acid on the {1 1 $\overline{2}$ 1} is like the {0 0 0 1} surface releases an energy of -138.0 kJmol^{-1}. The fluorapatite surface has PO_4 groups at the top of the surface with O atoms sticking out of the surface together with some exposed Ca atoms. Relaxation of the surface with the adsorbed acid molecule results in rotated PO_4 groups at the surface and Ca atoms have moved into the bulk. The acid become attached to the surface at an intermediate position between two surface Ca atoms through the carbonyl oxygen at distances; 2.40 and 2.39 Å (figure 5.11).

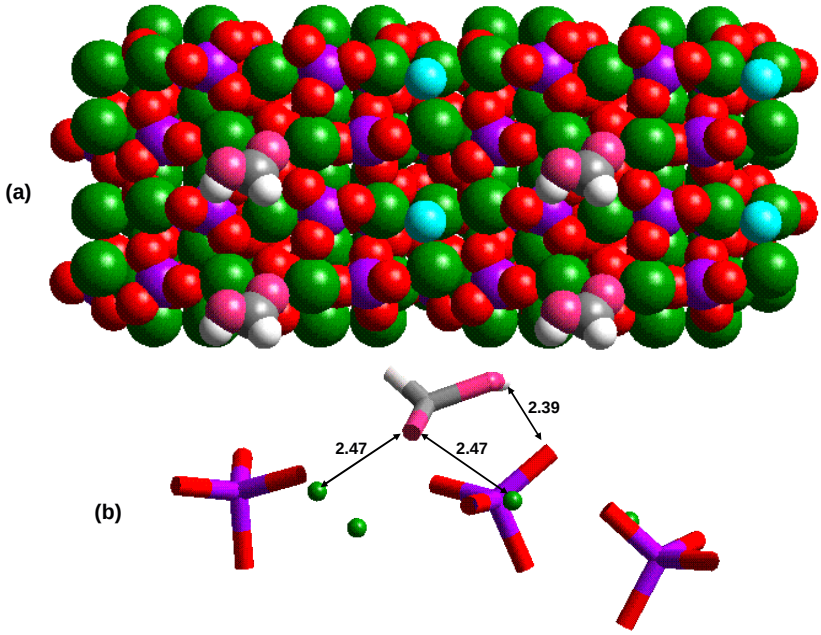

Figure 5.10: Most stable structure of Methanoic acid molecule attached to the $\{1\ 1\ \overline{2}\ 0\}$ surface, (a) plan view, and (b) a structure showing how the molecule ions interact with the apatite surface atoms with all bond distances shown in Å.with all bond distances shown in Å. Key: Ca = green, P = purple, F = light blue, $O_{apatite}$ = red, C = dark grey, H = white and $O_{methanoicacid}$ = pink.

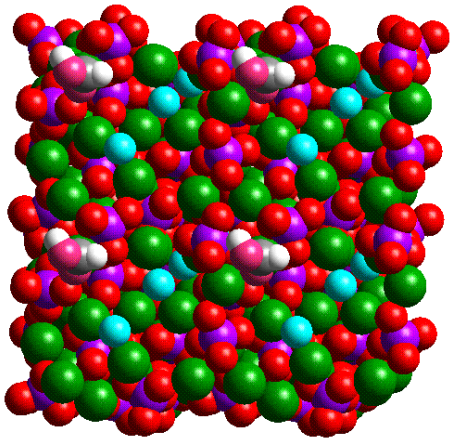

Figure 5.11: Methanoic acid attached to the {1 1 $\overline{2}$ 1} surface. Key: Ca = green, P = purple, F = light blue, $O_{apatite}$ = red, C = dark grey, H = white and $O_{methanoicacid}$ = pink.

{1 0 $\overline{1}$ 3} surface

The last surface to be studied with methanoic acid is the {1 0 $\overline{1}$ 3} surface, which has the largest surface area. From table 5.1, this adsorption release an energy of 105.3 kJmol^{-1} and is similar to the energy released on the most stable {0 0 0 1} surface. The acid again adsorbs almost flat onto the surface, but does not affect the structure of the underlying surface significantly. There is some slight movement of the fluorine channel atoms along the channel which however has a very minimal effect on the surface structure. The main attachment is through the carbonyl oxygens to surface Ca atoms at a short distance of 2.18 Å. In addition, there are some weak interactions by the carbonyl hydrogen to surface oxygen atoms at 2.56 and by the hydroxyl hydrogen to surface oxygens at 2.45 and 2.60 Å. Figure 5.12 shows a plan

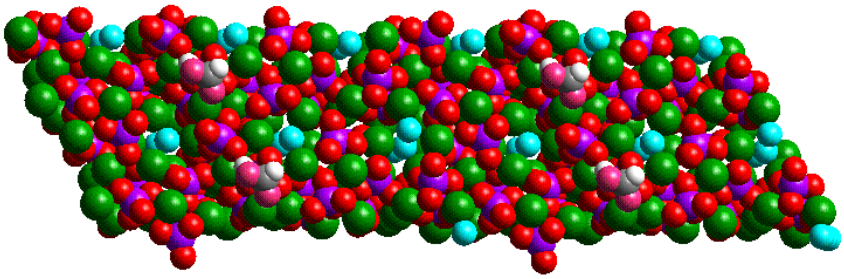

Figure 5.12: Methanoic acid attached to the {1 0 $\bar{1}$ 3} surface. Key: Ca = green, P = purple, F = light blue, $O_{apatite}$ = red, C = dark grey, H = white and $O_{methanoicacid}$ = pink.

view of the surface with the methanoic acid adsorbate.

5.2.2 "Cis" Hydroxamic Acid

{0 0 0 1} surface

The adsorption of the "cis" molecule of hydroxamic acid on the {0 0 0 1} surface is the second least energetically favourable for the range of six surfaces that we investigated, with an adsorption energy of -112.2 kJmol^{-1}. The acid lies almost flat on top of the surface though at a slight angle and figure 5.13 shows the plane view of the surface with the adsorbed molecule. It is

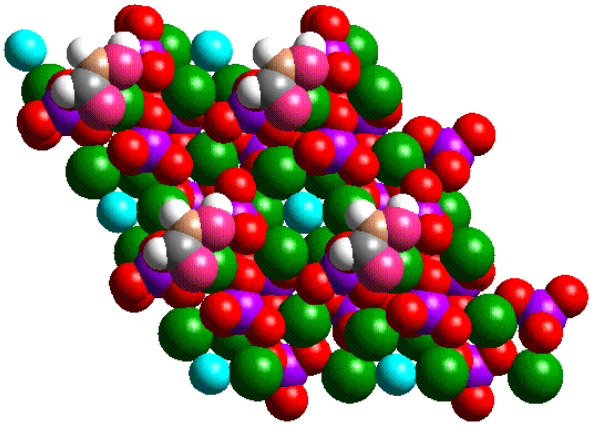

Figure 5.13: "Cis" hydroxamic molecule attached to the {0 0 0 1} surface. Key: Ca = green, P = purple, F = light blue, $O_{apatite}$ = red, C = dark grey, H = white and $O_{hydroxamic}$ = pink, N = light brown.

attached to the surface Ca atoms by its carbonyl oxygen at a short distance of 2.17 Å. Similar to what we saw with the methanoic acid, the interactions of the hydroxyl hydrogens to the surface oxygens are weak, at a nearest distance of 2.48 Å and the carbonyl hydrogens only interacts with surface oxygens at a distance of 2.57 Å. We also note that the hydroxyl oxygen forms a close interaction with the surface Ca at a distance of 2.41 Å. After surface relaxation with the acid the surface Ca atoms have relaxed less than in the pure surface, now with Ca - O distances of 2.45 Å and 2.49 Å, compared to the pure surface Ca - O distance of 2.36 Å.

{1 0 $\bar{1}$ 0} surface

The adsorption of the "cis" hydroxamic acid molecule onto the {1 0 $\bar{1}$ 0} surface is the most favourable process (table 5.1) with an adsorption

energy of -203.0 kJmol^{-1}. The molecule lies completely flat on the surface with the carbonyl oxygen and the hydroxyl oxygen coordinating to the same surface Ca at distances of 2.20 and 2.29 Å respectively. The hydroxyl hydrogen interacts with two surface oxygens at distances of 2.44 and 2.43 Å. The amide hydrogen atom interacts with a surface oxygen as well at a distance of 2.52 Å and the carboxyl hydrogen interacts at 2.45 Å with a surface oxygen. The surface structure of the apatite surface remains virtually unchanged from the pure, relaxed surface and the surface with adsorbed molecule is shown in figure 5.14.

{1 0 $\bar{1}$ 1} surface

Adsorption of the {1 0 $\bar{1}$ 1} surface releases an adsorption energy of -185.8 kJmol^{-1}. However, here the molecule do not adsorb flat on the surface but at an angle, although less so than on the {0 0 0 1} surface. Similar to the adsorption at the {1 0 $\bar{1}$ 0} surface, the carbonyl and hydroxyl oxygens interact with the same surface Ca atom, on either side at distances of 2.24 and 2.28 Å respectively. This time there is also an interaction between the carbonyl hydrogen and F^- ions on the surface at a distance of 2.32, a trend we also noticed with methanoic acid on the same surfaces, where there is an interaction of a hydroxyl hydrogen to the F^- at 2.37 Å. The hydroxyl hydrogen this time interacts weakly with a surface oxygen at a distance of 2.50 Å. The amide hydrogen however does not coordinate to the surface ions. The adsorption structure is shown in figure 5.15.

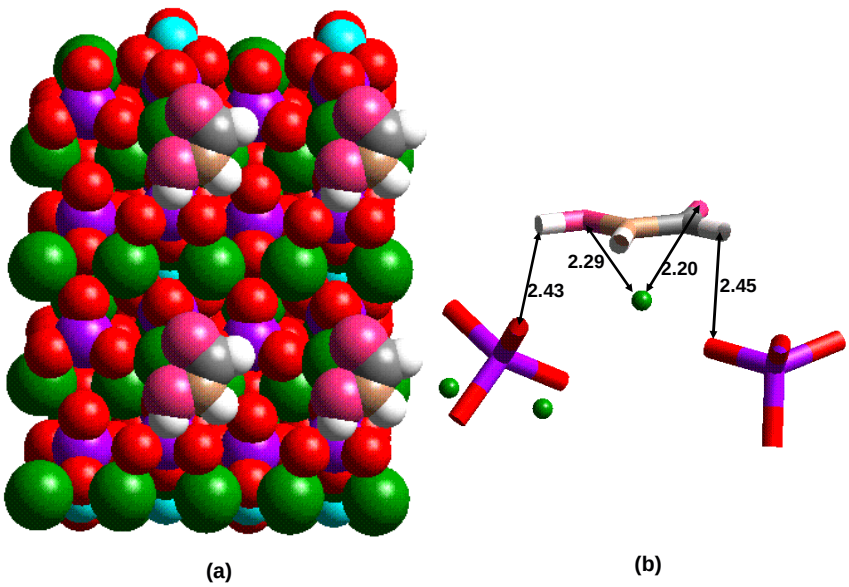

Figure 5.14: Most favourable structure of "Cis" hydroxamic molecule attached to the $\{1\ 0\ \bar{1}\ 0\}$ surface of fluorapatite, (a) plan view and (b) a structure showing how the molecule attaches to the apatite surface ions with all bond distances shown in Å. Key: Ca = green, P = purple, F = light blue, $O_{apatite}$ = red, C = dark grey, H = white and $O_{hydroxamic}$ = pink, N = light brown.

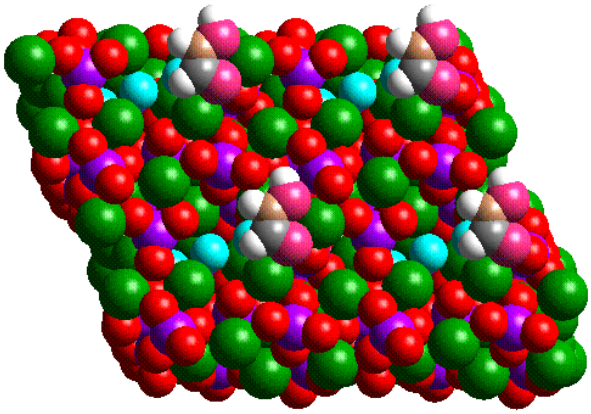

Figure 5.15: "Cis" hydroxamic molecule attached to the $\{1\ 0\ \overline{1}\ 1\}$ surface. Key: Ca = green, P = purple, F = light blue, $O_{apatite}$ = red, C = dark grey, H = white and $O_{hydroxamic}$ = pink, N = light brown.

$\{1\ 1\ \overline{2}\ 0\}$ surface

The energy of adsorption of "cis" hydroxyethanal acid at this surface is very similar to the $\{1\ 0\ \overline{1}\ 0\}$ surface, at 185.4 kJmol^{-1}. Again the molecule adsorbs flat onto the surface, attaching to the surface Ca atoms via both carbonyl and hydroxyl oxygens. However in this case the molecule does not interact with the top most Ca atoms but with those in the second layer of the Ca atoms. The carbonyl and hydroxyl oxygen atoms do not interact with the same Ca atom but with two different ones at distances of 2.24 Å for the carbonyl and 2.29 Å for the hydroxyl oxygen. The interaction between the carbonyl hydrogen and a surface F^- is weak at 2.46 Å and the hydroxyl hydrogen to surface oxygen coordination is also weak, at a distance of 2.51 Å. Figure 5.16 shows the structure of the adsorbed molecule on the surface. The

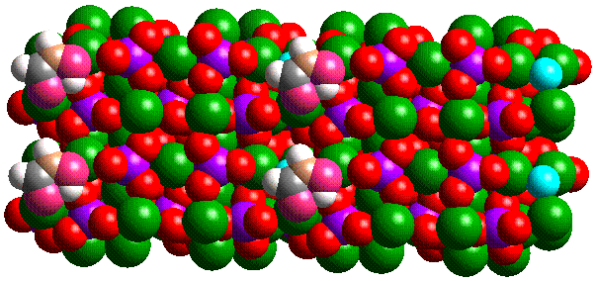

Figure 5.16: "Cis" hydroxamic molecule attached to the $\{1\ 1\ \overline{2}\ 0\}$ surface. Key: Ca = green, P = purple, F = light blue, $O_{apatite}$ = red, C = dark grey, H = white and $O_{hydroxamic}$ = pink, N = light brown.

surface structure of the apatite remains virtually the same as the pure relaxed surface with a slight rotation of the PO_4 groups due to some interaction with the surfactant ions.

{1 1 $\overline{2}$ 1} surface

The surface area of this surface is relatively large compared to the other surfaces, apart from the $\{1\ 0\ \overline{1}\ 3\}$ surface and there are hence a variety of surface sites available for adsorption. This surface again has some oxygens sticking out ready to interact actively with surfactants or water etc. However, the molecule again prefers to attach to the surface Ca via the carbonyl oxygen at an interaction distance of 2.31 Å and also to the same Ca atom by the hydroxyl oxygen at 2.41 Å. We also noticed that the molecule is coordinated to the surface very closely, although it does not lie completely flat on the

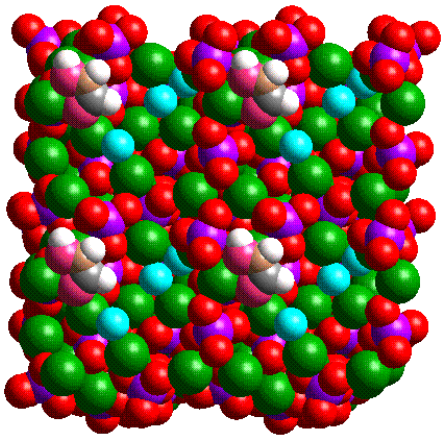

Figure 5.17: "Cis" hydroxamic molecule attached to the $\{1\ 1\ \overline{2}\ 1\}$ surface. Key: Ca = green, P = purple, F = light blue, $O_{apatite}$ = red, C = dark grey, H = white and $O_{hydroxamic}$ = pink, N = light brown.

surface. The interactions between the hydrogen atoms and the surface oxygens are still weak, with distances of of 2.52 Å for the amide hydrogen to surface oxygen and 2.52 Å for the hydroxyl hydrogen to another surface oxygen. The adsorbed surface structure is shown in figure 5.17. Although the molecule is close to the surface, the surface structure has virtually remained the same as the pure surface after relaxation, where the F^- diagonal channel is distorted by the second F^- ion in the channel, which moves up into to the surface. The adsorption energy for this surface molecule is intermediate at -169.7 $kJmol^{-1}$.

{1 0 $\bar{1}$ 3}

The {1 0 $\bar{1}$ 3} plane is the surface with the largest surface area. The molecule again lies fairly flat on the surface but not as close to it as on the {1 1 $\bar{2}$ 1} surface. The adsorption energy of -98.4 kJmol^{-1} is the highest of the surfaces studied (table 5.1) and the adsorption surface structure is shown in figure 5.18. The molecule is closely coordinate to the surface via its carbonyl oxygen to a surface Ca at a distance of 2.21 Å. The hydroxyl hydrogen also interacts with the surface by coordinating weakly to a surface oxygen at 2.56 Å. However this H - O interaction leads to the hydroxyl oxygen coordinating to the same Ca atom that the carbonyl oxygen is already attached to, (at a distance of 2.35 Å). The carbonyl hydrogen interacts with the oxygen that protrudes from the surface at distance of 2.49 Å, but this leaves the carbonyl atom pointing away from the surface, and hence the molecule does not lie flat on the surface. The surface structure of the apatite mineral has not changed noticeably from the pure relaxed surface.

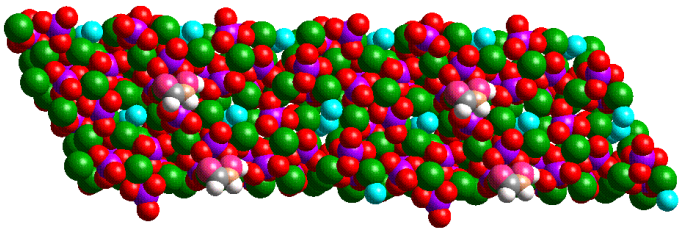

Figure 5.18: "Cis" hydroxamic molecule attached to the {1 0 $\bar{1}$ 3} surface. Key: Ca = green, P = purple, F = light blue, $O_{apatite}$ = red, C = dark grey, H = white and $O_{hydroxamic}$ = pink, N = light brown.

5.2.3 "Trans" Hydroxamic acid

From the adsorption energies in table 5.1 we realise that the adsorption of the "cis" structure of the hydroxamic acid is energetically more favourable on all the surfaces than the adsorption of the "trans" structure except for the {0 0 0 1} and the {1 0 $\bar{1}$ 3} surfaces. We now discuss the adsorption of the trans molecule on the different surfaces.

{0 0 0 1} surface

Similar to the structure on the {0 0 0 1} surface, the molecule adsorbs at an angle to the surface with the carbonyl oxygen attached to the surface Ca at a close distance of 2.19 Å. The carbonyl, amine and hydroxyl hydrogen

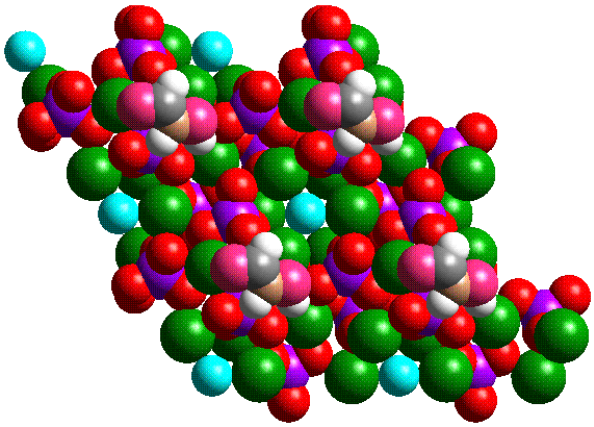

Figure 5.19: "Trans" hydroxamic molecule attached to the {0 0 0 1} surface. Key: Ca = green, P = purple, F = light blue, $O_{apatite}$ = red, C = dark grey, H = white and $O_{hydroxamic}$ = pink, N = light brown.

atoms all form weak interactions to different surface oxygens at 2.45, 2.43 and 2.45 Å respectively. The hydroxyl hydrogen interact with an oxygen in the "second layer" of the surface and the molecule is hence twisted about the axis. However, as in the "cis" structure the twist still leaves the carbonyl oxygen and hydrogen pointing away from the surface. The surface structure of the apatite has not changed significantly from the pure structure and figure 5.19 shows the plan view of the adsorption surface structure.

{1 0 $\bar{1}$ 0} surface

Unlike in the "cis" structure, the different starting configurations of the adsorption of the "trans" molecule on this surface all resulted in the same structure in which the molecule points away from the surface. The carbonyl oxygen still forms the main interaction to the surface at a short Ca - O dis-

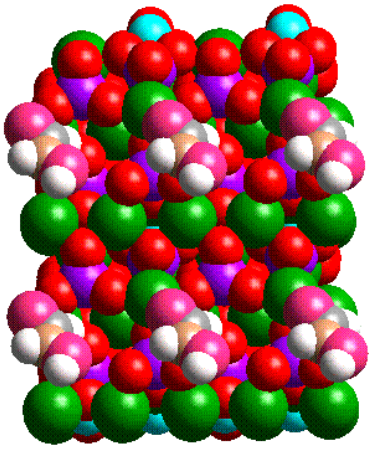

Figure 5.20: "Trans" hydroxamic molecule attached to the {1 0 $\bar{1}$ 0} surface. Key: Ca = green, P = purple, F = light blue, $O_{apatite}$ = red, C = dark grey, H = white and $O_{hydroxamic}$ = pink, N = light brown.

tance of 2.14 Å and the carbonyl hydrogen coordinates to a surface oxygen at 2.61 Å at the closest. The hydroxyl oxygen and hydrogen and amine hydrogen are pointing away from the surface making no close interaction with the surface ions, thus leaving the underlying surface structure of the apatite virtually the same as that of the pure, relaxed surface. The adsorption surface structure is shown in figure 5.20.

{1 0 $\bar{1}$ 1} surface

On the {1 0 $\bar{1}$ 1} surface the molecule adsorbs to the surface at a small angle similar to the "cis" structure. The carbonyl oxygen forms the main interaction to Ca at a short distance of 2.16 Å. This time we also notice the hydroxyl hydrogen interacting to a surface oxygen at a relatively close distance of 2.38 Å. The carbonyl hydrogen coordinates to a F^- close to the

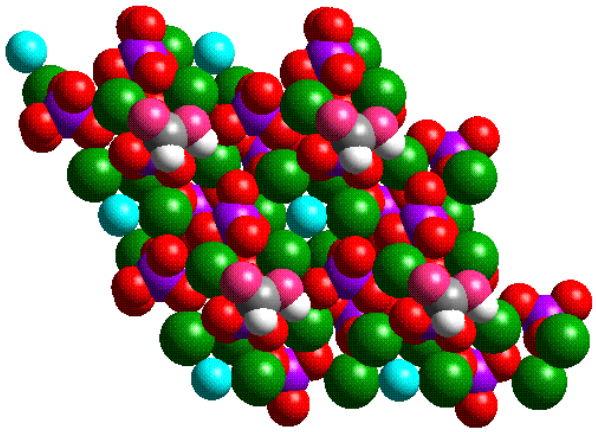

Figure 5.21: "Trans" hydroxamic molecule attached to the {1 0 $\bar{1}$ 1} surface. Key: Ca = green, P = purple, F = light blue, $O_{apatite}$ = red, C = dark grey, H = white and $O_{hydroxamic}$ = pink, N = light brown.

surface at 2.394 Å and the amine hydrogen interacts with a surface oxygen at a long hydrogen-bond distance of 2.57 Å. Unlike the "cis" structure, where the amine hydrogen did not interact with any of the surface ions, this amine hydrogen is the one interacting now, whereas the hydroxyl hydrogen is not. The adsorption structure shown as a plane view with the molecule on top of the surface is shown in figure 5.21. The surface structure of the apatite mineral has not noticeably changed from the pure, relaxed surface.

{1 1 $\bar{2}$ 0} surface

The adsorption of the "trans" form of hydroxamic acid to the {1 1 $\bar{2}$ 0} surface is by far the most energetically favourable with an adsorption energy of -172.0 kJmol^{-1}. The methanoic acid as well has shown adsorption at the same surface to be the most stable. The main interaction with the surface is

via the carbonyl oxygen to a surface Ca at a distance of 2.43 Å and also via the hydroxyl oxygen to another surface Ca at a distance of 2.49 Å, whereas in the "cis" structure it interacted with the Ca atoms in the "second layer" at shorter distances of 2.24 and 2.29 Å respectively. The hydroxyl hydrogen has come closer to the surface oxygen at a distance of about 2.49 Å and the amine hydrogen forms a weak interaction at a distance of 2.54 Å to one of the surface oxygens. The PO_4 groups on the surface have rotated, letting the oxygen protrude from the surface to interact with the hydroxyl hydrogen. However the whole apatite surface structure has not changed significantly relative to the pure, relaxed surface. The adsorption structure is shown in figure 5.22

{1 1 $\overline{2}$ 1}

Adsorption of the {1 1 $\overline{2}$ 1} surface is intermediate of other surfaces with an adsorption energy of -115.5 kJmol^{-1}. We notice that the molecule does not lie flat on the surface, is angled away from the plane. The carbonyl oxygen and the hydroxyl hydrogen are the only atoms interacting closely with the surface Ca and oxygen at distances of 2.26 Å and 2.58 Å (minimum) respectively. The hydroxyl oxygen and carbonyl hydrogen point away from the surface. Figure 5.23 shows the adsorption surface structure. There is no clear rotation of the ions in the surface due to any interactions with the molecule. Hence the surface structure is similar to the relaxed surface with the F^- ion distorted from the diagonal channel towards the surface.

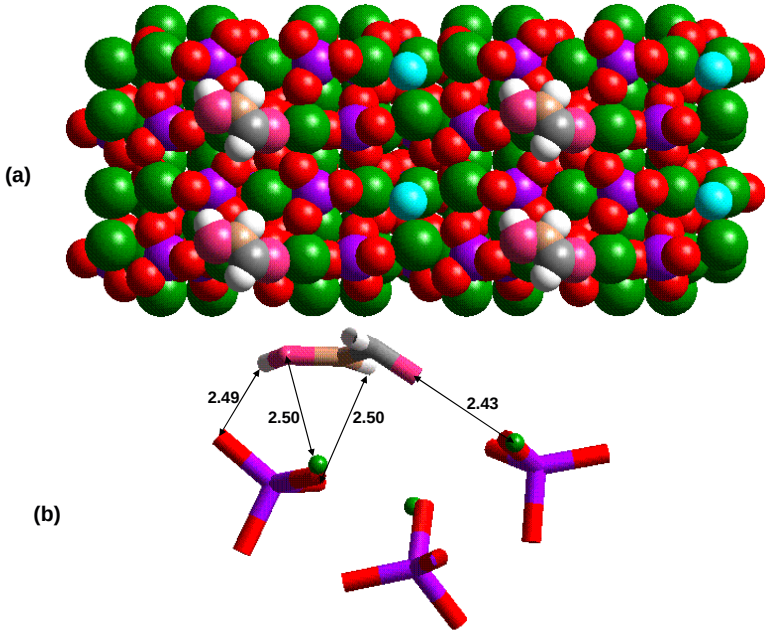

Figure 5.22: Most favourable structure of "Trans" hydroxamic molecule attached to the $\{1\ 1\ \overline{2}\ 0\}$ surface, (a) plan view and (b) a structure showing how the molecule interact with the surface ions with all bond distances shown in Å. Key: Ca = green, P = purple, F = light blue, $O_{apatite}$ = red, C = dark grey, H = white and $O_{hydroxamic}$ = pink, N = light brown.

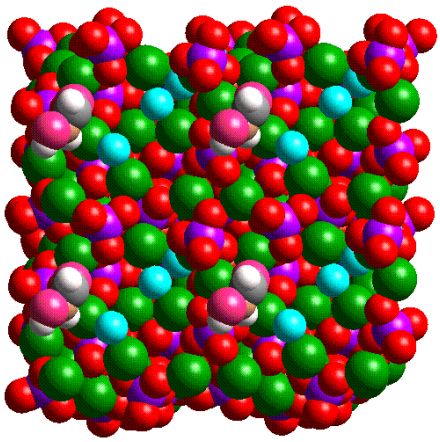

Figure 5.23: "Trans" hydroxamic molecule attached to the $\{1\ 1\ \overline{2}\ 1\}$ surface. Key: Ca = green, P = purple, F = light blue, $O_{apatite}$ = red, C = dark grey, H = white and $O_{hydroxamic}$ = pink, N = light brown.

{1 0 $\overline{1}$ 3} surface

On this plane with a large surface area, the molecule once again adsorbs flat onto the surface, suggesting interactions by most or all of the molecule's ions to the surface species. The main interaction is via the carbonyl oxygen to a surface Ca at 2.30 Å. The carbonyl and amine hydrogens interact with different surface oxygens at 2.55 Å and 2.49 Å respectively. However, despite the flat adsorption structure the hydroxyl hydrogen and oxygen do not interact closely with any of the surface apatite ions. The adsorption structure is shown in figure 5.24. The structure of the apatite surface remains virtually unchanged from the pure surface.

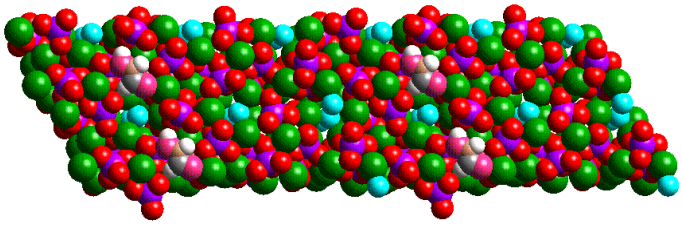

Figure 5.24: "Trans" hydroxamic molecule attached to the $\{1\ 0\ \overline{1}\ 3\}$ surface. Key: Ca = green, P = purple, F = light blue, $O_{apatite}$ = red, C = dark grey, H = white and $O_{hydroxamic}$ = pink, N = light brown.

5.2.4 Methylamine Molecule

From table 5.1 we notice that the adsorption of the methylamine molecule to the different surfaces is energetically the least favourable than the other molecules. This is the molecule in which the main adsorption to the surfaces is via the N atom of the molecule which is the only atom that can form an ionic interaction to the surface Ca ions. We next discuss how the molecule is adsorbed at each surface.

{0 0 0 1} surface

The adsorption of methylamine on this most stable surface of fluorapatite is one of the least favourable (table 5.1) of all the different surfaces investigated,

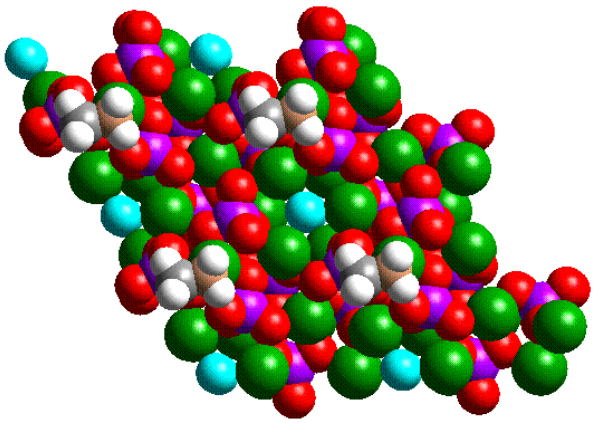

Figure 5.25: Methylamine molecule attached to the {0 0 0 1} surface. Key: Ca = green, P = purple, F = light blue, $O_{apatite}$ = red, C = dark grey, H = white and N = pink.

with an adsorption energy of -30.3 kJmol^{-1}. The molecule lies flat on the surface, attaching to a surface Ca via its N atom at a distance of 2.28 Å. The interaction of the hydrogens of the molecule to the surface oxygens is only weak. We note a distant interaction of two of the methyl hydrogens to one surface oxygen at 2.62 and 2.64 Å. The surface structure remains virtually unchanged with a slight movement of the Ca atoms on the surface upward, lengthening the distance of Ca to O to 2.39 and 2.40 Å from the Ca - O distance in the pure surface of 2.36 Å. Figure 5.25 shows the surface structure with the adsorbed surfactant.

{1 0 $\bar{1}$ 0} surface

The adsorption of the methylamine molecule at this surface is energetically more favourable as compared to other surfaces, releasing 83.0 kJmol^{-1}. Again

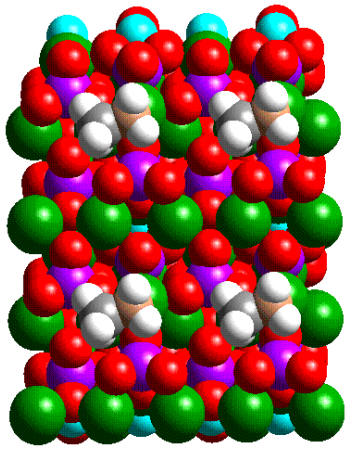

Figure 5.26: Methylamine molecule attached to the {1 0 $\bar{1}$ 0} surface. Key: Ca = green, P = purple, F = light blue, $O_{apatite}$ = red, C = dark grey, H = white and N = pink.

the molecule lies flat on the surface and becomes attached to a surface Ca by its N at a distance of 2.27 Å. There are two weak interactions of the methyl hydrogens to surface oxygens at 2.56 and 2.63 Å. Adsorption of this molecule at the surface does not affect the surface structure, which remains virtually the same. The adsorption surface structure is shown in figure 5.26.

{1 0 $\bar{1}$ 1} surface

The adsorption energy of methylamine at this surface is -52.0 kJmol^{-1}. We again see a flat adsorption configuration and as expected the molecule becomes attached to the Ca by its N at a distance of 2.27 Å. There is no strong interaction of the methyl hydrogens to the surface oxygens, with the nearest distance at 2.71 Å. Again the surface structure remains the same and figure 5.27 shows the surface with the adsorbed molecule.

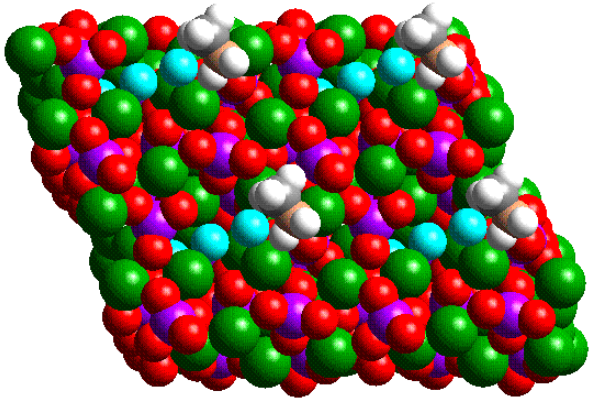

Figure 5.27: Methylamine molecule attached to the $\{1\ 0\ \bar{1}\ 1\}$ surface. Key: Ca = green, P = purple, F = light blue, $O_{apatite}$ = red, C = dark grey, H = white and N = pink.

{1 1 $\bar{2}$ 0} surface

The adsorption of the methylamine molecule at this surface is energetically the most favourable process, releasing an energy of 95.3 kJmol^{-1} upon adsorption. Similar to the other surfaces the methylamine attaches to the fluorapatite surface via its N to a surface Ca at a distance of 2.26 Å. There are two interactions of the methyl hydrogens to two different surface oxygens at closest distances of 2.65 Å each. Figure 5.28 shows the structure of the surface with the adsorbed methylamine surfactant. The surface structure remains unchanged, still showing the zigzag pattern of the fluorine atoms close to the surface.

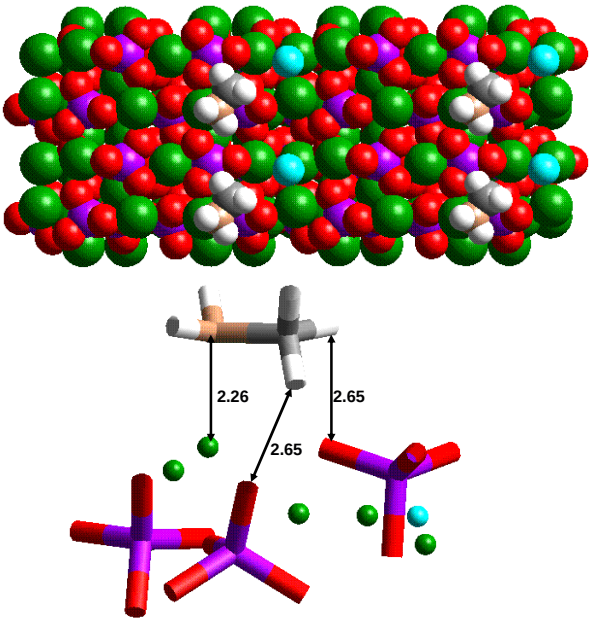

Figure 5.28: Most favourable structure of Methylamine molecule attached to the $\{1\ 1\ \bar{1}\ 0\}$ surface of apatite, (a) plan view and (b) a structure showing how the molecule attaches to the apatite surface ions with all bond distances shown in Å. Key: Ca = green, P = purple, F = light blue, $O_{apatite}$ = red, C = dark grey, H = white and N = pink.

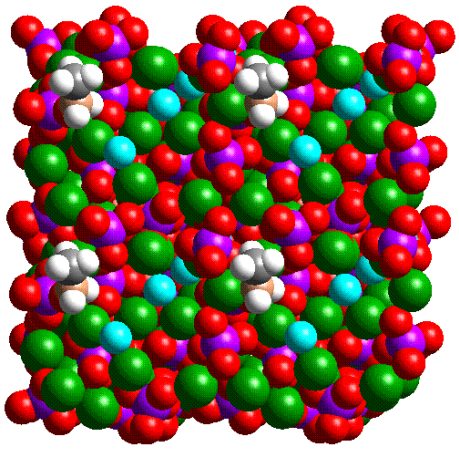

Figure 5.29: Methylamine molecule attached to the {1 1 $\overline{2}$ 1} surface. Key: Ca = green, P = purple, F = light blue, $O_{apatite}$ = red, C = dark grey, H = white and N = pink.

{1 1 $\overline{2}$ 1} surface

The {1 1 $\overline{2}$ 1} surface has some oxygens protruding from the surface and here we notice a change in the trend in which the methylamine molecule attaches to the surface. On the previous surfaces it adsorbed flat onto the surface, whereas on this plane it adsorbs an angle to the horizontal of the surface. The N to Ca interaction is again the main one at a distance of 2.31 Å. Although the molecule seems to be angled away in an attempt to interact with the protruding surface oxygens, the closest interaction is between one methyl hydrogen to an oxygen at a distance of 2.62 Å. Figure 5.29 shows the plane view of the surface with the surfactant. The surface structure remains virtually the same as the pure {1 1 $\overline{2}$ 1} relaxed surface.

{1 0 $\bar{1}$ 3} surface

As mentioned before the {1 0 $\bar{1}$ 3} surface has the largest surface area of the surface unit cell and hence the molecule has a range of surface sites available for adsorption. Some of the surface oxygens protrude from the surface, which has caused the surfactant molecule to adsorb at an angle to the surface. The molecule is attached to a surface Ca via its N at a distance of 2.29 Å and two methyl hydrogens coordinate to one of the protruding surface oxygens as well, at distances of 2.61 and 2.62 Å. However, the surface structure remains unchanged from the pure {1 0 $\bar{1}$ 3} relaxed structure and the surface with the surfactant is shown in figure 5.30 in a plan view. In addition this adsorption is the least energetically favourable as compared to the other surfaces and also the least energetically favourable of all the surfactants on all different surfaces.

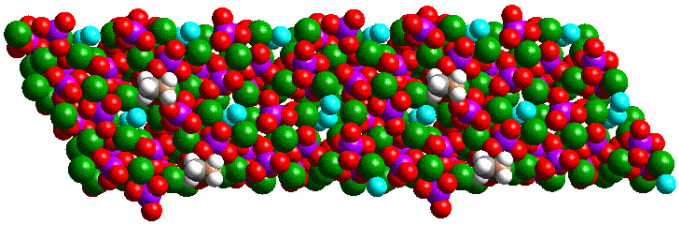

Figure 5.30: Methylamine molecule attached to the $\{1\ 0\ \bar{1}\ 3\}$ surface. Key: Ca = green, P = purple, F = light blue, $O_{apatite}$ = red, C = dark grey, H = white and N = pink.

5.2.5 "Cis" Hydroxyethanal

The hydroxyethanal molecule is different from the hydroxamic in that it has two carbon atoms forming the backbone unlike the carbon and nitrogen in hydroxamic acid. Though it has two oxygen atoms, it also has one extra hydrogen on the carbon that is bonded to the hydroxyl group. In the following sections we discuss how the "cis" and "trans" forms of the hydroxyethanal adsorb to the different surfaces.

{0 0 0 1} surface

The "cis" hydroxyethanal adsorbs flat onto the surface, releasing 142.1 $kJmol^{-1}$ with the hydroxyl oxygen and hydrogen forming a foot that has the other

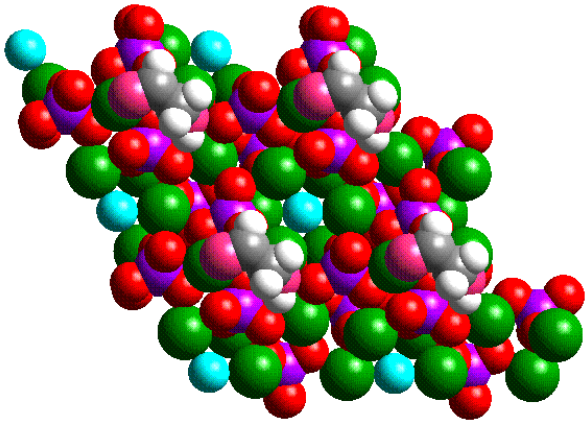

Figure 5.31: "Cis" hydroxyethanal molecule attached to the {0 0 0 1} surface. Key: Ca = green, P = purple, F = light blue, $O_{apatite}$ = red, C = dark grey, H = white and $O_{hydroxyethanal}$ = pink.

ions of the molecule lying flat along the surface (figure 5.31). The molecule has twisted away from the pure "cis" configuration with the carbonyl and hydroxyl oxygens no longer on the same side but rotated at an angle of about 90^0. The main interaction of the molecule to the surface is by its carbonyl oxygen to a surface Ca at a distance of 2.20 Å. The carbonyl hydrogen co-ordinates to a surface oxygen at a distance of 2.45 Å. We also notice an interaction of the hydroxyl oxygen to the surface, interacting to a surface Ca at a distance of 2.32 Å. There is also a weak interaction of the hydroxyl hydrogen to a surface oxygen at a distance of 2.49 Å. The other two carbonyl hydrogens are pointing away from the surface and they form no interaction with the surface ions.

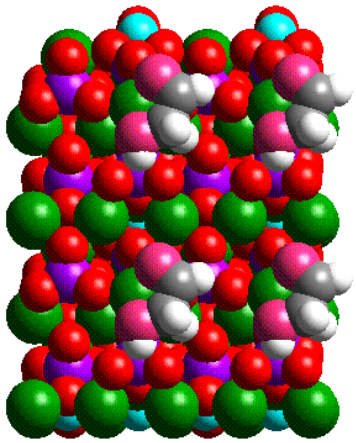

Figure 5.32: "Cis" hydroxyethanal molecule attached to the $\{1\ 0\ \bar{1}\ 0\}$ surface. Key: Ca = green, P = purple, F = light blue, $O_{apatite}$ = red, C = dark grey, H = white and $O_{hydroxyethanal}$ = pink.

{1 0 $\bar{1}$ 0} surface

The adsorption of the molecule on the $\{1\ 0\ \bar{1}\ 0\}$ surface releases a fairly low energy of 196.3 kJmol^{-1}. On this surface the molecule has kept its structural "cis" form and lies flat on the surface with the hydroxyl oxygen and hydrogen and the carbonyl oxygen on the same side along the horizontal of the surface. The carbonyl and the hydroxyl oxygens are interacting with a surface Ca in a bidentate fashion at distances of 2.36 and 2.26 Å respectively. The hydroxyl hydrogen interacts weakly with a surface oxygen at a distance of 2.50 Å, and the carbonyl hydrogen with one oxygen at a distance of 2.54 and another at 2.60 Å. The adsorption surface structure is shown in figure 5.32.

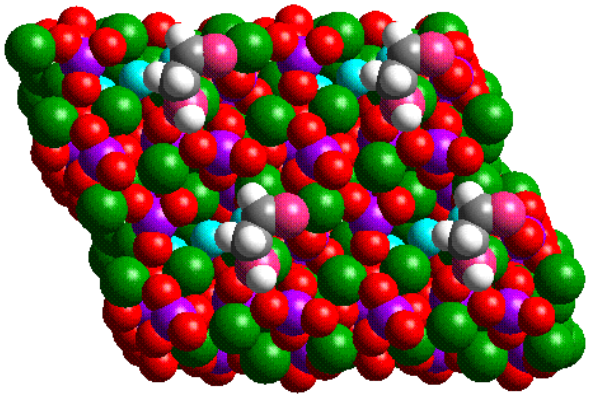

Figure 5.33: "Cis" hydroxyethanal molecule attached to the $\{1\ 0\ \bar{1}\ 1\}$ surface. Key: Ca = green, P = purple, F = light blue, $O_{apatite}$ = red, C = dark grey, H = white and $O_{hydroxyethanal}$ = pink.

$\{1\ 0\ \bar{1}\ 1\}$ surface

The energy released upon adsorption at the $\{1\ 0\ \bar{1}\ 1\}$ surface is 193.0 kJmol^{-1}. Again the molecule lies almost flat on the surface, and its structure is virtually unchanged, with only a slight twist but still with the carbonyl oxygen and the hydroxyl oxygen at the same side. It interacts with two different Ca atoms on the surface at a distance from one Ca to the carbonyl oxygen of 2.16 Å and the other Ca to the hydroxyl oxygen at a distance of 2.27 Å. The hydroxyl hydrogen coordinates to one of the surface oxygens at 2.61 Å. The structure of the surfactant on the surface is shown in figure 5.33.

$\{1\ 1\ \bar{2}\ 0\}$ surface

Adsorption of "cis" hydroxyethanal on this surface is the most favourable releasing 212.6 kJmol^{-1}. The structural "cis" form of the molecule has been

kept with the carbonyl and hydroxyl oxygens on the same side, although it appears to be slightly twisted to interact with ions on the surface. The main interaction is via surface Ca to the carbonyl and hydroxyl oxygens, which interact closely to the same Ca at a distance of 2.35 Å and 2.23Å respectively. We notice here that the shorter interaction distance is between the hydroxyl oxygen to surface Ca instead of the carbonyl oxygen as on the other surface. The carbonyl and hydroxyl hydrogens have a relatively close interaction with surface oxygens at 2.49 Å and 2.48 Å, and to lesser extent by the carbonyl hydrogen to a surface oxygen at a distance of 2.57 Å. There is a slight rotation of the surface PO_4 groups in the surface due to the interaction with the surfactant but the overall structure hasn't changed much. Figure 5.34 shows a plan view of the surface with the adsorbed molecule.

{1 1 $\overline{2}$ 1} surface

On the {1 1 $\overline{2}$ 1}, the molecule prefers to adsorb at an angle to the surface, releasing 185.8 kJmol−1. The carbonyl and the hydroxyl oxygens interact closely to two different Ca atoms with Ca - O distances of 2.32 Å and 2.82 Å respectively. The only H - O interaction is between one carbonyl hydrogen to an oxygen at 2.53 Å, whereas the hydroxyl hydrogen and the other two carbonyl hydrogen atoms are pointing away from the surface and do not interact with the surface. The structure of the surface with the adsorbate is shown in figure 5.35.

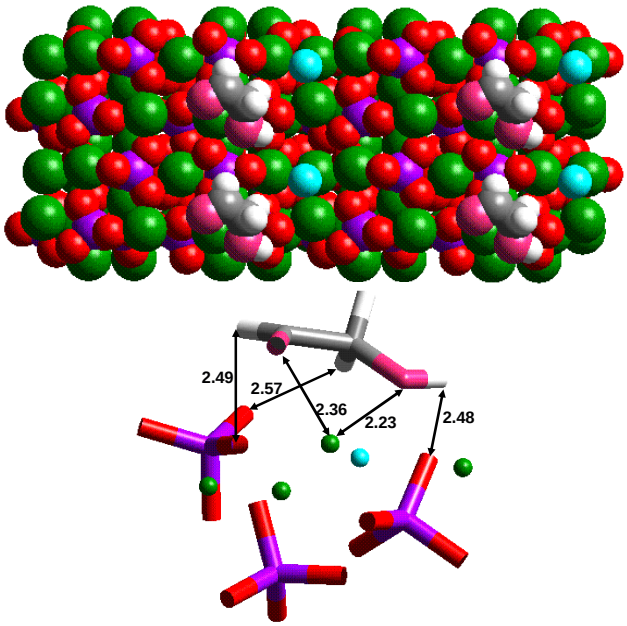

Figure 5.34: Most favourable structure of "Cis" hydroxyethanal molecule attached to the $\{1\ 1\ \overline{2}\ 0\}$ surface of apatite, (a) plan view and (b) a structure showing how the molecule attaches to the surface atoms with all bond distances shown in Å. Key: Ca = green, P = purple, F = light blue, $O_{apatite}$ = red, C = dark grey, H = white and $O_{hydroxyethanal}$ = pink.

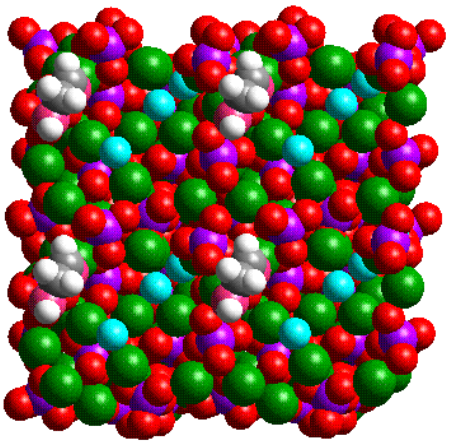

Figure 5.35: "Cis" hydroxyethanal molecule attached to the $\{1\ 1\ \bar{2}\ 1\}$ surface. Key: Ca = green, P = purple, F = light blue, $O_{apatite}$ = red, C = dark grey, H = white and $O_{hydroxyethanal}$ = pink.

{1 0 $\bar{1}$ 3} surface

Adsorption at the $\{1\ 0\ \bar{1}\ 3\}$ surface is the least favourable of the surfaces studied, with an adsorption energy of -134.8 kJmol^{-1}. The hydroxyethanal molecule prefers to adsorb virtually flat on the surface where it maintains its structural "cis" form with oxygens on the same side. The main adsorption interaction is via both the carbonyl and the hydroxyl oxygens attaching to the same surface Ca at a distance of 2.41 Å and 2.31 Å respectively. The hydroxyl hydrogen interacts with the surface oxygen that protrude from the surface at a distance of 2.568 Å. The surface structure with the molecule is shown in figure 5.36.

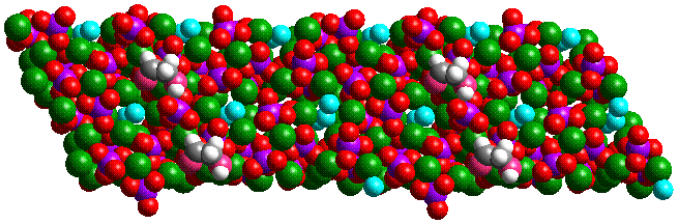

Figure 5.36: "Cis" hydroxyethanal molecule attached to the $\{1\ 0\ \overline{1}\ 3\}$ surface. Key: Ca = green, P = purple, F = light blue, $O_{apatite}$ = red, C = dark grey, H = white and $O_{hydroxyethanal}$ = pink.

5.2.6 "Trans" Hydroxyethanal

The last molecule we have investigated is the "trans" form of hydroxyethanal. Unlike the "cis" structure discussed above the two oxygens are now at opposite sides of the C - C bond, although free rotation around this bond is of course allowed. From table 5.1 we realise that between the two forms, adsorption of the "cis" structure is energetically more favourable, with an exception of three surfaces ($\{1\ 0\ \overline{1}\ 0\}$, $\{1\ 1\ \overline{2}\ 1\}$ and $\{1\ 0\ \overline{1}\ 3\}$) of the "trans" form which are energetically more favourable than the "cis" form, though structurally the molecule have rotated to adopt the "cis" form. We now discuss the adsorption at the different surfaces individually.

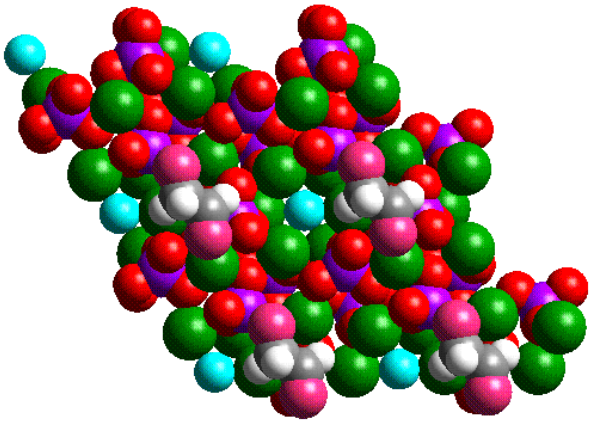

Figure 5.37: "Trans" hydroxyethanal molecule attached to the {0 0 0 1} surface. Key: Ca = green, P = purple, F = light blue, $O_{apatite}$ = red, C = dark grey, H = white and $O_{hydroxyethanal}$ = pink.

{0 0 0 1} surface

Adsorption at the {0 0 0 1} surface releases an energy of 122.8 $kJmol^{-1}$, making it the least energetically favourable of all the surfaces. The molecule is adsorbed flat onto the surface with its molecular structure kept intact. The main interaction is via the carbonyl oxygen to the surface Ca at a distance of 2.17 Å, while the carbonyl and the hydroxyl hydrogens coordinate to the surface oxygens at 2.49 and 2.57 Å respectively. The surface structure of the fluorapatite is virtually unaltered with a slight contraction of the C - O bonds from the pure relaxed surface value of 3.60 Å to new 2.39 and 2.41 Å. The surface structure is shown in figure 5.37.

{1 0 $\bar{1}$ 0} surface

The adsorption at this {1 0 $\bar{1}$ 0} surface is energetically the most favourable process of the series of surfaces, with adsorption energy of -214.6 kJmol^{-1}. The molecule is again adsorbed flat on the surface with the molecular structure virtually unchanged although the hydroxyl oxygen has twisted slightly. The molecule bridges by its oxygen atoms between two surface calcium atoms, at a distance of 2.41 by the carbonyl oxygen and at 2.40 Å by the hydroxyl oxygen. Again we notice a closer interaction with the hydroxyl oxygen than with the more exposed carbonyl oxygen. The hydroxyl hydrogen coordinates to a surface oxygen at a distance of 2.48 and one carbonyl hydrogen coordinates to different surface oxygens with the closest interaction distance of 2.52 Å. The surface adsorbate structure is shown in plan view in figure 5.38.

{1 0 $\bar{1}$ 1} surface

The molecule adsorbs at an angle to the {1 0 $\bar{1}$ 1} surface releasing an adsorption energy of 135.9 kJmol^{-1}. The Ca to carbonyl oxygen distance is 2.14 Å and other interactions involve the hydroxyl hydrogen to two different oxygens on the surface at distances of 2.49 and 2.55 Å. The carbonyl hydrogen interacts with a surface oxygen at a distance of 2.50 Å. Neither the hydroxyl oxygen or the other two carbonyl hydrogens interact with the surface ions. The figure that shows the surface with adsorbate is shown in figure 5.39.

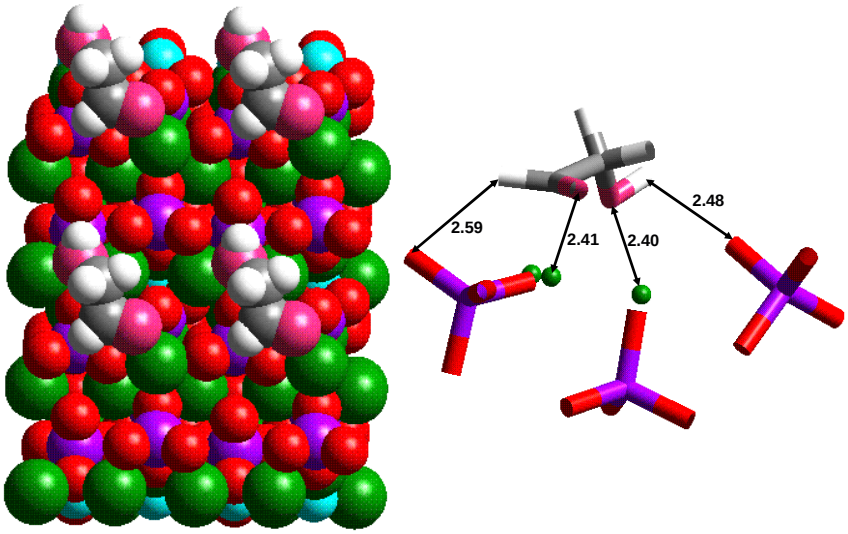

Figure 5.38: Most favourable structure of "Trans" hydroxyethanal molecule attached to the $\{1\ 0\ \bar{1}\ 0\}$ surface of apatite, (a) plan view and (b) a structure showing how the molecule attaches to the surface atoms with all bond distances shown in Å. Key: Ca = green, P = purple, F = light blue, $O_{apatite}$ = red, C = dark grey, H = white and $O_{hydroxyethanal}$ = pink.

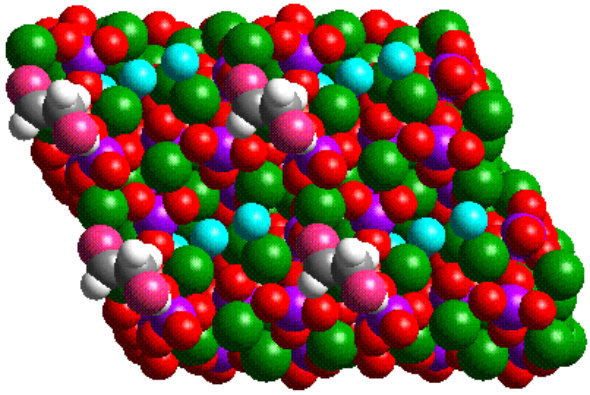

Figure 5.39: "Trans" hydroxyethanal molecule attached to the {1 0 $\bar{1}$ 1} surface. Key: Ca = green, P = purple, F = light blue, $O_{apatite}$ = red, C = dark grey, H = white and $O_{hydroxyethanal}$ = pink.

{1 1 $\bar{2}$ 0} surface

Unlike the other surfactants discussed above, where the adsorption at this surface is the most favourable, adsorption of "trans" hydroxyethanal is not the most favourable at the {1 1 $\bar{2}$ 0} surface (-159.6 kJmol^{-1}). The molecule the horizontal, where the main interaction is the carbonyl oxygen to surface Ca coordination at 2.24 Å, while weaker interactions are formed by the carbonyl and hydroxyl hydrogens to surface oxygens at 2.45 Å and 2.46 Å respectively. Figure 5.40 shows a plan view of the surface with the molecule. The hydroxyl oxygen and the two carbonyl oxygens are pointing away from the surface and do not interact with the surface ions.

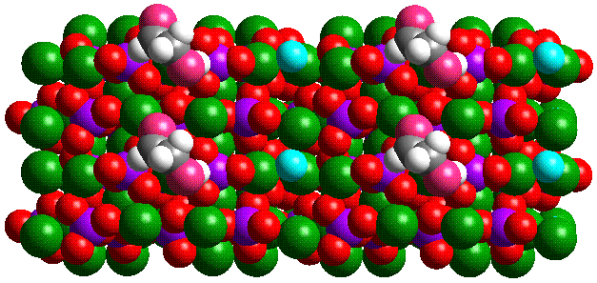

Figure 5.40: "Trans" hydroxyethanal molecule attached to the $\{1\ 1\ \overline{2}\ 0\}$ surface. Key: Ca = green, P = purple, F = light blue, $O_{apatite}$ = red, C = dark grey, H = white and $O_{hydroxyethanal}$ = pink.

$\{1\ 1\ \overline{2}\ 1\}$

The adsorption of the "trans" hydroxyethanal molecule on the $\{1\ 1\ \overline{2}\ 1\}$ is more energetically favourable releasing energy of 187.3 $kJmol^{-1}$. The molecule has virtually fallen onto the surface. It has rotated around the C - C axis and now the carbonyl and hydroxyl oxygens are on the same side which is basically the "cis" form. The two oxygens interacts with the same Ca atom on the surface. The carbonyl and hydroxyl oxygens interact with the Ca atom at 2.39 Å and 2.37 Å respectively. There is no noticeable rotations or rearrangement of the apatite surface from the pure relaxed surface. Figure 5.41 shows a plan view of the fluorapatite mineral with the adsorbate attached.

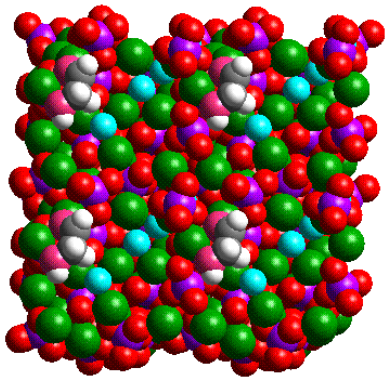

Figure 5.41: "Trans" hydroxyethanal molecule attached to the {1 1 $\bar{2}$ 1} surface. Key: Ca = green, P = purple, F = light blue, $O_{apatite}$ = red, C = dark grey, H = white and $O_{hydroxyethanal}$ = pink.

{1 0 $\bar{1}$ 3}

Figure 5.42 shows the {1 0 $\bar{1}$ 3} surface with "trans" hydroxyethanal adsorbate attached, releasing adsorption energy of 137.4 kJmol^{-1}. The molecule adsorbs flat onto the surface. The molecule has rotated around C - C axis and now the carbonyl and hydroxyl oxygens are at about 90^0 to each other a trend that we have seen with "cis" hydroxyethanal when adsorbing onto the {0 0 0 1} surface. The molecule interacts with the surface via the carbonyl oxygen to the surface Ca at a distance of 2.37 Å and also the hydroxyl oxygen to another Ca into the into the surface at 2.38 Å. The closest interaction between the hydrogens and surface oxygens is by carbonyl hydrogen and hydroxyl hydrogen which interact to the surface oxygens at an intermediate distance of 2.98 and 2.93 Å respectively. The structure of the apatite surface remains virtually unchanged from the pure, relaxed {1 0 $\bar{1}$ 3} surface.

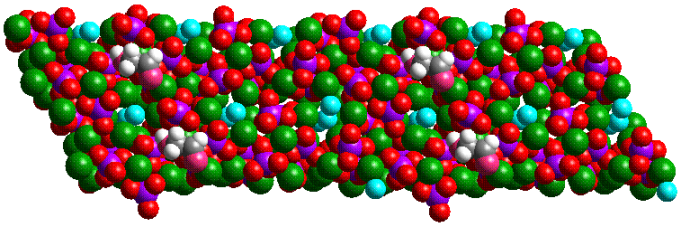

Figure 5.42: "Trans" hydroxyethanal molecule attached to the {1 0 $\bar{1}$ 3} surface. Key: Ca = green, P = purple, F = light blue, $O_{apatite}$ = red, C = dark grey, H = white and $O_{hydroxyethanal}$ = pink.

5.3 Discussion

Now that we have described the way in which each of the surfactant molecules under investigation adsorbs onto each of the different surfaces of fluorapatite, we need to identify any adsorption trends and to compare the different adsorbates. For example, from table 5.1 we see that in general the strongest adsorption is by hydroxyethanal, with adsorption energies of both "cis" and "trans" forms lower than for most of the molecules at the same surfaces. In addition, we already saw in chapter 4 that the {0 0 0 1} surface of fluorapatite is the most stable surface both when dehydrated and even more so when hydrated. Due to its stability it is relatively inactive towards all the adsorbates as is shown by relatively higher adsorption energies.

This study also supplies an indication of the effect of separating the =O and -OH groups of the organics, where in hydroxyethanal they are separated by a second carbon in the carbon back-bone and by a nitrogen in hydroxamic acid, as well as the influence of N on the strength of interaction. We have seen that for all the surfactants, the main strong interaction with the mineral surfaces is by the oxygen (mostly the carbonyl oxygen) to the calcium atoms on the surfaces. In the case of the methylamine, which does not have any oxygens, attachment is mainly via the nitrogen to the surface calcium atoms. The interaction between the surfactants hydrogen atoms and surface oxygens is fairly weak for all the surfactants, with distances between surface oxygen and hydrogen atoms well over 2.4 Å.

The methanoic acid always attaches to the surface Ca atoms via the carbonyl oxygen forming a strong interaction to the surface calcium atoms. In structures like the $\{1\ 1\ \overline{2}\ 0\}$ and $\{1\ 1\ \overline{2}\ 1\}$ planes where we find two calcium atoms on the surface not far from each other, the methanoic acid was shown to adsorb preferentially with the carbonyl oxygen atom at an intermediate position between the two calcium atoms. The hydroxyl oxygen shows no active interaction between itself and surface Ca atoms and any ancillary interactions are mainly via the hydrogens of the molecule to the surface oxygens.

Comparing the two forms ("cis" and "trans") of the hydroxyethanal and the hydroxamic acid molecules, we see that adsorption of the "cis" form is generally more exothermic than the "trans" form, because the molecules in the "cis" form interact more closely with the surfaces via both the carbonyl

and the hydroxyl oxygens, which attach either to the same Ca atom or to two different Ca atoms (2.20 to 2.40 Å). From table 5.1 we see that for the hydroxyethanal there are three surfaces ($\{1\ 0\ \overline{1}\ 0\}$, $\{1\ 1\ \overline{2}\ 1\}$ and $\{1\ 0\ \overline{1}\ 3\}$) where the "trans" from adsorbs more strongly than the "cis" form. However, in these cases, the molecule has rotated about the C - C axis to alow both of the oxygens to interact with the surface Ca atoms and it has hence taken up a "cis"-like configuration.

When we compare the adsorption of the methanoic acid to the hydroxyethanal we see that adsorption of the latter is more exothermic on all surfaces, because the extra carbon has added some flexibility to the molecule enabling it to rotate around C - C axis, to optimise adsorption of the =O and -OH although the main interaction between the surfaces and the molecule is still via the carbonyl (=O) oxygen to surface calcium atoms. Here, we only compare with the "cis" form of hydroxyethanal adsorption, both because this form generally leads to a stronger adsorption and also because the "cis" form structurally resembles the methanoic acid more closely than the "trans" form, with the only difference being the second carbon in the backbone. When we study this adsorption, we see that in addition to the active =O interaction with surface Ca we also have an active interaction of the hydroxyl oxygen to surface Ca unlike methanoic acid. The two oxygens (carbonyl and hydroxyl) generally form a strong interaction bridging between different surface Ca atoms on the $\{0\ 0\ 0\ 1\}$, $\{1\ 0\ \overline{1}\ 1\}$ and $\{1\ 1\ \overline{2}\ 1\}$ surfaces while forming bidentate interactions with the same surface Ca atom at the $\{1\ 0\ \overline{1}\ 0\}$, $\{1\ 1\ \overline{2}\ 0\}$ and $\{1\ 0\ \overline{1}\ 3\}$ surfaces.

The hydroxamic and hydroxyethanal molecules can also be compared with a view to assessing the effect of replacing one carbon by a nitrogen. We again concentrate our comparison on the most active forms of the structures, which is usually the "cis" form for both adsorbates. Adsorption of hydroxyethanal is again more exothermic, although the two molecules show similar adsorption trends when adsorbed at the surfaces: Both carbonyl and hydroxyl oxygens form active interactions with surface calcium atoms. For the hydroxamic acid we noted the interaction of the carbonyl and the hydroxyl oxygens with different surface calcium atoms at the $\{0\ 0\ 0\ 1\}$ and $\{1\ 1\ \overline{2}\ 0\}$ surfaces, and on the other four surfaces the interaction is with the same surface calcium atom. This trend is opposite to the hydroxyethanal adsorption on two surfaces, viz; $\{1\ 0\ \overline{1}\ 1\}$ and $\{1\ 1\ \overline{2}\ 0\}$ planes. The hydroxyethanal adsorbs to the same calcium via both hydroxyl and carbonyl oxygens at the $\{1\ 1\ \overline{2}\ 0\}$ surface and to different surface calcium atoms at the $\{1\ 0\ \overline{1}\ 1\}$ surface. However the molecules in both cases remain unchanged, i.e they do not rotate around the C-C or C-N bond. We also note that the "cis" hydroxyethanal adsorbs almost always virtually flat onto the surfaces whereas the hydroxamic acid adsorbs at an angle. The higher exothermicity of adsorption of hydroxyethanal is due to the shorter interaction distances of the hydroxyl and carbonyl oxygens to the surface calcium atoms.

The methylamine molecule has only one functional group (the amine) and hence cannot form multiple interactions on the surface like the hydroxyethanal and the hydroxamic acid. Although methanoic acid also has the one carboxylic acid functional group, it consists of the two oxygen atoms,

which can both form strong interactions to the surface Ca atoms. As a result adsorption of methylamine is least exothermic of the adsorbates at all the surfaces. Only the -NH_2 functional group interacts with the surfaces and these interactions are not as strong as those formed by the oxygen ions of the functional groups of the other adsorbates. In addition, there is steric hindrance by the hydrogen atoms of the -NH_2 group which make the nitrogen atom less accessible than the oxygen atoms in carbonyl and hydroxyl groups.

Thus the nature of the organic molecule and the number of interactions that the molecules make with the surfaces play an important role in the strength of adsorption of the molecules to the mineral surfaces.

Chapter 6

SOLID/SOLID INTERFACES BETWEEN FLUORAPATITE AND α-QUARTZ

Understanding the nature of the solid/solid interface between complex materials is of increasing significance in itself. Previous computational studies of solid-solid interfaces, for example grain boundaries in geological systems,[145, 146], and thin films of catalytic materials,[147], show that the authors always started their calculations from unrelaxed interfaces, that is where the two blocks of material were initially fitted together as bulk-terminated blocks before, only then, allowing the interface to relax in an energy minimization or molecular dynamics simulation. However, in experiment, the substrate relaxes instantaneously upon formation of the surface,[148] well before attachment of the film and we therefore investigated whether pre-relaxation of the substrate before attachment of the film significantly affected the interfacial structures and energies or whether the final structures and energies would be the same, regardless of the starting configuration of the substrate

surface. In the former case we would need to include surface pre-relaxation in these and future interfacial calculations to ensure that the correct structures and energies are calculated. We hence considered both the interfaces between substrate and film starting from a bulk-terminated α-quartz surface and from a pre-relaxed α-quartz surface.

We are interested in the interfaces between apatite and silicate implants. We have concentrated on α-quartz as a model for a range of silicate materials and silica-rich bio-glasses.

In this chapter we report detailed atomistic models for the interfaces between apatite thin films and α-quartz, based on the atomistic simulation methods described in chapter 2. In addition to the epitaxial fitting of apatite thin films to dry quartz surfaces, we have also investigated the effect of hydration of the quartz substrate on the interfacial structures and energies.

6.1 Quartz surfaces

Different surfaces of both fluorapatite and α-quartz have been checked as likely candidates for the interface studies. In this kind of simulation study, it is important that the surfaces of the two materials have lattice vectors that are compatible as the apatite thin film will have to accommodate itself to the substrate lattice. The $\{0\ 0\ 0\ 1\}$ fluorapatite and the $\{0\ 0\ 0\ 1\}$ α-quartz surfaces have compatible lattice vectors as well as the $\{1\ 0\ \overline{1}\ 1\}$ fluorapatite and $\{1\ 0\ \overline{1}\ 0\}$ α-quartz planes.

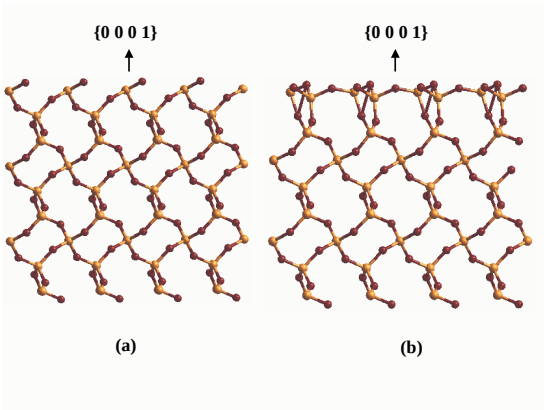

Figure 6.1: The (a) unrelaxed and (b) relaxed α-quartz $\{0001\}$ surface, showing low-coordinated surface Si and O species on the unrelaxed surface, which upon relaxation have regained their four-fold and two-fold bulk coordination number for Si and O respectively (Si = yellow, O = maroon).

6.1.1 Dry Surfaces

In the bulk terminated $\{0\ 0\ 0\ 1\}$ surface of α-quartz, the surface silicon atoms are only coordinated to three oxygen atoms, while the oxygen atoms are forming just a single bond to one surface silicon atom each as shown in Figure 6.1(a). Upon relaxation the surface Si and O atoms form bonds parallel to the surface and hence regain their bulk coordination numbers of four and two respectively, which is shown in figure 6.1(b).[28] As a result of this surface relaxation and recovery of the bulk coordination of the surface ions, the unrelaxed and relaxed surfaces are not identical and we may therefore expect that they will interact with the apatite films in different ways.

Figure 6.2 shows the bulk terminated (unrelaxed) structure of the $\{1\ 0\ \bar{1}\ 0\}$ surface of α-quartz. The structure shows some dangling bonds of Si

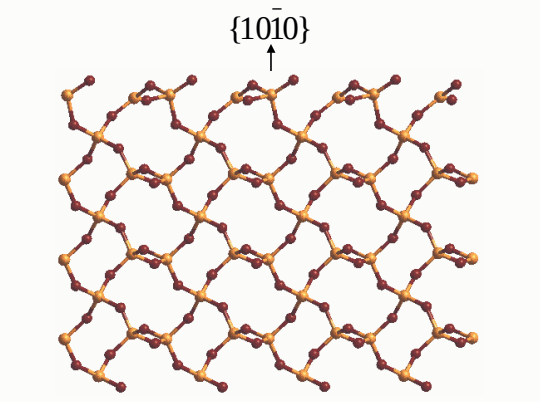

Figure 6.2: Figure shows the unrelaxed α-quartz $\{10\bar{1}0\}$ surface, showing low-coordinated surface Si and O species, which remain the same upon relaxation (Si = yellow, O = maroon).

and O at the surface. However, on this surface the surface Si and O remain under-coordinated upon geometry optimisation.

6.1.2 Hydrated Surfaces

We also investigate the hydrated surfaces of α-quartz as substrates for the apatite thin films. As was shown by de Leeuw *et al*[28], hydration of α-quartz surfaces, with dissociated water is more favourable than associative adsorption of water and we have thus based our simulations of hydrated surfaces of α-quartz on these hydroxylated surfaces. We first establish which atoms are clearly exposed at the bulk terminated surfaces of α-quartz. For example, there are four O and four Si atoms at the surface of the $\{0\ 0\ 0\ 1\}$ simulation cell. Now we attach the $(OH)^{1.4-}$ species through its O to the surface Si, because the surface Si in the unrelaxed surface are three fold

coordinated to oxygen atoms instead of a tetrahedral coordination as it is in the bulk crystal of α-quartz. The hydroxyl ions are attached to these reactive surface Si and protons are attached to surface oxygen atoms.

The $H^{0.4}$ is thus attached to the surface O^{2-} but for practical reasons these surface O^{2-} need to be changed to $O^{1.4-}$, as discussed in chapter 3, where we discussed the potential model. Thus this will leave the surface with a neutral charge. The surface with the adsorbed OH and H ions is then geometry optimised by energy minimisation. The resulting relaxed hydroxylated surface is the one we use for the interface calculations with fluorapatite thin films.

6.2 Interfaces of Fluorapatite Thin Film with Dry α-Quartz Surfaces

6.2.1 Lateral Scanning of Apatite Film Over Quartz Surface

Figure 6.3 shows how the apatite thin film was brought down upon the unrelaxed quartz {0 0 0 1} surface. Before energy minimisation of the interfacial system, the apatite film was kept at a constant height above the surface, but moved laterally with respect to the quartz surface without relaxation of the substrate or film, that is for the interface shown in figure 6.3, the apatite film would be moved systematically in the a- and b-directions and the interfacial energy for this unrelaxed system would be calculated for a series of points on a grid. The grid was determined by the surface lattice vectors of the system in the a- and b-direction, in this case 9 Å in the a-direction and

8 Å in the b-direction and the interfacial energy was calculated at intervals of 1 Å. This scan thus supplied us with an interfacial energy at each point on the grid, hence identifying the lowest energy relative lateral displacement of the film with respect to the substrate in the unrelaxed system. This was then taken as our starting point for our energy minimisation calculation of the substrate/film interface.

We studied a range of rotations of the film with respect to the underlying substrate for each interfacial system and figure 6.4 shows the energy contour map obtained from the lateral scan of one of the interfaces. For the 0^0 rotated interface shown in figure 6.3 the lowest energy displacement was at a = 3 Å and b = 3 Å. The displacements for the other rotations were all different, i.e. for 60^0, a = 6 Å and b = 1 Å, for 120^0, a = 5 Å and b = 7 Å for 180^0, a = 1 Å and b = 1 Å, for 240^0, a = 5 Å and b = 7 Å, for 300^0, a = 1 Å and b = 1 Å. In addition, the energy contour map of the unrelaxed interfacial energy with respect to lateral position of the film above the substrate, shown in Figure 6.4 for the 0^0 rotated interface of figure 6.3, also identifies lowest energy pathways for moving the film over the substrate.

The same lateral scanning operation has been applied to the interface of the fluorapatite $\{1\ 0\ \overline{1}\ 1\}$ plane with the α-quartz $\{1\ 0\ \overline{1}\ 0\}$ surface. For this interface only two rotations were found to be feasible for the calculations, namely: at 0^0 and 180^0. The lattice vectors of the two blocks of material in the other rotations were not compatible. The grid in this case was based on lattice vectors a=10 Å and b=11 Å and the displacements for the rotations were found to be: for 0^0, a=4 Å, and b=1 Å and for 180^0, a=9 Å and b=1Å.

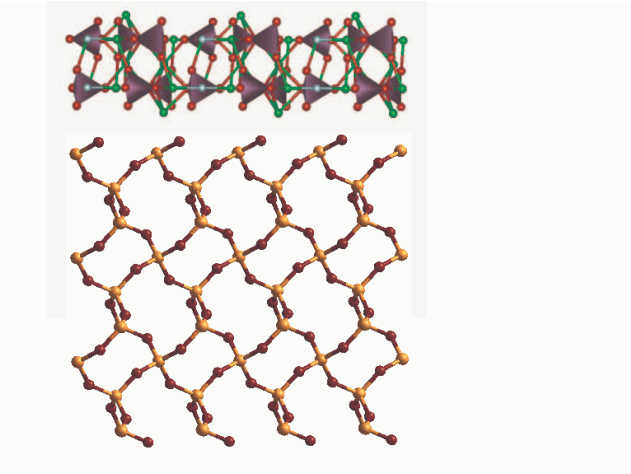

Figure 6.3: Diagram showing how a thin layer of {0001} fluorapatite surface is brought down upon the unrelaxed quartz {0001} surface (Si = yellow, O_{quartz} = maroon, $O_{apatite}$ = red, F = pale blue, P = purple, Ca = green, PO_4 group shown as tetrahedra).

Once the most energetically favourable initial lateral film/substrate orientation was thus identified, the initial height above the surface was varied in a series of calculations to check that this parameter did not affect the final energy and to ensure that the lowest energy configuration is obtained for each rotation. A full geometry optimisation was performed to obtain the energy of the relaxed interfacial system, where the optimisation algorithm used is the Newton-Raphson variable matrix method, which takes into account not only the first derivative of the energy with respect to ion position (the forces on the ions during minimisation), but also the second derivative of the energy

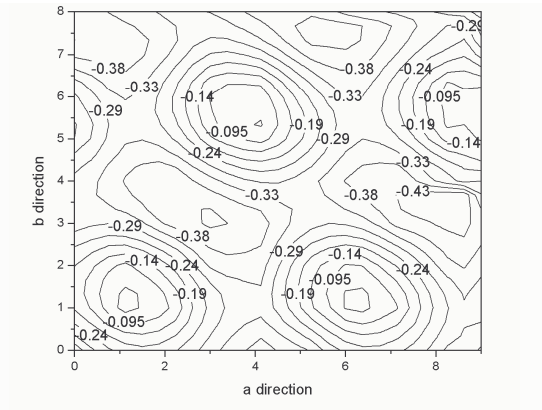

Figure 6.4: Contour map of the interfacial energies of the unrelaxed quartz/apatite system with respect to lateral position, from a horizontal scan of the unrelaxed 0^0 rotated apatite film over the unrelaxed quartz {0001} surface (energies shown in eV, the units on the axes are distances in Å along the surface a- and b-vectors of the simulation cell).

as described in chapter two.

During geometry optimisation, not only was the apatite film free to move in any direction with respect to the underlying quartz surface, but all atoms in the apatite film and in a quartz surface region up to about 22 Å into the bulk (region I) were also completely unconstrained so as not to prejudice the geometry of the interface. The complete process was then repeated for the series of rotations of the apatite thin films with respect to the quartz substrate and the adhesion energies were calculated (Table 6.1).

The same procedure as described above has been followed on all the interfaces of the different surfaces that will be discussed, (viz: fluorapatite $\{0\ 0\ 0\ 1\}$ thin film onto α-quartz $\{0\ 0\ 0\ 1\}$ surface, fluorapatite $\{1\ 0\ \overline{1}\ 1\}$ thin film onto α-quartz $\{1\ 0\ \overline{1}\ 0\}$ surface) but the lateral scanning was carried out

only on an interface of a single layer of thin film and the result transferred to thicker layers as well, because the film thickness of the unrelaxed film in the direction perpendicular to the interface does not affect the stability parallel to the interface.

6.2.2 Fluorapatite {0 0 0 1} Film on Unrelaxed Quartz {0 0 0 1} Surface

Both α-quartz and apatite have a hexagonal crystal structure, where the basal {0 0 0 1} planes were shown to be the dominant surfaces[3, 28, 2] and also in chapters 4 and section 6.1 of this work. We therefore decided to first use the α-quartz {0 0 0 1} surface as the substrate for the layer growth of apatite material, also in the {0 0 0 1} orientation although the apatite thin films have to accommodate themselves to the α-quartz lattice vectors.
α-Quartz has lattice parameters of a = b = 4.913 Å, c = 5.404 Å, while the lattice parameters of fluorapatite are a = b = 9.370 Å, c = 6.880 Å.[29] After relaxation of the bulk, the lattice vectors of the fluorapatite {0 0 0 1} surface simulation cell are $\mathbf{x} = \mathbf{y} = 9.365$ Å, and $\mathbf{z} = 6.868$ Å and those of α-quartz are $\mathbf{x} = \mathbf{y} = 4.866$ Å and $\mathbf{z} = 5.375$ Å. We therefore had to grow the quartz substrate to a 2x2 surface supercell, $\mathbf{x} = \mathbf{y} = 9.732$ Å, which could accommodate an overlayer of apatite with a misfit of -3.78%. We only need to consider the **x**- and **y**-lattice vectors as they are the ones directly involved in the interface whereas the **z** vectors point away from the interface itself into the material. We calculated the adhesion energies for the interfaces as a function of rotation of the apatite layer with respect to the underlying quartz

Table 6.1: Adhesion energies (γ_{adh} in Jm^{-2}) for the interfaces between single and double films of fluorapatite at the unrelaxed α-quartz substrate.

	Unrelaxed	**α-quartz surface**
Rotation of thin film	Thin layer	Thick layer
$0^0/360^0$	0.74	1.31
60^0	0.90	1.50
120^0	1.07	1.62
180^0	0.64	1.53
240^0	1.22	1.62
300^0	0.72	1.72

substrate. The adhesion energy γ_{adh} is a measure of the stability of the interface with respect to the free quartz {0 0 0 1} surface and bulk apatite, which is calculated as follows:

$$\gamma_{adh} = \frac{E_{int} - (E_{surf-quartz} + E_{bulk-apatite})}{A} \tag{6.1}$$

where E_{int} is the energy of the interfacial system, $E_{surf-quartz}$ is the energy of the free quartz surface, and $E_{bulk-apatite}$ is the energy of the relevant number of bulk apatite units in the film and A is the area of the interfacial region. We have explored six different angles of rotation on which the apatite {0 0 0 1} thin film can be placed upon the {0 0 0 1} surface of α-quartz.

The calculated adhesion energies for the thin film on the unrelaxed {0 0 0 1} quartz substrate are shown in table 6.1 and for the pre-relaxed

quartz substrate they are shown in table 6.2, where the most stable interface has the lowest positive value of γ_{adh}. We calculated the adhesion energy with respect to the apatite units in the bulk material as we are interested in the formation and stability of a thin apatite film on the substrate surface, rather than the intergrowth of two materials. For example, if we were to investigate the intergrowth of two rock minerals in geological applications, the calculation of the interfacial stability with respect to the free surfaces of both quartz and apatite would be more appropriate. However, this calculation would only add a constant term to each of the different columns of adhesion energies in Table 6.1 and 6.2, rather than alter the relative energies and hence stabilities of the interfaces, which would remain the same. We therefore do not quote both values.

Thin Layer of Fluorapatite 180^0 Rotation on the Unrelaxed {0 0 0 1} surface

We first fitted a single apatite layer to the quartz substrate, where the quartz surface was kept as a bulk-terminated plane, which had not been relaxed before creating the interface. Comparing the structures of the interfaces due to the different rotations, we observe that the stability of the interface as given by its adhesion energy depends on a number of factors. The number of bonds that can form between the calcium and oxygen ions of the apatite film to oxygen and silicon ions respectively in the quartz substrate plays a role, but more so the lengths of the bonds. The most stable interface at a rotation of 180^0, shown in figure 6.5, contains both a large number of bonds between the film and substrate, which are also short ($O_{apatite}$ - Si = 1.90, 1.92

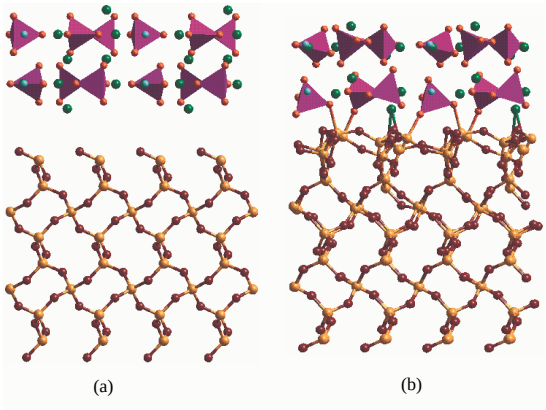

Figure 6.5: The geometry optimised structure of a single layer of apatite {0001} film grown onto the unrelaxed quartz {0001} surface at a rotation of 180^0, showing rotation of the PO_4 groups and distortion of the F chains (Si = yellow, O_{quartz} = maroon, $O_{apatite}$ = red, F = pale blue, P = purple, Ca = green, PO_4 groups shown as tetrahedra).

and 2.13 Å, Ca - O_{quartz} = 2.34-2.46 Å) and often the oxygen and calcium ions of apatite form multiple bonds across the interface. The other factor, which determines the stability of the interface is the size of the empty region between substrate and film. In the 180^0 rotation, the film fits closely to the substrate and the interfacial region is relatively dense. For example, the gap between the topmost quartz silicon atom and the bottom calcium atom in the apatite layer is only 1.61 Å wide in the c-direction only, (the closest actual Ca - Si distance is 3.47 Å). The structure of the apatite thin film after relaxation of the interface is heavily distorted as is seen in figure 6.5 when compared to the one before minimisation shown in figure 6.3. The fluoride channels have become distorted in the apatite thin film, away from the straight channels in the c-direction of the bulk apatite structure, and the PO_4 groups have

rotated at the interface.

Thin Layer of Fluorapatite 240^0 Rotation

In the less stable interfaces, larger interfacial cavities and channels are formed, which destabilize these interfacial regions. The same effect is seen to occur in rock grain boundaries, where large cavities lead to unstable grain boundary regions, which only become stable when the cavities collapse or are filled with interstitial species such as water molecules.[145]

The interface at 240^0 is the least energetically favorable rotation as shown in table 6.1. Again, this interface has many interactions across the boundary with interatomic distances of Ca - O_{quartz} between 2.21 and 2.96 Å and bond distances between Si and $O_{apatite}$ of 1.81 and 1.82 Å. However the interfacial space between the two materials is open, compared to the more stable 180^0 interface with a distance between the bottom-most Ca of apatite and top-most Si of quartz of 2.331 Å. Again the thin film is highly distorted which may add to the instability of the interface. Figure 6.6 shows the structure of the interface at a 240^0 rotation. And as we can see, the oxygen atoms of both quartz substrate and apatite layer are located in the interfacial area, forming a network of close interactions between both materials. As to the other less stable interfaces; the 0^0 rotational interface forms only two bonds per apatite unit cell to the underlying quartz structure, one O-Si bond of 1.80 Å and one Ca-O bond of 2.36 Å, while the 60^0 rotation forms several Ca-O and O-Si bonds, which are all, however, longer than 2.50 Å and 1.84 Å respectively and as we can see from Table 6.1, the 60^0 interface is much

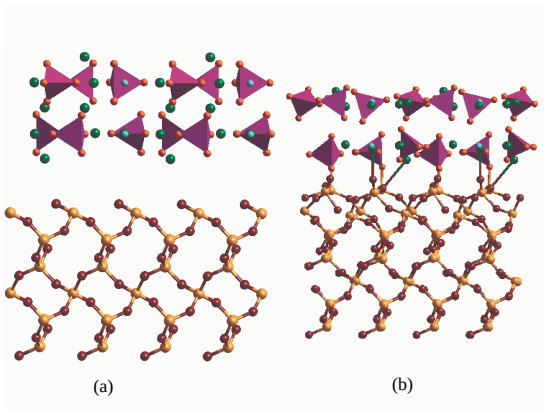

Figure 6.6: The geometry optimised structure of a single layer of apatite {0001} film grown onto the unrelaxed quartz {0001} surface at a rotation of 240^0, showing rotation of the PO_4 groups and distortion of the F chains (Si = yellow, O_{quartz} = maroon, $O_{apatite}$ = red, F = pale blue, P = purple, Ca = green, PO_4 groups shown as tetrahedra).

less stable.

Thick Layer of Fluorapatite 0^0 Rotation

Following our simulations of single apatite layers on the quartz substrate, we also studied the interfacial structures and energies of a series of thicker apatite films of two unit cells deep (14 Å). From the adhesion energies in Table 6.1, it is clear that the effect of the increased thickness is to destabilize the interfaces in all cases and also to alter the relative stabilities of the rotations. We see that the 0^0 rotation, rather than the 180^0 rotations in the thin layer, is now the preferred configuration for the apatite film. The spread in adhesion energies is less than for the single apatite layer, varying by about 15% from the average of 1.55 Jm^{-2}, whereas for the single layer the difference

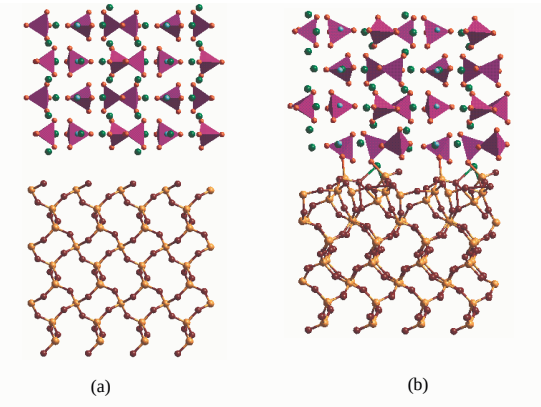

Figure 6.7: Geometry optimised structure of a double layer of apatite {0001} film grown onto the unrelaxed quartz {0001} surface at a rotation of 0^0 (Si = yellow, O_{quartz} = maroon, $O_{apatite}$ = red, F = pale blue, P = purple, Ca = green, PO_4 groups shown as tetrahedra).

between the average adhesion energy of 0.88 Jm^{-2} and the lowest (180^0) of 0.63 Jm^{-2} is 27%. The higher adhesion energies and their relative invariance across the series of rotations is due to a lesser flexibility of the double apatite layer. The ions in the thicker film are more constrained to remain in an environment, which is approximating the apatite crystal structure, although stretched to accommodate the underlying quartz lattice. In the single layers the PO_4 groups had rotated freely and the Ca and F ions had also shifted, in the a- and b-directions, as shown for example in figure 6.6, but in the thicker film the basic structure of the apatite lattice remains intact and is similar to the unrelaxed structure of figure 6.3. Figure 6.7 shows the interfacial structure of the double apatite layer where we see that the PO_4 groups are no longer rotated with respect to the apatite lattice and the fluoride ions

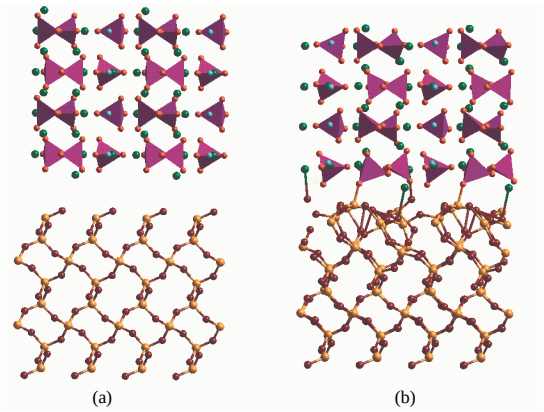

Figure 6.8: Geometry optimised structure of a double layer of apatite {0001} film grown onto the unrelaxed quartz {0001} surface at a rotation of 300^0 (Si = yellow, O_{quartz} = maroon, $O_{apatite}$ = red, F = pale blue, P = purple, Ca = green, PO_4 groups shown as tetrahedra).

remain in regular columns. The distance between the top-most Si and the bottom Ca is 0.91 Å while we have the Ca-O_{quartz} bonds at 2.37 Å and 2.51 Å. The Si-$O_{apatite}$ bond lengths are 1.77 Å and 1.95 Å.

Thick Layer of Fluorapatite 300^0 Rotation

The least stable interface for the double layer is the 300^0 rotation and we show its structure in figure 6.8. Similar to the 0^0 rotation, the apatite film is not as heavily as the single layers were distorted. The structure of the fluoride channels is practically the same as in the apatite structure before the formation of the interface. However, the surface has Ca - O_{quartz} distances of 2.44 Å and only one long Si - $O_{apatite}$ bond distance of 1.79 Å. The interface is farther apart than in the most stable rotation with a distance between the top-most Si and bottom Ca of 1.45 Å.

6.2.3 Fluorapatite {0 0 0 1} Film on Relaxed Quartz {0 0 0 1} Surface

We next considered growing single and double apatite layers on a pre-relaxed quartz surface and comparing these calculations with the previous simulations of the bulk-terminated substrate surfaces. As shown in section 6.1 and figure 6.1, the main difference between the unrelaxed and relaxed quartz surfaces is the presence of dangling bonds on the unrelaxed surface of quartz, where the surface silicon and oxygen atoms have a lower coordination than in the bulk material. A pre-relaxed substrate is more realistic and we assumed that the two surfaces might react differently to the apatite film which is why we investigated both cases. The adhesion energies are shown in table 6.2.

Thin Layer of Fluorapatite 240^0

As a result of the dangling bonds, the unrelaxed quartz surface is highly reactive towards the apatite film, forming bonds between the under-coordinated surface species to oxygen and calcium atoms in the apatite film, discussed above and shown for example in figure 6.5. However, we saw that this enhanced reactivity of the substrate leads to irregular and semi-distorted structures of the apatite films and also an irregular surface of the α-quartz. Conversely, when the quartz surface is relaxed before attachment of the apatite thin film, the structure of the quartz surface does not alter significantly upon adhesion of the apatite film. The silicon and oxygen atoms retain their four- and two-fold coordination to the O and Si atoms in the quartz surface, rather

Table 6.2: Adhesion energies (γ_{adh} in Jm^{-2}) for the interfaces between single and double films of fluorapatite at the pre-relaxed α-quartz substrate, calculated with respect to the relaxed quartz surface and bulk apatite (equation 6.1).

	Relaxed	**α-quartz surface**
Rotation of thin film	Thin layer	Thick layer
$0^0/360^0$	0.58	0.83
60^0	0.57	1.05
120^0	0.57	0.89
180^0	0.73	0.83
240^0	0.55	0.82
300^0	0.65	1.11

than form bonds to calcium and oxygen atoms in the apatite thin film. The interactions which are formed between the quartz surface and the apatite thin film are therefore much weaker as they are over and beyond the normal coordination number of the oxygen and silicon atoms in the substrate. Si-$O_{apatite}$ (greater than or equal to 2.02 Å) and Ca-O_{quartz} (greater than or equal to 2.52 Å) distances are much longer than we found when the substrate was not pre-relaxed, shown for example in the most stable 240^0 (figure 6.9). The interfacial gap between the two materials is also much wider. The closest distance between oxygen atoms of the two materials is 1.79 Å in the c-direction with the actual closest O_{quartz} - $O_{apatite}$ distance at 2.78 Å, whereas for the unrelaxed substrate we found that the O_{quartz} - $O_{apatite}$ distance was 1.61 Å.

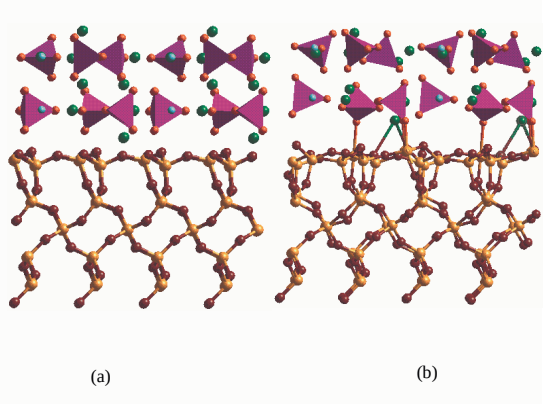

Figure 6.9: The geometry optimised structure of a single layer of apatite {0001} film grown onto the relaxed quartz {0001} surface at a rotation of 240^0, showing Ca-O_{quartz} distances up to 2.5 Å and $O_{apatite}$-Si distances up to 3.0 Å. (Si = yellow, O_{quartz} = maroon, $O_{apatite}$ = red, F = pale blue, P = purple, Ca = green, PO_4 groups shown as tetrahedra).

It is also noteworthy that the adhesion energies fall in a fairly narrow band, for example within 9% of the average adhesion energy for the thin layer.

Thin Layer of Fluorapatite 180^0 Rotation

The least stable interface rotation is 180^0, shown in figure 6.10. The two minerals in this interface are far apart when compared to the most stable 240^0 rotation, with the distance between the bottom-most Ca of apatite and the top-most Si of α-quartz being 2.16 Å, while for the most stable interface it is 2.03 Å. There is only one Si - $O_{apatite}$ bond at 2.03 Å and the closest Ca - O_{quartz} distances are at 2.72 Å and 2.97 Å. The channel with F^- ions is twisted to the side when we compare it with the structure of the interface before minimisation. We also see that the short Si-$O_{apatite}$

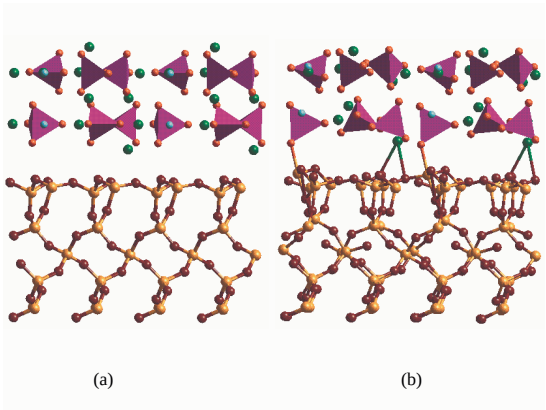

Figure 6.10: The geometry optimised structure of a single layer of apatite {0001} film grown onto the relaxed quartz {0001} surface at a rotation of 180^0, showing Ca-O_{quartz} distances up to 2.97 Å and Si-$O_{apatite}$ distances up to 2.03 Å. (Si = yellow, O_{quartz} = maroon, $O_{apatite}$ = red, F = pale blue, P = purple, Ca = green, PO_4 groups shown as tetrahedra).

distances as compared to the most stable 240^0 rotation cause the one Si to become five coordinated which contributes to the instability of the interface. Five coordinated Silicon is not unknown in high pressure phases or glassy silicates, but it is not the preferred coordination for silicon.

Thick Layer of Fluorapatite 240^0 Rotation

When the thickness of the apatite film is increased from a single to a double layer, this does not effect a significant change in the structure of the apatite film, opposite to what was seen at the unrelaxed quartz surface. As a result the same rotation of 240^0, shown in Figure 6.9 for the thin film, remains the preferred configuration. We see from Table 6.2 that despite the lower reactivity of the relaxed quartz surface and the more open structure of the interfacial

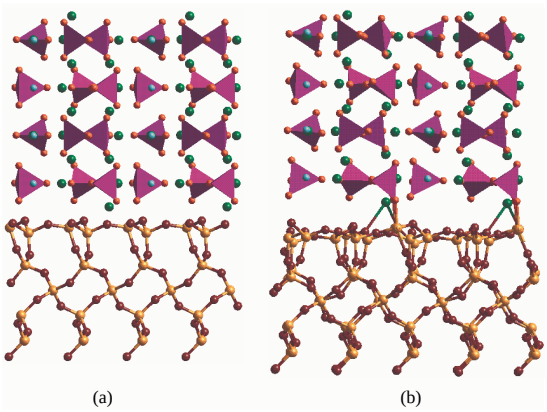

Figure 6.11: The geometry optimised structure of a double layer of apatite {0001} film grown onto the relaxed quartz {0001} surface at a rotation of 240^0 (Si = yellow, O_{quartz} = maroon, $O_{apatite}$ = red, F = pale blue, P = purple, Ca = green, PO_4 groups shown as tetrahedra).

region, the energies of adhesion of the double layers to the pre-relaxed quartz surface are generally lower than for the unrelaxed quartz surface and hence these interfaces are more stable.The enhanced stabilities of these interfaces and the similarities in the interfacial energies are due to the fact that the apatite layer attached to the pre-relaxed quartz surface shown in Figure 6.11 for the most stable 240^0 rotation, has regular Ca - O_{quartz} distances of about 2.4 Å and Si - $O_{apatite}$ distances of 1.9 Å. In addition, neither the apatite nor the quartz surface are significantly distorted.

From table 6.2 we see that for the most stable 240^0 rotation, the adhesion energy of the interface with a thin layer is 0.55 Jm^{-2} and 0.82 Jm^{-2} for the double layer. Hence to get the second layer of apatite attached to the interface we only need 0.27 Jm^{-2}, i.e. half the energy for the first layer and

the layer growth of apatite on the substrate is thus convergent in energy. This behaviour, unlike the adhesion of apatite layers at the unrelaxed quartz surface where the rotation of 180^0 was preferred for the thin film, but a rotation of 0^0 once the apatite was more constrained in the thicker film, shows that the apatite film once formed at the pre-relaxed surface could easily be grown in a layer by layer deposition, which agrees with experimental findings where apatite is found to grow at silicate surfaces.[20, 21]

Thick Layer of Fluorapatite 300^0 Rotation

The interface at a rotation of 300^0 is the least stable of the series, which we have investigated in detail as well to study any differences with the most stable rotation. We realize that the materials are farther apart which is similar to the differences between rotations at the unrelaxed substrate discussed above. The distance between the top-most Si of quartz and the bottom-most Ca of apatite is 2.82 Å while for the most stable rotation (240^0) it is 1.79 Å. The shortest Si - $O_{apatite}$ distance is 3.10 Å and the shortest Ca - O_{quartz} distance is 2.89 Å. However, like the 240^0 rotation, the structure of the apatite remains similar to the bulk material and the PO_4 groups are not rotated. Figure 6.12 shows the structure of this interface.

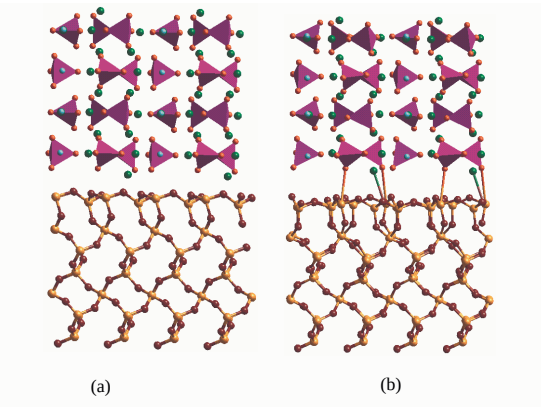

Figure 6.12: The geometry optimised structure of a double layer of apatite {0001} film grown onto the relaxed quartz {0001} surface at a rotation of 300^0. (Si = yellow, O_{quartz} = maroon, $O_{apatite}$ = red, F = pale blue, P = purple, Ca = green, PO_4 groups shown as tetrahedra).

6.2.4 Fluorapatite {1 0 $\bar{1}$ 1} Film on Relaxed Quartz {1 0 $\bar{1}$ 0} Surface

In addition to the apatite {0 0 0 1}/quartz {0 0 0 1} interfaces, we also studied the interfaces between fluorapatite {1 0 $\bar{1}$ 1} films and α-quartz {1 0 $\bar{1}$ 0} surfaces. From table 4.4 we see that the {1 0 $\bar{1}$ 1} surface of apatite is the second most stable plane after the {0 0 0 1} surface and the {1 0 $\bar{1}$ 0} surface of α-quartz is also one of the principal planes shown in the morphology.[149] Again the choice of these surfaces was also based on the compatibility of the lattice vectors. The fluorapatite {1 0 $\bar{1}$ 1} surface simulation cell has lattice vectors **x** = 9.365 Å, **y** = 10.627 Å and **z** = 5.241 Å, whereas the α-quartz {1 0 $\bar{1}$ 0} cell has lattice vectors, **x** = 4.866 Å, **y**

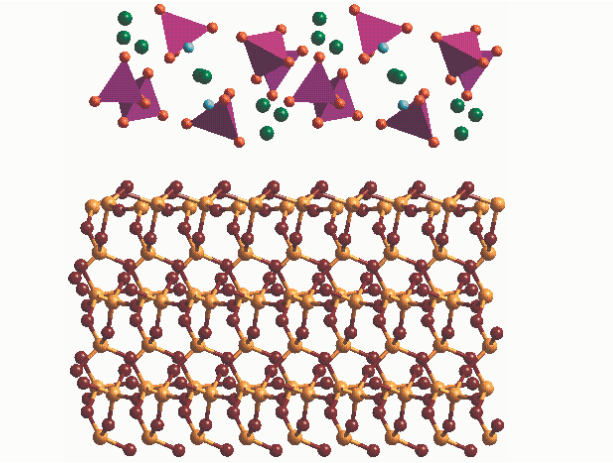

Figure 6.13: Structure of a single layer of apatite $\{10\bar{1}1\}$ film brought down onto the relaxed quartz $\{10\bar{1}0\}$ surface at a rotation of 0^0 before minimisation. (Si = yellow, O_{quartz} = maroon, $O_{apatite}$ = red, F = pale blue, P = purple, Ca = green, PO_4 groups shown as tetrahedra).

= 5.374 Å and **z** = 4.214 Å. We therefore had to grow the α-quartz surface cell to a 2x2 cell to accommodate the apatite surface cell. The grown lattice vectors for the α-quartz are then **x** = 9.733 Å and **y** = 10.749 Å, which gives a misfit of about 3.8% in the **x** and about 1% in the **y** direction.

Following our investigation (section 6.2.2) of the effect of interfacing unrelaxed and pre-relaxed surfaces of quartz with apatite thin films, we have modelled the interfaces between the $\{1\ 0\ \bar{1}\ 1\}$ apatite and $\{1\ 0\ \bar{1}\ 0\}$ surface of α-quartz only on pre-relaxed surface of α-quartz. Figure 6.13 shows the structure of the interface at 0^0 rotation before energy minimisation.

Table 6.3: Adhesion energies (γ_{adh} in Jm^{-2}) for the interfaces between single and double films of FAP $\{1\ 0\ \overline{1}\ 1\}$ at the relaxed α-quartz $\{1\ 0\ \overline{1}\ 0\}$substrate, calculated with respect to the relaxed quartz surface and bulk apatite (equation 6.1).

Rotation	Thin layer	Thick layer
$0^0/360^0$	0.81	1.08
180^0	0.33	0.68

Thin Layer of Fluorapatite 0^0 Rotation

The interface between the two minerals at this angle shows many interactions between the species across the boundary. Though the thin film is fitted to the relaxed surface of α-quartz, the substrate still has under-coordinated Si on the surface, which are reactive to any O that is brought close to it. This behaviour is shown in figure 6.14, where the distance between the top-most Si and the bottom-most Ca of the apatite is 2.42 Å. Unlike the $\{0\ 0\ 0\ 1\}$ interfaces the apatite structure here is distorted significantly. Some O from the quartz have moved up into the interfacial region, enhancing the mix between the two minerals. The PO_4 groups have been rotated to allow their O to bond to the surface Si. The F^- channels keep the diagonal shape as shown in figure 6.13 for the unrelaxed interface but they have moved away from the interface. However the Si - $O_{apatite}$ bond distances are not short, at 2.03 and 2.08 Å, although we find relatively short Ca - O_{quartz} distances at 2.34, 2.35 and 2.61 Å. The adhesion energies of these α-quartz $\{1\ 0\ \overline{1}\ 0\}$ and fluorapatite $\{1\ 0\ \overline{1}\ 1\}$ interfaces, for both thin and thick films, are shown in

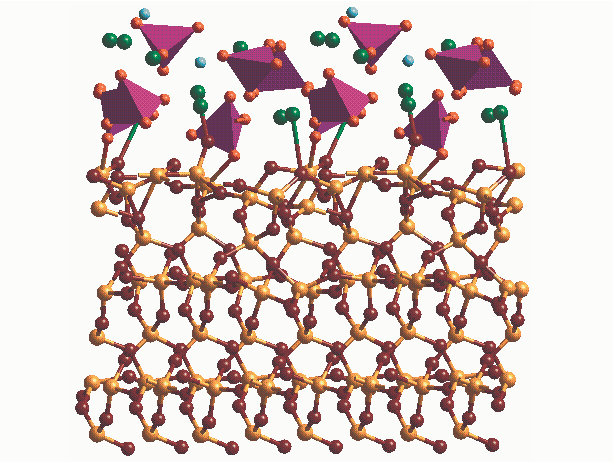

Figure 6.14: Geometry optimised structure of a single layer of apatite $\{10\bar{1}1\}$ film grown onto the relaxed quartz $\{10\bar{1}0\}$ surface at a rotation of 0^0 (Si = yellow, O_{quartz} = maroon, $O_{apatite}$ = red, F = pale blue, P = purple, Ca = green, PO_4 groups shown as tetrahedra).

table 6.3, where we see that the 0^0 rotation interface is less stable than the 180^0 rotation.

Thin Layer of Fluorapatite 180^0 Rotation

The second possible rotation for this interface is 180^0, shown in figure 6.15,which is more stable than the 0^0 rotation. The distance between the bottom-most Ca of the apatite and the top-most Si of quartz is 2.75 Å, which shows that the two materials are farther apart than at 0^0, and might would expect the interaction to be less. However, we notice a different case. The F^- ions in the diagonal channels have moved from their position away from the interface, just as in the 0^0 rotation, and the PO_4 have also rotated to allow the O to react with the under-coordinated surface Si of quartz, again similar to

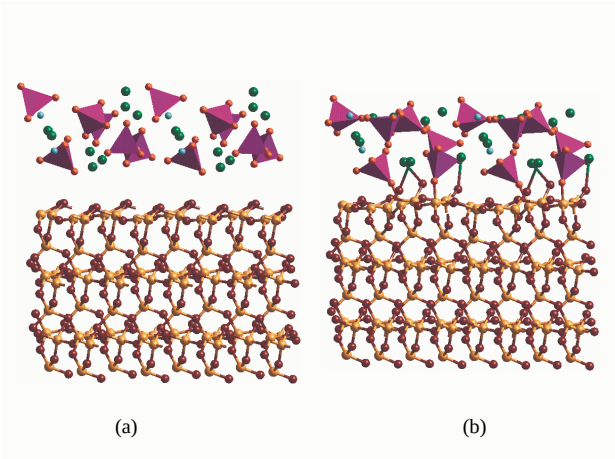

Figure 6.15: Geometry optimised structure of a single layer of apatite $\{10\bar{1}1\}$ film grown onto the relaxed quartz $\{10\bar{1}0\}$ surface at a rotation of 180^0 (Si = yellow, O_{quartz} = maroon, $O_{apatite}$ = red, F = pale blue, P = purple, Ca = green, PO_4 groups shown as tetrahedra).

the 0^0 rotation. As a result the Si - $O_{apatite}$ bond distances are significantly shorter at 1.64 - 1.69 Å and equally the Ca - O_{quartz} bonds at 2.28 - 2.29 Å. The long distance between the top most Si and the bottom most Ca in the interface in this rotation is due to the rearrangement of the apatite thin film to enhance bonding across the interface and hence in this case it does not mean that the interaction is weak. The short distances between the ions of the two minerals are due to the significant rotation and rearrangement of ions from their initial positions coupled with the surface atoms of the quartz which move up into the interfacial region to maximize the interactions.

Thick Layer of Fluorapatite 0^0 Rotation

Similar to the interfaces of the {0 0 0 1} surfaces, we next grew the apatite layer to double the thickness to see what effect this would have on the interfacial structures and energies. Figure 6.16 shows the structure of the interface between the two minerals at 0^0 rotation. The distance between the Ca and the Si of the two minerals at the bottom of apatite and the top of the quartz respectively is 2.39 Å. Here we notice that, just like the interfaces of the {0 0 0 1} surfaces with the unrelaxed substrate, once again the structure of the apatite remains intact. No significant rotation of the PO_4 groups occurs and the F^- channel remains diagonal, although some of the atoms move in the a-b direction exposing the F^- that are not visible before optimisation. Some O_{quartz} protrude into the interfacial region to react with the Ca of the apatite and the bond distances for Si - $O_{apatite}$ are 1.68 and 2.01 Å and for Ca - O_{quartz} 2.15, 2.19 and 2.34 Å. From table 6.3 we see that similar to the thin films, this interface is not the most stable rotation.

Thick Layer of Fluorapatite 180^0 Rotation

Figure 6.17 shows the structure of the more stable interface at 180^0. Like the interfaces of the {0 0 0 1} surfaces with the pre-relaxed substrate, the same rotation is preferred for both thin and thick films. Unlike at 0^0, however the PO_4 groups have moved and rotated, although the diagonal F^- channel remains intact. The distance between the bottom-most Ca of the apatite and the top-most Si of the α-quartz is small at 2.16 Å. The Si - $O_{apatite}$ bond lengths are 1.71, 1.79, and 1.82 Å and the Ca - O_{quartz} distances are 2.24,

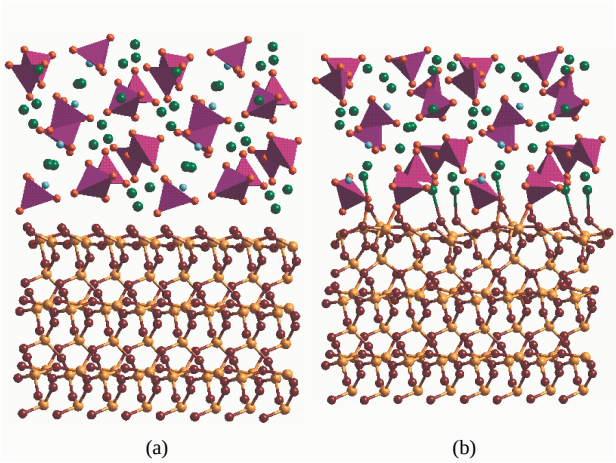

Figure 6.16: Geometry optimised structure of a double layer of apatite $\{10\bar{1}1\}$ film grown onto the relaxed quartz $\{10\bar{1}0\}$ surface at a rotation of 0^0 (Si = yellow, O_{quartz} = maroon, $O_{apatite}$ = red, F = pale blue, P = purple, Ca = green, PO_4 groups shown as tetrahedra).

2.35 and 2.58 Å. The structure of this interface shows us that, unlike the interfaces of the {0 0 0 1} surfaces, where the layer growth of apatite thin films kept the apatite structure intact, here the apatite structure is distorted even when grown in layers, which may be partly due to the high reactivity of the $\{1\ 0\ \bar{1}\ 0\}$ surface of α-quartz with its dangling bonds. We find that the adhesion energy for one layer of apatite in this case is 0.33 Jm^{-2} and for double layer it is 0.68 Jm^{-2}. Thus, adding one more layer on top of the first layer will need 0.35 Jm^{-2}, which is more by 0.02 Jm^{-2} than growing the first layer. The {0 0 0 1} interfaces where the adhesion energy decreases with thickness, should therefore be the prefered interface direction for growth.

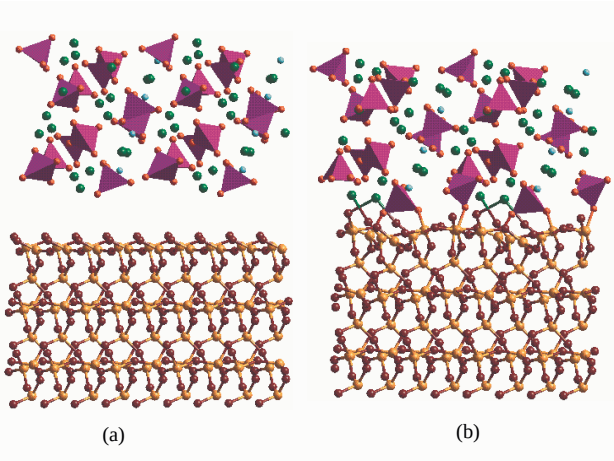

Figure 6.17: Geometry optimised structure of a double layer of apatite $\{10\bar{1}1\}$ film grown onto the relaxed quartz $\{10\bar{1}0\}$ surface at a rotation of 180^0 (Si = yellow, O_{quartz} = maroon, $O_{apatite}$ = red, F = pale blue, P = purple, Ca = green, PO_4 groups shown as tetrahedra).

6.3 Interfaces of Fluorapatite Thin Films with Hydroxylated α-Quartz Surfaces

Unless surfaces are created and kept under ultra-high vacuum (UHV) condition, water will be present to adsorb to the surfaces. DeLeeuw *et al*[28] showed that the dissociative adsorption of water at quartz surfaces is preferred over associative adsorption, leading to hydroxylated quartz planes. Experimentally it is difficult to remove the hydroxyl groups[128, 129] and we therefore need to take them into account in our simulations.

In this section we report the results obtained when the fluorapatite films were interfaced with the hydroxylated surfaces of quartz. The lateral scanning of the two blocks to obtain the initial starting position for the thin films

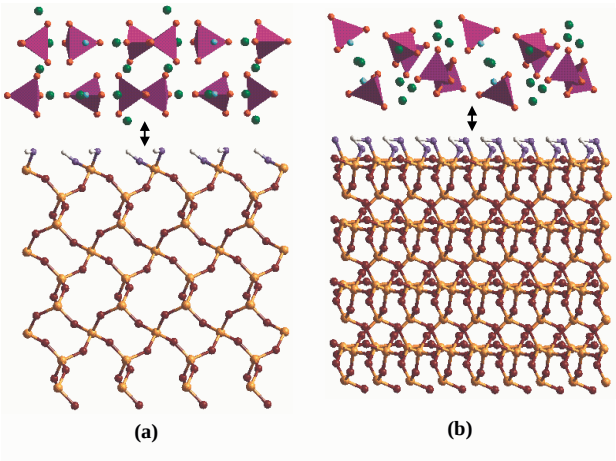

Figure 6.18: Structures of the interface (a) α-quartz {0001} relaxed hydroxylated surface with a single {0001} fluorapatite layer and (b) α-quartz relaxed hydroxylated $\{10\bar{1}0\}$ surface with $\{10\bar{1}1\}$ thin layer of fluorapatite at 0^0 rotation before minimisation. (Si = yellow, O_{quartz} = maroon, $O_{apatite}$ = red, O_{OH} = navy-blue, H = white, F = pale blue, P = purple, Ca = green, PO_4 groups shown as tetrahedra).

on top of the surfaces was the same process as discussed in section 6.2.1.

Figure 6.18 (a) and (b) shows the relaxed hydroxylated structures of the {0 0 0 1} and {1 0 $\bar{1}$ 0} surfaces of α-quartz with single layers of apatite in the {0 0 0 1} and {1 0 $\bar{1}$ 1} orientation respectively before minimization of the interface.

6.3.1 Fluorapatite {0 0 0 1} Films on the Relaxed Hydroxylated Quartz {0 0 0 1} Surface

Thin and thick layers of apatite layers of apatite in a {0 0 0 1} orientation were fitted onto the relaxed hydroxylated {0 0 0 1} surface of α-quartz using the same procedure as before. Adhesion energies were calculated using

Table 6.4: Adhesion energies (γ_{adh} in Jm^{-2}) for the interfaces between single and double {0 0 0 1} films of fluorapatite on the relaxed hydroxylated α-quartz {0 0 0 1} surface, calculated with respect to the relaxed hydroxylated α-quartz surface and bulk apatite (equation 6.1).

Rotation	Thin layer	Thick layer
$0^0/360^0$	1.36	1.64
60^0	1.45	1.63
120^0	1.37	1.63
180^0	1.35	1.63
240^0	1.36	1.64
300^0	1.45	1.63

equation 6.1, where $E_{surface-quartz}$ is now the energy of the free hydroxylated surface of quartz. The adhesion energies are shown in table 6.4.

Thin Layer of Fluorapatite 60^0 Rotation

As we can see from table 6.4, we have again simulated rotations of the apatite films with respect to the substrate. When we compare the adhesion energies with those of table 6.3 we note that they are higher for the hydroxylated interfaces, which is due to the lesser interaction between the two materials. Here the apatite film interacts merely with a topmost layer consisting of Hydrogen ions, rather than Si and oxygen ions.

We first discuss the 60^0 rotation which is shown in figure 6.19. This interface is the least stable of the series together with the 300^0 rotation. We note that the structure of the interface with the hydroxylated surface of

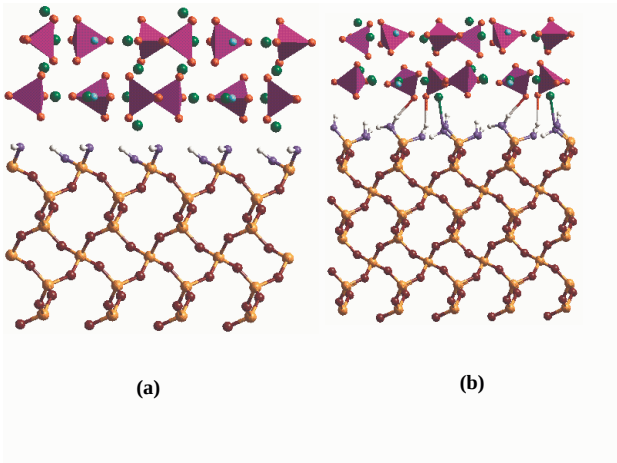

Figure 6.19: Geometry optimised structure of a single layer apatite {0001} film grown onto the relaxed hydroxylated quartz {0001} surface at a rotation of 60^0 (Si = yellow, O_{quartz} = maroon, $O_{apatite}$ = red, O_{OH} = navy-blue, H = white, F = pale blue, P = purple, Ca = green, PO_4 groups shown as tetrahedra).

quartz is different from the interface with the dry surface of quartz. Looking at figure 6.19 for the 60^0 rotation, the distance between the bottom-most Ca of the apatite and the top-most Si of quartz is 2.49 Å. For the single layer on the relaxed dry surface of quartz, the least stable interface was at 180^0 with a Si - Ca distance of 2.16 Å. The interactions are now between the surface OH groups and protons where the H - $O_{apatite}$ is at hydrogen-bond distances of 2.02 and 2.19 Å, The Ca - O_{OH} interaction distance is 2.59 Å, and the PO_4 are rotated to allow the O to interact with surface H ions. The F^- channels remain unchanged and we also notice some H_{OH} turning downwards in an attempt to coordinate to some surface O_{quartz} though the distance remains larger than 2.0 Å.

Thin Layer of Fluorapatite 180^0 Rotation

Table 6.4 shows that the 180^0 rotation is the most stable interface, the structure of which we now compare with the least stable rotation. We see that the distance between the top-most Si of the α-quartz and the bottom-most Ca of the apatite is 3.37 Å. Again we see that the F channels are retained while the PO_4 has rotated a bit to allow the O to react to the surface H. H-$O_{apatite}$ distances are 1.92 and 2.11 Å, with a Ca - O_{OH} distance of 2.80 Å. Here, there are no H or OH ions pointing down to react to other surface atoms of quartz or the H and OH themselves, but they all point into the interfacial region, hence stabilising the interface rather than the quartz surface. The structure of this interface is shown in figure 6.20.

Thick Layer of Fluorapatite 0^0 Rotation

From the interface with the dry relaxed surface of α-quartz, we saw that the energy of growing the thin film to two layers was convergent. Similarly, we now consider the behaviour of the hydrated interface, when we grow the apatite thin film to a double layer but on the hydroxylated surface of α-quartz. Table 6.4 shows that all rotations now have virtually the same adhesion energy, and that again the extra energy needed to attach the second layer is small compared to the singe layer. We first study the structure of the 0^0 rotation, where we see that the distance between the Si at the top of the quartz surface and the Ca at the bottom of the apatite layer is 3.42 Å. The H_{OH}-$O_{apatite}$ distance is 2.09 Å and the Ca - O_{OH} are 2.81 Å apart. There is no significant rotation of the PO_4 but they move in the a-b direction and

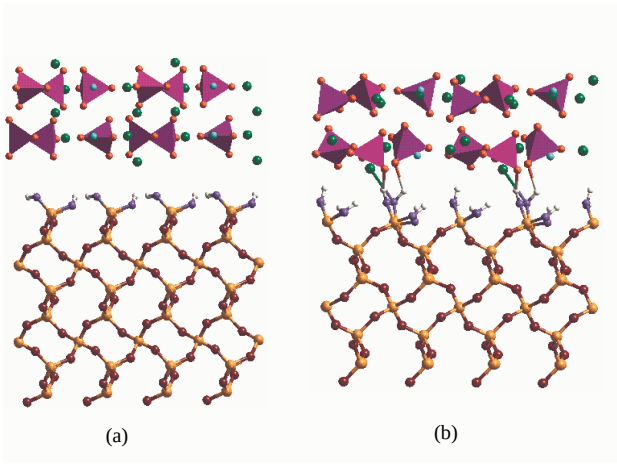

Figure 6.20: Geometry optimised structure of a single layer of apatite {0001} film grown onto the relaxed hydroxylated quartz {0001} surface at a rotation of 180^0 (Si = yellow, O_{quartz} = maroon, $O_{apatite}$ = red, O_{OH} = navy-blue, H = white, F = pale blue, P = purple, Ca = green, PO_4 groups shown as tetrahedra).

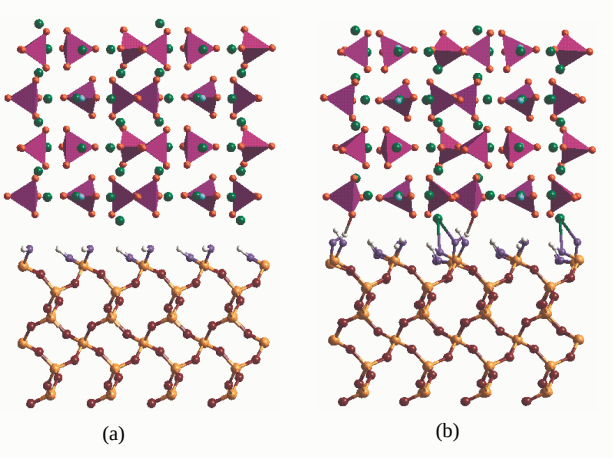

Figure 6.21: Geometry optimised structure of the double layer of apatite {0001} film grown onto the relaxed hydroxylated quartz {0001} surface at a rotation of 0^0 (Si = yellow, O_{quartz} = maroon, $O_{apatite}$ = red, O_{OH} = navy-blue, H = white, F = pale blue, P = purple, Ca = green, PO_4 groups shown as tetrahedra).

relax away from the surface into the bulk material. Figure 6.21 shows the structure of the interface.

Thick Layer of Fluorapatite 60^0 Rotation

The 60^0 rotation, shown in figure 6.22 has exactly the same adhesion energy as the 120^0, 180^0 and 300^0 interfaces. The distance between the top-most Si of the quartz and the bottom-most Ca of apatite is 2.82 Å, which is much closer than in the slightly less stable 0^0 interface. The PO_4 and F^- have relocated from the face of the plan view into the bulk of the film, leaving Ca impeding the visibility in the figure of one F from the channel (second and third layers of F from the interfacial region), though this F^- remains in the column and there is no rotation of the PO_4. The H-$O_{apatite}$ distance is 2.18 and 2.28 Å which interaction was absent in the 0^0 interface, the H_{OH}-$O_{apatite}$ is 2.41 Å and the Ca-O_{OH} interaction distance is 2.82 Å. There are many more interactions between the materials for this rotation than in the slightly less stable one. The adhesion energy for the most stable single layer interface is 1.35 Jm^{-2} at 180^0 rotation. For this double layer at 60^0 and also at 120^0, 180^0 and 300^0 rotation the adhesion energy is 1.63 Jm^{-2}, which means that adding one layer on top of the initial film will need only 0.28 Jm^{-2} which is far less than the energy of putting on the first layer. Hence, though the interface on the hydroxylated {0 0 0 1} surface of α-quartz is energetically less favorable compared to the dry quartz surface, once formed growth of further layers should be rapid.

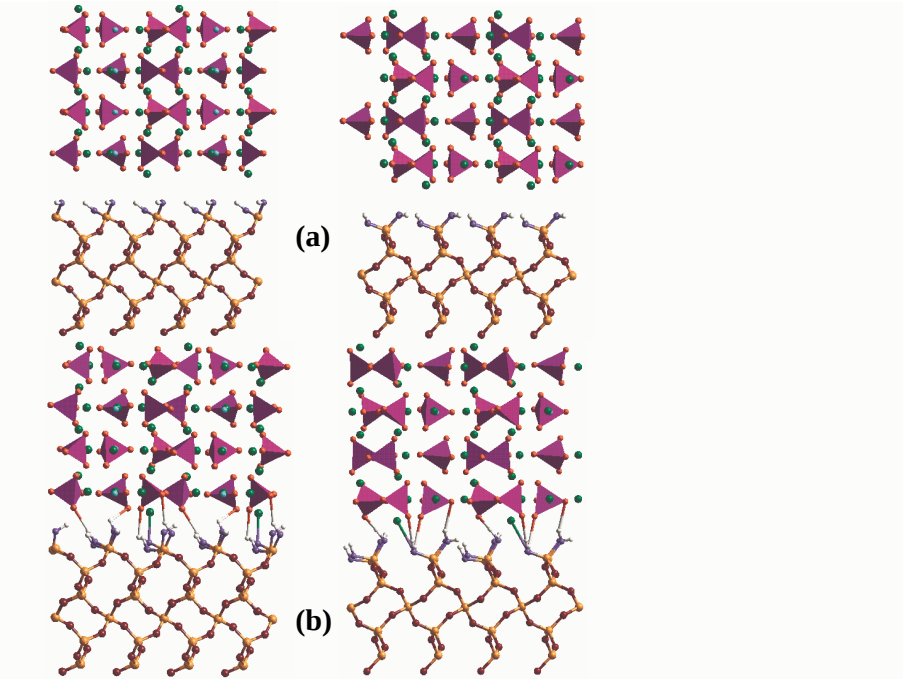

Figure 6.22: Two views of the geometry optimised structure of the double layer of apatite {0001} grown onto the relaxed hydroxylated quartz {0001} surface at a rotation of 60^0 (Si = yellow, O_{quartz} = maroon, $O_{apatite}$ = red, O_{OH} = navy-blue, H = white, F = pale blue, P = purple, Ca = green, PO_4 groups shown as tetrahedra).

Table 6.5: Adhesion energies (γ_{adh} in Jm^{-2}) for the interfaces between single and double films of fluorapatite $\{1\ 0\ \bar{1}\ 1\}$ surface on the relaxed hydroxylated α-quartz $\{1\ 0\ \bar{1}\ 0\}$ substrate, calculated with respect to the relaxed hydroxylated α-quartz surface and bulk apatite (equation 6.1).

Rotation	Thin layer	Thick layer
$0^0/360^0$	1.48	1.66
180^0	1.45	1.67

6.3.2 Fluorapatite {1 0 $\bar{1}$ 1} Film on Relaxed Hydroxylated Quartz {1 0 $\bar{1}$ 0} Surface

Having investigated the interface of the $\{1\ 0\ \bar{1}\ 1\}$ thin film of fluorapatite onto the dry $\{1\ 0\ \bar{1}\ 0\}$ surface of α-quartz, we now proceed to the interface with the hydroxylated surface of quartz, again with both thin and thick films of apatite. Table 6.5 shows the adhesion energies of both thin and thick films on the hydroxylated surface for both the 0^0 and 180^0 rotations. Again, we see that the adhesion energies for the two rotations are very similar and virtually identical for the thick layer.

Thin Layer of Fluorapatite 0^0 Rotation

Figure 6.23 shows the structure of the interface at 0^0 rotation where the distance between the top-most Si of the quartz and the bottom Ca of apatite is 4.10 Å, suggesting that the two materials are rather far apart. The structure of the apatite is rearranged and the PO_4 groups have rotated. The H-$O_{apatite}$ distance is 1.97 Å, and we also notice a close interaction between the F-H at 2.04 and 2.19 Å. The Ca are far from the O_{OH} of the quartz surface (2.84

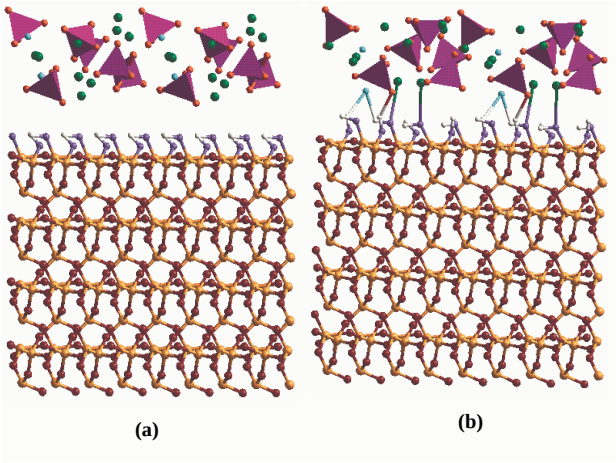

Figure 6.23: Geometry optimised structure of a single layer of apatite $\{10\bar{1}1\}$ film grown onto the relaxed hydroxylated quartz $\{10\bar{1}0\}$ surface at a rotation of 0^0 (Si = yellow, O_{quartz} = maroon, $O_{apatite}$ = red, O_{OH} = navy-blue, H = white, F = pale blue, P = purple, Ca = green, PO_4 groups shown as tetrahedra).

and 2.89 Å), but the H and the OH protrude into the interfacial space, rather than interacting along the quartz surface.

Thin Layer of Fluorapatite 180^0 Rotation

The interfacial region of the 180^0 rotation is denser than the 0^0 rotation, with a distance between the top-most Si to the bottom-most Ca of 3.45 Å. Here we have some interactions that we did not have on the less stable 0^0 interface and figure 6.24 shows the interfacial structure. The F-H is at 2.06 Å while Ca - O_{OH} is at 2.86 Å. The H and OH again protrude into the interfacial region. The PO_4 have rotated and the diagonal F^- pair has moved away from its initial position. These increased interactions contribute to the stability of

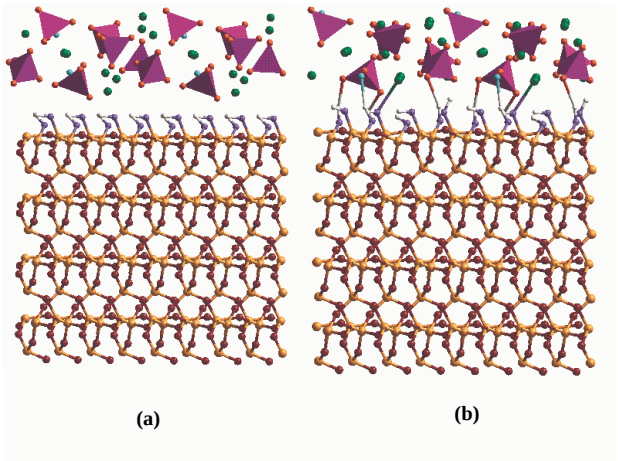

Figure 6.24: Geometry optimised structure of a single layer of apatite $\{10\bar{1}1\}$ film grown onto the relaxed hydroxylated quartz $\{10\bar{1}0\}$ surface at a rotation of 180^0 (Si = yellow, O_{quartz} = maroon, $O_{apatite}$ = red, O_{OH} = navy-blue, H = white, F = pale blue, P = purple, Ca = green, PO_4 groups shown as tetrahedra).

this interface. Unlike what we saw with the hydroxylated {0 0 0 1} interfaces where the thin film did not change much in shape from the bulk crystal structure, here we notice that the film is considerably distorted.

Thick Layer of Fluorapatite 0^0 Rotation

We see from table 6.5 that the 0^0 rotation of the double layer is the most stable one, although the difference between the adhesion energies is insignificant at 0.01 Jm^{-2}. In both cases the interface is denser than for the single layer, with the distance between the top-most Ca of the apatite and top-most Si of the α-quartz at 3.11 Å. The H-$O_{apatite}$ distance is short at 2.01 Å and the Ca - O_{OH} is 2.90 Å. Movement of ions is different from the interface with

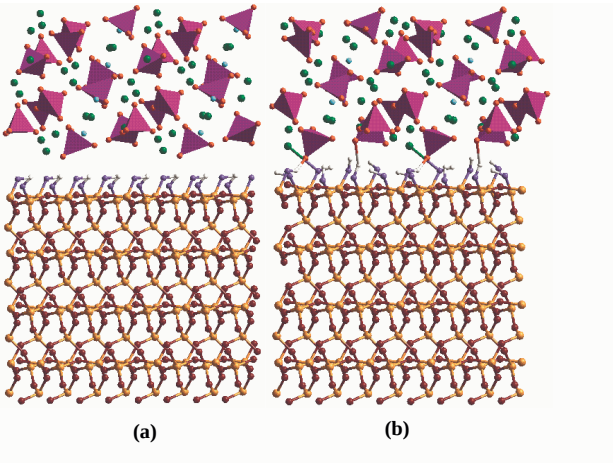

Figure 6.25: Geometry optimised structure of a double layer of apatite $\{10\bar{1}1\}$ film grown onto the relaxed hydroxylated quartz $\{10\bar{1}0\}$ surface at a rotation of 0^0 (Si = yellow, O_{quartz} = maroon, $O_{apatite}$ = red, O_{OH} = navy-blue, H = white, F = pale blue, P = purple, Ca = green, PO_4 groups shown as tetrahedra).

the single layer interface, though the F column is shifted in the a-b plane, it remains in the form of a column. This time the F-H interaction is negligible at not less than 3.5 Å. The H and OH ions stick out into the interfacial region. The optimised structure of this interface is shown in figure 6.25. We see from table 6.5 that the adhesion energy on adding an extra layer on the single film is only 0.21 Jm^{-2}, similar to the hydrated {0 0 0 1} interfaces.

Thick Layer of Fluorapatite 180^0 Rotation

In the 180^0 rotation, the distance between the top-most Si of the α-quartz and the bottom-most Ca of apatite is 3.12 Å, which is comparable to the 0^0 rotation. Less rearrangement of the interface has taken place in terms of

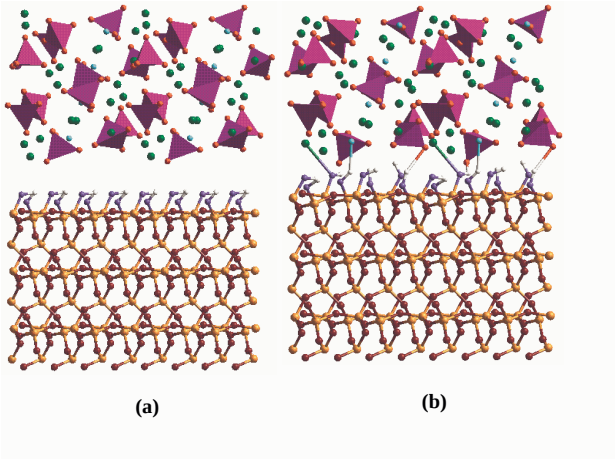

Figure 6.26: Geometry optimised structure of a double layer of apatite $\{10\bar{1}1\}$ film grown onto the relaxed hydroxylated quartz $\{10\bar{1}0\}$ surface at a rotation of 180^0 (Si = yellow, O_{quartz} = maroon, $O_{apatite}$ = red, O_{OH} = navy-blue, H = white, F = pale blue, P = purple, Ca = green, PO_4 groups shown as tetrahedra).

rotations and relocation of atoms and ions, as we can see from the interfacial structure in figure 6.26. The apatite structure is kept almost intact. The surface H and OH ions protrude to interact with the rather more rigid apatite double layer. The F-H distance is 2.15 Å and the Ca - O_{OH} distance is 2.94 at its closest. Compared to the general behaviour of the interface of fluorapatite $\{1\ 0\ \bar{1}\ 1\}$ and α-quartz $\{1\ 0\ \bar{1}\ 0\}$, where the thin film rearranges in both single and double layers, this 180^0 rotation on the hydroxylated surface keeps the apatite double layer virtually intact.

6.4 Discussion

In this chapter we have used atomistic simulation techniques to model the interface between the two complex materials (fluorapatite and α-quartz). The results have shown that the nature of the substrate is crucial when the two minerals are to be interfaced. Also the trend in which to two minerals adhere to each other has been reported. We have modelled the interface of fluorapatite thin film (thickness equal to one unit cell) onto unrelaxed and relaxed surfaces of α-quartz. Firstly we modelled the interface of the fluorapatite $\{0\ 0\ 0\ 1\}$ thin film with unrelaxed $\{0\ 0\ 0\ 1\}$ surface of α-quartz. During the relaxation of the interface, both the thin film and the first region of the substrate were allowed to relax to mechanical equilibrium. The results have shown that the thin film got distorted from its original structure. This has been caused by high reactiveness of the low coordinated α-quartz surface, that has some dangling bonds (figure 6.1 a). Also the number of interactions between the substrate and the thin film had an effect on the distortion of the thin film's structure. Again the interfacial region is very tense keeping the two minerals close together, and the two minerals interface mainly by the Ca of the fluorapatite to the O of the substrate. Figure 6.5 b for example shows how the interfacial region of 180^0 rotation which is the most favourable as seen from table 6.1 of adhesion energies. Again from the same table we have seen that film growth on the substrate is energetically increasingly unfavourable.

However this was found to be a different case when modelling the interface between the thin film and the pre-relaxed surface of α-quartz. The thin film has now kept its bulk structure and there is less number of interactions

between the surfaces's ions. This interface is energetically the most stable, as shown in table 6.2 and figure 6.9 b shows the most energetically favourble 240^0 rotation structure of the interface. Though the adhesion energy after attaching double layer of apatite on the substrate is higher compared to one layer, we noticed that film growth is convergent with energy for this interface. The amount of energy released when attaching the second layer of apatite is less than the amount of energy that was released when attaching the first layer (0.55 kJmol^{-1} for single layer and 0.82 kJmol^{-1} for two layers meaning it needed 0.27 kJmol^0 to add a second layer). Lastly the same rotation (240^0) that is most stable during interface with single layer of fluorapatite is the same rotation that is most stable with double layer unlike in the case of the interface on un-relaxed substrate.

Interface between the $\{1\ 0\ \overline{1}\ 1\}$ fluorapatite thin film and the $\{1\ 0\ \overline{1}\ 0\}$ surface of α-quartz has given less adhesion energies than the $\{0\ 0\ 0\ 1\}$ surfaces. This is caused by the number of interactions between the two surfaces ions at the interfacial region. The α-quartz $\{1\ 0\ \overline{1}\ 0\}$ surface is less coordinated on top of the surface both when relaxed and unrelaxed as shown in figure 6.2. Figure 6.15 b for example shows the interface structure of the most stable 180^0 rotation after minimisation which shows the two minerals to be much closer together. We noticed that the dangling bonds of the $\{1\ 0\ \overline{1}\ 0\}$ surface has caused the oxygens of the fluarapatite to interact more with the α-quartz Si ions. Hence the resulting structure has the fluarapatite film distorted from the original structure. From table 6.3 we see that like with the $\{0\ 0\ 0\ 1\}$ interfaces, film growth on the substrate is less energetically

favourable than single layer, however it is not convergent with energy (0.33 kJmol^{-1} for single layer and 0.68 kJmol^{-1} fro two layers meaning it needed 0.35 kJmol^{-1} to add the second layer), which was a different case with $\{0\ 0\ 0\ 1\}$ interfaces.

We have as well modelled the interface between the fluorapatite thin film and hydroxylated surfaces of α-quartz. The interface is mainly between the hydroxyl groups on top of the α-quartz surfaces and the fluorapatite thin films. We have noticed that these interfaces are energetically much less favourable than interfaces on dry surfaces of α-quartz. However they leave the fluorapatite thin films in its original form and the interfacial region is not complex. The interactions are mainly between the thin film's Ca atoms and the oxygens of the hydroxyl groups on the surfaces of α-quartz. From table 6.4, we have noticed that there is no significant difference in the adhesion energies of the interface between the $\{0\ 0\ 0\ 1\}$ surfaces. Figure 6.20 and 6.22 for example shows the interfaced structures of the 180^0 rotation with single layer and 60^0 with double layer respectively, where in both cases we see that the thin film structure is kept in its original form even after relaxation. Though energetically less favourbale than interfaces with dry surfaces, film growth on hydroxylated surfaces is still convergent with energy (1.35 kJmol^{-1} for one layer and 1.63 kJmol^{-1} meaning it needed 0.28 kJmol^{-1} to add the second layer). The interface between the $\{1\ 0\ \overline{1}\ 1\}$ surface of fluorapatite and $\{1\ 0\ \overline{1}\ 0\}$ hydroxylated surface of α-quartz is now convergent with energy as seen from table 6.5 (1.45 kJmol^{-1} for single layer and 1.67 kJmol^{-1} for double layer, meaning it needed 0.22 kJmol^{-1} to add the second layer). However

the adhesion energies for these interfaces as shown in table 6.5 are higher as compared to adhesion energies for the {0 0 0 1} interfaces.

Hence, we conclude that if we are to interpret experimental findings correctly and predict growth behavior and energies for use in film deposition onto inorganic surfaces, the nature of the substrate surface needs to be included in the computer simulations.

Chapter 7

7.1 CONCLUSION

We have presented the results of atomistic simulation studies of surface and interfacial structures of fluorapatite material. We have studied the effect of water or hydration on the different surfaces and have further reported on the effect of different organic surfactants on the surface structures and stabilities. Lastly as one of the motives of the study was due to the importance of the apatite mineral in biological applications e.g as a candidate to be used in repairing diseased and broken bones, we have reported the results of interface calculations of fluorapatite thin films to α-quartz surfaces as a simple model for bioglasses.

The potential parameters that we have derived and reported in chapter 3 reproduced the experimental parameters of the fluorapatite structure very well. As potential parameters are generally transferable from bulk to surface structure for ionic systems, we have used the same potentials in our studies of the mineral surfaces. We have further derived suitable potentials that enabled us to study the effect of water on the mineral surfaces. Finally in chapter 3

we have reported the potentials that we have used to study the adsorption of a range of organic surfactant on the surfaces, and the potential parameters that we derived for the study of the interfaces between the fluorapatite thin films and the α-quartz surfaces.

The $\{0\ 0\ 0\ 1\}$ and $\{1\ 0\ \bar{1}\ 0\}$ experimental cleavage planes of the system have been reproduced as the most stable surfaces of the system, as shown by the calculated surface energies of the different simulated surfaces. Furthermore the calculated morphologies of the mineral express these experimental cleavage planes.

Upon geometry optimisation there is a considerable relaxation of the first and to a lesser extent the second and third surface layers on all the surfaces, where the surface Ca ions move into the bulk material to form stronger interactions with the O ions in the next layer, thus compensating for the loss of coordination caused by the cleavage of the surface from the bulk material. The least stable surfaces are those that have large surface areas and irregular surface topologies, e.g the $\{1\ 0\ \bar{1}\ 3\}$ surface.

Introduction of water on the surfaces was shown to have a stabilising effect,although the most stable surface still prevail. We noted that the adsorption of the water molecules on the surfaces is mainly through the oxygen ions to the surface calcium ions, then to other exposed surface and near surface ions. The other factor that leads to stable hydrated surfaces is the interaction between the water molecules themselves. Hydration of the surfaces has produced the $\{1\ 1\ \bar{2}\ 1\}$ twinning plane of the material, in the calculated morphologies. The calculated morphology for hydrated surfaces

has a rounded hexagonal shape similar to the experimental apatite crystals in bone, which are found to be nanosized platelets.

In chapter 5 we have presented the results obtained from our studies of the adsorption of different organic molecules on the surfaces under study. The different trends in which the surfactants adsorb onto the surfaces has been reported. We have observed that in general adsorption of the hydroxyethanal molecule is the most energetically favourable in both the "cis" and "trans" forms. We noted that for all the surfactant molecules, the main interaction with the mineral surfaces is through the oxygen atoms, especially the carbonyl oxygen, to the surface calcium atoms. In the case of methylamine, which does not have any oxygens, the interaction is by its nitrogen atom to the surface calcium atoms. The most stable surface of the fluorapatite ($\{0\ 0\ 0\ 1\}$) was found to be relatively inactive towards the various adsorbates.

For the hydroxyethanal molecule it was found that the adsorption of the "cis" form on the surfaces is more exothermic than the "trans" form, due to the interaction of the molecule by both carbonyl and hydroxyl oxygens with the surfaces. The adsorption of methanoic acid is exothermic on all the surfaces and the main interaction is via the carbonyl oxygen. We noted that the additional carbon in the methanoic acid sometimes allows either bidentate or bridging adsorption through both carbonyl and hydroxyl oxygen atoms. The hydroxamic acid actively interact in its "cis" form, and the interaction is again via both the carbonyl and hydroxyl oxygens. This trend was found to be similar to the hydroxyethanal "cis" form. The interaction of methylamine with the surfaces was found to be least exothermic, due to

its single functional group, whereas the two oxygen atoms of the methanoic acid, hydroxamic acid and hydroxyethanal lead to strong interactions to the surface calcium atom. The number of interactions between the ions of adsorbate molecule and the mineral surfaces thus contribute significantly to the exothemicity of adsorption.

In chapter 6 we have presented the results of our studies of the solid/solid interfaces between fluorapatite thin films and α-quartz surfaces, considering different rotations of the thin films with respect to the substrate surface and different surface terminations of the substrate.

We showed that when the substrate surface has dangling bonds as on the $\{1\ 0\ \bar{1}\ 0\}$ and unrelaxed $\{0\ 0\ 0\ 1\}$ surfaces, the substrate is highly reactive towards the apatite thin film, leading to a high density interface where the fluorapatite structure is often distorted. The relative orientation of substrate surface and apatite thin film is important, shown by the orientation in adhesion energy within film rotation.

When the substrate surface contains fully coordinated surface species, exemplified by the relaxed $\{0\ 0\ 0\ 1\}$ quartz surface, the interface with the apatite film is less dense and the film resembles the bulk apatite structure more closely. The interface between film and fully coordinated surface is more stable, as shown by the adhesion energies, than at the uncoordinated substrate surface, probably due to the fact that the film structure is less distorted. The relative orientation of substrate surface and thin film no longer affects the adhesion energies when the substrate surface species are fully coordinated.

Finally, the interface with the hydrated substrate surfaces are the least stable. Although the structures of the thin films are ordered and bulk-like, the attachment to the substrate is only through relatively weak hydrogen-bonded interactions. As the hydrated substrate surfaces are very stable themselves, adding a thin film of apatite is energetically not particularly favourable.

Rotation of thin films with respect to the substrate surfaces is irrelevant, as is the structure/ orientation of the substrate surface, i.e. $\{0\ 0\ 0\ 1\}$ or $\{1\ 0\ \bar{1}\ 0\}$, because each film is terminated by a full layer of hydroxy groups which are the only species interacting with the apatite films. Hence, it is clear from above that the most stable and regular interface are obtained from dry substrate surfaces, which are terminated by fully coordinated surface species.

7.2 Recommendations and Future work

Future work on apatite minerals in biomaterials applications will include calculations of impurity uptake into the apatite crystal, such as Mg ions and CO_3 groups, which are important substitutional defects in bone material, and the investigation of interfaces between apatite materials and calcium carbonate, which is another major constituents of bones and teeth.

As biological apatite nucleates and grows from organic templates formed by a selection of proteins, the interaction between apatite clusters and protein scaffolds is another area of further research.

Bibliography

[1] E.H Nickel, Mineralogy and Petrology, 1995, **55**, 323.

[2] W.A. Deer, R.A. Howie and J. Zussman, in An introduction to the rock-forming minerals, Longman, UK, 1992.

[3] J.C. Elliott, in Structure and chemistry of the apatites nd other calcium orthophosphates, Studies in inorganic chemistry 18, Elsevier, Amsterdam, 1994.

[4] R.L. Romer, Geochim. Cosmochim. Acta 1996, **60**, 1951.

[5] M. Menzies, K. Gallagher, A. Yelland and A.J. Hurford, Geochim. Cosmochim. Acta 1997, **61**, 2511.

[6] F. Corfu and D. Stone, Geochim. Cosmochim. Acta 1998, **62**, 2979.

[7] P. Pellas, C. Fieni, M. Trieloff and E.K. Jessberger, Geochim. Cosmochim. Acta 1997, **61**, 3477.

[8] R.A. Wolf, K.A. Farley and L.T. Silver, Geochim. Cosmochim. Acta 1996, **60**, 4231.

[9] K.A. Farley, R.A. Wolf and L.T. Silver, Geochim. Cosmochim. Acta 1996, **60**, 4223.

[10] T. Sasada, H. Hiyagon, K. Bell and M. Ebihara, Geochim. Cosmochim. Acta 1997, **61**, 4219.

[11] A.C. Warnock, P.K. Zeitler, R.A. Wolf and S.C. Bergman, Geochim. Cosmochim. Acta 1997, **61**, 5371.

[12] F. Betts, N.C. Blumenthal and A.S. Posner, J. Cryst. Growth, 1981, **53**, 63.

[13] L.L Hench, R. J. Splinter. W. C. Allen and T. K. Greenlee Jr., J. Biomed. Mater. Res, 1972, **2**, 117.

[14] L. L. Hench, Edited by P. Ducheyne and J. Lemons, Annals N.Y. Acad. Sci., Bioactive Ceramics, 1988 **523** 54.

[15] U. Gross, R. Kinne, H. J. Schmitz, V. Strunz, CRC Critical Reviews in Biocompatibility, 1988, **4** No. 2.

[16] L.L. Hench, Chem. Ind., 1995, **14**, 547.

[17] R.G.T Geesink, K. d Groot and A.K.T. Christel, Clin. Orthop., 1997, **225**, 147.

[18] G.L de Lange and K. Donath, Biomaterials, 1989, **10**, No. 2, 121.

[19] L. Gineste, M. Gineste, X. Ranz, et al. J. Biomed Mater Res. 1999, **48**, No. 3, 224.

[20] T. Kokubo, Acta Mater., 1998, **46**, 2519.

[21] F. Miyaji, M. Iwai, T. Kokubo, T. Nakamura, J. Ma ter. Sci-Mater. Med., 1998, **9**, 61.

[22] Enrico Ciliberto and Giuseppe Spoto, Chem. Commun., 1997, 1483.

[23] W.J.A. Dhert, C.P.A.T. Klein, J.A. Jansen, E.A. ven der Velde, R.C. Vriesde, P.M. Rozing and K. De Groot, J. Biomed. Mater. Res., 1993, **27**, 127.

[24] L. Heling, R. Heindel, and B. Merin, J. Oral Imlantol. 1981, **9**, 548.

[25] T.J. McCoy, M. Wadhwa and K. Keil, Geochim. Cosmochim. Acta 1999, **63**, 1249.

[26] S.K. Lower, P.A. Maurice and S.J. Traina, Geochim. Cosmochim. Acta 1998, **62**, 1773.

[27] L.R. Lang, A.P.W Makepeace, M. Moore, Miner. Mag., 1994, **58**, 87.

[28] N.H. de Leeuw, F.M. Higgins, S.C. Parker, J. Phys. Chem. B, 1999, **103**, 1270.

[29] S.B. Hendricks, M.E. Jefferson and V.M. Mosley, Z. Kristall, Kristallgeom. Kristallphys. Kristallchem. 1932, **81**, 352.

[30] J.A. Moriarty, V. Vitek, V.V. Bulatov and S. YIP, Computer-Aided Materials Design, 2002, **9**, 99.

[31] R.C Baetzold, Phys. Rev. **B**, 1987, **36**, 9182.

[32] L. G. Hector, D. J. Siegel, J. B Adams, Proceedings: Integration of Material, Process, and Product Design, Seven Springs PA, 1998, 39.

[33] M. Born; K. Huang; Dynamical Theory of Crystal Lattices Oxford University Press; Oxford, 1954.

[34] P.P. Ewald; Ann. Physik.; 1921; **64**; 253.

[35] C. Kittel; Introduction to Solid state Physics, John Willy Sons Inc. New York; 1953.

[36] A.R. Leach; Molecular Modelling, Principles and Applications; 1999.

[37] C. Kittel; introduction to solid state Physics, 1996.

[38] D.E. Parry; Surface Science; 1975; **49**; 433.

[39] D.M. Hayes, M. Baber, and J.H.R. Clarke; J. Chem. Soc. Faraday Trans.; 1977; **10**; 1485.

[40] M.J. Norgett, R. Fletcher; J. Phys. C.; 1970; **3**; L190.

[41] M. Born, K. Huang; Oxford University Press: Oxford, England, 1954.

[42] W.C. Davidon; AEC Report ANL-5990; 1959.

[43] R. Fletcher, M.J.D. Powell; Computer J.; 1963; **6**; 16.

[44] R. Fletcher' C.M. Reeves; Computer J.; 1964; **7**; 149.

[45] C.R.A. Catlow; Computer Modelling in Inorganic Crystallography, ed. C.R.A. Catlow, Academic Press, London; 1997.

[46] C.R.A. Catlow, M.J. Norgett; UKAEA report AERE-M2936; 1976.

[47] G.W. Watson, E.T. Kelsey, N.H. de Leeuw, D.J. Harris and S.C. Parker, J. Chem. Soc., Faraday Trans. 1996, **92**, 433.

[48] P.W. Tasker; Philos. Mag. A; 1979, **39**; 119.

[49] D.W. Lewis; R.G. Bell; P.A. Wright; C.R.A. Catlow; J.M. Thomas; Stud. Surf. Sci. Catal.; 1997; **105**; 2291.

[50] K. Wright; C.R.A. Catlow; Phys. Chem. Miner.; 1994; **20**; 515.

[51] P.M. Oliver; S.C. Parker; R.G. Egdell; F.H. Jones; J. Chem. Soc. Faraday Trans.; 1996; **92**, 2049.

[52] J.H. Harding; D.J. Harris; S.C. Parker; Phys. Rev. B; 1999; **60**; 2740.

[53] N.H. de Leeuw; G.W. Watson; S.C. Parker; J. Phys. Chem.; 1995; **99**, 17219.

[54] N.H. de Leeuw, S.C. Parker and K.H. Rao; Langmuir; 1998; **14**; 5900.

[55] J.D. Gale; GULP Manual.

[56] F. Bertaut; C. R. Acad. Sci.; Paris; 1958; 3447.

[57] P.M. Oliver; S.C. Parker;W.C. Mackrodt; Medelling Simul. Mater. Sci. Eng.; 1993; **1**; 755.

[58] G. Wulff; Z. Kristallogr. Kristallgeom.; 1901; **39**; 449.

[59] J.W. Gibbs; in Collected works; Longman; New York; 1928.

[60] V.L. Tauson, M.G. Abromovich, V.V. Akimov; Geochim. Cosmochim. Acta.; 1993; **54**(4); 815.

[61] S.C. Parker, 2002, private communication

[62] M.B. Taylor, C.E. Sims, G.D. Barrera and N.L. Allan, Phys. Rev. B 1999, **59**, 6742.

[63] A.M. Stoneham; Defects and their Structure in Non-metallic Solids, edited by B. Henderson and A.E. Hughes, Olenum, New York; 1976.

[64] M.P.Allen, D.J. Tildelsley; Oxford University Press, Oxford; 1993.

[65] P.W.M. Jacobs, Z.A. Reycerz; Academic Press, London, ed. by C.R.A. Catlow; 1997.

[66] C.W. Gear; Report ANL 7126' Argonne National Laboratory; 1966.

[67] W.F. va Guntersten, H.J.C. Berendsen; Mol. Phys.; 1977; **34**; 1311.

[68] H.J.C. Berendsen, W.F. va Guntersten; Proc. Enreico Fermi Summer School, North holland, Amsterdam; 1986; 43.

[69] L. Verlet; Phys. Rev.; 1967; $bf159$; 98.

[70] R.W. Hockney; Methods Comput. Phys.; 1970; $bf9$; 136.

[71] D. Potter; Computational Physics, Wiley, New Y ork; 1972.

[72] W.C. Swope, H.C. Underson, P.H. Berens, K.R. Wilson; Chem. Phys.; 1982; **76**; 637.

[73] D. Beeman; J. Comp. Phys.; 1976; **20**; 130.

[74] R. Elliot; The Physics and Chemistry of Solids; 2000.

[75] T.R. Forester and W. Smith; DL_POLY user manual; Daresburay Laboratoty, England, UK.

[76] V. Milman, B. Winkler, J.A White et al, Int. J. Quant. Chem. **77**, 2000, 895.

[77] E. Wimmer, Materials Science and Engineering, **B37**, 1996, 72-82.

[78] R. Dovesi, V.R. Saunders, C. Roetti, M. Causà, N.M. Harrison, R. Orlando, E. Aprà. CRYSTAL98 Users manual, March 4, 1999.

[79] M.C. Payne, M.P Teter and D.C. Allan, T.A. Arias and J.D. Joannopoulos, Rev. Mod. Phys. **64**, 1992, 1045.

[80] E. Wimmer, Molecular Simulations Inc. documentation, 1997.

[81] J.P Perdew and Y. Wang, Phys. Rev. **B45**, 1992, 13244.

[82] J.H. Harding; Rep. Prog. Phys.; 1990; **53**, 1403-1466.

[83] M.J. Norgett; J. Physics C; 1971; **4**; 298.

[84] I.D. Faux; J. Physics C; 1971; **4**; L211.

[85] B. G. Dick, A.W. Overhouser; Phys. Rv. 1958; **B112**; 90.

[86] C.R.A. Catlow; P.S. Baram; S.C. Parker; J. Purton; K.V. Wright; Phil. Trans. R. Soc. Lond. A, 1995; **350**; 265.

[87] C.M. Freeman; J.M.Newsam; C.R.A.Catlow; J. Mater. Chem. 1993; **3**(**5**); 531.

[88] E.A. Colbourn; Surf. Sci. Reports.; 1992; **25**; 281.

[89] W.C. Mackrodt; R.F. Stewart; J. Phys. 1979; C **12**; 5015.

[90] J.D. Gale; C.R.A. Catlow and W.C. Mackrodt; Modelling Simul. Mater. Sci. Eng.; 1992; **1**; 73.

[91] L.G. Ferreira, V. Ozalins, A. Zunger; Phys. Rev. B; 1999; **60**; 1687.

[92] Y. Mishin, D. Farkas, M.J. Mehl and D.A. Papaconstantopoulos; Phys. Rev. B; 1999; **59**; 3393.

[93] Y. Mishin, M.J. Mehl and D.A. Papaconstantopoulos, A.F. Voter and J.D. Kress; Phys. Rev. B; 2001; **63**; 224106.

[94] Y. Mishin, M.J. Mehl and D.A. Papaconstantopoulos; Phys. Rev. B; 2002; **65**; 224114.

[95] R.R. Zope and Y Mishin; Phys. Rev. B; 2003; **68**; 024102.

[96] P.J. Lawrence, S.C. Parker, P.W. Tasker; J. Amer. Ceram. Soc; 1988; **71**; 389.

[97] G.V. Lewis; C.R.A. Catlow; J. Phys-C-Solid State Phys.; 1985; **18**(6); 1149.

[98] T.S. Bush; J.D. Gale; C.R.A Catlow; P.D. Battle; J. Matter. Chem.; 1994; **4**(6); 831.

[99] G.D. Price; S.C. Parker; M. Leslie; Phys. Chem. Miner.; 1987; **15**(2); 181.

[100] A.N. Cormack; G.V. Lewis; S.C. Parker; C.R.A. Catlow; J. Phys. Chem. Solids; 1988; **49**(1); 53.

[101] J. Purton; C.R.A Catlow; Amer. Mineral. 1990; **75**(11-12); 1268.

[102] G.B. Telfer; J.D. Gale; K.J. Roberts; R.A. Jackson; P.J. Wilde; P. Meenan; Acta. Crystallogr. A; 1997; **53**; 415.

[103] V. Swamy; J.D. Gale; Phys. Rev. B; 2000; **62**(9); 5406.

[104] S. Girard; J.D. Gale; C. Mellot-Draznieks; G. Ferey; Chem. Mater.; 2001; **13**(5); 1732.

[105] S.C. Parker and G.D. Price, Advances in Solid State Chemistry, 1989, **1**, 295.

[106] J.D. Gale, J. Chem. Soc. Faraday Trans. 1997, **93**, 629.

[107] W.T. Lee, M.T. Dove and E.K.H. Salje, J. Phys. Condens. Matter 2000, **12**, 9829.

[108] C. Meis, J.D. Gale, L. Boyer, J. Carpena and D. Gosset, J. Phys. Chem. A, 2000, **104**, 5380.

[109] A. Pavese, M. Catti, S.C. Parker and A. Wall, Phys. Chem. Miner., 1996, **23**, 89.

[110] C.R.A. Catlow, M.J. Norgett and A. Ross, J. Phys. C 1977, **10**, 1630.

[111] N.H. de Leeuw, Chem. Mater. 2002, **14**, 435.

[112] D.R. Lide, in CRC Handbook of Chemistry and Physics, **CRC**, Boca Raton, F**L** 2000.

[113] M.G. Taylor, S.F. Parker, K. Simkiss and P.C.H. Mitchell, Phys. Chem. Chem. Phys. 2001, **3**, 1514.

[114] N.H. de Leeuw and S.C. Parker, J. Chem. Soc. Faraday Trans. 1997, **93**, 467.

[115] N.H. de Leeuw, S.C. Parker and J.H. Harding, Phys. Rev. B 1999, **60**, 13792.

[116] N.H. de Leeuw and S.C. Parker, J. Chem. Phys. 2000, $_{112}$, 4326.

[117] N.H. de Leeuw and S.C. Parker, Phys. Chem. Chem. Phys. 2001, **3**, 3217.

[118] N.H. de Leeuw and S.C. Parker, Phys. Rev. B 1998, **58**, 13901.

[119] N.H. de Leeuw and S.C. Parker, J. Phys. Chem. B 1998, **102**, 2914.

[120] N.H. de Leeuw and S.C. Parker, Mol. Simul. 2000, **24**, 71.

[121] R.D. Shannon and G.R. Rossman, Phys. Chem. Miner. 1992, **19**, 157.

[122] www.deltacnt.com/99-00032.htm or 9-00032.pdf

[123] S. Hontsu, T. Matsumoto, J. Ishii, M. Nakamori, H. Tabata and T. Kawai, Thin Solid Films 1997, **295**, 214.

[124] M.C. Sha, Z. Li and R.C. Brandt, J. Appl. Phys. 1994, $bf75$, 7784.

[125] P. Comodi, Y. Liu, P.F. Zanazzi and M. Montagnoli, Phys. Chem. Miner. 2001, **28**, 219.

[126] M.J. Sanders; M. Leslie; C.R.A Catlow; J. Chem. Soc. Chem. Commun. 1984, 1271.

[127] K.P. Schröder; J. Sauer; M. Leslie; C.R.A. Catlow; Chem. Phys. Lett. 1992, **188**, 320.

[128] O. Sneh, S.M. George; J. Phys. Chem.; 1995; **99**; 4639.

[129] C.M. Koretsky, D.A. Sverjensky, J.W. Salisbury, D.M. D'Aria; Geochim. Cosmochim. Acta; 1997; **61**; 2193.

[130] P. Dauber-Osguthorpe; V.A. Roberts; D.J. Osguthorpe; J. Wolff; M. genest; A.T. Hagler; Proteins: Structure, Functions and 1988; **4**; 31.

[131] . T.G. Cooper; PHD Thesis; University of Reading; UK; 2003.

[132] S.C. Parker, N.H. de Leeuw and S.E. Redfern, Faraday Discussions, 1999, **114**, 381.

[133] N.H. de Leeuw, Chem. Commun. 2001, 1646.

[134] Z. Duan, N. Moller and J.H. Weare, Geochim. Cosmochim. Acta 1995, **59**, 3273.

[135] T.G. Cooper and N.H. de Leeuw, J. Matter. Chem., 2004, 1927 - 1935.

[136] P.A. Mulheran, Philos. Mag. A 1993, **68**, 799.

[137] N.L. Allan, G.D. Barrera, J.A. Purton, C.E. Sims, M.B. Taylor, Phys. Chem. Chem. Phys. 2000, **2**, 1099.

[138] S.C. Parker, E.T. Kelsey, P.M. Oliver and J.O. Titiloye, Faraday Discuss. 1993, **95**, 75.

[139] N.H. de Leeuw, S.C. Parker, C.R.A. Catlow, G.D. Price, Phys. Chem. Miner. 2000, **27**, 332.

[140] N.M. Harrison, X.G. Wang, J. Muscat and M. Scheffler; Faraday Discuss.; 1999; **114**; 305.

[141] J.O. Titiloye, S.C. Parker and S. Mann, J. Cryst. Growth, 1993, **131**, 533.

[142] D.H. Gay and A.L. Rohl, J. Chem. Soc. Faraday Trans. 1995, **91**, 925.

[143] J. Rakovan and R.J. Reeder, Am. Miner. 1994, **79**, 892.

[144] S. Weiner H.D. Wagner, Ann. Rev. Mater. Sci. 1998, **28**, 271.

[145] N.H. de Leeuw; S.C. Parker; C.R.A. Catlow; G.D. Price; Am. Mineral. 2000, **85**, 1143.

[146] J.H. Harding; D.J. Harris; S.C. Parker; Phys. Rev. B 1999, **60**, 2740.

[147] D.C. Sayle; C.R.A. Catlow; J.H. Harding; M.J.F. Healy; S.A. Maicaneanu; S.C. Parker; B. Slater; G.W. Watson; J. Mat. Chem. 2000, **10**, 1315.

[148] G. Attard; C. Barnes; Surfaces, Oxford University Press: Oxford, 1998.

[149] E.S Dana; Manual of Mineralogy; C.S Hurlbut, Ed.; John Willy and Sons: London, 1941.

[150] T.S.B. Narasaraju, D.E.J Phebe, J. Mater. Sci. 1996, **31**, 1.

[151] T.G. Cooper, N.H. de Leeuw; J. Mater. Chem., 2004; **14**; 1927.

Appendix A

Fluorapatite Surfaces Slices

In this section we show the various possible cuts (Code) for each surface studied in fluorapatite. The miller index shows the surface, eg. Miller Index 001 represent the {0 0 0 1} surface. The "height" is the depth of the surface, "charge atom" represent the charge, and the "atom arrangement" represent the atoms that are at that particular depth of the surface. Each code has its unique arrangement of atoms, which could be classified under the three types of surfaces discussed in chapter 2. There are other cuts that are repeating themselves on different codes, such as code (34) and code (68) in the {0 0 0 1} surface, where either one of the cuts should be considered in the calculations.

Table 1: Miller Index: **{0 0 0 1}**, **Zone Axis:** 0.00000E+00 0.00000E+00 1.00000, **PLDRAW:** Code (34) with dipole = -1.1208811656615580E-12

height	**charge**	**atom arrangement**
0.2	2.0	CA–
0.4	0.0	
0.6	0.0	
0.8	0.0	
1.0	0.0	
1.2	0.0	
1.4	0.0	
1.6	0.0	
1.8	-4.0	F–CA–CA–CA–POOOO–POOOO–POOOO–F–
2.0	0.0	
2.2	0.0	
2.4	0.0	
2.6	0.0	
2.8	0.0	
3.0	0.0	
3.2	0.0	
3.4	0.0	
3.6	4.0	CA–CA–
3.8	0.0	
4.0	0.0	
4.2	0.0	
4.4	0.0	
4.6	0.0	
4.8	0.0	
5.0	0.0	
5.2	-4.0	F–CA–CA–CA–POOOO–POOOO–POOOO–F–
5.4	0.0	
5.6	0.0	
5.8	0.0	
6.0	0.0	
6.2	0.0	
6.4	0.0	
6.6	0.0	
6.8	0.0	
7.0	2.0	CA–

Table 2: Miller Index: **{0 0 0 1}**, **Zone Axis:** 0.00000E+00 0.00000E+00 1.00000, **PLDRAW:** Code (68) with dipole = -1.1546319456101628E-12

height	**charge**	**atom arrangement**
0.2	2.0	CA–
0.4	0.0	
0.6	0.0	
0.8	0.0	
1.0	0.0	
1.2	0.0	
1.4	0.0	
1.6	0.0	
1.8	-4.0	F–CA–CA–CA–POOOO–POOOO–POOOO–F–
2.0	0.0	
2.2	0.0	
2.4	0.0	
2.6	0.0	
2.8	0.0	
3.0	0.0	
3.2	0.0	
3.4	0.0	
3.6	4.0	CA–CA–
3.8	0.0	
4.0	0.0	
4.2	0.0	
4.4	0.0	
4.6	0.0	
4.8	0.0	
5.0	0.0	
5.2	-4.0	F–CA–CA–CA–POOOO–POOOO–POOOO–F–
5.4	0.0	
5.6	0.0	
5.8	0.0	
6.0	0.0	
6.2	0.0	
6.4	0.0	
6.6	0.0	
6.8	0.0	
7.0	2.0	CA–

Table 3: Miller Index: **{1 0 $\bar{1}$ 0}**, **Zone Axis:** 0.8660254037844605 0.4999999999999621 0.0000000000000000E+00, **PLDRAW:** Code (1) with dipole = 9.7699626167013776E-14

height	**charge**	**atom arrangement**
0.2	-3.0	POOOO–
0.4	-3.0	POOOO–
0.6	4.0	CA–CA–
0.8	0.0	
1.0	0.0	
1.2	0.0	
1.4	4.0	CA–CA–
1.6	0.0	
1.8	0.0	
2.0	0.0	
2.2	0.0	
2.4	0.0	
2.6	0.0	
2.8	0.0	
3.0	0.0	
3.2	-3.0	POOOO–
3.4	2.0	CA–F–F–F–F–CA–
3.6	-3.0	POOOO–
3.8	0.0	
4.0	0.0	
4.2	0.0	
4.4	0.0	
4.6	0.0	
4.8	0.0	
5.0	0.0	
5.2	0.0	
5.4	4.0	CA–CA–
5.6	0.0	
5.8	0.0	
6.0	0.0	
6.2	4.0	CA–CA–
6.4	-3.0	POOOO–
6.6	0.0	
6.8	-3.0	POOOO–

Table 4: Miller Index: **{1 0 $\bar{1}$ 0}**, **Zone Axis:** 0.8660254037844605 0.4999999999999621 0.0000000000000000E+00, **PLDRAW:** Code (22) with dipole = 1.0658141036401503E-13

height	**charge**	**atom arrangement**
0.2	2.0	CA–
0.4	0.0	
0.6	0.0	
0.8	0.0	
1.0	0.0	
1.2	0.0	
1.4	0.0	
1.6	0.0	
1.8	-3.0	POOOO–
2.0	2.0	CA–
2.2	0.0	F–F–F–F–CA–
2.4	-3.0	POOOO–
2.6	0.0	
2.8	0.0	
3.0	0.0	
3.2	0.0	
3.4	0.0	
3.6	0.0	
3.8	0.0	
4.0	0.0	
4.2	4.0	CA–CA–
4.4	0.0	
4.6	0.0	
4.8	4.0	CA–CA–
5.0	0.0	
5.2	-3.0	POOOO–
5.4	-3.0	POOOO–
5.6	0.0	
5.8	0.0	
6.0	0.0	
6.2	0.0	
6.4	0.0	
6.6	0.0	
6.8	0.0	
7.0	-3.0	POOOO–
7.2	-3.0	POOOO–

height	charge	atom arrangement
7.4	0.0	
7.6	4.0	CA–CA–
7.8	0.0	
8.0	0.0	
8.2	2.0	CA–

Table 5: Miller Index: **{1 0 $\bar{1}$ 0}**, **Zone Axis:** 0.8660254037844605 0.4999999999999621 0.0000000000000000E+00, **PLDRAW:** Code (48) with dipole = 1.2434497875801753E-13

height	**charge**	**atom arrangement**
0.2	2.0	CA–
0.4	0.0	
0.6	0.0	
0.8	4.0	CA–CA–
1.0	-3.0	POOOO–
1.2	0.0	
1.4	-3.0	POOOO–
1.6	0.0	
1.8	0.0	
2.0	0.0	
2.2	0.0	
2.4	0.0	
2.6	0.0	
2.8	-3.0	POOOO–
3.0	-3.0	POOOO–
3.2	0.0	
3.4	4.0	CA–CA–
3.6	0.0	
3.8	0.0	
4.0	2.0	CA–
4.2	2.0	CA–
4.4	0.0	
4.6	0.0	
4.8	0.0	
5.0	0.0	
5.2	0.0	
5.4	0.0	
5.6	0.0	
5.8	-3.0	POOOO–
6.0	2.0	CA–
6.2	0.0	F–F–F–F–CA–
6.4	-3.0	POOOO–
6.6	0.0	
6.8	0.0	

height	charge	atom arrangement
7.0	0.0	
7.2	0.0	
7.4	0.0	
7.6	0.0	
7.8	0.0	
8.0	0.0	
8.2	2.0	CA–

Table 6: Miller Index: **{1 0 $\bar{1}$ 0}**, **Zone Axis:** 0.8660254037844605 0.4999999999999621 0.0000000000000000E+00, **PLDRAW:** Code (69) with dipole = 1.6697754290362354E-13

height	**charge**	**atom arrangement**
13.0	-3.0	POOOO–
13.2	-3.0	POOOO–
13.4	0.0	
13.6	4.0	CA–CA–
13.8	0.0	
14.0	0.0	
14.2	2.0	CA–
14.4	2.0	CA–
14.6	0.0	
14.8	0.0	
15.0	0.0	
15.2	0.0	
15.4	0.0	
15.6	0.0	
15.8	0.0	
16.0	-3.0	POOOO–
16.2	2.0	CA–
16.4	0.0	F–F–F–F–CA–
16.6	-3.0	POOOO–
16.8	0.0	
17.0	0.0	
17.2	0.0	
17.4	0.0	
17.6	0.0	
17.8	0.0	
18.0	0.0	
18.2	0.0	
18.4	4.0	CA–CA–
18.6	0.0	
18.8	0.0	
19.0	4.0	CA–CA–
19.2	0.0	
19.4	-3.0	POOOO–
19.6	-3.0	POOOO–

Table 7: Miller Index: **{1 0 $\bar{1}$ 1}**, **Zone Axis:** 0.5596421974361950 0.3231095733396282 0.7631518947529845, **PLDRAW:** Code (1) with dipole = -7.9403150721191196E-13

height	**charge**	**atom arrangement**
0.2	2.0	CA–
0.4	0.0	
0.6	0.0	
0.8	0.0	
1.0	-1.0	POOOO–CA–
1.2	0.0	
1.4	1.0	CA–F–F–
1.6	-3.0	POOOO–
1.8	2.0	CA–
2.0	-3.0	POOOO–
2.2	0.0	
2.4	0.0	
2.6	2.0	CA–
2.8	2.0	CA–
3.0	0.0	
3.2	0.0	
3.4	-3.0	POOOO–
3.6	2.0	CA–
3.8	-3.0	POOOO–
4.0	1.0	F–F–CA–
4.2	0.0	
4.4	2.0	CA–
4.6	-3.0	POOOO–
4.8	0.0	
5.0	0.0	
5.2	0.0	
5.4	2.0	CA–

Table 8: Miller Index: **{1 0 $\bar{1}$ 1}**, **Zone Axis:** 0.5596421974361950 0.3231095733396282 0.7631518947529845, **PLDRAW:** Code (35) with dipole = -7.9047879353311146E-13

height	**charge**	**atom arrangement**
0.2	2.0	CA–
0.4	0.0	
0.6	0.0	
0.8	-3.0	POOOO–
1.0	2.0	CA–
1.2	-3.0	POOOO–
1.4	1.0	F–F–CA–
1.6	0.0	
1.8	-1.0	CA–POOOO–
2.0	0.0	
2.2	0.0	
2.4	0.0	
2.6	4.0	CA–CA–
2.8	0.0	
3.0	0.0	
3.2	0.0	
3.4	0.0	
3.6	-1.0	POOOO–CA–
3.8	0.0	
4.0	1.0	CA–F–F–
4.2	-3.0	POOOO–
4.4	2.0	CA–
4.6	-3.0	POOOO–
4.8	0.0	
5.0	0.0	
5.2	2.0	CA–

Table 9: Miller Index: **{1 1 $\overline{2}$ 0}**, **Zone Axis:** 0.5000000000000379 0.8660254037844167 0.0000000000000000E+00, **PLDRAW:** Code (2) with dipole = 9.2903462700633099E-13

height	**charge**	**atom arrangement**
0.2	2.0	CA–
0.4	-3.0	POOOO–
0.6	0.0	
0.8	-3.0	POOOO–
1.0	0.0	
1.2	4.0	CA–CA–
1.4	-3.0	POOOO–
1.6	0.0	
1.8	0.0	
2.0	0.0	
2.2	0.0	
2.4	6.0	CA–CA–F–F–F–F–CA–CA–
2.6	0.0	
2.8	0.0	
3.0	0.0	
3.2	0.0	
3.4	-3.0	POOOO–
3.6	4.0	CA–CA–
3.8	0.0	
4.0	-3.0	POOOO–
4.2	0.0	
4.4	-3.0	POOOO–
4.6	0.0	
4.8	2.0	CA–

Table 10: Miller Index: **{1 1 $\bar{2}$ 0}**, **Zone Axis:** 0.5000000000000379 0.8660254037844167 0.0000000000000000E+00, **PLDRAW:** Code (23) with dipole = 9.2725827016693074E-13

height	**charge**	**atom arrangement**
0.2	-3.0	POOOO–
0.4	0.0	
0.6	0.0	
0.8	0.0	
1.0	0.0	
1.2	6.0	CA–CA–F–F–F–F–CA–CA–
1.4	0.0	
1.6	0.0	
1.8	0.0	
2.0	0.0	
2.2	-1.0	POOOO–CA–
2.4	2.0	CA–
2.6	0.0	
2.8	-3.0	POOOO–
3.0	0.0	
3.2	-3.0	POOOO–
3.4	4.0	CA–CA–
3.6	0.0	
3.8	-3.0	POOOO–
4.0	0.0	
4.2	-3.0	POOOO–
4.4	0.0	
4.6	4.0	CA–CA–

Table 11: Miller Index: **{1 1 $\bar{2}$ 0}**, **Zone Axis:** 0.5000000000000379 0.8660254037844167 0.0000000000000000E+00, **PLDRAW:** Code (49) with dipole = 9.3436369752453174E-13

height	**charge**	**atom arrangement**
0.2	4.0	CA–CA–
0.4	0.0	
0.6	-3.0	POOOO–
0.8	0.0	
1.0	-3.0	POOOO–
1.2	2.0	CA–
1.4	2.0	CA–
1.6	-3.0	POOOO–
1.8	0.0	
2.0	-3.0	POOOO–
2.2	0.0	
2.4	4.0	CA–CA–
2.6	-3.0	POOOO–
2.8	0.0	
3.0	0.0	
3.2	0.0	
3.4	0.0	
3.6	6.0	CA–CA–F–F–F–F–CA–CA–
3.8	0.0	
4.0	0.0	
4.2	0.0	
4.4	0.0	
4.6	-3.0	POOOO-

Table 12: Miller Index: **{1 1 $\bar{2}$ 1}**, **Zone Axis:** 0.4131130798113238 0.7155328435043972 0.5633385599755396, **PLDRAW:** Code (4) with dipole = 1.1368683772161603E-13

height	**charge**	**atom arrangement**
0.2	6.0	CA–CA–CA–
0.4	0.0	
0.6	0.0	
0.8	0.0	
1.0	1.0	CA–F–F–
1.2	-3.0	POOOO–
1.4	0.0	
1.6	-3.0	POOOO–
1.8	0.0	
2.0	1.0	POOOO–CA–CA–
2.2	-3.0	POOOO–
2.4	-3.0	POOOO–
2.6	0.0	
2.8	-3.0	POOOO–
3.0	1.0	F–F–CA–
3.2	0.0	
3.4	0.0	
3.6	0.0	
3.8	0.0	
4.0	6.0	CA–CA–CA–

Table 13: Miller Index: **{1 1 $\overline{2}$ 1}**, **Zone Axis:** 0.4131130798113238 0.7155328435043972 0.5633385599755396, **PLDRAW:** Code (38) with dipole = 1.1457501614131615E-13

height	**charge**	**atom arrangement**
0.2	-1.0	CA–POOOO–
0.4	-3.0	POOOO–
0.6	0.0	
0.8	-3.0	POOOO–
1.0	1.0	F–F–CA–
1.2	0.0	
1.4	0.0	
1.6	0.0	
1.8	0.0	
2.0	12.0	CA–CA–CA–CA–CA–CA–
2.2	0.0	
2.4	0.0	
2.6	0.0	
2.8	0.0	
3.0	1.0	CA–F–F–
3.2	-3.0	POOOO–
3.4	0.0	
3.6	-3.0	POOOO–
3.8	-3.0	POOOO–
4.0	2.0	CA–

Table 14: Miller Index: **{1 0 $\bar{1}$ 3}**, **Zone Axis:** 0.2352516520489299 0.1358226046377401 0.9623974648125738, **PLDRAW:** Code (1) with dipole = -1.0818013151947525E-12

height	**charge**	**atom arrangement**
0.2	2.0	CA–
0.4	-1.0	POOOO–CA–
0.6	-2.0	POOOO–F–F–CA–
0.8	-1.0	CA–POOOO–
1.0	0.0	
1.2	4.0	CA–CA–
1.4	0.0	
1.6	-1.0	POOOO–CA–
1.8	-2.0	CA–F–F–POOOO–
2.0	-1.0	CA–POOOO–
2.2	2.0	CA–

Table 15: Miller Index: **{1 0 $\bar{1}$ 3}**, **Zone Axis:** 0.2352516520489299 0.1358226046377401 0.9623974648125738, **PLDRAW:** Code (35) with dipole = -1.0782486015159520E-12

height	**charge**	**atom arrangement**
0.2	2.0	CA–
0.4	-1.0	POOOO–CA–
0.6	1.0	CA–F–F–
0.8	-1.0	POOOO–CA–
1.0	-3.0	POOOO–
1.2	4.0	CA–CA–
1.4	-3.0	POOOO–
1.6	-1.0	CA–POOOO–
1.8	1.0	F–F–CA–
2.0	-1.0	CA–POOOO–
2.2	0.0	
2.4	2.0	CA–

Appendix B

DATA USED IN THE CALCULATION OF VARIOUS ENERGIES.

In this section we show the various data used to calculate the different energies in the thesis. viz: Surface energies of both the dry and hydrated surfaces, adsorption energies of organic molecules on fluorapatite surfaces and adhesion energies of the interfaces between the fluorapatite and α-quartz.

Table 16: Energies used to calculate surface energies (from equation 2.40) for different region sizes of fluorapatite {0001} surface in chapter 4 table 4.1. With U_B always divided by 2 (two) to get the energy of equal number of species to the surface. Resulting surfaces were multiplied by a conversion factor: 16.021 to have them in Jm^{-2}.

Surface	**Region**	$\mathbf{U}_B$ (eV)	$\mathbf{U}_{s-unrel}$ (eV)	$\mathbf{U}_{s-rel}$ (eV)	**Area** ($\AA^2$)	γ_{untel} (Jm^{-2})	γ_{rel} (Jm^{-2})
{0001}	1	-937.7156	-463.2040	-465.1701	75.95	1.1926	0.7779
	2	-1864.1240	-926.4081	-928.3895	75.95	1.1927	0.7747
	3	-2790.5321	-1389.6121	-1391.5940	75.95	1.1927	0.7746
	4	-3716.9401	-1852.8161	-1854.7980	75.95	1.1927	0.7746
	5	-4643.3482	-2316.0201	-2318.0020	75.95	1.1927	0.7746
	6	-5569.7562	-2779.2242	-2781.2061	75.95	1.1927	0.7746

Table 17: Surface energies of bulk-terminated and geometry optimised dehydrated/dry fluorapatite surfaces calculated from equation 2.40 multiplied by 16.021 to have the final value in Jm^{-2}. N.B. U_B is always divided by 2 (two) to get the energy of equal number of species to the surface. From chapter 4, table 4.2

Miler	$\mathbf{U}_B$ (eV)	$\mathbf{U}_{S_{unrel}}$ (eV)	$\mathbf{U}_{S_{rel}}$ (eV)	**Area** ($\AA^2$)	$\gamma_{unrelaxed}$ (Jm^{-2})	$\gamma_{relaxed}$ (Jm^{-2})
{0001}	-3716.94	-1852.82	-1854.80	75.95	1.19	0.77
$\{10\bar{1}0\}$	-3728.45	-1852.82	-1858.92	64.32	2.84	1.32
$\{10\bar{1}1\}$	-3728.11	-1852.82	-1857.84	99.53	1.81	1.00
$\{11\bar{2}0\}$	-3737.33	-1852.82	-1860.88	111.4	2.28	1.12
$\{11\bar{2}1\}$	-3749.72	-1852.82	-1865.48	134.83	2.62	1.11

Table 18: Surface energies (from equation 2.41 multiplied by 16.021) and hydration energies (from equation 2.42 multiplied by 96.4856) of hydrated fluorapatite surfaces. N.B. U_B is always divided by 2 (two) to get the energy of equal number of species to the surface. Chapter 4, table 4.3.

Miller	**n**	$\mathbf{U}_B$ (eV)	$\mathbf{U}_S$ (eV)	$\mathbf{U}_H$ (eV)	$\mathbf{U}_{(H_2O)_{Liq}}$ (eV)	$\mathbf{U}_{(H_2O)_{gas}}$ (eV)	**Area** ($\mathring{A}^2$)	$\gamma_{hydr.}$ (Jm^{-2})
{0001}	5	-3716.94	-1854.8	-1904.10	-47.75	-45.50	75.95	0.45
$\{10\bar{1}0\}$	5	-3728.45	-1858.92	-1908.95	-47.75	-45.50	64.32	0.75
$\{10\bar{1}1\}$	6	-3728.11	-1857.84	-1917.58	-57.30	-54.60	99.53	0.61
$\{11\bar{2}0\}$	6	-3737.33	-1860.88	-1920.98	-57.30	-54.60	111.40	0.72
$\{11\bar{2}1\}$	5	-3749.72	-1865.48	-1915.19	-47.75	-45.5	134.83	0.88
$\mathbf{E}_{ads.}$ ($kJmol^{-1}$)								
-73								
-87								
-83								
-88								
-81								

Table 19: Adsorption energies from equation 2.42 ($kJmol^{-1}$) of all different surfaces with different surfactant molecules as discussed in chapter 5, table 5.1

METHANOIC ACID					
miller	**n**	$\mathbf{U}_s$ (eV)	$\mathbf{U}_{surfactant}$ (eV)	$\mathbf{U}_{s+surfactant}$ (eV)	$\mathbf{E}_{ads}$ ($kJmol^{-1}$)
$\{0001\}$	1	-1854.80	-19.85	-1875.74	-105.2
$\{10\bar{1}0\}$	1	-1858.50	-19.85	-1880.11	-170.1
$\{10\bar{1}1\}$	1	-1857.84	-19.85	-1879.10	-136.0
$\{11\bar{2}0\}$	1	-1860.88	-19.85	-1882.51	-171.5
$\{11\bar{2}1\}$	1	-1867.16	-19.85	-1888.44	-134.0
$\{10\bar{1}3\}$	1	-1868.01	-19.85	-1888.96	-105.3
METHYLAMINE					
$\{0001\}$	1	-1854.80	-15.31	-1870.42	-30.3
$\{10\bar{1}0\}$	1	-1858.49	-15.31	-1874.66	-83.0
$\{10\bar{1}1\}$	1	-1857.84	-15.31	-1873.69	-52.0
$\{11\bar{2}0\}$	1	-1860.88	-15.31	-1877.17	-95.3
$\{11\bar{2}1\}$	1	-1867.16	-15.31	-1883.00	-51.3
$\{10\bar{1}3\}$	1	-1868.01	-15.31	-1883.58	-25.0

HYDROXAMIC ACID "CIS"					
miller	**n**	$\mathbf{U}_s$ (eV)	$\mathbf{U}_{surfactant}$ (eV)	$\mathbf{U}_{s+surfactant}$ (eV)	$\mathbf{E}_{ads}$ ($kJmol^{-1}$)
$\{0001\}$	1	-1854.80	-25.82	-1881.78	-112.24
$\{10\bar{1}0\}$	1	-1858.49	-25.82	-1886.42	-203.0
$\{10\bar{1}1\}$	1	-1857.84	-25.82	-1885.58	-185.8
$\{11\bar{2}0\}$	1	-1860.88	-25.82	-1888.62	-185.4
$\{11\bar{2}1\}$	1	-1867.16	-25.82	-1894.74	-169.7
$\{10\bar{1}3\}$	1	-1868.01	-25.82	-1894.85	-98.4
HYDROXAMIC ACID "TRANS"					
$\{0001\}$	1	-1858.49	-26.00	-1885.70	-116.4
$\{10\bar{1}0\}$	1	-1854.80	-26.00	-1881.96	-112.4
$\{10\bar{1}1\}$	1	-1857.84	-26.00	-1885.21	-132.9
$\{11\bar{2}0\}$	1	-1860.88	-26.00	-1888.66	-172.0
$\{11\bar{2}1\}$	1	-1867.16	-26.00	-1894.35	-115.5
$\{10\bar{1}3\}$	1	-1868.01	-26.00	-1895.04	-99.4

HYDROXYETHANAL "CIS"					
miller	**n**	$\mathbf{U}_s$ (eV)	$\mathbf{U}_{surfactant}$ (eV)	$\mathbf{U}_{s+surfactant}$ (eV)	$\mathbf{E}_{ads}$ ($kJmol^{-1}$)
$\{0001\}$	1	-1854.80	-31.10	-1887.37	-142.1
$\{10\bar{1}0\}$	1	-1858.49	-31.10	-1891.62	-196.26
$\{10\bar{1}1\}$	1	-1857.84	-31.10	-1890.94	-193.0
$\{11\bar{2}0\}$	1	-1860.88	-31.10	-1894.18	-212.6
$\{11\bar{2}1\}$	1	-1867.16	-31.10	-1900.18	-185.8
$\{10\bar{1}3\}$	1	-1868.01	-31.10	-1900.51	-134.8
HYDROXYETHANAL "TRANS"					
$\{0001\}$	1	-1854.80	-31.11	-1887.18	-122.8
$\{10\bar{1}0\}$	1	-1858.49	-31.11	-1891.83	-214.6
$\{10\bar{1}1\}$	1	-1857.84	-31.11	-1890.36	-135.9
$\{11\bar{2}0\}$	1	-1860.88	-31.11	-1893.65	-159.6
$\{11\bar{2}1\}$	1	-1867.16	-31.11	-1900.21	-187.3
$\{10\bar{1}3\}$	1	-1868.01	-31.11	-1900.55	-137.4

Table 20: Energies used to calculate adhesion energies in (table 6.1) of thin and thick layer {0001} surface of apatite on an unrelaxed {0001} surface of α-quartz substrate, from equation 6.1 with conversion factor of 16.021 to have results in Jm^{-2}.

Thin Layer					
Angle (degrees)	$\mathbf{E}_{int.}$ (eV)	$\mathbf{E}_{surf-quartz}$ (eV)	$\mathbf{E}_{bulk-apatite}$ (eV)	**Area** ($\mathring{A}^2$)	γ_{adh} (Jm^{-2})
0^0	-6655.56	-6196.13	-463.23	82.04	0.74
60^0	-6654.74	-6196.13	-463.23	82.04	0.90
120^0	-6653.87	-6196.13	-463.23	82.04	1.07
180^0	-6656.08	-6196.13	-463.23	82.04	0.64
240^0	-6653.11	-6196.13	-463.23	82.04	1.22
300^0	-6655.67	-6196.13	-463.23	82.04	0.72
Thick Layer					
0^0	-7115.85	-6196.13	-926.45	82.04	1.31
60^0	-7114.93	-6196.13	-926.45	82.04	1.50
120^0	-7114.29	-6196.13	-926.45	82.04	1.62
180^0	-7114.74	-6196.13	-926.45	82.04	1.53
240^0	-7114.28	-6196.13	-926.45	82.04	1.62
300^0	-7113.78	-6196.13	-926.45	82.04	1.72

Table 21: Energies used to calculate adhesion energies in (table 6.2) of thin and thick layer {0001} surface of apatite on a pre-relaxed {0001} surface of α-quartz substrate, from equation 6.1 with conversion factor of 16.021 to have results in Jm^{-2}.

Thin Layer					
Angle (degrees)	$\mathbf{E}_{int.}$ (eV)	$\mathbf{E}_{surf-quartz}$ (eV)	$\mathbf{E}_{bulk-apatite}$ (eV)	**Area** ($\mathring{A}^2$)	γ_{adh} (Jm^{-2})
0^0	-6656.37	-6196.13	-463.23	82.04	0.58
60^0	-6656.44	-6196.13	-463.23	82.04	0.57
120^0	-6656.44	-6196.13	-463.23	82.04	0.57
180^0	-6655.64	-6196.13	-463.23	82.04	0.73
240^0	-6656.56	-6196.13	-463.23	82.04	0.55
300^0	-6656.02	-6196.13	-463.23	82.04	0.65
Thick Layer					
0^0	-7118.32	-6196.13	-926.45	82.04	0.83
60^0	-7117.21	-6196.13	-926.45	82.04	1.05
120^0	-7118.04	-6196.13	-926.45	82.04	0.89
180^0	-7118.35	-6196.13	-926.45	82.04	0.83
240^0	-7118.37	-6196.13	-926.45	82.04	0.82
300^0	-7116.90	-6196.13	-926.45	82.04	1.11

Table 22: Energies used to calculate adhesion energies in (table 6.3) of thin and thick layer $\{10\bar{1}1\}$ surface of apatite on a pre-relaxed $\{10\bar{1}0\}$ surface of α-quartz substrate, from equation 6.1 with conversion factor of 16.021 to have results in Jm^{-2}.

Thin Layer					
Angle (degrees)	$\mathbf{E}_{int.}$ (eV)	$\mathbf{E}_{surf-quartz}$ (eV)	$\mathbf{E}_{bulk-apatite}$ (eV)	**Area** ($\mathring{A}^2$)	γ_{adh} (Jm^{-2})
0^0	-6651.11	-6193.15	-463.23	104.62	0.81
180^0	-6654.22	-6193.15	-463.23	104.62	0.33
Thick Layer					
0^0	-7112.53	-6193.15	-926.45	104.62	1.08
180^0	-7115.14	-6193.15	-926.45	104.62	0.68

Table 23: Energies used to calculate adhesion energies in (table 6.2) of thin and thick layer {0001} surface of apatite on a hydroxylated {0001} surface of α-quartz substrate, from equation 6.1 with conversion factor of 16.021 to have results in Jm^{-2}.

Thin Layer					
Angle (degrees)	$\mathbf{E}_{int.}$ (eV)	$\mathbf{E}_{surf-quartz}$ (eV)	$\mathbf{E}_{bulk-apatite}$ (eV)	**Area** ($\mathring{A}^2$)	γ_{adh} (Jm^{-2})
0^0	-6629.07	-6172.79	-463.23	82.04	1.36
60^0	-6628.58	-6172.79	-463.23	82.04	1.45
120^0	-6629.00	-6172.79	-463.23	82.04	1.37
180^0	-6629.08	-6172.79	-463.23	82.04	1.35
240^0	-6629.07	-6172.79	-463.23	82.04	1.36
300^0	-6628.58	-6172.79	-463.23	82.04	1.45
Thick Layer					
0^0	-7090.87	-6172.79	-926.45	82.04	1.64
60^0	-7090.91	-6172.79	-926.45	82.04	1.63
120^0	-7090.91	-6172.79	-926.45	82.04	1.63
180^0	-7090.91	-6172.79	-926.45	82.04	1.63
240^0	-7090.87	-6172.79	-926.45	82.04	1.64
300^0	-7090.91	-6172.79	-926.45	82.04	1.63

Table 24: Energies used to calculate adhesion energies in (table 6.2) of thin and thick layer $\{10\bar{1}1\}$ surface of apatite on a hydroxylated $\{10\bar{1}0\}$ surface of α-quartz substrate, from equation 6.1 with conversion factor of 16.021 to have results in Jm^{-2}.

Angle (degrees)	$\mathbf{E}_{int.}$ (eV)	$\mathbf{E}_{surf-quartz}$ (eV)	$\mathbf{E}_{bulk-apatite}$ (eV)	**Area** ($\mathring{A}^2$)	γ_{adh} (Jm^{-2})
0^0	-6631.31	-6177.77	-463.23	104.62	1.48
180^0	-6631.52	-6177.77	-463.23	104.62	1.45
Thick Layer					
0^0	-7093.35	-6177.77	-926.45	104.62	1.66
180^0	-7093.29	-6177.77	-926.45	104.62	1.67

Appendix C

Publications

D. Mkhonto et all, "Computer simulation of Surfaces of Metals and metal-Oxides Materials." Computational Materials Science.; Edited by Richard Catlow and Eugine Kotomin; NATO Science Series III: Computer and Systems Sciences - 2003, Vol. 187, Pages 218-244.

D. Mkhonto, et al, "A computer Modelling Study of the Effect of Water on the Surface Structure and Morphology of Fluorapatite: Introducing a $Ca_{10}(PO_4)_6F_2$ Potential Model." Journal of Materials Chemistry, 2002, Volme 12, Pages 2633-2642.

D. Mkhonto, et al, "A Computer Modeling Study of the Adhesion of Apatite Thin Films on Silicate Surfaces." The journal of Physical Chemistry B, Letters, 2003, Volume 107, Number 1.

D. Mkhonto, et al, "Computer Simulation Study of the Effect of Surface Pre-Relaxation on the Adhesion of Apatite Thin Films to the (0001) Surface

of α-Quartz." Chemistry of Materials, 2003, Volume 15, Number 8, Pages 1567-1574.

Appendix D

Papers presented at conferences

D. Mkhonto, et al, "Computer Simulations of Hydrated Surfaces of Fluorapatite ($Ca_{10}(PO_4)_6F_2$)." Presented at NATO Advanced Science Institute (ASI) in Computational Materials Science, 09-22 September 2001, held at Il Ciocco Conference Centre, Lucca, Italy.

D. Mkhonto, et al, "Computer Simulations of Interfaces of Fluoraptite ($Ca_{10}(PO_4)_6F_2$) and Quartz (SiO_4)." Presented at the Royal Society of Chemistry Solid State Group: Surfaces and Surface Processes in Inorganic Materials, 25-27 March 2002, held at the Mansfield College, Oxford, UK.

D. Mkhonto, et al, "A Computer Modelling Study of the Effect of Water on the Surface Structure and Morphology of Fluorapatite ($Ca_{10}(PO_4)_6F_2$)." Presented at the South African Institute of Physics (SAIP), 23-27 September 2002, held at Potchefstroom University, Potchefstroom. RSA.

D. Mkhonto, et al, "A Computer Simulation Study of the Adhesion of Apatite thin Films to α-Quartz Surfaces". Presented at RSC-Theoretical Chemistry Group / CCP5 Meeting "Modelling of Materials: Atomistic and Ab Initio Approaches" 9-10 April 2003, held at the Mansfield College, Oxford, UK.

D. Mkhonto, et al, "Computational Studies of Interface of Apatite Thin Film with Quartz Surfaces." Presented at the 4^{th} International Workshop on Surface and Interface Segregation, (IWSIS-4), 17-22 August 2003, held at ITHEMBA Labs, Cape Town, RSA.

D. Mkhonto, et al, "Computational Studies of Interface of Apatite Thin Film with Quartz Surfaces." Presented at the Interscience Conference, 1-3 October 2003, held at the University of the North, RSA.

D. Mkhonto, et al, "Atomistic Simulation Studies of the Interface of Apatite Thin Film with α-Quartz Surfaces." Presented at the South African Institute of Physics (SAIP), 29 June-2 July 2004, held at University of Bloemfontein, Bloemfontein, RSA.

D. Mkhonto, et al, "Computer Modelling Study of Fluorapatite Surfaces and Adhesion of Apatite Thin Film on α-quartz Surfaces." Presented at the NRF/RS workshop, 23-24 August 2004, held at the Sheraton Hotel, Pretoria, RSA.